A Novel Methodology to Include Differential Diffusion in Numerical Simulations of Reactive Flows

Een nieuwe methodologie om differentiële diffusie op te nemen in numerieke simulaties van reactieve stromingen

Georgios Maragkos

Promotoren: prof. dr. ir. B. Merci, dr. ir. P. Rauwoens
Proefschrift ingediend tot het behalen van de graad van
Doctor in de Ingenieurswetenschappen: Werktuigkunde-Elektrotechniek

Vakgroep Mechanica van Stroming, Warmte en Verbranding
Voorzitter: prof. dr. ir. J. Vierendeels
Faculteit Ingenieurswetenschappen en Architectuur
Academiejaar 2013 - 2014

UNIVERSITEIT
GENT

ISBN 978-90-8578-649-8
NUR 978
Wettelijk depot: D/2013/10.500/82

Promotors: prof. dr. ir. B. Merci, dr. ir. P. Rauwoens

Vakgroep Mechanica van Stroming, Warmte en Verbranding
Sint-Pietersnieuwstraat 41
B-9000 Gent
België

Acknowledgments

First of all, I would like to thank my promoter, Prof. Bart Merci, for giving me the opportunity to join his group and to work on this project. Thank you for all your support but also for your guidance and valuable discussions that we had during these last 4 years. I feel extremely happy and lucky to have had the opportunity to work with you.

Equally important was the guidance of my co-promoter, Dr. Pieter Rauwoens, who helped me complete this research. His enthusiasm and willingness to share his knowledge and expertise was a real gift to me. Thank you for all the interesting discussions that we had, they provided me with a lot of food for thought.

Further, I would like to express my gratitude to Dr. Yi Wang of FM Global who helped a lot during the first years of my PhD with FireFOAM, the code that I used for my research. Thank you for always being open for discussions and willing to share your knowledge and experiences with me. I would also like to acknowledge the help of Prof. Rob Bastiaans who provided feedback and valuable suggestions for improving my work.

Also thanks to all the colleagues at the department with whom a had a really nice time during lunch times and conference trips. Special gratitude goes to Dr. Dieter Fauconnier for his advices and guidance during my research. His expertise on turbulence and modelling was of big help to me. Also thanks to Yves Maenhout who was always ready to assist me whenever I encountered a computer or server problem. Last but not least, I would like to thank my colleague and friend Dr. Tarek Beji for all the good times that we had together and for all the valuable conversations every Saturday morning during coffee.

A special acknowledgment also goes to Prof. Nikolaos Siakavellas from University of Patras in Greece for introducing me into programming and for sharing his knowledge while working with him. I also wish to express my gratitude to my parents, my brother Andreas Maragkos and to his wife Elena Hadou for their endless support all these years.

Finally, I would especially like to thank my girlfriend Ruxandra Ioana Popescu for all her moral support and for helping me translating the summary of the thesis in dutch.

Summary

There is a great economic and ecologic interest in developing combustion devices that can achieve higher efficiency and lower pollutant emissions, such as carbon monoxide (CO), unburned hydrocarbons and nitrogen oxides (NO_x). In this direction, new fuels like hydrogen can play an important role since they can be burned as a pure substance, or as a component in a fuel, originating from e.g. biomass.

A way of modelling these combustion devices is by performing numerical simulations with Computational Fluid Dynamics (CFD) codes. With the use of numerical simulations, the efficiency and pollutant emissions of the combustion devices can be calculated beforehand over a wide range of parameters with good accuracy and at relatively low cost. Most of the combustion applications usually occur in a turbulent environment. In order for numerical simulations to be able to describe these processes, different approaches exist. The Large Eddy Simulations (LES) approach, in which the turbulent large scales are resolved while the effect of the smaller ones is modelled using sub-grid models, is adopted here because of its ability to capture the unsteady features of the flow at a relatively affordable computation cost.

Numerical simulations of combustion applications typically involve mixtures of different chemical species, each one with different properties. Hydrogen, being a light chemical specie, diffuses faster than other chemical components in a mixture. This differential diffusion effect is typical of light chemical species, like e.g. hydrogen and helium, and occurs at a molecular level. Numerical simulations of turbulent combustion nowadays often rely upon the assumption that every chemical component diffuses at the same rate. Even though this assumption is reasonable in the case of fossil fuels, it is not valid for hydrogen combustion. Mostly, this differential diffusion effect is ignored when performing numerical simulations of turbulent combustion because it either leads to great modelling complications or because it is expected that turbulent mixing is a far more dominant process than molecular mixing. However, there is vast experimental and numerical evidence indicating that molecular differential diffusion can be important in low, moderate and high

Reynolds number flows. Even though differential diffusion effects typically decrease with increasing Reynolds number, they can still be present in turbulent flows close to the combustion nozzle. The inclusion of differential diffusion effects can be important for flame calculations of reacting flows, where an accurate prediction of species is needed, since they are a prerequisite for accurately predicting the local temperatures, chemical reaction rates and pollutant concentrations.

Focus in this thesis is non-premixed combustion, where fuel and oxidizer are initially separated. In this case, the combustion processes depend on the molecular mixing of species and chemical reactions occur only when fuel and oxidizer are well mixed. Two of the main methodologies used in the past decades for modelling non-premixed combustion applications include the solution of transport equations for chemical species and the conserved scalar approach. Differential diffusion effects can be incorporated in both methodologies in physical space (in the transport equations) and in chemical space (in the combustion model). The first method (solution of transport equations for chemical species) is generally the most accurate way of taking into account differential diffusion effects in numerical simulations of reactive flows. The set of equations to be solved is, however, very stiff due to the wide range of chemical scales involved, mainly due to the species chemical source terms. The mathematical formulation of the second method (conserved scalar approach) is based on the assumption that all chemical species have the same mass diffusivity, making the method less suitable for hydrogen combustion.

A new methodology to incorporate differential diffusion effects in CFD simulations of reactive flows is presented in this thesis, by combining the two aforementioned methodologies. Compared to the classical conserved scalar approach, within this new methodology, differential diffusion effects are taken into account in physical space (in the transport equations of the conserved scalars). In this case the diffusion term in the transport equations of the conserved scalars consists of two parts, one expressing the diffusion of the conserved scalars and the other expressing the feedback from the combustion model. The second diffusion term is shown to have a substantial influence in the flow field. With this new methodology, not all transport equations for the conserved scalars have to be solved and differential diffusion effects can easily be incorporated in both physical (transport equations for the conserved scalars) and chemical space (in the combustion model).

In the first part of the thesis, a brief summary of the different methodologies used in research of non-premixed combustion, along with previous modelling efforts of differential diffusion is given. The governing equations used to perform numerical simulations of reactive flows and all the sub-models needed to close them, are presented. The mixture

fraction model is analyzed in order to compare it with the newly proposed methodology presented later in the thesis. In addition, the filtered LES equations are presented along with the sub-models used for turbulence, combustion and turbulence-chemistry interaction. Finally, the mathematical formulation of the new methodology is described for both laminar and turbulent reactive flows and a discussion on its capabilities is given.

The second half of the thesis includes numerical results from the different test cases considered in this research. A validation study of the CFD package FireFOAM 1.6, used for the numerical simulations in the thesis, is presented in order to evaluate its accuracy and capabilities in simulating turbulent flows. Large eddy simulations are conducted in the near-field region of a large turbulent buoyant helium plume and compared to the well-documented experiment performed by O'Hern et al. [79]. In general, the LES calculations reproduce the main features of the turbulent plume. In particular, the puffing cycle is recovered in the simulations with correct frequency. The mean and rms values of the velocity components are well predicted, even on relatively coarse meshes. Agreement for the species mass fraction (mean and rms values) is less satisfactory, but in line with results found in the literature.

The effects of differential diffusion are first investigated in a non-reacting test case and a quantification of their influence with increasing Reynolds number is made. Large eddy simulations of non-reacting H_2/CO_2 jets mixing with air are performed and the calculations are compared with the experiments reported by Smith et al. [106]. The influence of differential diffusion effects for flows with Reynolds number $Re = 1000 - 8000$ is analyzed not only in physical space but also with scatter plots and histograms. The simulation results reveal that differential diffusion effects are significant at downstream locations (more than 15 nozzle diameters away from the inlet) only for the lower Reynolds number flows ($Re = 1000 - 2000$). However, differential diffusion effects are present for all Reynolds number flows examined close to the inlet (closer than 10 nozzle diameters). This is an important indication that differential diffusion should be included in numerical simulations of turbulent reacting flows in order to improve accuracy. The H_2 concentrations are over-predicted by up to 50% on the centerline at all downstream locations examined if differential diffusion is not taken into account.

The newly proposed methodology is then applied to a laminar, axi-symmetric H_2/N_2 - air diffusion flame and the calculations are compared with the experimental data of Toro et al. [115]. If differential diffusion effects are taken into account, the comparison of the simulated results with the experimental data is very good for the temperature and main species mole fractions, at all locations examined. Without differential diffusion effects, the predicted results are not in good agreement with the experiments, due to lack of H_2 diffusion close to the jet inlet. This leads to a wrong prediction of the location and the peak of the flame temperature, but also to a strong over-prediction of the species mole fractions at all locations. Differential diffusion effects are present at the edges of the inlet, where H_2 diffuses faster than other species, and also on the centerline at locations more than 10 nozzle diameters downstream, where there is less H_2 compared to other species. The inclusion of the second diffusion term is shown to be important in order to accurately predict the temperature and species mole fractions.

Subsequently, results from the application of the new methodology to the 'H3' benchmark flame [66, 83] from the Turbulent Non-premixed Flames (TNF) workshop are presented. The study focuses on assessing the accuracy of the proposed methodology but also on examining the influence of differential diffusion in numerical simulations of turbulent reactive flows involving species with vastly different mass diffusivities. Fairly good agreement is obtained between numerical simulations of the proposed methodology and experimental data if differential diffusion effects are considered. Differential diffusion effects are shown to be significant close to the inlet but also to downstream locations up to 20 nozzle diameters. They have a strong influence on the stabilization mechanism of the flame and on the predicted profiles of temperature and species concentration. Temperatures above the adiabatic one are obtained if differential diffusion effects are considered, in line with what is reported in literature in the past, due to faster diffusion of H_2 towards the reaction zone, altering the gas composition at this location. On the other hand, large discrepancies between numerical simulations and experiments are found in the radial and axial profiles of temperature and species concentration if differential diffusion effects are ignored. Again, the second diffusion term is shown to have a substantial influence in the flow field of this test case. It is concluded that incorporation of differential diffusion in numerical simulations of turbulent reactive flows is necessary in order to improve accuracy.

Finally, the main conclusions of this work are summarized, suggestions about modeling differential diffusion in reactive flows are given and plans for future work are presented.

Samenvatting

Het is van groot economisch en ecologisch belang om verbrandingstoestellen te ontwikkelen, die een hogere efficintie en een lagere uitstoot van schadelijke stoffen, zoals koolmonoxide (CO), onverbrande koolwaterstoffen en stikstofoxiden (NO_x) kunnen bereiken. In die zin kunnen nieuwe brandstoffen zoals waterstof een belangrijke rol spelen, aangezien ze als zuivere stof verbrand kunnen worden of als een component in een brandstof die afkomstig is van bijv. biomassa.

Een manier van modellering van deze verbrandingsapparaten is door het uitvoeren van numerieke simulaties met Computational Fluid Dynamics (CFD) codes. Door middel van numerieke simulaties kunnen de efficintie en de verontreinigende emissies op voorhand worden berekend, over een groot bereik aan parameters, met goede nauwkeurigheid en tegen betrekkelijk lage kost. De meeste verbrandingstoepassingen treden meestal in een turbulente omgeving op. Opdat numerieke simulaties deze processen kunnen beschrijven, bestaan er verschillende benaderingen. De Large Eddy Simulation (LES) benadering, waarbij de turbulente grote schaal wordt opgelost terwijl het effect van de kleinere wordt gemodelleerd met behulp van subgrid-scale modellering, wordt hier gebruikt vanwege haar vermogen om de transinte eigenschappen van de stroming vast te leggen tegen relatief betaalbare berekeningskost.

Numerieke simulaties van verbrandingstoepassingen omvatten typisch verschillende chemische species, elk met verschillende eigenschappen. Waterstof, zijnde een lichte chemische specie, diffundeert sneller dan andere chemische componenten in een mengsel. Dit differentiële diffusie effect is kenmerkend voor lichte chemische stoffen, zoals bijvoorbeeld waterstof en helium, en gebeurt op moleculair niveau. Numerieke simulaties van turbulente verbranding baseren zich tegenwoordig vaak op de veronderstelling dat iedere chemische component diffundeert op hetzelfde tempo. Hoewel deze hypothese redelijk is bij fossiele brandstoffen, is het niet geldig voor waterstofverbranding. Meestal wordt dit differentiële diffusie effect genegeerd bij het uitvoeren van numerieke simulaties van turbulente verbranding, ofwel omdat het leidt tot grote vereenvoudigingen in de modellering, ofwel omdat er wordt verwacht dat turbulente menging een veel dominanter proces is dan moleculaire menging. Er bestaat echter uitgebreid experimenteel en numeriek bewijsmateriaal dat aangeeft dat moleculaire differentiële diffusie belangrijk kan zijn bij lage, matige en hoge Reynoldsgetallen. Ook al nemen differentiële diffusie effecten meestal af bij toenemende Reynoldsgetallen, ze kunnen nog steeds aanwezig zijn bij turbulente stromingen dicht bij de branderkop. Het in rekening brengen van differentiële diffusie effecten kan belangrijk zijn voor vlamberekening van reagerende stromingen, waarbij een nauwkeurige voorspelling van species nodig is, aangezien dit een vereiste is voor het nauwkeurig voorspellen van de lokale temperaturen, chemische reactiesnelheden en concentraties van verontreinigende stoffen.

Het onderhavige proefschrift richt zich op niet-voorgemengde verbranding, waarbij brandstof en oxidans aanvankelijk gescheiden zijn. In dit geval zijn de verbrandingsprocessen afhankelijk van de moleculaire menging van species en chemische reacties treden op pas wanneer brandstof en oxidans goed gemengd zijn. Twee van de belangrijkste in de afgelopen decennia ontwikkelde methodologien voor het modelleren van niet-voorgemengde verbrandingstoepassingen, omvatten de oplossing van transportvergelijkingen voor chemische species en de behouden scalaire benadering. Differentiële diffusie effecten kunnen in beide methodologien in fysieke ruimte (in de transportvergelijkingen) en in chemische ruimte (in het verbrandingsmodel) worden opgenomen. De eerste methode (de oplossing van transportvergelijkingen voor chemische species) is over het algemeen de meest accurate manier om rekening te houden met differentiële diffusie effecten in numerieke simulaties van reactieve stromingen. De set van vergelijkingen die moeten worden opgelost is echter zeer ingewikkeld vanwege de brede waaier van de betrokken chemische schalen, voornamelijk als gevolg van de chemische brontermen van de species. De wiskundige formulering van de tweede methode (behouden scalaire benadering) is gebaseerd op de aanname dat alle chemische species dezelfde diffusiecofficint hebben, waardoor de werkwijze minder geschikt wordt voor waterstofverbranding.

Een nieuwe methodologie om differentiële diffusie effecten te verwerken in CFD simulaties van reactieve stromingen wordt gepresenteerd in het onderhavige proefschrift, door het combineren van de twee eerder genoemde methodologien. In tegenstelling tot de behouden scalaire benadering wordt er binnen deze nieuwe methodologie rekening gehouden met differentiële diffusie effecten in de fysieke ruimte (in de transportvergelijkingen van de behouden scalairen), terwijl de nadelen verbonden met de klassieke behouden benadering worden vermeden. In dit geval bestaat de diffusieterm in de transportvergelijkingen van de behouden scalairen uit twee delen, n die de diffusie tussen de behouden scalairen uitdrukt en n die de terugkoppeling van het verbrandingsmodel uitdrukt. De tweede diffusieterm blijkt een aanzienlijke invloed te hebben op het stromingsveld. Met deze nieuwe methodologie moeten niet alle transportvergelijkingen voor de behouden scalairen opgelost worden en differentiële diffusie effecten kunnen eenvoudig in zowel fysieke (transportvergelijkingen voor de behouden scalairen) als in chemische ruimte (in de verbrandingsmodel) worden opgenomen.

In het eerste deel van dit proefschrift wordt er een korte samenvatting gegeven van de verschillende methodologien die bij het onderzoek van niet-voorgemengde verbranding werden gebruikt, samen met voorafgaande inspanningen m.b.t. modellering van differentiële diffusie. De overheersende vergelijkingen gebruikt bij het uitvoeren van numerieke simulaties van reactieve stromingen, samen met alle sub-modellen die nodig waren om hen te sluiten, worden gepresenteerd. Het mengfractiemodel wordt geanalyseerd, teneinde het te vergelijken met de nieuw voorgestelde methodologie later gepresenteerd in dit proefschrift. Bovendien worden de gefilterde LES-vergelijkingen gepresenteerd samen met de sub-modellen voor turbulentie, verbranding en turbulentie-chemie interactie. Ten slotte wordt de wiskundige formulering van de nieuwe methodologie beschreven voor zowel laminaire als turbulente reactieve stromingen en er wordt een discussie over haar mogelijkheden gegeven.

De tweede helft van de thesis omvat numerieke resultaten van verschillende testgevallen die in dit onderzoek behandeld worden. Een valideringsonderzoek van het voor de numerieke simulaties in dit proefschrift gebruikte CFD-pakket FireFOAM 1.6 wordt voorgesteld om zijn nauwkeurigheid en bekwaamheid bij het simuleren van turbulente stromingen te beoordelen. Large Eddy Simulations zijn uitgevoerd in het nabije-veld gebied van een grote turbulente natuurlijk opstijgende helium pluim en vergeleken met het goed gedocumenteerde experiment uitgevoerd door O'Hern et al. [79]. Over het algemeen reproduceren de LES berekeningen de voornaamste kenmerken van de turbulente pluim. In het bijzonder wordt de puf cyclus teruggevonden in de simulaties met de juiste frequentie. De gemiddelde en effectieve waarden van de snelheidscomponenten zijn goed voorspeld, zelfs op relatief grove rekenroosters. Overeenstemming met de species massafractie (gemiddelde en effectieve waarden) is minder bevredigend, maar wel in lijn met resultaten uit de literatuur.

De effecten van differentiële diffusie worden eerst onderzocht in een niet-reagerend testgeval en hun invloed bij een toenemende Reynoldsgetal wordt gekwantificeerd. Large Eddy Simulations van niet-reagerende H_2/CO_2 jets, zich vermengend met lucht, worden uitgevoerd en berekeningen worden vergeleken met de experimenten beschreven door

Smith et al. [106]. De invloed van differentiële diffusie effecten bij Reynoldsgetallen $Re = 1000 - 8000$ wordt geanalyseerd, niet alleen in de fysieke ruimte, maar ook met wolkfiguren en histogrammen. De simulatieresultaten tonen aan dat differentiële diffusie effecten enkel aanzienlijk zijn op stroomafwaartse locaties (meer dan 15 verbrandingspijp-diameters weg van de inlaat) voor de lagere Reynoldsgetallen ($Re = 1000 - 2000$). Differentiële diffusie effecten zijn echter aanwezig voor alle onderzochte Reynoldsgetallen dicht bij de inlaat (dichter dan 10 verbrandingspijp-diameters). Dit is een belangrijke aanwijzing dat differentiële diffusie in numerieke simulaties van turbulente reagerende stromingen moet worden opgenomen om de nauwkeurigheid te verbeteren. De H_2 concentraties worden overschat met maximaal 50% op de centrale as op alle onderzochte stroomafwaartse locaties als men geen rekening houdt met de differentiële diffusie.

De nieuw voorgestelde methodologie wordt vervolgens toegepast op een laminaire, axi-symmetrische H_2/N_2 - lucht diffusievlam en de berekeningen worden vergeleken met de experimentele gegevens van Toro et al. [115]. Als er rekening wordt gehouden met differentiële diffusie effecten, komen de gesimuleerde resultaten zeer goed overeen met de experimentele gegevens voor de temperatuur en de molfracties van de belangrijkste species, op alle onderzochte locaties. Zonder differentiële diffusie effecten zijn de voorspelde resultaten niet in goede overeenstemming met de experimenten, door gebrek aan H_2 diffusie dichtbij de straal inlaat. Dit leidt tot een verkeerde voorspelling van de locatie en de piek van de vlamtemperatuur, maar ook een sterke overschatting van de species molfracties op alle locaties. Differentiële diffusie effecten zijn aanwezig aan de randen van de inlaat, waar H_2 sneller diffundeert dan de andere species, maar ook op de centrale as op locaties meer dan 10 branderkopdiameters stroomafwaarts, waar er minder H_2 voorkomt in vergelijking met andere species. De opname van de tweede diffusieterm blijkt belangrijk te zijn om de temperatuur en de species molfracties nauwkeurig te voorspellen.

Vervolgens worden de resultaten gepresenteerd van de toepassing van de nieuwe methodologie, voor de testvlam 'H3' [66, 83] van de Turbulent Non-premixed Flames (TNF) workshop. De studie richt zich op de beoordeling van de nauwkeurigheid van de voorgestelde methodologie, maar ook op het onderzoek van de invloed van differentiële diffusie in numerieke simulaties van turbulente reactieve stromingen waarbij species worden gebruikt met zeer verschillende diffusiviteitscofficinten. Vrij behoorlijke overeenkomst wordt verkregen tussen numerieke simulaties van de voorgestelde methodologie en experimentele waarnemingen indien differentiële diffusie effecten in rekening worden gebracht. Differentiële diffusie effecten zijn aanzienlijk dicht bij de inlaat, maar ook op stroomafwaartse locaties tot 20 verbrandingspijp-diameters en hebben een sterke invloed op het stabilisatiemechanisme van de vlam, maar ook op de voorspelde temperatuurprofielen en species concentratie. Temperaturen boven de adiabatische evenwichtstemperatuur worden verkregen als de differentiële diffusie effecten worden beschouwd, in lijn met wat in de literatuur van vroeger is vermeld, vanwege de snellere diffusie van H_2 naar de reactiezone, hetgeen de gassamenstelling op deze locatie verandert. Daarentegen worden grote discrepanties tussen numerieke simulaties en experimenten gevonden in de radiale en axiale profielen van temperatuur en species concentraties als de differentiële diffusie effecten genegeerd worden. De tweede diffusieterm blijkt ook een substantile invloed op het stromingsveld van deze testcase te hebben. Geconcludeerd wordt dat de opname van differentiële diffusie in numerieke simulaties van turbulente reactieve stromingen noodzakelijk is om de nauwkeurigheid te verbeteren.

Tenslotte worden de belangrijkste conclusies van dit werk samengevat, worden suggesties over het modelleren van differentiële diffusie in reactieve stromingen gegeven en worden plannen voor toekomstige werkzaamheden gepresenteerd.

Contents

Acknowledgments **iii**

Summary **v**

Samenvatting **ix**

List of Figures **xix**

List of Tables **xxvi**

Nomenclature **xxix**

1 Introduction **1**
- 1.1 Motivation . . . 1
- 1.2 Modelling differential diffusion in reactive flows . . . 2
  - 1.2.1 Transport of chemical species . . . 3
  - 1.2.2 Conserved scalar approach . . . 4
  - 1.2.3 Transported PDF-FDF methods . . . 8
- 1.3 Objectives . . . 8
- 1.4 Outline . . . 9

2 Governing equations **11**
- 2.1 Instantaneous equations . . . 11
- 2.2 Constitutive relations . . . 12
  - 2.2.1 Ideal gas law . . . 12
  - 2.2.2 Viscous stress tensor . . . 13
  - 2.2.3 Diffusion flux . . . 13
  - 2.2.4 Chemical source term . . . 15
  - 2.2.5 Energy flux . . . 16

2.2.6 Caloric equation of state 16
2.3 Mixture fraction 17
2.3.1 Based on species mass fraction 17
2.3.2 Based on elemental mass fractions 20
2.4 Example 21
2.4.1 Based on species mass fraction 21
2.4.2 Based on elemental mass fractions 22
2.5 Large Eddy Simulations 24
2.5.1 Introduction 24
2.5.2 LES filter 24
2.5.3 Filtered conservation equations 25
2.5.4 Filtered mixture fraction 26
2.5.5 Filtered mixture fraction variance 26
2.6 Turbulent combustion modelling 27
2.6.1 Turbulence modelling 27
2.6.2 Combustion modelling 29
2.6.3 Turbulence-Chemistry modelling 30

3 Methodology development **33**
3.1 Introduction 33
3.2 Formulation of methodology 33
3.2.1 Laminar flows 36
3.2.2 Turbulent flows 36
3.2.3 Discussion 37
3.2.4 Extension to multi-species diffusion descriptions 39
3.3 Implementation of the methodology 41
3.4 Example: H_2/N_2 - air diffusion flame 42

4 Validation of FireFOAM **49**
4.1 Introduction 49
4.2 Mathematical formulation 51
4.2.1 Governing equations 51
4.2.2 Turbulence modelling 52
4.3 Experimental set-up 52
4.4 Numerical set-up 53
4.5 Results 56

4.5.1 Instability modes 56
4.5.2 Vortex dynamics 56
4.5.3 Puffing frequency 63
4.5.4 Mean and rms values for velocities and helium mass fractions . . . 66
4.5.5 Correlation between velocity and density 77
4.6 LES resolution 78
4.7 Sensitivity analysis 80
4.8 Conclusions 83

5 Non-reacting, turbulent jets of H_2/CO_2 mixing with air 85
5.1 Introduction 85
5.2 Experimental set-up 86
5.3 Mathematical formulation 87
5.3.1 Governing equations 87
5.3.2 Turbulence modelling 88
5.4 Numerical set-up 88
5.5 Results 90
5.5.1 Instantaneous results 90
5.5.2 Scatter plots 92
5.5.3 Results for mean quantities 93
5.5.4 Histograms 98
5.5.5 LES resolution 102
5.6 Conclusions 102

6 Laminar, axi-symmetric H_2/N_2 diffusion flame 111
6.1 Introduction 111
6.2 Experimental set-up 112
6.3 Mathematical formulation 112
6.3.1 Governing equations 112
6.3.2 Combustion modelling 113
6.4 Numerical set-up 113
6.5 Results 115
6.5.1 Flame structure 115
6.5.2 Mean results 115
6.5.3 Magnitude of diffusion terms D_1 and D_2 123
6.5.4 Conclusions 123

7 Turbulent, axi-symmetric H_2/N_2 diffusion flame 127

7.1 Introduction . . . 127

7.2 Mathematical formulation . . . 128

7.2.1 Governing equations . . . 128

7.2.2 Turbulence modelling . . . 129

7.2.3 Combustion modelling . . . 130

7.2.4 Turbulence - Chemistry interaction . . . 130

7.3 Experimental set-up . . . 131

7.4 Numerical set-up . . . 131

7.5 Results . . . 132

7.5.1 Flame structure . . . 132

7.5.2 Mean and rms results . . . 133

7.5.3 Quantification of differential diffusion . . . 143

7.6 Sensitivity analysis . . . 146

7.6.1 LES resolution . . . 146

7.6.2 Turbulent Schmidt and Prandtl numbers . . . 148

7.6.3 Influence of diffusion terms D_1 and D_2 . . . 148

7.7 Conclusions . . . 152

8 Conclusions and future work 155

8.1 Conclusions . . . 155

8.2 Future work . . . 158

Bibliography 161

List of Figures

2.1 Burke-Schumann solution for irreversible infinitely fast chemistry for (a) oxidizer and (b) fuel. 30

4.1 Schematic representation of the fine mesh used for the helium inlet in the simulations. 54
4.2 Density as a function of helium volume fraction ϕ_{He} 55
4.3 Instantaneous snapshots of a typical puffing cycle from LES showing isocountours of density (kg/m^3) with superimposed velocity magnitude (m/s) vectors for the fine grid with SGS model at times (a) 10.2 s, (b) 10.26 s, (c) 10.74 s and (d) 11.02 s. 57
4.4 Misalignment of density gradients (kg/m^4) (white arrows) and pressure gradients (kg/m^{2}s^2) (black arrows) near the base of the plume at times (a) 0.2 sec, (b) 0.4 sec, (c) 0.6 sec and (d) 0.8 sec. 58
4.5 Instantaneous snapshots of puff cycle showing isosurfaces of gravitational torque magnitude at 1% of the maximum value at times (a) 10.2 s, (b) 10.26 s, (c) 10.74 s and (d) 11.02 s. 59
4.6 Instantaneous snapshots of puffing cycle showing isosurfaces of baroclinic torque magnitude at 1% of the maximum value at times (a) 10.2 s, (b) 10.26 s, (c) 10.74 s and (d) 11.02 s. 60
4.7 Vorticity budgets from Equation (11) for the fine grid with the Smagorinsky SGS model at (a) $y = 0.0$ m, (b) $y = 0.2$ m, (c) $y = 0.4$ m, (d) $y = 0.6$ m and (e) on the centerline up to $y = 1.0$ m. 62
4.8 Time trace of centerline streamwise velocity at $y = 0.5$ m above the base of the plume for (a) coarse grid and (b) fine grid. 64
4.9 Power spectrum of streamwise velocity on the centerline at $y = 0.5$ m above the base of the plume for coarse grid with (a) no SGS , (b) Smagorinsky model and fine grid with (c) no SGS, (d) Smagorinsky model. 65

4.10 Comparison of density-weighted, time-averaged (a) mean and (b) rms values for the centerline streamwise velocity up to $y = 0.8$ m above the base of the plume. 67

4.11 Comparison of density-weighted, time-averaged (a) mean and (b) rms centerline values for the helium mass fraction up to $y = 0.8$ m above the base of the plume. 67

4.12 Comparison of density-weighted, time-averaged streamwise velocities at heights $y =$ (a) 0.2 m, (b) 0.4 m and (c) 0.6 m. 69

4.13 Comparison of density-weighted, time-averaged rms streamwise velocities at heights $y =$ (a) 0.2 m, (b) 0.4 m and (c) 0.6 m. 70

4.14 Comparison of density-weighted, time-averaged cross-stream velocities at heights $y =$ (a) 0.2 m, (b) 0.4 m and (c) 0.6 m. 71

4.15 Comparison of density-weighted, time-averaged rms cross-stream velocities at heights $y =$ (a) 0.2 m, (b) 0.4 m and (c) 0.6 m. 72

4.16 Comparison of density-weighted, time-averaged mass fractions at heights $y =$ (a) 0.2 m, (b) 0.4 m and (c) 0.6 m. 73

4.17 Comparison of density-weighted, time-averaged rms mass fractions at heights $y =$ (a) 0.2 m, (b) 0.4 m and (c) 0.6 m. 74

4.18 Comparison of density-weighted, time-averaged product of rms streamwise and rms cross-stream velocities at heights $y =$ (a) 0.2 m, (b) 0.4 m and (c) 0.6 m. 75

4.19 Comparison of density-weighted, time-averaged turbulent kinetic energy at heights $y =$ (a) 0.2 m, (b) 0.4 m and (c) 0.6 m. 76

4.20 Instantaneous vertical velocity component u vs density at $x =$0.03 m, $y =$0.46 m for coarse grid with (a) no SGS , (b) Smagorinsky model and fine grid with (c) no SGS, (d) Smagorinsky model. 77

4.21 Density - streamwise velocity correlation coefficient up to $y = 3.5$ m above the base of the plume. 78

4.22 Ratio of turbulent to laminar viscosity, μ_t/μ, with the Smagorinsky model for the (a) coarse and (b) fine grid. 79

4.23 Ratio of turbulent to laminar viscosity, μ_t/μ, with the Smagorinsky model on the centerline. 79

4.24 Ratio of grid spacing, Δ, to the Kolmogorov length scale, η_K, for (a) Smagorinsky coarse and (b) Smagorinsky fine. 80

4.25 Effect of Smagorinsky constant, c_s, in the fine mesh with turbulent Schmidt number, $Sc_t = 0.5$, at height $y = 0.6$ m on (a) streamwise velocity, (b) cross-stream velocity, (c) rms streamwise velocity, (d) rms cross-stream velocity, (e) mass fraction and (f) centerline streamwise velocity. 81

4.26 Effect of turbulent Schmidt number, Sc_t, in the fine mesh with Smagorinsky model, $c_s = 0.1$, at height $y = 0.6$ m on (a) streamwise velocity, (b) cross-stream velocity, (c) rms streamwise velocity, (d) rms cross-stream velocity, (e) mass fraction and (f) centerline streamwise velocity. 82

5.1 Plots of instantaneous X_{H_2} in a symmetry plane for (a) $Re = 1000$, (b) $Re = 2000$, (c) $Re = 4000$ and (d) $Re = 8000$ with different diffusivities. . 91

5.2 Plots of instantaneous X_{H_2} in a symmetry plane for (a) $Re = 1000$, (b) $Re = 2000$, (c) $Re = 4000$ and (d) $Re = 8000$ with equal diffusivities. . . . 91

5.3 Instantaneous plots of the differential diffusion parameter, ξ (Eq. 5.7), for (a) $Re = 1000$, (b) $Re = 2000$, (c) $Re = 4000$ and (d) $Re = 8000$. Locations $y/d = 5, 15, 30$ and radial distances $r/d = 0, 1, 2, 3$ are indicated. 92

5.4 Scatter plots of instantaneous X_{H_2} vs X_{CO_2}, normalized by their inlet value, at location $y/d = 30$ for (a) $Re = 1000$, (b) $Re = 2000$, (c) $Re = 4000$ and (d) $Re = 8000$. 94

5.5 Scatter plots of instantaneous X_{H_2} vs X_{CO_2}, normalized by their inlet value, at location $y/d = 30$ for (a) $Re = 1000$, (b) $Re = 4000$, (c) $Re = 16000$ and (d) $Re = 64000$ as reported by Smith et al. [106]. 95

5.6 Mean X_{H_2} at location $y/D = 15$ for (a) $Re = 1000 - 2000$ and (b) $Re = 4000 - 8000$ 96

5.7 Mean X_{CO_2} at location $y/D = 15$ for (a) $Re = 1000 - 2000$ and (b) $Re = 4000 - 8000$ 96

5.8 Mean X_{H_2} at location $y/D = 30$ for (a) $Re = 1000 - 2000$ and (b) $Re = 4000 - 8000$ 97

5.9 Mean X_{CO_2} at location $y/D = 30$ for (a) $Re = 1000 - 2000$ and (b) $Re = 4000 - 8000$ 97

5.10 Mean X_{H_2} vs X_{CO_2}, normalized by their inlet value, for Reynolds numbers $Re = 1000 - 8000$ at location (a) $y/d = 30$, (b) $y/d = 15$ and (c) $y/d = 5$. White symbols: experimental data. 99

5.11 Mean X_{CO_2}/X_{H_2} vs X_{CO_2}, normalized by their inlet value, for Reynolds numbers $Re = 1000-8000$ at location (a) $y/d = 30$, (b) $y/d = 15$ and (c) $y/d = 5$. White symbols: experimental data. 100

5.12 Mean differential diffusion parameter, ξ (Eq. 5.7), for $Re = 1000-8000$ at location (a) $y/D = 30$, (b) $y/D = 15$ and (c) $y/D = 5$. 101

5.13 Histograms of ξ distribution for $Re = 2000$ at location $y/d = 15$ for (a) $r/d = 0$, (b) $r/d = 1$ and (c) $r/d = 2$. 103

5.14 Histograms of ξ distribution for $Re = 2000$ at location $y/d = 30$ for (a) $r/d = 0$, (b) $r/d = 2$ and (c) $r/d = 3$. 104

5.15 Histograms of ξ distribution for $Re = 2000$ at location $y/d = 15$ for (a) $r/d = 0$ and (b) $r/d = 2$ as reported by Smith et al. [106]. 105

5.16 Histograms of ξ distribution for $Re = 2000$ at location $y/d = 15$ for (a) $r/d = 0$ and (b) $r/d = 3$ as reported by Smith et al. [106]. 106

5.17 Ratio of turbulent to laminar viscosity, μ_t/μ, for (a) $Re = 1000$, (b) $Re = 2000$, (c) $Re = 4000$ and (d) $Re = 8000$. 107

5.18 Ratio of grid spacing, Δ, to the Kolmogorov length scale, η_K, for (a) $Re = 1000$, (b) $Re = 2000$, (c) $Re = 4000$ and (d) $Re = 8000$. 108

6.1 Burke-Schumann solution for irreversible infinitely fast chemistry, based on elemental mass fractions η'_H and η'_N, for (a) O_2, (b) H_2 and (c) H_2O. The stoichiometric elemental mass fraction of H is $\eta'_{H_{st}} = 0.1119$. 114

6.2 Schematic of mesh for fuel inlet used in the simulations 114

6.3 Two-dimensional snapshots of temperature distribution (a) without differential diffusion and (b) with differential diffusion 116

6.4 Streamwise velocities at (a) $y = 3$ mm, (b) $y = 10$ mm, (c) $y = 20$ mm, (d) $y = 30$ mm and (e) axially. With diff. diff. (D_1 and D_2): solid lines, with diff. diff. (only D_1): dotted lines, without diff. diff.: dashed lines. . . 117

6.5 Axial temperature and species mole fractions up to $y = 100$ mm. Exp. data: symbols, with diff. diff. (D_1 and D_2): solid lines, with diff. diff. (only D_1): dotted lines, without diff. diff.: dashed lines. 118

6.6 Radial temperature and species mole fractions at $y = 3$ mm. Experimental data: symbols, with diff. diff. (D_1 and D_2): solid lines, with diff. diff. (only D_1): dotted lines, without diff. diff.: dashed lines. 119

6.7 Radial temperature and species mole fractions at $y = 10$ mm. Experimental data: symbols, with diff. diff. (D_1 and D_2): solid lines, with diff. diff. (only D_1): dotted lines, without diff. diff.: dashed lines. 120

6.8 Radial temperature and species mole fractions at $y = 20$ mm. Experimental data: symbols, with diff. diff. (D_1 and D_2): solid lines, with diff. diff. (only D_1): dotted lines, without diff. diff.: dashed lines. 120

6.9 Radial temperature and species mole fractions at $y = 30$ mm. Experimental data: symbols, with diff. diff. (D_1 and D_2): solid lines, with diff. diff. (only D_1): dotted lines, without diff. diff.: dashed lines. 121

6.10 Mean differential diffusion parameter, $\xi = z_H - z_N$, at (a) different heights and (b) axial locations. 122

6.11 Magnitude of normalized diffusion terms D_1 and D_2 for η_H at (a) $y = 3$ mm, (b) $y = 10$ mm, (c) $y = 20$ mm, (d) $y = 30$ mm and (e) on the centerline up to height $y = 100$ mm. The dotted black line indicates the location of the maximum flame temperature. 124

6.12 Magnitude of normalized diffusion terms D_1 and D_2 for η_N at (a) $y = 3$ mm, (b) $y = 10$ mm, (c) $y = 20$ mm, (d) $y = 30$ mm and (e) on the centerline up to height $y = 100$ mm. The dotted black line indicates the location of the maximum flame temperature. 125

7.1 Schematic representation of the mesh used in the fuel inlet in the simulations. 132

7.2 Two-dimensional plots of mean temperature distribution (a) with differential diffusion and (b) without differential diffusion. 133

7.3 Mean and rms streamwise velocity at location (a) $y/d = 5$, (b) $y/d = 20$, (c) $y/d = 40$ and (d) axially. Experimental data: symbols, with diff. diff. (D_1 and D_2): solid lines, with diff. diff. (only D_1): dotted lines, without diff. diff.: dashed lines. 134

7.4 Mean and rms results versus downstream distance for (a) T, (b) species and (c) mixture fraction. Experimental data: symbols, with diff. diff. (D_1 and D_2): solid lines, with diff. diff. (only D_1): dotted lines, without diff. diff.: dashed lines. 136

7.5 Mean and rms results at location $y/d = 2.5$ for (a) T, (b) H_2, (c) H_2O, (d) O_2, (e) N_2 and (f) mixture fraction. Experimental data: symbols, with diff. diff. (D_1 and D_2): solid lines, with diff. diff. (only D_1): dotted lines, without diff. diff.: dashed lines. 137

7.6 Mean and rms results at location $y/d = 5$ for (a) T, (b) H_2, (c) H_2O, (d) O_2, (e) N_2 and (f) mixture fraction. Experimental data: symbols, with diff. diff. (D_1 and D_2): solid lines, with diff. diff. (only D_1): dotted lines, without diff. diff.: dashed lines. 138

7.7 Mean and rms results at location $y/d = 10$ for (a) T, (b) H_2, (c) H_2O, (d) O_2, (e) N_2 and (f) mixture fraction. Experimental data: symbols, with diff. diff. (D_1 and D_2): solid lines, with diff. diff. (only D_1): dotted lines, without diff. diff.: dashed lines. 139

7.8 Mean and rms results at location $y/d = 20$ for (a) T, (b) H_2, (c) H_2O, (d) O_2, (e) N_2 and (f) mixture fraction. Experimental data: symbols, with diff. diff. (D_1 and D_2): solid lines, with diff. diff. (only D_1): dotted lines, without diff. diff.: dashed lines. 140

7.9 Mean and rms results at location $y/d = 40$ for (a) T, (b) H_2, (c) H_2O, (d) O_2, (e) N_2 and (f) mixture fraction. Experimental data: symbols, with diff. diff. (D_1 and D_2): solid lines, with diff. diff. (only D_1): dotted lines, without diff. diff.: dashed lines. 141

7.10 Elemental mixture fractions, z_H and z_N, and differential diffusion parameter, $\xi = z_H - z_N$, versus mixture fraction, z, at location (a) $y/d = 5$ and (b) $y/d = 20$. With diff. diff. (D_1 and D_2): solid lines, with diff. diff. (only D_1): dotted lines. 144

7.11 Elemental mixture fraction z_H versus elemental mixture fraction z_N at various downstream locations. 144

7.12 Temperature versus mixture fraction in comparison to adiabatic equilibrium results at location (a) $y/d = 5$ and (b) $y/d = 20$. 145

7.13 Ratio of turbulent to laminar viscosity, μ_t/μ, at location (a) $y/d = 5$, (b) $y/d = 20$, (c) $y/d = 40$ and (d) axially. With diff. diff. (D_1 and D_2): solid lines, with diff. diff. (only D_1): dotted lines, without diff. diff.: dashed lines.146

7.14 Ratio of grid spacing, Δ, to the Kolmogorov length scale, η_K, at location (a) $y/d = 5$, (b) $y/d = 20$, (c) $y/d = 40$ and (d) axially. With diff. diff. (D_1 and D_2): solid lines, with diff. diff. (only D_1): dotted lines, without diff. diff.: dashed lines. 147

7.15 Influence of turbulent Schmidt, Sc_t, and Prandtl, Pr_t, numbers on mean and rms results at location $y/d = 5$ for (a) T, (b) H_2, (c) H_2O, (d) O_2, (e) N_2 and (f) mixture fraction. Symbols: experimental data, solid lines: $Sc_t = 0.7$, $Pr_t = 0.6$, dashed lines: $Sc_t = 0.7$, $Pr_t = 0.7$, dotted lines: $Sc_t = 0.6$, $Pr_t = 0.6$. 149

7.16 Magnitude of normalized diffusion terms D_1 and D_2 for η_H at location (a) $y/d = 5$, (b) $y/d = 20$, (c) $y/d = 40$ and (d) axially. The dotted black line indicates the location of the maximum flame temperature. 150

7.17 Magnitude of normalized diffusion terms D_1 and D_2 for η_N at location (a) $y/d = 5$, (b) $y/d = 20$, (c) $y/d = 40$ and (d) axially. The dotted black line indicates the location of the maximum flame temperature. 151

List of Tables

2.1 Boundary conditions for conserved scalar Z. 19
2.2 Boundary conditions for species mass fraction and mixture fraction z. . . . 19
2.3 Weighting factors, γ_λ, as proposed by Bilger [6]. 21

4.1 Boundary conditions as specified in the simulations (OpenFOAM terminology [38]). 54

5.1 Flow parameters at the inlet 90

7.1 Error analysis of the maximum flame temperature in the numerical simulations. 142
7.2 Error analysis of the position of the maximum flame temperature in the numerical simulations. 142

Nomenclature

Acronyms

1D	One-dimensional
2D	Two-dimensional
3D	Three-dimensional
BEM	Boundary Element Method
CFD	Computational Fluid Dynamics
CMC	Conditional Moment Closure
DNS	Direct Numerical Simulation
ESM	Equivalent Source Method
FDF	Filtered Density Function
FDS	Fire Dynamics Simulator
FGM	Flamelet Generated Manifold
FLAME	Fire Laboratory for Accreditation of Models and Experiments
LES	Large Eddy Simulation
LFM	Langrangian Flamelet Model
ODT	One-Dimensional Turbulence
PDF	Probability Density Function
PISO	Pressure Implicit with Splitting of Operators
PIV	Particle Image Velocimetry
PLIF	Planar Laser Induced Fluorescence
RANS	Reynolds-Averaged Navier Stokes
SGS	Sub-Grid Scale
TDF	Turbulent Diffusion Flames
TNF	Turbulent Non-premixed Flames
TVD	Total Variation Diminishing

Greek Symbols

α	Thermal diffusivity, kg/(m $\cdot$ s)
β	Arrhenius constant
β	Coupling function
$\Delta h^{0}_{f,k}$	Enthalpy of formation
Δ	Filter width, cell size
δ	Kronecker symbol
$\dot{\omega}$	Chemical source term, kg/(m^3 $\cdot$ s)
ε	Turbulent dissipation rate, m^2/s^3
η'	Elemental mass fraction
η_K	Kolmogorov length scale, m
γ	Weighting factor
λ	Thermal conductivity, W/(m $\cdot$ K)
μ	Dynamic viscosity, kg/(m $\cdot$ s)
ν	Kinematic viscosity, m^2/s
ν	Reaction constant, mol
ω	Vorticity, s^{-2}
ϕ	Equivalence ratio
ϕ	Volume fraction
ρ	Density, kg/m^3
τ	Viscous stress tensor, Pa
ξ	Differential diffusion parameter
B	Beta function

Other Symbols

$(\cdot)^*$	Indicates integration or averaging over a certain region/scalar
$\cdot\|z$	Conditioned on mixture fraction z
$:$	Double product
$\int$	Integral
∇	Divergence/Gradient operator
∂	Partial derivative
$\prod$	Product
$\sum$	Sum

Roman Symbols

$\dot{Q}$	Radiative source term, J/(m^3 · s)
$\mathscr{C}$	Function $\mathscr{C}$
$\overline{R}$	Gas constant, J/(kg · K)
A	Amplitude of azimuthal forcing
A	Arrhenius constant, (K · s)$^{-1}$
a, b	Parameters of beta PDF
A_s, T_s	Coefficients of Sutherland's law model
B	Orthogonal projection matrix B
B'	Projection matrix B'
c_k, c_ε	One equation turbulence model constants
c_p	Specific heat capacity at constant pressure, J/(kg · K)
c_s	Smagorinsky model constant
c_v	Specific heat capacity at constant volume, J/(kg · K)
c_z	Mixture fraction variance model constant
Co	Courant number
D	Mass diffusion coefficient, m^2/s
d	Diameter, m
D^{th}	Thermal diffusion coefficient, m^2/s
E	Activation energy, J/mol
F	Filter function
f	Body force
f	Frequency, Hz
f	Non-filtered quantity
Fr	Froude number
g	Gravitational constant, m/s^2
h	Total enthalpy, J/kg
J	Diffusive mass flux, kg/(m^2 · s)
K	Reaction rate coefficient, s^{-1}
k	Turbulent kinetic energy, m^2/s^2
Ka	Karlovitz number
Le	Lewis number
M	Number of reactions
N	Number of modes for azimuthal forcing
N_e	Number of elements

N_s	Number of species
P	Probability Density Function
p	Pressure, Pa
Pr	Prandtl number
Q	Progress rate, $(\mathrm{m}^3 \cdot \mathrm{s})^{-1}$
q	Energy flux, $\mathrm{W/m}^2$
R	Transformation matrix
R	Universal gas constant, $\mathrm{J/(kmol \cdot K)}$
Re	Reynolds number
Ri	Richardson number
S	Rate of strain, s^{-1}
s	Stoichiometric ratio
$S_{i,j}$	Rate of strain tensor, s^{-1}
Sc	Schmidt number
T	Temperature, K
t	Time, s
U	Orthogonal matrix U
u	Velocity m/s
u,v,w	Velocity components, m
V	Diffusion velocity, m/s
W	Molecular weight, kg/kmol
X	Mole fraction
x,y,z	Coordinates, m
Y	Mass fraction
Z	Conserved scalar
z	Mixture fraction

Subscripts and Superscripts

$'$	Residual part of a variable
$''$	Fluctuation
$-$	Filtered/Averaged
0	Initial value
λ	Elements index
$\rightrightarrows$	Tensor

$\vec{}$	Vector
$\tilde{}$	Favre filtered/Favre averaged
b	Backward
F	Fuel
f	Forward
i, j, k	Coordinate index
j	Reaction index
k, l	Species index
mix	Mixture
O	Oxidizer
ref	Reference
s	Sensible
sgs	Sub-grid scale
st	Stoichiometric
T	Transpose
t	Turbulent
x, y, z	Direction

Chapter 1

Introduction

1.1 Motivation

Numerical simulations of turbulent combustion are used more and more systematically in the optimization of combustion devices in order to achieve lower emissions and higher efficiency. The benefits of those better devices are both economic and ecological. In order to lower pollutant emissions such as carbon monoxide (CO), unburned hydrocarbons and nitrogen oxides (NO_x), new fuels are to be used. Hydrogen is an important fuel of the future and can be burned as a pure substance, or as a component in a fuel, originating from e.g. biomass [119].

Nowadays a lot of experimental and numerical work is carried out in the area of turbulent combustion aiming at getting a better insight into the combustion phenomena involved in reactive flows. By the use of experimental techniques turbulent flames can be studied in a reliable and accurate way and can provide scientists with a better understanding of the physics behind combustion processes. The experimental tests, even though they are accurate, can also be very expensive, especially if they have to be performed over a wide range of flame parameters. A good alternative to this problem is the numerical simulations of combustion applications with Computational Fluid Dynamics (CFD) codes. With the use of CFD codes a wide range of numerical experiments can be performed at a relatively much lower cost than with experiments. However the accuracy of the numerical simulations strongly depends on the modelling methods used to deal with combustion, turbulence and turbulence-chemistry interaction. These modelling methods in turn are tested for their accuracy with experimental data so it is clear that the experimental techniques and numerical simulations are strongly coupled and depend on each other. The advancement in one area can benefit from the other and vice versa. A good example of such collaboration is the International Workshop on Measurements and Computation of Turbulent Non-premixed Flames (TNF) [126].

Numerical simulations of reactive flows typically involve mixtures of different chemical species, each one with different properties. Hydrogen is a much lighter chemical species when compared to other chemical components (e.g. CO_2, N_2 or O_2). This much smaller molecular weight of hydrogen causes it to behave differently than other chemical species in a mixture, e.g. to diffuse at a different rate. Differential molecular diffusion refers to the property of the chemical species to diffuse faster (e.g. H_2) or slower (e.g. CO_2) than others in a mixture. In practice, combustion processes occur in a turbulent environment. Numerical simulations of turbulent combustion nowadays often rely on the assumption that every chemical component diffuses at the same rate. In the case of fossil fuel this assumption is reasonable. In the case of hydrogen combustion, however, this assumption is less valid, since H_2 diffuses more rapidly than other chemical components. Mostly, this differential diffusion effect is ignored when performing numerical simulations of turbulent combustion because it either leads to great modelling complications or because it is expected that turbulent mixing is a far more dominant process than molecular mixing so that the turbulent diffusivity is an order of magnitude larger than the molecular diffusivity.

However, there is a vast amount of experimental and numerical evidence indicating that molecular differential diffusion can be important in low [20, 21, 106], moderate [4, 1, 65, 3] and high [62, 105] Reynolds number flows. Even though differential diffusion effects typically decrease with increasing Reynolds number [77, 106], they can still be present in turbulent flows, e.g. close to the combustion nozzle. This has been reported in the past in [66, 67] for nitrogen-diluted H_2 flames and in [3] for $CH_4/H_2/N_2$ flames. The inclusion of differential diffusion effects can be important for flame calculations of reacting flows, where an accurate prediction of species is needed, since they are prerequisite for accurately predicting the local temperatures [30, 33, 113], chemical reaction rates and pollutant concentrations [67, 19, 49].

1.2 Modelling differential diffusion in reactive flows

Depending on how fuel and oxidizer are brought into contact in a combustion system, three different combustion regimes can be identified in reactive flows: the premixed, non-premixed and partially-premixed regime. Focus of the thesis is the non premixed regime, where fuel and oxidizer are initially separated. In this case, the combustion processes depend on the diffusive molecular mixing of the species and chemical reactions occur only when fuel and oxidizer are well mixed.

Most of the modelling efforts made in the past decades in non-premixed combustion research of reactive flows can be categorized on two main methodologies in terms of the governing equations solved:

- Transport of chemical species
- Conserved scalar approach
- Transported Probability Density Function (PDF) / Filtered Density Function (FDF) models

Differential diffusion effects can be incorporated in all the above mentioned methodologies. Depending on the methodology, the inclusion of differential diffusion becomes a modelling task occurring at a different level, with different complexity. In general, there are two ways of including differential diffusion in numerical simulations of reactive flows:

- In physical space (in the transport equations)
- In chemical space (in the combustion model)

A brief summary of the different methodologies used in research of non-premixed combustion, along with previous modelling efforts of differential diffusion is presented below.

1.2.1 Transport of chemical species

The first method implies the solution of transport equations for all but one (typically N_2) chemical species with different mass diffusivities, including computing the species chemical source term. In this case, differential diffusion effects are incorporated in both physical space (in the transport equations of the chemical species) and chemical space (by computing the species chemical source terms) without much added modelling complexity. Depending on the modelling methods used for combustion and turbulence in the numerical simulations, this is the most accurate way of taking into account differential diffusion effects in numerical simulations of combustion applications. The set of equations to be solved is, however, very stiff due to the wide range of chemical scales involved, mainly due to the species chemical source terms. Solving the transport equations of chemical species with detailed chemistry can, therefore, be computationally very expensive, especially if 3D simulations are to be performed. This is the reason why this methodology was not adopted for the numerical simulations presented in the thesis. A selection of previous works that have used this methodology in the past in order to study the effects of differential diffusion in reactive flows can be found in [30, 33, 29, 50, 49].

1.2.2 Conserved scalar approach

Apart from assuming equal mass diffusivities for all chemical species, another usual assumption made when modelling reactive flows is to consider equal thermal and mass diffusivities, leading to unity Lewis number for all chemical species. The use of these two assumptions, along with the consideration of a single-step chemical reaction, leads to the definition of a conserved scalar, the mixture fraction, which uniquely describes the transport of species [90]. By making use of conserved scalars (scalars whose value does not alter when they undergo a chemical reaction) the solution of the fluid movement is decoupled from the chemical reactions. This framework has formed the basis upon which many combustion models rely. The mathematical deduction of these scalars relies on the assumption that all chemical components diffuse equally but in reality this is not the case. Yet, this is often ignored because no simple model exists that can include them or because an appropriate diffusion coefficient has to be selected for the mixture fraction in order to account for the different diffusivities of the chemical species [111]. For example, in the case of hydrogen combustion, where the chemical species mass diffusivities are vastly different, it is arguable whether it is possible to get an accurate description of the diffusion processes occurring both on the rich side of the flame (where there would be mainly H_2 diffusing faster than the other species) and on the lean side of the flame (where there would be mainly combustion products and air diffusing slower than H_2) [20]. In this case, the inclusion of differential diffusion effects in physical space is not so straightforward at the level of the conserved scalars. Instead, what is usually done in the research community is to use the conserved scalar approach but only including differential diffusion effects in chemical space (in the combustion model).

An alternative formulation has also been proposed [89] in which the mixture fraction is not related directly to any combination of the reactive scalars, but defined from the solution of a conservation equation with an arbitrary diffusion coefficient and appropriate boundary conditions. Other works based on the conserved scalar approach include the use of a composite mixture fraction in [54] as well as the derivation of a mixture fraction from elemental mass fractions in [111].

A brief description of the different combustion models used in conjunction with the conserved scalar approach along with work done in order to study and model differential diffusion in reactive flows with the conserved scalar approach in the past, is presented below.

Flame sheet model

The flame sheet model, also known as Burke-Schumann model [9], assumes a one-step, infinitely fast, irreversible chemical reaction between fuel and oxidizer. Reaction takes place only where fuel and oxidizer are at stoichiometry, that is where the mixture fraction, z, corresponds to the stoichiometric mixture fraction $(z = z_{st})$. In any other case, inert mixing of oxidizer and products takes place if $z < z_{st}$ while inert mixing of fuel and products occurs if $z > z_{st}$. This way the species mass fractions are a piecewise linear function of the mixture fraction. In its simplicity, though, the Burke-Schuman model is not entirely realistic and has its limitations. In reality, the chemical reactions between fuel and oxidizer can occur in a region much wider than just at stoichiometric conditions $(z = z_{st})$, as the flame sheet model assumes. In addition, the chemical reactions are not infinitely fast and irreversible but intermediate species can be created, something that the Burke-Schumann model cannot take into account. Moreover, differential diffusion effects and non-unity Lewis number cannot be considered in the Burke-Schumann model.

An extension of the flame sheet model is the generalized Burke-Schumann formulation for hydrogen-oxygen diffusion flames [98]. It is based on a three-step reduced mechanism which assumes partial equilibrium of the two-body chain-carrying reactions yielding an infinitely fast radical-production step, and considers the finite rates of the three-body radical-recombination reactions. This formulation results in a chemical mechanism with H as the only intermediate species while the concentrations of the radicals O, OH and HO_2 are related to that of H through steady states. The set of conservation equations are then formulated in terms of generalized coupling functions that account for differential diffusion effects and non-unity Lewis number, providing a set of equations that describe the flame structure for strain conditions ranging from near extinction to weakly strained flames. A study where the generalized Burke-Schumann formulation was applied in order to study the influence of differential diffusion in reactive flows can be found in [31].

Chemical equilibrium model

The chemical equilibrium model assumes infinitely fast but reversible reactions between the chemical species and as such, all species are in chemical equilibrium at every value of the mixture fraction. The advantage of this model, when compared with the flame sheet model, is that intermediate species can be be accounted for. The main assumption of this model, however, is that all chemical reactions have enough time to reach the equilibrium state, but in reality this is not always fulfilled. For example in turbulent reacting flows, that would imply that the chemical time scales must be much smaller than the smallest scales of turbulence (Kolmogorov scales), i.e. that the Karlovitz number is much less than unity, $Ka << 1$. This is not always true in a turbulent flow since the local diffusive time scales can vary considerably. In addition, differential diffusion effects and non-unity Lewis number cannot be considered with the chemical equilibrium model.

Flamelet models

Flamelet models were first introduced by Peters [81] for non-premixed combustion. The basic assumption of the flamelet model is that reactions occur in a thin layer region around the stoichiometric mixture where the chemical time scales are much smaller than the time scales of turbulence. This implies that the reaction zone is laminar-like and that diffusive processes occur only in the direction normal to the surface of the stoichiometric mixture. Subsequently, the equations for scalar transport and temperature can then be transformed into a system where the mixture fraction is an independent coordinate. The steady laminar flamelet model is obtained by assuming a steady flame structure. It is a relatively simple model and suitable for applications where fast chemical processes are present. However, it it not suitable for application in flows where slow chemical processes occur, e.g. formation of pollutants. An extension of this theory was made by introducing the unsteady flamelet model, also called the Langrangian Flamelet Model (LFM) [87]. A flamelet library can be created from a 1-D counterflow diffusion flames with detailed chemistry in which differential molecular diffusion and non-unity Lewis number are considered. The flamelet profiles obtained in physical space can then be converted into mixture fraction space by using e.g. Bilger's definition for mixture fraction [6]. Flamelet models have been used in the past in order to model differential diffusion effects in reactive flows. A typical example can be found in [87, 89].

Flamelet/Progress variable method

The Flamelet/Progress variable method was first developed by Pierce & Moin [85, 86] especially for Large Eddy Simulations (LES). The model uses a steady-state flamelet library, but instead of using the scalar dissipation rate as a parameter in the flamelet library, a reaction progress variable is used for the parameterization. The progress variable is a non-conserved scalar and is usually expressed as a linear combination of the mass fraction of major reaction products [39, 86, 118]. Typically a transport equation is solved for the filtered reaction progress variable while the filtered chemical source term in these equations is closed by the use of a flamelet library in conjunction with a joint Filtered Density Function (FDF) of the mixture fraction and the reaction progress variable. An advantage of this method is the different way of parameterizing the flamelet library which essentially gives a better description of local extinction and re-ignition phenomena but also of flame liftoff. However, care must be taken when modelling the joint FDF of the mixture fraction and the progress reaction variable [88].

Within the Flamelet/Progress variable context the Flamelet Generated Manifold (FGM) method has also been introduced. Within the FGM method 1D flame structures, called flamelets, are used to generate a manifold. The advantage of FGM is that not only chemistry is taken into account, but also (diffusive) transport, which can be in the same order of magnitude in areas of the flow where chemistry is not dominant. Differential diffusion effects and non-unity Lewis number can be considered in the construction of the FGM table in a way similar to the one previously described for flamelet models. The FGM method has been extended in order to be applicable in both premixed [117, 118] and non-premixed combustion [17] and has been applied in order to study differential diffusion effects in numerical simulations of reactive flows [16, 120].

Conditional moment closure

In the Conditional Moment Closure (CMC) model, first proposed in Reynolds-Averaged Navier Stokes (RANS) context [52], transport equations are derived for mixture fraction-conditioned averages of the reactive scalars. The resulting transport equations are then time, three spatial dimensions and mixture fraction dependent. This conditioning on mixture fraction makes it then easier to model the chemical species source term. The CMC model was also extended in LES context [51] where models were provided for all unclosed terms and tested with DNS data. However, when the full CMC model is applied in practical LES applications issues regarding the boundary conditions and numerical efficiency arise [51]. Examples of modelling and studying differential diffusion effects with the CMC model can be found in [53, 54]. In the work by Kronenburg et al. [53] a model accounting for differential diffusion effects was presented based on the analysis of DNS data. The model considered differential diffusion but provided a term that tends to move the species profiles closer to that which was obtained with equal species mass diffusivities as observed by the DNS data. The evaluation of this term required the solution of additional transport equations for each differentially diffusing scalar.

1.2.3 Transported PDF-FDF methods

The Probability Density Function (PDF) approach, first introduced in RANS context [92], is an alternative method of modelling strong turbulence-chemistry interactions in which transport equations for the joint PDF of all variables are solved. The main advantage of the method is that the chemical source term in the equations appears in a closed form. However, molecular mixing (micro-mixing) needs to be modelled. In this case, differential diffusion effects are considered in physical space by taking them into account in the micro-mixing models. A brief overview of the various micro-mixing models proposed in literature can be found in [97]. The method is also extended for LES by making use of the Filtered Density Function (FDF), first introduced in [93]. The joint scalar FDF, however, depends on space, time and all independent scalars. Therefore the FDF transport equations cannot be solved by finite-volume or finite-difference methods. Instead, an equivalent system of particles is used where ordinary differential equations are solved for particle motions, temperature and species mass fractions. This increases the computational cost of the method, especially for numerical simulations of practical applications where a good spatial resolution is required. The effects of differential diffusion have been modelled within the PDF-FDF context in the past and a brief overview can be found in [13, 46, 63, 69, 97].

1.3 Objectives

The main objective of this thesis is to present a new methodology that will incorporate differential diffusion effects in CFD simulations of reactive flows, by combining two of the main methodologies presented before (the solution of the chemical species transport equations and the conserved scalar approach). Within this new methodology, differential diffusion effects are taken into account in physical space (in the transport equations of the conserved scalars), while the disadvantages related with the classical mixture fraction approach are avoided. In this case the diffusion term in the transport equations of the conserved scalars consists of two parts, one expressing the diffusion of the conserved scalars and the other retrieved from the combustion model. With this new methodology differential diffusion effects can easily be incorporated in both physical (transport equations for the conserved scalars) and chemical space (in the combustion model). It will be investigated how important is the inclusion of differential diffusion effects in physical space in turbulent combustion of hydrogen. These effects are usually neglected in numerical simulations of turbulent combustion and are only taken into account in chemical space by e.g. including them in a flamelet table.

1.4 Outline

Chapter 2 introduces the governing equations used in order to perform numerical simulations of reactive flows, along with all the sub-models needed. In addition, the mixture fraction model is analyzed in order to compare it with the newly proposed methodology presented later in the thesis. Lastly, the filtered LES equations are presented along with the sub-models used for turbulence, combustion and turbulence-chemistry interaction. In Chapter 3, the mathematical formulation of the new methodology is presented for both laminar and turbulent reactive flows and a discussion on its capabilities is given. A validation study of the CFD code FireFOAM used for the numerical simulations is presented in Chapter 4 in order to evaluate its accuracy and capabilities in simulating turbulent flows. Subsequently, in Chapter 5, the effects of differential diffusion are first investigated in a non-reacting test case and a quantification of their influence with increasing Reynolds number is made. The application of the methodology to laminar and turbulent hydrogen flames is presented in Chapters 6 and 7, respectively, in which the accuracy of the method is assessed and the effects of differential diffusion are analyzed qualitatively and quantitatively. Finally, in Chapter 8, the main conclusions of this work are summarized, suggestions about modelling differential diffusion in reactive flows are given and plans about future work are presented.

Chapter 2

Governing equations

2.1 Instantaneous equations

In order to perform numerical simulation with CFD codes, first a mathematical formulation of the problem has to be established. Flames are chemically reacting flows which are governed by a set of conservation equations describing the flow (Navier-Stokes equations), the chemical species mass fractions and the enthalpy. The set of conservation equations which can fully describe a combustion process is given below [90]:

- Conservation of mass:

$$\frac{\partial \rho}{\partial t} + \frac{\partial (\rho u_i)}{\partial x_i} = 0 \tag{2.1}$$

where ρ is the density and u_i is the velocity in the i direction.

- Conservation of momentum:

$$\frac{\partial (\rho u_j)}{\partial t} + \frac{\partial (\rho u_i u_j)}{\partial x_i} = -\frac{\partial p}{\partial x_j} + \frac{\partial \tau_{ij}}{\partial x_i} + \rho g_j, \qquad j = 1,2,3 \tag{2.2}$$

where p is the pressure, τ_{ij} denotes the viscous stress tensor and g_j is the gravitational acceleration.

- Conservation of chemical species:

$$\frac{\partial (\rho Y_k)}{\partial t} + \frac{\partial (\rho u_i Y_k)}{\partial x_i} = -\frac{\partial J_{k,i}}{\partial x_i} + \dot{\omega}_k, \qquad k = 1,...,N_s \tag{2.3}$$

where $J_{k,i}$ and $\dot{\omega}_k$ are the molecular diffusive mass flux and reaction rate of species k, respectively.

- Conservation of energy:

$$\frac{\partial(\rho h)}{\partial t}+\frac{(\rho u_i h)}{\partial x_i}=\frac{Dp}{Dt}-\frac{\partial q_i}{\partial x_i}+\tau_{ij}\frac{\partial u_i}{\partial x_j}+\dot{Q} \tag{2.4}$$

where h is the total enthalpy (sensible plus chemical), q_i is the energy flux and $\dot{Q}$ is the radiative source term.

2.2 Constitutive relations

The above system of conservation equations contains several quantities, such as the viscous stress tensor, τ_{ij}, the species molecular diffusive mass flux, $J_{k,i}$, and the species reaction rate, $\dot{\omega}_k$, that need to be modelled. A brief summary of the various sub-models to close these terms, as well as additional relationships needed, is presented below.

2.2.1 Ideal gas law

In most combustion applications, the gases are considered to behave as ideal gases. This way density and temperature are related through the equation of state as:

$$\rho=\frac{p}{RT} \tag{2.5}$$

where R is the mixture gas constant given by:

$$R=\sum_{k=1}^{N_s} Y_k R_k \tag{2.6}$$

with

$$R_k=\frac{R}{W_k} \tag{2.7}$$

where R is the universal gas constant and W_k is the species molecular weight. By combining Eqs 2.5-2.7, we can obtain a relationship between the mixture density, pressure, temperature and mixture composition:

$$\rho=\frac{p}{RT\sum_{k=1}^{N_s}\frac{Y_k}{W_k}} \tag{2.8}$$

2.2.2 Viscous stress tensor

In practical applications, fluids are assumed to be Newtonian, so that the viscous stress tensor can be expressed by Newton's law as:

$$\tau_{ij} = \mu \left(\frac{\partial u_i}{\partial x_j} + \frac{\partial u_j}{\partial x_i} \right) - \frac{2}{3} \mu \frac{\partial u_k}{\partial x_k} \delta_{ij} \tag{2.9}$$

where μ is the molecular dynamic viscosity and δ_{ij} is the Kronecker symbol.

2.2.3 Diffusion flux

The species molecular diffusive mass flux is expressed as:

$$J_{k,i} = \rho V_{k,i} Y_k \tag{2.10}$$

where $V_{k,i}$ are the diffusion velocities of species k that need to be approximated.

The most general and accurate way of obtaining $V_{k,i}$ is by solving the Stefan-Maxwell equations [29]. Then the species diffusion velocities are the solution of the system:

$$\begin{aligned} \nabla X_k = \sum_{l=1,\ l\neq k}^{N_s} \frac{X_l X_k}{D_{lk}} (V_{l,i} - V_{k,i}) + (Y_k - X_k) \frac{\nabla p}{p} + \frac{\rho}{p} \sum_{l=1,\ l\neq k}^{N_s} Y_l Y_k (f_{k,i} - f_{l,i}) \\ + \sum_{l=1,\ l\neq k}^{N_s} \frac{X_l X_k}{\rho D_{lk}} \left(\frac{D_l^T}{Y_l} - \frac{D_k^T}{Y_k} \right) \frac{\nabla T}{T} \end{aligned} \tag{2.11}$$

where $D_{lk} = D_{kl}$ is the binary mass diffusion coefficient of species l into species k, X_k is the mole fraction, Y_k is the mass fraction, f_k is the body force per unit mass and D_k^T is the thermo-diffusion coefficient.

A more simplified model in order to calculate the species diffusion velocities is Fick's law where the species molecular diffusive mass flux is approximated as:

$$J_{k,i} = \rho V_{k,i} Y_k = -\rho D_k \nabla Y_k \tag{2.12}$$

Even though Fick's law is only valid for binary mixtures and cannot account for thermo-diffusion (Soret effect), it is generally adopted for simplicity, also for multicomponent mixtures.

An alternative but still simple approximation is the Hirschfelder-Curtiss law, in which the species diffusion velocities are approximated as:

$$J_{k,i} = \rho V_{k,i} Y_k = -\rho Y_k D_k \frac{\nabla X_k}{X_k} - \rho D_k^{th} \frac{\nabla T}{T} = -\rho \frac{W_k}{W_{mix}} D_k \nabla X_k - \rho D_k^{th} \frac{\nabla T}{T} \tag{2.13}$$

where the last term expressing the Soret effect (mass diffusion due to temperature gradients) is sometimes neglected.

Calculation of the species mass diffusion coefficient

In order to calculate the species mass diffusion coefficient, D_k, different models exist. A simplified expression, originally proposed by Stefan [110] and later used by Hirschfelder and Curtiss [34], is the calculation of an effective diffusion coefficient of the k-th species into the mixture (mixture-average assumption) as:

$$D_k = \frac{1 - Y_k}{\sum_{k=1,\ k \neq l}^{N_s} \frac{X_k}{D_{kl}}} \tag{2.14}$$

It is an accurate approximation of obtaining the species mass diffusion coefficients but it is also rather computationally expensive as it requires the calculation of the species binary mass diffusion coefficients, D_{kl}, by means of kinetic theory [34].

Other more simplified models to calculate the species mass diffusion coefficients exist in literature [90]. In this case, D_k, can be calculated by assuming a constant species Schmidt number, Sc_k, as:

$$D_k = \frac{\mu}{\rho Sc_k} \tag{2.15}$$

or a constant species Lewis number, Le_k, as:

$$D_k = \frac{\alpha}{Le_k} \tag{2.16}$$

where α is the thermal diffusivity.

The molecular dynamic viscosity, μ, is a function of temperature, calculated by Sutherland's law as:

$$\mu = \frac{A_s \sqrt{T}}{1 + T_s/T} \tag{2.17}$$

where A_s and T_s are two Sutherland coefficients dependant on the mixture [99].

The molecular thermal diffusivity, α, is calculated as:

$$\alpha = \frac{\mu c_v[1.32 + 1.77(\overline{R}/c_v)]}{\overline{c}_p} \tag{2.18}$$

where c_v is the specific heat capacity at constant volume, $\overline{R}$ is the gas constant and $\overline{c}_p$ is the mean specific heat capacity at constant pressure.

These methods are usually adopted in numerical simulations of combustion applications in CFD codes as it is computationally less expensive than using Eqs 2.14. However, the variation of the species Lewis number with temperature has been found to be very broad for both premixed and non-premixed flames, making the constant Lewis number assumption not valid. Instead, the constant Schmidt number assumption is more appropriate for calculating the species mass diffusion coefficients [29].

2.2.4 Chemical source term

A chemical system of N_s species reacting through M reactions is considered:

$$\sum_{k=1}^{N_s} \nu'_{k,j} M_k \rightleftharpoons \sum_{k=1}^{N_s} \nu''_{k,j} M_k, \qquad j = 1, ..., M \tag{2.19}$$

where M_k is a symbol for chemical species k, $\nu'_{k,j}$ and $\nu''_{k,j}$ are the molar stoichiometric coefficients of species k in reaction j.

The chemical species reaction rate, $\dot{\omega}_k$, is the sum of all reaction rates $\dot{\omega}_{k,j}$ produced by all M reactions:

$$\dot{\omega}_k = \sum_{j=1}^{M} \dot{\omega}_{k,j} = W_k \sum_{j=1}^{M} \nu_{k,j} Q_j \tag{2.20}$$

with

$$Q_j = \frac{\dot{\omega}_{k,j}}{W_k \nu_{k,j}} \tag{2.21}$$

where Q_j is the rate of progress of reaction j.

The reaction rate of species k in reaction j is a function of the species concentrations and of the forward, $K_{f,j}$, and backward, $K_{b,j}$, reaction rate coefficients [90]:

$$\dot{\omega}_{k,j} = W_k(\nu''_{k,j} - \nu'_{k,j})\left(K_{f,j}\prod_{k=1}^{N_s}\left(\frac{\rho Y_k}{W_k}\right)^{\nu'_{k,j}} - K_{b,j}\prod_{k=1}^{N_s}\left(\frac{\rho Y_k}{W_k}\right)^{\nu''_{k,j}}\right) \tag{2.22}$$

The reaction rate coefficients are usually modelled using the empirical Arrhenius law as:

$$K_j = A_j T^{\beta_j}\ exp\left(-\frac{E_j}{RT}\right) \tag{2.23}$$

where A_j is the pre-exponential constant, T^{β_j} is the temperature exponent and E_j is the activation energy.

2.2.5 Energy flux

The energy flux in Eqs 7.4 is calculated as:

$$q_i = -\lambda\frac{\partial T}{\partial x_i} + \rho\sum_{k=1}^{N_s} h_k V_{k,i} Y_k + RT\sum_{k=1}^{N_s}\sum_{l=1}^{N_s}\frac{X_l D_k^T}{W_k D_{kl}}(V_{k,i} - V_{l,i}) \tag{2.24}$$

where λ is the thermal conductivity. The first term in the right hand side of Eqs 2.24 expresses the heat diffusion, given by Fourier's law, the second term accounts for the diffusion of species with different enthalpies and the last term expresses the Dufour effect (energy flux due to concentration gradients).

The thermal conductivity, λ, is calculated by a modified Euchen formula [7] as:

$$\lambda = \mu c_v[1.32 + 1.77(\overline{R}/c_v)] \tag{2.25}$$

2.2.6 Caloric equation of state

The total enthalpy per unit of mass of a mixture is the sum of the individual species static enthalpies:

$$h = \sum_{k=1}^{N_s} h_k Y_k \tag{2.26}$$

where h_k is the total enthalpy of species k, defined as the sum of their sensible and chemical enthalpies:

$$h_k = \underbrace{\int_{T_{ref}}^{T} c_{p,k}\, dT}_{sensible} + \underbrace{\Delta h^0_{f,k}}_{chemical} \tag{2.27}$$

with $\Delta h^0_{f,k}$ the chemical enthalpy of formation of species k at reference temperature T_{ref}, and $c_{p,k}$ the specific heat of species k.

Furthermore, the specific enthalpy and enthalpy of formation of a mixture are calculated as:

$$c_p = \sum_{k=1}^{N_s} c_{p,k} Y_k \tag{2.28}$$

and

$$\Delta h^0_f = \sum_{k=1}^{N_s} \Delta^0_{f,k} Y_k \tag{2.29}$$

2.3 Mixture fraction

The conserved scalar approach (mixture fraction z), previously mentioned in 1.2.2, is a methodology typically used in studies of non-premixed combustion (diffusion flames). The derivation of a transport equation for the mixture fraction can be based on species mass fractions or on elemental mass fractions and requires several assumptions. Both ways of deriving the transport equation for the mixture fraction are presented below and serve as an introduction for the newly proposed methodology to include differential diffusion effects in reactive flows presented later in Chapter 3.

2.3.1 Based on species mass fraction

In the simple case of a single-step reaction involving only fuel (F), oxidizer (O) and products (P):

$$\nu_F F + \nu_O O \rightleftharpoons \nu_P P \tag{2.30}$$

the mass fraction of fuel, oxidizer and products follows the conservation equation of chemical species (Eqs 2.3). By using Fick's law to calculate the species diffusive mass fluxes, assuming equal species mass diffusivities, $D_k = D$, the transport equations for fuel and oxidizer can be written as:

$$\frac{\partial(\rho Y_F)}{\partial t} + \frac{\partial(\rho u_i Y_F)}{\partial x_i} = \frac{\partial}{\partial x_i}\left(\rho D \frac{\partial Y_F}{\partial x_i}\right) + \dot{\omega}_F \tag{2.31}$$

$$\frac{\partial(\rho Y_O)}{\partial t} + \frac{\partial(\rho u_i Y_O)}{\partial x_i} = \frac{\partial}{\partial x_i}\left(\rho D \frac{\partial Y_O}{\partial x_i}\right) + \dot{\omega}_O \tag{2.32}$$

The species reaction rates, $\dot{\omega}_k$, are all related to the single-step reaction rate, Q, through Eqs 2.20:

$$\dot{\omega}_k = W_k \nu_k Q \tag{2.33}$$

so that the oxidizer reaction rate is related to the fuel reaction rate as:

$$\dot{\omega}_O = s\dot{\omega}_F \tag{2.34}$$

with

$$s = \frac{\nu_O W_O}{\nu_F W_F} \tag{2.35}$$

where s is the stoichiometric ratio.

By combining Eqs 2.31, 2.32 and 2.34, now the quantity $Z = sY_F - Y_O$ follows a transport equation without source term:

$$\frac{\partial(\rho Z)}{\partial t} + \frac{\partial(\rho u_i Z)}{\partial x_i} = \frac{\partial}{\partial x_i}\left(\rho D \frac{\partial Z}{\partial x_i}\right) \tag{2.36}$$

where Z is a conserved scalar and its value can be changed due to convection and diffusion but not by chemical reaction. However, reaction still plays an indirect role in Z since it controls temperature, that in turn changes the velocity and density fields. The boundary conditions of Z are then defined in Table 2.1.

Table 2.1: Boundary conditions for conserved scalar Z.

Conserved scalar	Fuel value Z_F	Oxidizer value Z_O
Z	sY_F^0	$-Y_O^0$

By normalizing the conserved scalar, Z, as:

$$z = \frac{Z - Z_O}{Z_F - Z_O} \tag{2.37}$$

now the reduced variable, z, (also known as mixture fraction) follows the same convection/diffusion transport equation:

$$\frac{\partial(\rho z)}{\partial t} + \frac{\partial(\rho u_i z)}{\partial x_i} = \frac{\partial}{\partial x_i}\left(\rho D \frac{\partial z}{\partial x_i}\right) \tag{2.38}$$

and has as boundary conditions: $z = 1$ in the fuel stream and $z = 0$ in the oxidizer stream (Table 2.2). Note, however, that equal species mass diffusivities have been assumed when deriving Eqs 2.38 so that differential diffusion effects are neglected.

Table 2.2: Boundary conditions for species mass fraction and mixture fraction z.

Variable	Fuel value	Oxidizer value
Fuel mass fraction	Y_F^0	0
Oxidizer mass fraction	0	Y_O^0
Mixture fraction z	1	0

Expressing the mixture fraction, z, with the boundary conditions defined in Table 2.1 leads to:

$$z = \frac{sY_F - Y_O + Y_O^0}{sY_F^0 + Y_O^0} = \frac{1}{1+\phi}\left(\phi \frac{Y_F}{Y_F^0} - \frac{Y_O}{Y_O^0} + 1\right) \tag{2.39}$$

where ϕ is the equivalence ratio defined as:

$$\phi = s\frac{Y_F^0}{Y_O^0} \tag{2.40}$$

2.3.2 Based on elemental mass fractions

An alternative formulation of the transport equation for the mixture fraction, z, can be derived by writing it in terms of elemental mass fractions [111]. Starting point is the transport equation for chemical species:

$$\frac{\partial(\rho Y_k)}{\partial t} + \frac{\partial(\rho u_i Y_k)}{\partial x_i} = -\frac{\partial J_{k,i}}{\partial x_i} + \dot{\omega}_k, \qquad k = 1,...,N_s \tag{2.41}$$

Linear combinations of Eqs 2.41 can be made such that the species chemical source term, $\dot{\omega}_k$, vanishes, resulting in N_e $(1 \leq N_e \leq N_s)$ transport equations for the elemental mass fractions, η'_λ, which reads:

$$\frac{\partial(\rho \eta'_\lambda)}{\partial t} + \frac{\partial(\rho u_i \eta'_\lambda)}{\partial x_i} = -\sum_{k=1}^{N_s} \frac{a_{\lambda,k} W_\lambda}{W_k} \frac{\partial J_{k,i}}{\partial x_i}, \qquad \lambda = 1,...,N_e \tag{2.42}$$

where the elemental mass fractions, η'_λ, relate to the species mass fraction, Y_k, as:

$$\eta'_\lambda = \sum_{k=1}^{N_s} \frac{a_{\lambda,k} W_\lambda}{W_k} Y_k \tag{2.43}$$

with $a_{\lambda,k}$ the number of element atoms λ $(\lambda = 1,\dots,N_e)$ in species k and W_λ, W_k the elemental and species molecular weights, respectively.

Mixture fraction, z, can be written in terms of coupling functions, β, as [125]:

$$z = \frac{\beta - \beta_O}{\beta_F - \beta_O} \tag{2.44}$$

where β_F and β_O are constants evaluated in the fuel and oxidizer streams, respectively.

The coupling function, β, is a function of the elemental mass fractions, η'_λ, and defined as:

$$\beta = \sum_{\lambda=1}^{N_e} \gamma_\lambda \eta'_\lambda = \sum_{\lambda=1}^{N_e} \gamma_\lambda \sum_{k=1}^{N_s} \frac{a_{\lambda,k} W_\lambda Y_k}{W_k} \tag{2.45}$$

where γ_λ are weighting factors.

By combining Eqs 2.42, 2.44 and 2.45, a transport equation for the mixture fraction,

z, based on elemental mass fractions can be written as:

$$\frac{\partial(\rho z)}{\partial t} + \frac{\partial(\rho u_i z)}{\partial x_i} = \frac{-1}{\beta_F - \beta_O} \sum_{\lambda=1}^{N_e} \gamma_\lambda \left(\sum_{k=1}^{N_s} \frac{a_{\lambda,k} W_\lambda}{W_k} \frac{\partial J_{k,i}}{\partial x_i} \right) \tag{2.46}$$

The species diffusive mass fluxes, $J_{k,i}$, have to be evaluated in Eqs 2.46. By choosing different mass diffusion coefficients for the various chemical species, differential diffusion effects can be included in the transport equation for the mixture fraction, z. The weighting factors, γ_λ, are commonly assigned the values proposed by Bilger [6], given in table 2.3.

Table 2.3: Weighting factors, γ_λ, as proposed by Bilger [6].

γ_C	$2/W_C$
γ_H	$1/(2W_H)$
γ_O	$-1/W_O$
γ_N	0

By making use of Eqs 2.44, 2.45 and the weighting factors, γ_λ, defined in table 2.3, Bilger's definition of the mixture fraction is obtained:

$$z = \frac{2(Y_C - Y_{C,O})/W_C + (Y_H - Y_{H,O})/2W_H - (Y_O - Y_{O,O})/W_O}{2(Y_{C,F} - Y_{C,O})/W_C + (Y_{H,F} - Y_{H,O})/2W_H - (Y_{O,F} - Y_{O,O})/W_O} \tag{2.47}$$

where the subscripts F and O denote the fuel and oxidizer streams, respectively. Bilger's definition of the mixture fraction has the advantage that not only differential diffusion effects are included but it also preserves the stoichiometric value of the mixture fraction.

2.4 Example

Following the theoretical analysis previously presented in section 2.3, two examples for deriving a transport equation for the mixture fraction, z, based on species mass fractions and on elemental mass fraction in the case of H_2 combustion are given in this section. The presentation of these two examples is instructive since a similar derivation is performed in the newly proposed methodology presented later in Chapter 3.

2.4.1 Based on species mass fraction

In the simple case of hydrogen combustion, considering $N_s = 4$ species k, with H_2 as fuel, air (23.2% O_2, 76.8% N_2 (inert gas)) as oxidizer and H_2O as products, the single-step reaction can be written as:

$$2H_2+(O_2+3.76N_2)\rightarrow 2H_2O+3.76N_2 \tag{2.48}$$

Assuming equal species mass diffusivities and unity Lewis number, the transport equations for fuel (H_2) and oxidizer (O_2) can be written as:

$$\frac{\partial(\rho Y_{H_2})}{\partial t}+\frac{\partial(\rho u_i Y_{H_2})}{\partial x_i}=\frac{\partial}{\partial x_i}\left(\rho D\frac{\partial Y_{H_2}}{\partial x_i}\right)+\dot{\omega}_{H_2} \tag{2.49}$$

$$\frac{\partial(\rho Y_{O_2})}{\partial t}+\frac{\partial(\rho u_i Y_{O_2})}{\partial x_i}=\frac{\partial}{\partial x_i}\left(\rho D\frac{\partial Y_{O_2}}{\partial x_i}\right)+\dot{\omega}_{O_2} \tag{2.50}$$

The oxidizer reaction rate is then related to the fuel reaction rate as:

$$\dot{\omega}_{O_2}=s\dot{\omega}_{H_2} \tag{2.51}$$

where the stoichiometric ratio is:

$$s=\frac{\nu_{O_2}W_{O_2}}{\nu_{H_2}W_{H_2}}=\frac{0.5\cdot 31.9988}{1\cdot 2.01594}=7.9364 \tag{2.52}$$

Then the equivalence ratio is calculated as:

$$\phi=s\frac{Y^0_{H_2}}{Y^0_{O_2}}=7.9364\cdot\frac{1.0}{0.232}=34.2086 \tag{2.53}$$

By combining Eqs 2.49, 2.50 and 2.51, the conserved scalar Z, defined as $Z=7.9364Y_{H_2}-Y_{O_2}$, follows the transport Eqs 2.36. Following the same normalization procedure, previously described in section 2.3.1, the transport equation for the mixture fraction, z, is obtained (Eqs 2.38).

2.4.2 Based on elemental mass fractions

In the simple case of hydrogen combustion presented before, considering $N_s=4$ species k (H_2, H_2O, O_2, N_2) and $N_\lambda=3$ elements λ (H, O, N) the transport equations for the species mass fractions can be written as:

$$\frac{\partial(\rho Y_k)}{\partial t} + \frac{\partial(\rho u_i Y_k)}{\partial x_i} = -\frac{\partial J_{k,i}}{\partial x_i} + W_k \dot{\omega}_k, \qquad k = H_2,\ H_2O,\ O_2,\ N_2 \tag{2.54}$$

The transport equations for the elemental mass fractions, η'_λ, can be written as:

$$\frac{\partial(\rho \eta'_\lambda)}{\partial t} + \frac{\partial(\rho u_i \eta'_\lambda)}{\partial x_i} = -\sum_{k=1}^{N_s} \frac{a_{\lambda,k} W_\lambda}{W_k} \frac{\partial J_{k,i}}{\partial x_i}, \qquad \lambda = H,\ O,\ N \tag{2.55}$$

The elemental mass fractions, η'_λ, relate to the species mass fraction, Y_k, as:

$$\eta'_\lambda = \sum_{k=1}^{N_s} \frac{a_{\lambda,k} W_\lambda}{W_k} Y_k \tag{2.56}$$

where

$$\eta'_H = \frac{2 \cdot 1.00797}{2.01594} Y_{H_2} + \frac{2 \cdot 1.00797}{18.0153} Y_{H_2O} \tag{2.57}$$

$$\eta'_O = \frac{2 \cdot 15.9994}{31.9988} Y_{O_2} + \frac{1 \cdot 15.9994}{18.0153} Y_{H_2O} \tag{2.58}$$

$$\eta'_N = \frac{2 \cdot 14.0067}{28.0153} Y_{N_2} \tag{2.59}$$

with $W_{H_2} = 2.01594$ g/mol, $W_{H_2O} = 18.0153$ g/mol, $W_{O_2} = 31.9988$ g/mol and $W_{N_2} = 28.0134$ g/mol.

The coupling function, β, with the use of Bilger's weighting factors, γ_λ, defined in Table 2.3, can be written as:

$$\beta = \sum_{\lambda=1}^{N_e} \gamma_\lambda \eta'_\lambda = \frac{1}{2W_H}\eta'_H - \frac{1}{W_O}\eta'_O \tag{2.60}$$

The evaluation of the coupling function, β, in the fuel and oxidizer streams provide constants, β_F and β_O, respectively.

2.5 Large Eddy Simulations

2.5.1 Introduction

Most of the combustion applications usually occur in a turbulent environment. In order for numerical simulations to be able to describe these processes, three major techniques have been developed in the past. The Reynolds-Averaged Navier Stokes (RANS) approach was the first to be developed, in which only the mean values of all variables are solved. With the Large Eddy Simulations (LES) approach, the turbulent large scales are explicitly computed while the effect of the smaller ones is modelled using sub-grid models. Finally, with the Direct Numerical Simulations (DNS) the full set of the conservation equations are solved without the use of any model for turbulence. All turbulence scales are explicitly computed and their effect on combustion is accurately captured by the numerical simulation.

In the present thesis, the Large Eddy Simulation (LES) approach will be used for the numerical simulations. The motivation for this choice is that LES is able to capture the unsteady features of the flow, when compared to RANS, and is computationally less expensive, when compared to DNS.

2.5.2 LES filter

As mentioned above, in LES only the large scales of motion are computed while the small scales are modelled. In order to separate the large scales from the smaller ones, the variables are filtered in physical space (weighted average over a given volume). A filtered quantity is then defined as:

$$\overline{f}(x) = \int f(x')\ F(x-x')dx' \tag{2.61}$$

where F is the LES filter.

A box filter in physical space is a commonly used filter for Large Eddy Simulations and is defined as:

$$F(x) = F(x_1,x_2,x_3) = \begin{cases} 1/\Delta^3 & \text{if } |x_i| \leq \Delta/2, \quad i = 1,2,3 \\ 0 & \text{otherwise} \end{cases}$$

where (x_1,x_2,x_3) are the spatial coordinates of location x and $\Delta = (\Delta_1\Delta_2\Delta_3)^{1/3}$ is the representative filter width.

In this case a variable, f, is decomposed into a filtered quantity, $\overline{f}$, resolved in the numerical simulations and an unresolved part, f', due to unresolved flow motions ($f = \overline{f} + f'$).

For variable density flows, a mass weighted (Favre) filtering is used:

$$\overline{\rho}\widetilde{f}(x) = \int \rho f(x')\ F(x-x')dx' \tag{2.62}$$

where $\overline{\rho}$ is the filtered (resolved) density.

2.5.3 Filtered conservation equations

The application of a spatial filter in the instantaneous balance equations, Eqs 2.1 - 7.4, results in the following set of conservation equations:

- Conservation of mass:

$$\frac{\partial\overline{\rho}}{\partial t} + \frac{\partial(\overline{\rho}\widetilde{u}_i)}{\partial x_i} = 0 \tag{2.63}$$

- Conservation of momentum:

$$\frac{\partial(\overline{\rho}\widetilde{u}_j)}{\partial t} + \frac{\partial(\overline{\rho}\widetilde{u}_i\widetilde{u}_j)}{\partial x_i} = -\frac{\partial\overline{p}}{\partial x_j} + \frac{\partial\overline{\tau}_{ij}}{\partial x_i} - \frac{\partial}{\partial x_i}\left[\overline{\rho}(\widetilde{u_iu_j} - \widetilde{u}_i\widetilde{u}_j)\right] + \overline{\rho}g_j, \qquad j = 1,2,3 \tag{2.64}$$

where $\overline{\rho}(\widetilde{u_iu_j} - \widetilde{u}_i\widetilde{u}_j)$ represents the sub-grid scale stresses that need to be modelled.

- Conservation of chemical species:

$$\frac{\partial(\overline{\rho}\widetilde{Y}_k)}{\partial t} + \frac{\partial(\overline{\rho}\widetilde{u}_i\widetilde{Y}_k)}{\partial x_i} = -\frac{\partial\overline{J}_{k,i}}{\partial x_i} - \frac{\partial}{\partial x_i}\left[\overline{\rho}(\widetilde{u_iY_k} - \widetilde{u}_i\widetilde{Y}_k)\right] + \overline{\dot{\omega}}_k, \qquad k = 1,\ldots,N_s \tag{2.65}$$

where $\overline{\rho}(\widetilde{u_iY_k} - \widetilde{u}_i\widetilde{Y}_k)$ represents species transport due to sub-grid scale fluctuations, $\overline{J}_{k,i}$ are the filtered laminar mass diffusion fluxes and $\overline{\dot{\omega}}_k$ is the filtered chemical reaction rate that need to be modelled.

- Conservation of energy:

$$\frac{\partial(\overline{\rho}\widetilde{h})}{\partial t} + \frac{(\overline{\rho}\widetilde{u}_i\widetilde{h})}{\partial x_i} = \overline{\frac{Dp}{Dt}} - \frac{\partial\overline{q}_i}{\partial x_i} + \overline{\tau_{ij}\frac{\partial u_i}{\partial x_j}} - \frac{\partial}{\partial x_i}\left[\overline{\rho}(\widetilde{u_ih} - \widetilde{u}_i\widetilde{h})\right] + \overline{\dot{Q}} \tag{2.66}$$

where $\overline{\rho}(\widetilde{u_ih} - \widetilde{u}_i\widetilde{h})$ represents enthalpy transport due to sub-grid scale fluctiations and $\overline{q}_i$

are the laminar diffusion enthalpy fluxes that need to be modelled.

Models are needed for modelling the unclosed terms in the above equations. Models for turbulence, chemistry and turbulence-chemistry interaction have to be provided in order to close the full set of the conservation equations. A detailed description of the various models available in literature can be found in [90]. An overview of the models used for the numerical simulations in the thesis is presented in section 2.6.

Filtered laminar diffusion fluxes

The filtered laminar diffusion fluxes are commonly modelled by a simple gradient assumption. By using Fick's law in order to calculate the species diffusion mass fluxes in Eqs 2.10 and neglecting the Soret effect, the filtered laminar diffusion fluxes of species are calculated as:

$$\overline{J}_{k,i} = -\overline{\rho D_k \frac{\partial Y_k}{\partial x_i}} \approx -\overline{\rho} D_k \frac{\partial \widetilde{Y}_k}{\partial x_i} \tag{2.67}$$

by ignoring fluctuations of the mass diffusion coefficients D_k.

By neglecting the Dufour effect in the energy flux equation (Eqs 2.24), the filtered laminar diffusion fluxes of enthalpy are calculated as:

$$\overline{q}_i = -\lambda \frac{\partial \widetilde{T}}{\partial x_i} + \rho \sum_{k=1}^{N_s} h_k \overline{V_{k,i} Y_k} = -\frac{\lambda}{c_p} \frac{\partial \widetilde{h}}{\partial x_i} + \sum_{k=1}^{N_s} \left(\frac{1}{Le_k} - 1 \right) \frac{\partial}{\partial x_i} \left(\frac{\lambda}{c_p} h_k \frac{\partial \widetilde{Y}_k}{\partial x_i} \right) \tag{2.68}$$

by ignoring fluctuations of the thermal conductivity λ.

2.5.4 Filtered mixture fraction

Filtering the mixture fraction transport equation, Eq 2.38, results in:

$$\frac{\partial(\overline{\rho}\widetilde{z})}{\partial t} + \frac{\partial(\overline{\rho}\widetilde{u}_i\widetilde{z})}{\partial x_i} = \frac{\partial}{\partial x_i}\left(\overline{\rho} D \frac{\partial \widetilde{z}}{\partial x_i}\right) - \frac{\partial}{\partial x_i}\left[\overline{\rho}(\widetilde{u_i z} - \widetilde{u}_i \widetilde{z})\right] \tag{2.69}$$

where $\overline{\rho}(\widetilde{u_i z} - \widetilde{u}_i \widetilde{z})$ represents scalar transport due to sub-grid scale fluctuations that needs to be modelled.

2.5.5 Filtered mixture fraction variance

When modelling the turbulence-chemistry interaction, the shape of the z-probability density function (pdf) is presumed by a beta function, which is constructed from the filtered mixture fraction, $\widetilde{z}$, and mixture fraction variance, $\widetilde{z''^2}$. In LES the mixture fraction variance is usually modelled by a scale similarity assumption as [90]:

$$\widetilde{z''^2} = c_z \Delta^2 \left(\frac{\partial \widetilde{z}}{\partial x_k} \right)^2 \tag{2.70}$$

where c_z is a model parameter either assigned a constant value (e.g. $c_z = 0.15$ [101]) or determined dynamically. An alternative method is to solve a transport equation for the mixture fraction variance [90].

2.6 Turbulent combustion modelling

2.6.1 Turbulence modelling

Sub-grid scale stresses

A widely used turbulence model for closure of the sub-grid scale stress terms in the momentum equations is the standard Smagorinsky model [104]. It is an eddy viscosity type model where the sub-grid scale stress terms, $\overline{\rho}(\widetilde{u_i u_j} - \widetilde{u}_i \widetilde{u}_j)$, are expressed according to the Boussinesq assumption as:

$$\overline{\rho}(\widetilde{u_i u_j} - \widetilde{u}_i \widetilde{u}_j) = \mu_t \left[\left(\frac{\partial \widetilde{u}_i}{\partial x_j} + \frac{\partial \widetilde{u}_j}{\partial x_i} \right) - \frac{2}{3} \frac{\partial \widetilde{u}_k}{\partial x_k} \delta_{ij} \right] \tag{2.71}$$

The turbulent viscosity, μ_t, is then modelled as:

$$\mu_t = \overline{\rho} (c_s \, \Delta)^2 \widetilde{S} \tag{2.72}$$

where c_s is a model constant and $\widetilde{S}$ is the filtered strain rate:

$$\widetilde{S} = (2 \widetilde{S}_{ij} \widetilde{S}_{ij})^{1/2} \tag{2.73}$$

with the filtered strain rate tensor, $\widetilde{S}_{ij}$, expressed as:

$$\widetilde{S}_{ij} = \frac{1}{2} \left(\frac{\partial \widetilde{u}_i}{\partial x_j} + \frac{\partial \widetilde{u}_j}{\partial x_i} \right) \tag{2.74}$$

In the case of homogeneous isotropic turbulence, the model constant is estimated as $c_s \approx 0.17$ [91]. However, the Smagorinsky model is known to be too dissipative and

c_s depends on the flow configuration so values of $c_s \approx 0.1 - 0.2$ are often used [27]. An extension to the standard Smagorinsky model is to determine the constant, c_s, dynamically during the numerical simulations [28].

Another commonly used model to close the sub-grid scale stress terms is the one-equation turbulence model [102], in which turbulent viscosity, μ_t, is modelled as:

$$\mu_t = \overline{\rho} c_k \Delta\, \widetilde{k}^{\frac{1}{2}} \tag{2.75}$$

where c_k is a model constant determined dynamically in the simulation or assigned a constant value (e.g. $c_k = 0.07$ [26]). Within the one-equation turbulence model a transport equation for the sub-grid scale turbulent kinetic energy, k, is solved:

$$\frac{\partial(\overline{\rho}\widetilde{k})}{\partial t} + \frac{\partial(\overline{\rho}\widetilde{u}_i\widetilde{k})}{\partial x_i} = \frac{\partial}{\partial x_i}\left[\left(\mu + \frac{\mu_t}{Sc_t}\right)\frac{\partial \widetilde{k}}{\partial x_i}\right] + P - \overline{\rho}\widetilde{\varepsilon} \tag{2.76}$$

where P is the production rate of the sub-grid scale kinetic energy calculated as:

$$P = 2\mu_t\left[\widetilde{S} : \widetilde{S} - \frac{1}{3}\left(\frac{\partial \widetilde{u}_i}{\partial x_j}\right)^2\right] - \frac{2}{3}\overline{\rho}\widetilde{k}\frac{\partial \widetilde{u}_i}{\partial x_j} \tag{2.77}$$

and dissipation rate, ε, is expressed as:

$$\widetilde{\varepsilon} = c_\varepsilon \widetilde{k}^{\frac{3}{2}} \Delta^{-1} \tag{2.78}$$

with the dimensionless model coefficient, c_ε, assigned a constant value ($c_\varepsilon = 1.05$ [26]).

Once turbulent viscosity, μ_t, is obtained from a turbulence model then turbulent mass, D_t, and thermal, α_t, diffussivities can be calculated as:

$$D_t = \frac{\mu_t}{Sc_t} \tag{2.79}$$

$$\alpha_t = \frac{\mu_t}{Pr_t} \tag{2.80}$$

where Sc_t is the turbulent Schmidt number and Pr_t is the turbulent Prandtl number.

Sub-grid scale fluxes

The terms related with transport due to sub-grid scale fluctuations of species, $\overline{\rho}(\widetilde{u_iY_k} - \widetilde{u}_i\widetilde{Y}_k)$, enthalpy, $\overline{\rho}(\widetilde{u_ih} - \widetilde{u}_i\widetilde{h})$ and mixture fraction, $\overline{\rho}(\widetilde{u_iz} - \widetilde{u}_i\widetilde{z})$, in Eqs 2.65, 2.66 and 2.69, respectively, are commonly approximated by the gradient diffusion hypothesis model as:

$$\overline{\rho}(\widetilde{u_iY_k} - \widetilde{u}_i\widetilde{Y}_k) = -\frac{\mu_t}{Sc_t}\frac{\partial \widetilde{Y}_k}{\partial x_i} \tag{2.81}$$

$$\overline{\rho}(\widetilde{u_ih} - \widetilde{u}_i\widetilde{h}) = -\frac{\mu_t}{Pr_t}\frac{\partial \widetilde{h}}{\partial x_i} \tag{2.82}$$

$$\overline{\rho}(\widetilde{u_iz} - \widetilde{u}_i\widetilde{z}) = -\frac{\mu_t}{Sc_t}\frac{\partial \widetilde{z}}{\partial x_i} \tag{2.83}$$

where the turbulent viscosity, μ_t, is calculated from the turbulence model.

2.6.2 Combustion modelling

The Burke-Schumann model, also briefly presented in section 1.2.2, is used to model combustion in the numerical simulations of the thesis. It is a simple combustion model, which assumes infinitely fast chemistry, where fuel and oxidizer cannot coexist at the same location because the reaction rate is infinitely fast compared to all other time scales in the flame. In this case, the species mass fractions, Y_k, are a piecewise linear function of the mixture fraction, z, shown in Figure 2.1, and are simply related by setting either $Y_O = 0$ (on the fuel side) or $Y_F = 0$ (on the oxidizer side) in Eqs 2.39:

- On the fuel side ($z > z_{st}$):

$$Y_F(z) = zY_F^0 + (z-1)\frac{Y_O^0}{s} = Y_F^0\frac{z - z_{st}}{1 - z_{st}}$$
$$Y_O(z) = 0$$

- On the oxidizer side ($z < z_{st}$):

$$Y_F(z) = 0$$
$$Y_O(z) = Y_O^0\left(1 - \frac{z}{z_{st}}\right)$$

where Y_F^0 and Y_O^0 denote the inlet mass fractions at the fuel or oxidizer streams, respectively.

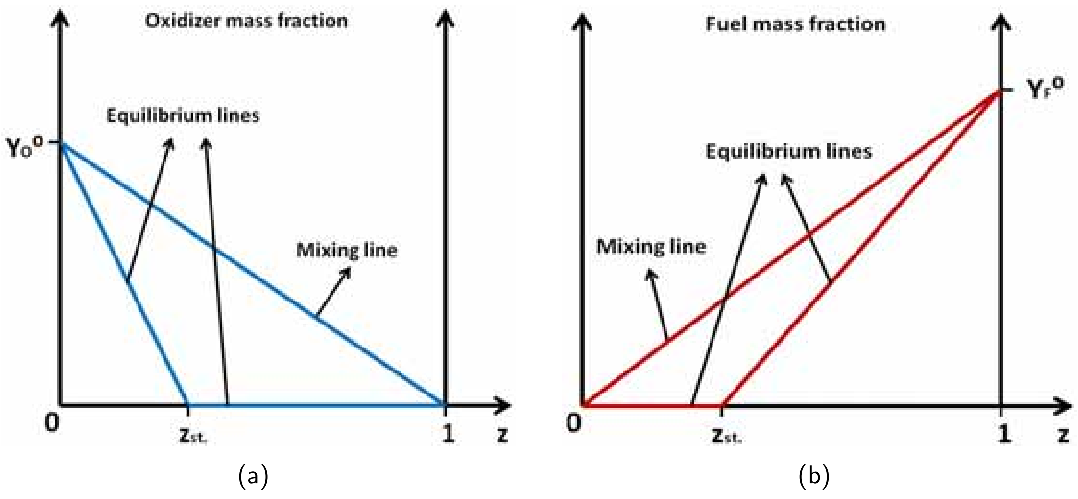

(a) (b)

Figure 2.1: Burke-Schumann solution for irreversible infinitely fast chemistry for (a) oxidizer and (b) fuel.

The stoichiometric mixture fraction corresponds at the location where both fuel and oxidizer are totally consumed ($Y_F = Y_O = 0$) and is defined by Eq 2.39 as:

$$z_{st} = \frac{Y_O^0}{sY_F^0 + Y_O^0} = \frac{1}{1 + \frac{sY_F^0}{Y_O^0}} = \frac{1}{1 + \frac{\nu_O W_O Y_F^0}{\nu_F W_F Y_O^0}} = \frac{1}{1+\phi} \tag{2.84}$$

The mixing lines shown in Figure 2.1 correspond to states where fuel and oxidizer would mix without reaction (pure mixing). In this case the pure mixing solution is:

$$Y_F = Y_F^0 z \tag{2.85}$$

$$Y_O = Y_O^0(1-z) \tag{2.86}$$

2.6.3 Turbulence-Chemistry interaction

In the case of laminar flames, the species mass fractions, Y_k, are a piecewise liner function of the mixture fraction, z. However, when turbulent flames are considered, additional problems arise related to the averaging procedures. In order to determine the average value of the species mass fractions, not only the mean value of the mixture fraction is needed but also higher moments (e.g. the mixture fraction variance). With these two parameters a probability density function (pdf) of the mixture fraction, $P(z)$, can be constructed and the average species mass fractions can be obtained as:

$$\overline{\rho}\widetilde{Y}_k = \int_0^1 \left(\overline{\rho Y_k|z^*}\right) P(z^*) dz^* \tag{2.87}$$

where $\overline{\rho Y_k|z^*}$ denotes the conditional species mass fraction for a given value of the mixture fraction, $z = z^*$, and $P(z^*)$ is the probability density function (pdf) of mixture fraction z.

For infinitely fast chemistry, reversible or not, the conditional averages $\left(\overline{\rho Y_k|z^*}\right)$ reduce to:

$$\left(\overline{\rho Y_k|z^*}\right) = \rho(z^*)\ Y_k(z^*) \tag{2.88}$$

so that the mean species mass fractions can be calculated as:

$$\overline{\rho}\widetilde{Y}_k = \int_0^1 \rho Y_k(z) P(z) dz \tag{2.89}$$

This way the determination of the species mean mass fraction, $\widetilde{Y}_k$, reduces to the determination of the probability density function, $P(z)$, of the mixture fraction z.

The probabilistic density function of z is assumed to follow a beta distribution, fully defined by the mean mixture fraction, $\widetilde{z}$, and the mixture fraction variance, $\widetilde{z''^2}$:

$$P(z) = \frac{z^{a-1}(1-z)^{b-1}}{B(a,b)} \tag{2.90}$$

where $B(a,b)$ is a beta function. The pdf parameters a and b are determined from $\widetilde{z}$ and $\widetilde{z''^2}$ as:

$$a = \widetilde{z}\left[\frac{\widetilde{z}(1-\widetilde{z})}{\widetilde{z''^2}} - 1\right], \quad b = \frac{a}{\widetilde{z}} - a \tag{2.91}$$

Even though the beta pdf is able to describe quite accurately the distribution of the mixture fraction in most cases, when used in CFD codes, it reduces to a Dirac delta function for $\widetilde{z} = 0$ and $\widetilde{z} = 1$ for numerical reasons [82].

Chapter 3

Methodology development

3.1 Introduction

In this chapter the formulation of the newly proposed methodology to incorporate differential diffusion effects in CFD simulations of reactive flows is presented. The derivation of the transport equations for the conserved scalar equations is given for both laminar and turbulent flows. In addition, the capabilities and advantages of the new methodology are presented and a comparison with existing models in literature is made.

This chapter is based on Maragkos et al. [60].

3.2 Formulation of methodology

The starting point is the set of transport equations for chemical species written in matrix notation:

$$\frac{\partial(\rho Y)}{\partial t} + \nabla \cdot (\rho u Y) = -\nabla \cdot J + \dot{\omega} \tag{3.1}$$

where $Y = [Y_1, \dots, Y_{N_s}]$, $J = [J_1, \dots, J_{N_s}]$ and $\dot{\omega} = [\dot{\omega}_1, \dots, \dot{\omega}_{N_s}]$ contain the mass fraction, diffusive mass flux and chemical source term of species k ($k = 1, \dots, N_s$), respectively, ρ is the density and u is the velocity vector. Using different diffusion coefficients for each of the chemical species, a correction velocity, u_c, must be added in the convection term of the transport equations to ensure mass conservation, $\sum_{k=1}^{N_s} J_k = \sum_{k=1}^{N_s} \rho Y_k V_{k,i} = 0$ [90, 29]. This way any additional non-zero diffusion mass flux is cancelled, and solving for $N_s - 1$ species results in a correct concentration for the last N_s species (typically obtained as $1 - \sum_{k=1}^{N_s-1} Y_k$).

In order to calculate the species mass diffusive flux, $J = \rho Y V$, the species diffusion velocities, V, have to be known. Several approximations exist in order to calculate them [29] (Stefan - Maxwell equations, Hirschfelder - Curtiss law, Fick's law) and in the present work Fick's law is adopted. This way the species diffusive mass flux, neglecting the Soret (mass diffusion due to temperature gradients) and Dufour (enthalpy flux due to concentration gradients) effects, can be calculated as:

$$J = \rho Y V = -\rho D \nabla Y \tag{3.2}$$

so that Eqs (3.1) can be re-written as:

$$\frac{\partial(\rho Y)}{\partial t} + \nabla \cdot (\rho u Y) = \nabla \cdot (\rho D \nabla Y) + \dot{\omega} \tag{3.3}$$

where D is the diagonal diffusion matrix of dimensions $N_s \times N_s$.

Linear combinations of species Eqs (3.3) can be made such that the chemical source term vanishes:

$$\frac{\partial(\rho B' Y)}{\partial t} + \nabla \cdot (\rho u B' Y) = \nabla \cdot (\rho B' D \nabla Y) + \underbrace{B' \dot{\omega}}_{=0} \tag{3.4}$$

resulting in transport equations for the elemental mass fractions $\eta' = B'Y = [\eta'_1, \dots, \eta'_{N_e}]$, which are conserved scalars. As such, we introduced the projection matrix B' of dimensions $N_e \times N_s$, projecting the full chemical space (species space) of dimensions N_s to a subspace of conserved scalars (element space) of dimensions N_e, which we consider as the resolved space. Indeed, the proposed methodology consists of solving transport equations for all possible conserved scalars and retrieves the unresolved chemical space from a combustion model (e.g. Burke-Schumann, equilibrium chemistry or a flamelet table). As such, the elements of matrix B' then read:

$$B'_{\lambda k} = \frac{a_{\lambda,k} W_\lambda}{W_k} \tag{3.5}$$

where $a_{\lambda,k}$ is the number of element atoms λ ($\lambda = 1, \dots, N_e$) in species k and W_λ, W_k are the elemental and species molecular weights, respectively.

It will prove convenient not to use the elemental mass fractions themselves, but to recombine them such that the rows of the projection matrix are orthonormal, i.e. $BB^T = I$, with I the identity matrix. The conserved scalars are now defined as $\eta = BY = [\eta_1, \dots, \eta_{N_e}]$. This is essentially a coordinate transformation from η' to η space. Note that if $BB^T = I$

and B is a square matrix then it is orthogonal and its transpose is equal to its inverse ($BB^T = B^T B = I$). However, if B is a rectangular matrix then the conditions $BB^T = I$ and $B^T B = I$ are not equivalent. The condition $BB^T = I$ implies that the rows of matrix B are orthonormal while the condition $B^T B = I$ implies that the columns of matrix B are orthonormal. In other words, matrix B is obtained by making the rows of matrix B' orthonormal. We also consider a matrix U with orthonormal rows (i.e. $UU^T = I$), which forms an orthogonal basis with B, (i.e. $UB^T = 0$; $BU^T = 0$), with dimensions $(N_s - N_e) \times N_s$, projecting the full chemical space to the unresolved space. By going from N_s transport equations for chemical species, Y, to N_e transport equations for conserved scalars, η, (dimensionality reduction) there is some unresolved chemical space that we consider with the U matrix. The use of orthogonal spaces results in minimum errors in approximations, without adding further complexity to the methodology. Because of orthogonality it can be verified that $B^T B + U^T U = I$, so that Eqs (3.4) are re-written as:

$$\frac{\partial(\rho BY)}{\partial t} + \nabla \cdot (\rho u BY) = \nabla \cdot [\rho BD \underbrace{(B^T B + U^T U)}_{I} \nabla Y] \tag{3.6}$$

and Eqs (3.6) can be further re-written as:

$$\frac{\partial(\rho BY)}{\partial t} + \nabla \cdot (\rho u BY) = \nabla \cdot (\rho BDB^T \nabla BY) + \nabla \cdot (\rho BDU^T \nabla UY) \tag{3.7}$$

At this point a distinction will be made in the formulation of the methodology for laminar and turbulent flows. The derivation of the equations for the two different cases, starting from Eqs (3.7), is presented in 3.2.1 and 3.2.2.

Mathematical proof of property $B^T B + U^T U = I$

From rectangular matrices B and U, a new square matrix A can be formed as:

$$A = \left| \frac{B}{U} \right|$$

It can be verified that $AA^T = I$:

$$\left| \frac{B}{U} \right| \left| \, B^T \mid U^T \, \right| = \begin{vmatrix} BB^T & BU^T \\ UB^T & UU^T \end{vmatrix} = \begin{vmatrix} I & 0 \\ 0 & I \end{vmatrix} = I$$

where $BU^T = 0$ and $UB^T = 0$ because matrices B and U form an orthogonal basis.

Since $AA^T = I$ and A is a square matrix then it is also orthogonal, i.e. $AA^T = A^TA = I$, which leads to:

$$A^TA = I \ \Rightarrow$$

$$\left|\begin{array}{c|c} B^T & U^T \end{array}\right| \left|\begin{array}{c} B \\ \hline U \end{array}\right| = \left|B^TB + U^TU\right| = I$$

3.2.1 Laminar flows

In the case of a laminar flow, the projection of the full chemical space to the unresolved space is such that $UY = \mathscr{C}(\eta)$ can be retrieved from the combustion model, with $\mathscr{C}$ being a multidimensional function from space N_e to space $N_s - N_e$.

By introducing the conserved scalars, η, Eqs (3.7) can be re-written as:

$$\frac{\partial(\rho\eta)}{\partial t} + \nabla\cdot(\rho u\eta) = \nabla\cdot(\rho \underbrace{BDB^T}_{D_1}\nabla\eta) + \nabla\cdot(\rho \underbrace{BDU^T\frac{\partial\mathscr{C}}{\partial\eta}}_{D_2}\nabla\eta) \tag{3.8}$$

where $\frac{\partial\mathscr{C}}{\partial\eta}$ is the Jacobian matrix of function $\mathscr{C}$, obtained from the combustion model.

3.2.2 Turbulent flows

In this section the extension of the methodology for turbulent flows, in the context of Large Eddy Simulations, is presented. By performing Favre averaging in space, Eqs (3.7), can be written for turbulent flows as:

$$\frac{\partial(\overline{\rho}B\widetilde{Y})}{\partial t} + \nabla\cdot(\overline{\rho}\widetilde{u}B\widetilde{Y}) = \nabla\cdot(\overline{\rho}BDB^T\nabla B\widetilde{Y}) - \underbrace{\nabla\cdot(\overline{\rho}[\widetilde{uBY} - \widetilde{u}B\widetilde{Y}])}_{A} + \underbrace{\nabla\cdot(\overline{\rho}BDU^T\nabla U\widetilde{Y})}_{B} \tag{3.9}$$

where the unclosed terms *A* and *B* have to be modelled.

Term *A*, expressing the unresolved chemical species fluxes, can be modelled by the gradient diffusion hypothesis model [90]as:

$$\nabla\cdot(\overline{\rho}[\widetilde{uBY} - \widetilde{u}B\widetilde{Y}]) = -\nabla\cdot(\overline{\rho}D_t\nabla B\widetilde{Y}) \tag{3.10}$$

Furthermore, the projection of the full chemical space to the unresolved space will now depend on both the mean value and the variance of the conserved scalars, η, and can be such that $U\widetilde{Y} = \widetilde{\mathscr{C}}(\widetilde{\eta},\widetilde{\eta''^2})$ can be retrieved from the combustion model as:

$$\nabla U\widetilde{Y} = \nabla\widetilde{\mathscr{C}}(\widetilde{\eta},\widetilde{\eta''^2}) = \frac{\partial\widetilde{\mathscr{C}}}{\partial\widetilde{\eta}}\nabla\widetilde{\eta} + \frac{\partial\widetilde{\mathscr{C}}}{\partial\widetilde{\eta''^2}}\nabla\widetilde{\eta''^2} \tag{3.11}$$

where the terms $\frac{\partial\widetilde{\mathscr{C}}}{\partial\widetilde{\eta}}$ and $\frac{\partial\widetilde{\mathscr{C}}}{\partial\widetilde{\eta''^2}}$ are the Jacobian matrices of function $\widetilde{\mathscr{C}}(\widetilde{\eta},\widetilde{\eta''^2})$.

By making use of Eqs (3.11), now term B can be re-written as:

$$\nabla\cdot(\overline{\rho}BDU^T\nabla U\widetilde{Y}) = \nabla\cdot\left(\overline{\rho}BDU^T\frac{\partial\widetilde{\mathscr{C}}}{\partial\widetilde{\eta}}\nabla\widetilde{\eta}\right) + \nabla\cdot\left(\overline{\rho}BDU^T\frac{\partial\widetilde{\mathscr{C}}}{\partial\widetilde{\eta''^2}}\nabla\widetilde{\eta''^2}\right) \tag{3.12}$$

The influence of the last term on the right hand side of Eqs (3.12) was small in the numerical simulations presented later in the thesis and is therefore omitted (variation of less than 1% in the maximum flame temperature). For completeness, the set of transport equations for conserved scalars, η, presented below (Eqs (3.13)) should contain this term.

By introducing the conserved scalars, η, and making use of Eqs (3.10, 3.11, 3.12) now Eqs (3.9) can be re-written as:

$$\frac{\partial(\overline{\rho}\widetilde{\eta})}{\partial t} + \nabla\cdot(\overline{\rho}\widetilde{u}\widetilde{\eta}) = \nabla\cdot(\overline{\rho}(\underbrace{BDB^T}_{D_1}+D_t)\nabla\widetilde{\eta}) + \nabla\cdot\left(\underbrace{\overline{\rho}BDU^T\frac{\partial\widetilde{\mathscr{C}}}{\partial\widetilde{\eta}}}_{D_2}\nabla\widetilde{\eta}\right) \tag{3.13}$$

where the term $\frac{\partial\widetilde{\mathscr{C}}}{\partial\widetilde{\eta}}$ is obtained from the combustion model.

3.2.3 Discussion

In comparison to the classical mixture fraction approach, now the diffusion term of the conserved scalars in Eqs (3.8) and (3.13) consists of two parts: D_1, expressing the diffusion of the conserved scalars and D_2, is obtained from the combustion model. The influence of the D_2 term is related to $\frac{\partial\mathscr{C}}{\partial\eta}$ for laminar flames and to $\frac{\partial\widetilde{\mathscr{C}}}{\partial\widetilde{\eta}}$ for turbulent flames, which represent the slopes of functions $\mathscr{C}(\eta)$ and $\widetilde{\mathscr{C}}(\widetilde{\eta})$, respectively, obtained from the combustion model. The slopes of the functions change between the lean side (receive negative values) and the rich side (receive positive values) of the flame (see Figure 2.1), modifying this way the D_2 term. Note that without differential diffusion ($D = \mathscr{D}.I$), $D_1 = \mathscr{D}.I$ and

$D_2 = 0$, all the N_e conserved scalars in Eqs (3.8) and (3.13) follow the same transport equation. In addition, compared to the classical approach of solving transport equations for the chemical species, now there is no chemical source term in Eqs (3.8) and (3.13) and the number of transport equations, to be solved in physical space, has been reduced from $N_s - 1$ to $N_e - 1$. The computational cost of the proposed methodology is, therefore, much less compared to the solution of the chemical species transport equations but slightly higher compared to the conserved scalar approach (since more than one conserved scalar equations will be solved). Finally, with the present methodology one does not have to include all chemical species transport equations and their source terms, but one has the possibility to select from a given set of scalars the ones that will best describe the problem.

In the proposed methodology, the species mass diffusive fluxes in Eqs (3.1) can also be calculated from multi-species diffusion descriptions such as the Hirschfelder-Curtiss law (Eqs (2.13)). In addition, Soret and Dufour effects can also be included in the transport equations for the conserved scalars, η. If for example Soret effects are included, then the transport equations for the conserved scalars, η, will also depend on temperature (on total enthalpy h). In this case the transport equation for total enthalpy, h, will be coupled with the transport equations for the conserved scalars, η, and h will have to be an additional variable in the resolved space BY.

Even though the formulation of the methodology was up to now discussed on the basis of conserved scalars, the methodology is not only restricted to that. It can also be applicable to premixed combustion where some non-conserved scalar transport equations must be solved. For example a transport equation for a progress variable can be included and is then just one extra variable in the resolved space, BY, which will then not only contain conserved scalars but also progress variables. In other words, the method presented is not restricted to conserved scalars.

With the present methodology differential diffusion effects can be incorporated in physical space e.g. in the transport equations of the conserved scalars η. In addition, differential diffusion effects can also be included in chemical space e.g. in the combustion model. For example the methodology can be used in conjunction with a flamelet table. In this case a set of 1D counter-flow diffusion flame calculations in physical space, including full chemistry and transport (with differential diffusion effects) in the equations for the species mass fractions, can be performed. From the numerical simulations then a 1D flamelet table can then be constructed. The number of dimensions of the solution table can be extended (e.g. by varying the boundary inlet fuel composition) to 2D (or higher), similar to what is done in the construction of a 2D Flamelet Generated Manifold (FGM) [117]. In the case of a hydro-carbon flame (considering 4 elements H, C, O and N) a table of 3 (i.e. 4 minus 1) dimensions would be the maximum needed to fill the entire space in conserved scalar space (η_1, η_2, η_3).

3.2.4 Extension to multi-species diffusion descriptions

The transport equations for species with the mass diffusive flux expressed by Hirschfelder-Curtiss law (Eqs 2.13), including Soret effect, can be written in matrix notation as:

$$\frac{\partial(\rho Y)}{\partial t}+\nabla\cdot(\rho u Y)=\nabla\cdot\left(\rho D\frac{W}{W_{mix}}\nabla X\right)+\nabla\cdot\left(\rho D^{th}\frac{\nabla T}{T}\right)+\dot{\omega} \tag{3.14}$$

where D^{th} is the thermal diffusion coefficient and W_{mix} the molecular weight of the mixture.

By introducing the species mass fractions ($X=YW_{mix}/W$) the above equations can be further re-written as:

$$\frac{\partial(\rho Y)}{\partial t}+\nabla\cdot(\rho u Y)=\nabla\cdot\left(\rho DY\frac{\nabla X}{X}\right)+\nabla\cdot\left(\rho D^{th}\frac{\nabla T}{T}\right)+\dot{\omega}\Rightarrow \tag{3.15}$$

$$\frac{\partial(\rho Y)}{\partial t}+\nabla\cdot(\rho u Y)=\nabla\cdot\left(\rho DY\left[\frac{\nabla Y}{Y}+\frac{\nabla W_{mix}}{W_{mix}}\right]\right)+\nabla\cdot\left(\rho D^{th}\frac{\nabla T}{T}\right)+\dot{\omega}\Rightarrow \tag{3.16}$$

$$\frac{\partial(\rho Y)}{\partial t}+\nabla\cdot(\rho u Y)=\nabla\cdot(\rho D\nabla Y)+\nabla\cdot\left(\frac{\rho DY}{W_{mix}}\nabla W_{mix}\right)+\nabla\cdot\left(\rho D^{th}\frac{\nabla T}{T}\right)+\dot{\omega} \tag{3.17}$$

Linear combinations of Eqs (3.17) can be made such that the chemical source term vanishes. As such, the projection matrix B' is introduced and Eqs (3.17) can be re-written as:

$$\frac{\partial(\rho B'Y)}{\partial t}+\nabla\cdot(\rho u B'Y)=\nabla\cdot(\rho B'D\nabla Y)+\nabla\cdot\left(\frac{\rho B'DY}{W_{mix}}\nabla W_{mix}\right)+\nabla\cdot\left(\rho B'D^{th}\frac{\nabla T}{T}\right)+\underbrace{B'\dot{\omega}}_{=0} \tag{3.18}$$

Making the rows of the projection matrix, B', orthonormal and introducing the property

$B^TB+U^TU=I$, Eqs 3.17, can be re-written as:

$$\frac{\partial(\rho BY)}{\partial t}+\nabla\cdot(\rho uBY)=\nabla\cdot(\rho BD[B^TB+U^TU]\nabla Y)$$
$$+\nabla\cdot\left(\frac{\rho BD[B^TB+U^TU]Y}{W_{mix}}\nabla W_{mix}\right)+\nabla\cdot\left(\rho BD^{th}\frac{\nabla T}{T}\right) \tag{3.19}$$

and by further re-arranging them, Eqs 3.19, can be written as:

$$\frac{\partial(\rho BY)}{\partial t}+\nabla\cdot(\rho uBY)=\nabla\cdot(\rho BDB^T\nabla BY)+\nabla\cdot(\rho BDU^T\nabla UY)$$
$$+\nabla\cdot\left(\rho BDB^T\frac{BY}{W_{mix}}\nabla W_{mix}\right)+\nabla\cdot\left(\rho BDU^T\frac{UY}{W_{mix}}\nabla W_{mix}\right)+\nabla\cdot\left(\rho BD^{th}\frac{\nabla T}{T}\right) \tag{3.20}$$

Since the mixture molecular weight, W_{mix}, is a function of the species mass fraction, Y_k, then it is also a function of the conserved scalars, η, and can be expressed as:

$$W_{mix}(Y_k)=\mathbf{W}_{mix}(\eta) \tag{3.21}$$

The total enthalpy, h, is the sum of the sensible and chemical enthalpy:

$$h=\underbrace{\sum_{k=1}^{N_s}c_{p,k}TY_k}_{sensible}+\underbrace{\sum_{k=1}^{N_s}\Delta h^0_{f,k}Y_k}_{chemical} \quad\Rightarrow\quad T=\frac{h-\sum_{k=1}^{N_s}\Delta h^0_{f,k}Y_k}{\sum_{k=1}^{N_s}c_{p,k}Y_k} \tag{3.22}$$

and the $\frac{\nabla T}{T}$ ratio in Eqs 3.20 can be expressed as:

$$\frac{\nabla T}{T}=\frac{\dfrac{\left(\sum_{k=1}^{N_s}c_{p,k}Y_k\right)\cdot\nabla\left(h-\sum_{k=1}^{N_s}\Delta h^0_{f,k}Y_k\right)-\left(h-\sum_{k=1}^{N_s}\Delta h^0_{f,k}Y_k\right)\cdot\nabla\left(\sum_{k=1}^{N_s}c_{p,k}Y_k\right)}{\left(\sum_{k=1}^{N_s}c_{p,k}Y_k\right)^2}}{\dfrac{h-\sum_{k=1}^{N_s}\Delta h^0_{f,k}Y_k}{\sum_{k=1}^{N_s}c_{p,k}Y_k}}=$$
$$=\frac{\nabla\left(h-\sum_{k=1}^{N_s}\Delta h^0_{f,k}Y_k\right)}{h-\sum_{k=1}^{N_s}\Delta h^0_{f,k}Y_k}-\frac{\nabla\left(\sum_{k=1}^{N_s}c_{p,k}Y_k\right)}{\sum_{k=1}^{N_s}c_{p,k}Y_k}=\frac{\nabla h_s(h,Y_k)}{h_s(h,Y_k)}-\frac{\nabla c_p(Y_k)}{c_p(Y_k)}=$$
$$=\frac{\nabla\mathbf{h}_s(h,\eta)}{\mathbf{h}_s(h,\eta)}-\frac{\nabla\mathbf{c_p}(\eta)}{\mathbf{c_p}(\eta)}=\frac{1}{\mathbf{h}_s}\frac{\partial\mathbf{h}_s}{\partial\eta}\nabla\eta+\frac{1}{\mathbf{h}_s}\frac{\partial\mathbf{h}_s}{\partial h}\nabla h-\frac{1}{\mathbf{c_p}}\frac{\partial\mathbf{c_p}}{\partial\eta}\nabla\eta \tag{3.23}$$

Substituting Eqs 3.21 and 3.23 into Eqs 3.20, with $\eta = BY$ results in:

$$\frac{\partial(\rho\eta)}{\partial t} + \nabla\cdot(\rho u\eta) = \nabla\cdot(\rho BDB^T\nabla\eta) + \nabla\cdot\left(\rho BDU^T\frac{\partial\mathscr{C}(\eta)}{\partial\eta}\nabla\eta\right)$$
$$+\nabla\cdot\left(\rho BDB^T\frac{\eta}{\mathbf{W}_{mix}}\frac{\partial\mathbf{W}_{mix}}{\partial\eta}\nabla\eta\right) + \nabla\cdot\left(\rho BDU^T\frac{\mathscr{C}(\eta)}{\mathbf{W}_{mix}}\frac{\partial\mathbf{W}_{mix}}{\partial\eta}\nabla\eta\right)$$
$$+\nabla\cdot\left(\rho BD^{th}\left[\frac{1}{\mathbf{h}_s}\frac{\partial\mathbf{h}_s}{\partial\eta}\nabla\eta + \frac{1}{\mathbf{h}_s}\frac{\partial\mathbf{h}_s}{\partial h}\nabla h - \frac{1}{\mathbf{c_p}}\frac{\partial\mathbf{c_p}}{\partial\eta}\nabla\eta\right]\right) \quad (3.24)$$

By re-arranging Eqs (3.24) we finally obtain the equation for conserved scalars, η, that need to be solved in the case of multi-species diffusion descriptions:

$$\frac{\partial(\rho\eta)}{\partial t} + \nabla\cdot(\rho u\eta) = \nabla\cdot(\rho BDB^T\nabla\eta) + \nabla\cdot\left(\rho BDU^T\frac{\partial\mathscr{C}(\eta)}{\partial\eta}\nabla\eta\right)$$
$$+\nabla\cdot\left(\rho BDB^T\frac{\eta}{\mathbf{W}_{mix}}\frac{\partial\mathbf{W}_{mix}}{\partial\eta}\nabla\eta\right) + \nabla\cdot\left(\rho BDU^T\frac{\mathscr{C}(\eta)}{\mathbf{W}_{mix}}\frac{\partial\mathbf{W}_{mix}}{\partial\eta}\nabla\eta\right)$$
$$+\nabla\cdot\left(\rho BD^{th}\frac{1}{\mathbf{h}_s}\frac{\partial\mathbf{h}_s}{\partial\eta}\nabla\eta\right) - \nabla\cdot\left(\rho BD^{th}\frac{1}{\mathbf{c_p}}\frac{\partial\mathbf{c_p}}{\partial\eta}\nabla\eta\right) + \nabla\cdot\left(\rho BD^{th}\frac{1}{\mathbf{h}_s}\frac{\partial\mathbf{h}_s}{\partial h}\nabla h\right) \quad (3.25)$$

3.3 Implementation of the methodology

The software package OpenFOAM 1.6 [38] is used for the numerical simulations. OpenFOAM is a set of object-oriented open source CFD toolboxes written in the C++ programming language. It utilizes the finite volume method on unstructured polyhedral 3D meshes and is highly scalable on massively parallel computers [124].

There is a wide range of available solvers in OpenFOAM, each one suitable for a different engineering application. Specifically, for reacting flows, solvers exist for both premixed and non-premixed combustion and the user is left with the choice to select the appropriate solver that will best fit his needs. A detailed description of the available turbulence and combustion models that can be applied for numerical simulations of reactive flows in OpenFOAM, along with methods of discretization and different boundary conditions can be found in [38].

From the OpenFOAM platform, the FireFOAM 1.6 solver is selected in order to perform numerical simulations and to apply the newly proposed methodology. FireFOAM is a relatively new CFD code which has been developed by FM Global [37] and it is suitable for simulating fires and turbulent diffusion flames. It is a LES code which solves the conservation equations for mass and momentum, along with transport equations for the mixture fraction and enthalpy, assuming infinitely fast chemistry and using a beta pdf to account for turbulence-chemistry interactions. The momentum and pressure equations are coupled through a predictor-corrector PISO (Pressure Implicit with Splitting of Operators) method [40]. It uses a collocated grid arrangement (variables are stored in the center of a grid cell) with a Rhie-Chow correction [96] to remove oscillations in the solutions. Several modification were made in the original implementation of FireFOAM in order to perform the numerical simulations of the various test cases presented in the thesis. An overview of these modifications is presented in the chapter of each test case.

3.4 Example: H_2/N_2 - air diffusion flame

In this section, an example of the newly proposed methodology is presented. The methodology is applied to a laminar H_2/N_2 - air diffusion flame test case by considering $N_s = 4$ species k (H_2, O_2, H_2O, N_2) and $N_\lambda = 3$ elements λ (H, O, N).

The elemental mass fractions, η'_λ, can be calculated as:

$$\eta'_\lambda = \sum_{k=1}^{4} \frac{a_{\lambda,k} W_\lambda}{W_k} Y_k = \sum_{k=1}^{4} B'_{\lambda k} Y_k, \quad \lambda = H, O, N \tag{3.26}$$

so the elemental mass fractions for H, O and N read:

$$\eta'_H = \frac{2 \cdot 1.00797}{2.01594} Y_{H_2} + \frac{2 \cdot 1.00797}{18.0153} Y_{H_2O} \tag{3.27}$$

$$\eta'_O = \frac{2 \cdot 15.9994}{31.9988} Y_{O_2} + \frac{1 \cdot 15.9994}{18.0153} Y_{H_2O} \tag{3.28}$$

$$\eta'_N = \frac{2 \cdot 14.0067}{28.0153} Y_{N_2} \tag{3.29}$$

with $W_{H_2} = 2.01594$ g/mol, $W_{O_2} = 31.9988$ g/mol, $W_{H_2O} = 18.0153$ g/mol and $W_{N_2} = 28.0134$ g/mol.

By considering the elemental mass fractions η'_H and η'_N and mass conservation, $\eta'_{sum} =$

$\sum_{\lambda=1}^{N_\lambda} \eta'_\lambda = 1$, B' becomes a 3x4 projection matrix with its elements expressed as:

$$\begin{array}{r|cccc|l} & H_2 & O_2 & H_2O & N_2 & \\ & 1 & 1 & 1 & 1 & \eta'_{sum} \\ B' = & 1 & 0 & 0.111902 & 0 & \eta'_H \\ & 0 & 0 & 0 & 1 & \eta'_N \end{array}$$

Linear combinations of the elemental mass fractions, $\eta' = B'Y = [\eta'_1, \dots, \eta'_{N_e}]$, are made such that the rows of the projection matrix, B', are orthonormal. The conserved scalars are now defined as $\eta = BY = [\eta_1, \dots, \eta_{N_e}]$ and the elements of B matrix are determined as:

$$\begin{array}{r|cccc|l} & H_2 & O_2 & H_2O & N_2 & \\ & 0.5 & 0.5 & 0.5 & 0.5 & \eta_{sum} \\ B = & 0.8608713144 & -0.3314307673 & -0.19800097798 & -0.3314307673 & \eta_H \\ & 0.044144375184 & -0.44975539584 & -0.3944858168 & 0.8000960234 & \eta_N \end{array}$$

Since B is not a square matrix the properties $BB^T = I$ and $B^T B = I$ are not equivalent:

$$BB^T = \begin{vmatrix} 1 & 0 & 0 \\ 0 & 1 & 0 \\ 0 & 0 & 1 \end{vmatrix}$$

while

$$B^T B = \begin{vmatrix} 0.9930480908 & -0.05517306743 & 0.06212497660 & 0 \\ -0.05517306743 & 0.5621249766 & 0.4930480908 & 0 \\ 0.06212497660 & 0.4930480908 & 0.4448269326 & 0 \\ 0 & 0 & 0 & 1 \end{vmatrix}$$

We also consider a matrix U with orthonormal rows (i.e. $UU^T = I$) which forms an orthogonal basis with B ($BU^T = 0$; $UB^T = 0$). Matrix U has dimensions such that the combined B and U matrix now form a square matrix. This way U is a 1×4 matrix with its elements evaluated from the constrains $BU^T = 0$ and $UU^T = I$ as:

$$U = \begin{vmatrix} U_1 & U_2 & U_3 & U_4 \end{vmatrix} = \begin{vmatrix} 0.08337810939 & 0.6617212581 & -0.7450993675 & 0 \end{vmatrix}$$

With the matrix U defined it can be verified that:

$$UU^T = \begin{vmatrix} 1 \end{vmatrix}$$

while

$$U^TU = \begin{vmatrix} 0.0069519092 & 0.05517306743 & -0.06212497660 & 0 \\ 0.05517306743 & 0.4378750234 & -0.4930480908 & 0 \\ -0.06212497660 & -0.4930480908 & 0.5551730674 & 0 \\ 0 & 0 & 0 & 0 \end{vmatrix}$$

In addition, the property $B^TB + U^TU = I$ is also satisfied:

$$B^TB + U^TU = \begin{vmatrix} 1 & 0 & 0 & 0 \\ 0 & 1 & 0 & 0 \\ 0 & 0 & 1 & 0 \\ 0 & 0 & 0 & 1 \end{vmatrix}$$

By introducing matrices B and U in Eqs 3.8 the transport equations for mass conservation, η_{sum}, and conserved scalars η_H and η_N are obtained:

$$\frac{\partial(\rho\eta_{sum})}{\partial t} + \nabla\cdot(\rho u\eta_{sum}) = \nabla\cdot\left[\rho\left(a\nabla\eta_H + b\nabla\eta_N + u_c\eta_{sum}\right)\right] \tag{3.30}$$

$$\frac{\partial(\rho\eta_H)}{\partial t} + \nabla\cdot(\rho u\eta_H) = \nabla\cdot\left[\rho\left(c\nabla\eta_H + d\nabla\eta_N + u_c\eta_H\right)\right] \tag{3.31}$$

$$\frac{\partial(\rho\eta_N)}{\partial t}+\nabla\cdot(\rho u\eta_N)=\nabla\cdot\left[\rho\left(e\nabla\eta_N+f\nabla\eta_H+u_c\eta_N\right)\right] \tag{3.32}$$

where u_c is a correction velocity introduced to ensure mass conservation and the coefficients a, b, c, d, e and f are calculated as:

$$\begin{aligned}a=&\,0.5D_{H_2}\left(0.8608713144+0.08337810939\frac{\mathscr{C}(\eta_H,\eta_N)}{\partial\eta_H}\right)\\&+0.5D_{O_2}\left(-0.3314307673+0.6617212581\frac{\mathscr{C}(\eta_H,\eta_N)}{\partial\eta_H}\right)\\&+0.5D_{H_2O}\left(-0.1980097798-0.7450993675\frac{\mathscr{C}(\eta_H,\eta_N)}{\partial\eta_H}\right)\\&-0.1657153836D_{N_2}\end{aligned} \tag{3.33}$$

$$\begin{aligned}b=&\,0.5D_{H_2}\left(0.04414375184+0.08337810939\frac{\mathscr{C}(\eta_H,\eta_N)}{\partial\eta_N}\right)\\&+0.5D_{O_2}\left(-0.4497539584+0.6617212581\frac{\mathscr{C}(\eta_H,\eta_N)}{\partial\eta_N}\right)\\&+0.5D_{H_2O}\left(-0.3944858168-0.7450993675\frac{\mathscr{C}(\eta_H,\eta_N)}{\partial\eta_N}\right)\\&+0.4000480117D_{N_2}\end{aligned} \tag{3.34}$$

$$\begin{aligned}c=&\,0.8608713144D_{H_2}\left(0.8608713144+0.08337810939\frac{\mathscr{C}(\eta_H,\eta_N)}{\partial\eta_H}\right)\\&-0.3314307673D_{O_2}\left(-0.3314307673+0.6617212581\frac{\mathscr{C}(\eta_H,\eta_N)}{\partial\eta_H}\right)\\&-0.1980097798D_{H_2O}\left(-0.1980097798-0.7450993675\frac{\mathscr{C}(\eta_H,\eta_N)}{\partial\eta_H}\right)\\&+0.1098463535D_{N_2}\end{aligned} \tag{3.35}$$

$$\begin{aligned}d = 0.8608713144 D_{H_2}\left(0.04414375184 + 0.08337810939\frac{\mathscr{C}(\eta_H,\eta_N)}{\partial\eta_N}\right)\\ - 0.3314307673 D_{O_2}\left(-0.4497539584 + 0.6617212581\frac{\mathscr{C}(\eta_H,\eta_N)}{\partial\eta_N}\right)\\ - 0.1980097798 D_{H_2O}\left(-0.3944858168 - 0.7450993675\frac{\mathscr{C}(\eta_H,\eta_N)}{\partial\eta_N}\right)\\ - 0.2651764389 D_{N_2}\end{aligned} \quad (3.36)$$

$$\begin{aligned}e = 0.04414375184 D_{H_2}\left(0.8608713144 + 0.08337810939\frac{\mathscr{C}(\eta_H,\eta_N)}{\partial\eta_H}\right)\\ - 0.4497539584 D_{O_2}\left(-0.3314307673 + 0.6617212581\frac{\mathscr{C}(\eta_H,\eta_N)}{\partial\eta_H}\right)\\ - 0.3944858168 D_{H_2O}\left(-0.1980097798 - 0.7450993675\frac{\mathscr{C}(\eta_H,\eta_N)}{\partial\eta_H}\right)\\ - 0.2651764389 D_{N_2}\end{aligned} \quad (3.37)$$

$$\begin{aligned}f = 0.04414375184 D_{H_2}\left(0.04414375184 + 0.08337810939\frac{\mathscr{C}(\eta_H,\eta_N)}{\partial\eta_N}\right)\\ - 0.4497539584 D_{O_2}\left(-0.4497539584 + 0.6617212581\frac{\mathscr{C}(\eta_H,\eta_N)}{\partial\eta_N}\right)\\ - 0.3944858168 D_{H_2O}\left(-0.3944858168 - 0.7450993675\frac{\mathscr{C}(\eta_H,\eta_N)}{\partial\eta_N}\right)\\ + 0.6401536467 D_{N_2}\end{aligned} \quad (3.38)$$

The correction velocity, u_c, can be calculated from the mass conservation equation, Eq. 3.30, as:

$$\frac{\partial(\rho\eta_{sum})}{\partial t} + \nabla\cdot(\rho u\eta_{sum}) = \nabla\cdot\left[\rho\left(a\nabla\eta_H + b\nabla\eta_N + u_c\eta_{sum}\right)\right] = 0 \quad \Rightarrow \quad (3.39)$$

$$\left(a\nabla\eta_H + b\nabla\eta_N + u_c\eta_{sum}\right) = 0 \quad \Rightarrow \quad u_c = \frac{-a\nabla\eta_H - b\nabla\eta_N}{0.5} \quad (3.40)$$

The instantaneous species mass fractions, Y, can be obtained from the Burke-Schumann solution as a function of the elemental mass fractions η'_H and η'_N or as a function of the conserved scalars η_H and η_N by doing a coordinate transformation from η'_λ to η_λ space.

With $\mathscr{C}(\eta_H,\eta_N) = UY$, $\mathscr{C}(\eta_H+\Delta\eta_H,\eta_N) = UY^*$ and $\mathscr{C}(\eta_H,\eta_N+\Delta\eta_N) = UY^{**}$ now terms $\frac{\mathscr{C}(\eta_H,\eta_N)}{\partial\eta_H}$ and $\frac{\mathscr{C}(\eta_H,\eta_N)}{\partial\eta_N}$ can be evaluated as:

$$\frac{\mathscr{C}(\eta_H,\eta_N)}{\partial\eta_H} = \frac{\mathscr{C}(\eta_H+\Delta\eta_H,\eta_N)-\mathscr{C}(\eta_H,\eta_N)}{\Delta\eta_H} = \frac{UY^*-UY}{\Delta\eta_H} \tag{3.41}$$

$$\frac{\mathscr{C}(\eta_H,\eta_N)}{\partial\eta_N} = \frac{\mathscr{C}(\eta_H,\eta_N+\Delta\eta_N)-\mathscr{C}(\eta_H,\eta_N)}{\Delta\eta_N} = \frac{UY^{**}-UY}{\Delta\eta_N} \tag{3.42}$$

where $\Delta\eta_H$ and $\Delta\eta_H$ are assigned a small value.

A matrix R, representing the coordinate transformation from η'_λ to η_λ space, can be constructed from the unit vectors of B' matrix:

$r'_1 = (1\ \ 1\ \ 1\ \ 1)$, $r'_2 = (1\ \ 0\ \ 0.111902\ \ 0)$, $r'_3 = (0\ \ 0\ \ 0\ \ 1)$

and from the unit vectors of B matrix:

$r_1 = (0.5\ \ 0.5\ \ 0.5\ \ 0.5)$,
$r_2 = (0.8608713144\ \ -0.3314307673\ \ -0.1980097798\ \ -0.3314307673)$,
$r_3 = (0.04414375184\ \ -0.4497539584\ \ -0.3944858168\ \ 0.8000960234)$

so its elements read:

$$R = \begin{vmatrix} r'_1\cdot r_1 & r'_1\cdot r_2 & r'_1\cdot r_3 \\ r'_2\cdot r_1 & r'_2\cdot r_2 & r'_2\cdot r_3 \\ r'_3\cdot r_1 & r'_3\cdot r_2 & r'_3\cdot r_3 \end{vmatrix} = \begin{vmatrix} 2 & 0 & 0 \\ 0.555951 & 0.838713624 & 0 \\ 0.5 & -0.3314307673 & 0.8000960234 \end{vmatrix}$$

Now the elemental mass fractions, η'_H and η'_N, are related to the conserved scalars, η_H and η_N, as $\eta'_\lambda = R\eta_\lambda$:

$$\begin{vmatrix} \eta'_{sum} \\ \eta'_H \\ \eta'_N \end{vmatrix} = \begin{vmatrix} 2 & 0 & 0 \\ 0.555951 & 0.838713624 & 0 \\ 0.5 & -0.3314307673 & 0.8000960234 \end{vmatrix} \begin{vmatrix} \eta_{sum} \\ \eta_H \\ \eta_N \end{vmatrix}$$

With $\eta_{sum} = 0.5$ it is finally:

$$\eta'_{sum} = 1 \tag{3.43}$$

$$\eta'_H = 0.2779755 + 0.838713624\eta_H \tag{3.44}$$

$$\eta'_N = 0.25 - 0.3314307673\eta_H + 0.8000960234\eta_N \tag{3.45}$$

With a given inlet mixture composition and co-flow of air, the initial and inlet boundary conditions for the conserved scalars η_H and η_N can be evaluated from Eqs 3.44 - 3.45.

To summarize, transport equations for the conserved scalars η_H and η_N are solved in the code. From the conserved scalars η_H and η_N, the elemental mass fractions η'_H and η'_N can be calculated. With the elemental mass fractions η'_H and η'_N known, the species mass fractions (H_2, O_2) are obtained from Burke-Schumann solution. N_2, is recovered from the elemental mass fraction of N, as $\eta'_N = N_2$ while H_2O is obtained from mass conservation as H_2O = 1.0 - H_2 - O_2 - N_2.

Chapter 4

Validation of FireFOAM

4.1 Introduction

In this chapter a validation study of the CFD code FireFOAM [36] is presented. FireFOAM is a relatively new solver and not many validation studies have been reported up to now in literature [121, 122]. Before applying the code to study differential diffusion effects in laminar and turbulent non-reacting/reacting flows, FireFOAM is applied to a turbulent buoyant helium plume test case where buoyancy induced turbulence and Rayleigh - Taylor instabilities are present. It is a challenging case where the capabilities of FireFOAM to accurately study turbulent flows can be evaluated.

The study of turbulent buoyant helium plumes is interesting for several reasons. First of all, the test case is challenging for CFD codes. Indeed, in the plume, there is a rapid transition from laminar to fully turbulent, usually within a few inlet diameters, created by strong buoyancy forces. The generation of vorticity within the interior of the flow is due to baroclinic and gravitational mechanisms, related to density - pressure gradients and gravity - density gradients, respectively. Two modes of turbulence can be identified [10]. The coherent structures created by puffing vortices and the finger-like structures caused by the Rayleigh - Taylor instability, which enhances mixing. Second, there is an interesting similarity of the flow field (such puffing frequency) to the flow field observed above pool fires.

An important mechanism in this kind of flows is the coupling between the momentum and species equations through density, since the mixture composition determines density through the mixture molecular weight. For buoyant, low Mach-number flows, the source term in the momentum equations is the product of density and gravity, hence, the forcing function for a buoyant flow. This buoyant forcing results in mixing that in turn changes density and thus the two sets of equations are coupled. Turbulence resulting directly from this coupling is referred to as 'buoyancy generated turbulence' [75]. It is postulated in [114] that a combination of vorticity generation and vorticity transport mechanisms are responsible for the turbulence created.

Much experimental work has been done on turbulent plumes. Small-scale experiments of buoyant helium plumes were performed by Cetegen et al. [11, 12] in order to identify the mechanism responsible for the periodic oscillations occurring near the plume source. Papanikolaou & List et al. [80] examined a momentum driven buoyant jet, where the buoyancy effects become dominant only far downstream of the source and investigated the turbulence properties and the transition from momentum-driven jets to buoyancy-driven plumes. Shabbir & George et al. [103] did experiments on a turbulent buoyant thermal plume and reported on the effect of buoyancy on turbulent buoyant plumes. In addition several numerical studies of turbulent plumes using DNS and LES have already appeared in the literature. Zhou et al. [132] performed LES of the near and far-field of a spatially-developing round turbulent buoyant plume showing that plumes, like cold jets, can also have several stages of vortex development such as roll-up and breakdown. Soteriou et al. [109] studied the unsteady dynamics of planar plumes using a high-resolution Lagrangian method, emphasizing on the pulsating instability characterizing the source near field. Chung & Devaud et al. [14] studied the near field of a helium plume using buoyancy corrected $k-\varepsilon$ models in Reynolds Averaged Navier-Stokes (RANS) calculations and with traditional eddy-viscosity LES methods. Pham et al. [84] performed DNS and LES simulations with the dynamic Smagorinsky eddy-viscosity model of a pure thermal plume and reported on the puffing phenomenon that occurs in the near-field region of the plume source. DesJardin et al. [18] explored the instability modes and flow dynamics of a large turbulent helium plume, as a function of grid resolution with and without the use of sub-grid scale (SGS) models, and reported on the energy transfer from small to large scales, i.e. inverse energy cascade.

In the study at hand, LES results obtained with a slightly modified version of the FireFOAM [36] code are compared to the well-documented experiment performed by O'Hern et al. [79]. By applying the code to a non-reacting plume, the effect of buoyancy generated turbulence can be tested, independently of the complexity introduced by turbulent combustion.

The specific motivation for this study, focusing on large eddy simulations (LES) in the near-field region of a large axi-symmetric turbulent buoyant helium plume, is therefore twofold. Firstly, the validation of the FireFOAM code in buoyancy driven flows, an application that has similar turbulent mixing characteristics with fire scenarios. The validation of the code will be of great interest to the research community and will give the opportunity to more researchers to use it for fire related applications and turbulent flame studies. Secondly, to get a better insight of the buoyancy generated turbulence and the generation of the Rayleigh-Taylor instability that determines the puffing cycle of the plume. This behavior is similar to the puffing frequency observed in pool fires and a better understanding of this mechanism will help to understand more about the flow dynamics in this kind of flows.

This chapter is based on Maragkos et al. [61]. An additional numerical study of this test case was also performed [59], in which results obtained with FireFOAM 1.6 [36] and the Fire Dynamics Simulator (FDS) 5.5.3 [35] were compared against the experimental data of O‘Hern et al. [79].

4.2 Mathematical formulation

4.2.1 Governing equations

A modified version of FireFOAM 1.6 [36] is used in this study. The default energy equation and equation of state have been removed, and mixture density is directly calculated from the species concentration. It solves the conservation equations for mass and momentum, along with a transport equation for helium mass fraction for a non-reacting, isothermal system. The set of governing equations needed for the numerical simulations is then:

$$\frac{\partial\overline{\rho}}{\partial t}+\frac{\partial(\overline{\rho}\widetilde{u}_i)}{\partial x_i}=0 \tag{4.1}$$

$$\frac{\partial(\overline{\rho}\widetilde{u}_j)}{\partial t}+\frac{\partial(\overline{\rho}\widetilde{u}_i\widetilde{u}_j)}{\partial x_i}=-\frac{\partial\overline{p}}{\partial x_j}+\frac{\partial}{\partial x_i}\left[(\mu+\mu_t)\left(\frac{\partial\widetilde{u}_i}{\partial x_j}+\frac{\partial\widetilde{u}_j}{\partial x_i}\right)\right]+\overline{\rho}g_j, \qquad j=1,2,3 \tag{4.2}$$

$$\frac{\partial(\overline{\rho}\widetilde{Y}_{He})}{\partial t}+\frac{\partial(\overline{\rho}\widetilde{u}_i\widetilde{Y}_{He})}{\partial x_i}=\frac{\partial}{\partial x_i}\left[\left(\frac{\mu}{Sc_{He}}+\frac{\mu_t}{Sc_t}\right)\frac{\partial\widetilde{Y}_{He}}{\partial x_i}\right] \tag{4.3}$$

The filtered density, $\overline{\rho}$, is a function of helium and air composition. Thus, the mixing induced by the momentum equations yields:

$$\overline{\rho} = \rho_{He}\,\overline{\phi}_{He} + \rho_{air}(1 - \overline{\phi}_{He}) \tag{4.4}$$

where $\overline{\phi}_{He}$ is the filtered volume fraction of helium and ρ_{He}, ρ_{air} are the densities of helium and air respectively, calculated by the ideal gas law. The volume fraction of helium is related to its mass fraction, solved by the transport equation, as:

$$Y_{He} = \frac{\rho_{He}\,\overline{\phi}_{He}}{\rho_{He}\,\overline{\phi}_{He} + \rho_{air}\,(1 - \overline{\phi}_{He})} \Rightarrow \overline{\phi}_{He} = \frac{\rho_{air}\,Y_{He}}{\rho_{He} + \rho_{air}\,Y - \rho_{He}\,Y_{He}} \tag{4.5}$$

4.2.2 Turbulence modelling

The standard Smagorinsky model [104] is used to model turbulence with a constant of $c_s = 0.1$. The sub-grid scale species fluxes in the species transport equation are modelled by the gradient diffusion hypothesis model, assuming a constant turbulent Schmidt number of $Sc_t = 0.5$ [14]. A sensitivity study on both these values is presented in section 4.7.

4.3 Experimental set-up

In this study comparisons are made to results from experiments performed in the Fire Laboratory for Accreditation of Models and Experiments (FLAME) at Sandia National Laboratories in Albuquerque, New Mexico, as reported by O'Hern et al. [79]. In the experiments two planar imaging techniques were simultaneously applied: Particle Image Velocimetry (PIV) for velocity field measurements and Planar Laser Induced Fluorescence (PLIF) for scalar field measurements (mass fractions).

The FLAME chamber consists of a 6.1 m cubical enclosure with a 2.4 m in diameter chimney located on top of the chamber. The experiment was designed to be a canonical buoyant plume so that the results would not be dependent on the specific experimental geometry. The plume source is 1 m in diameter, surrounded by a 0.51 m wide floor, the 'ground plane'. The plume was developed using helium issuing from the diffuser at an average velocity of 0.325 m/s. A detailed analysis of the spatial velocity distribution of the plume inlet (using air instead of helium) showed that the inlet velocity profile was uniform to within ± 6% [8]. For PLIF measurements, 1.7 ± 0.1% vol. acetone was injected into the helium flow as the fluorescent tracer gas. In addition 1.9 ± 0.2% vol. oxygen was added to quench acetone phosphorescence. The molecular weight of the helium/acetone/oxygen mixture was 5.45 ± 2.7% g/mol. The average mixture Reynolds number was $Re = (du)/\nu = 3200 \pm 0.6\%$, where d is the diameter of the plume source, u is the inlet velocity and ν the kinematic viscosity of the helium/acetone/oxygen mixture. The average mixture Richardson number was $Ri = (\rho_\infty - \rho_p)gd/(\rho_\infty u^2) = 76 \pm 6.5\%$, with ρ_∞ the external (air) density, ρ_p the plume fluid density and g the acceleration due to gravity. The experiment was performed at a low ambient pressure of $P = 80900$ Pa (due to the high altitude in which the facility was located) and at temperature $T = 285$ K.

The experimental uncertainty on the measured velocities and turbulent statistics are in the order of 20% and 30%, respectively. The values of concentration contain uncertainties in the order of 18%, plus fixed uncertainties of 5%, while the uncertainty on the concentration fluctuation in the order of 21%. [79].

4.4 Numerical set-up

The simulations are performed on a cylindrical mesh, 4 m in diameter and 4 m in the axial direction, with a rectangular grid in the core (0.3 m × 0.3 m). A 1 m diameter inflow of helium, located in the center of the bottom plane, is surrounded by a 0.5 m wide wall, which simulates a 'ground plane' causing air being entrained by the accelerating plume to flow radially inward over the floor. The inlet patch at the bottom plane consists of a uniform rectangular grid surrounded by a cylindrical mesh, shown in Figure 4.1. The grid resolution for the inlet patch in the coarse grid is set to 10×10 cells (rectangular) and 10×40 (cylindrical) resulting in a total of 500 cells. The grid resolution for the inlet patch in the fine grid is set to 20×20 cells (rectangular) and 20×80 (cylindrical), resulting in a total of 2000 cells. Outside the inlet patch 40 (coarse) or 80 (fine) cells were uniformly spaced radially. In the axial direction 75 (coarse) and 150 (fine) cells were used respectively. The total number of cells is then 0.157 million cells (coarse) or 1.26 million cells (fine). The grid has been compressed near the bottom of the plume source, ($y = 0$ m), resulting in a minimum and maximum grid spacing of 2.54 cm, 10.75 cm (coarse) and 1.23 cm, 5.39 cm (fine), respectively.

The governing equations are advanced in time using a second order implicit 'backward' scheme. All quantities are assigned to the cell centers (collocated grid) with velocities linearly interpolated to the cell faces. The convective terms are second order centrally differenced using 'Gauss linear' interpolation . No purely upwind schemes were used since the use of upwinding in LES can introduce undesirable artificial numerical dissipation, as has been noted by many studies, e.g. [72]. This was also noted in the present study where

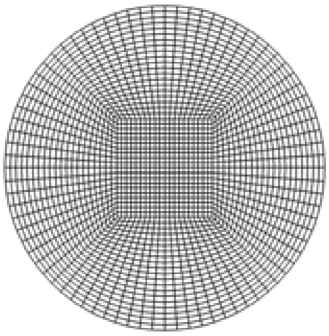

Figure 4.1: Schematic representation of the fine mesh used for the helium inlet in the simulations.

different schemes have been tested for discretizing the convective terms. Any blending of the linear scheme with upwind resulted in high levels of numerical dissipation (not shown here). For scalar transport, the bounded second order Total Variation Diminishing (TVD) scheme 'limitedLinear01' is used while the diffusive terms are centrally differenced and corrected for the non-orthogonality of the mesh with 'Gauss linear corrected'.

The bottom plane of the domain at $y = 0$ m employs a zero fixed value boundary condition for the cross-stream velocities and fixes the streamwise velocity of the inlet to $u_{inlet} = 0.325$ m/s in the core of the plume and to a small co-flow velocity $u_{co-flow} = 0.01$ m/s outside the 'ground plane' surrounding the plume inlet. At the 'ground plane' the co-flow velocity is set to zero. A 'zeroGradient' boundary condition is assigned for velocity at the sides of the domain and 'totalPressure' boundary condition for pressure. For the top outlet plane an 'inletOutlet' boundary condition is used for velocity and 'zeroGradient' for pressure. The 'inletOutlet' boundary condition assigns a 'zeroGradient' for outward velocity and fixes the inlet velocity to zero. The inlet boundary condition for the mass fraction of helium is set to uniform 'fixedValue 1.0'. A summary of the boundary conditions used in the numerical simulations is shown in Table 4.1

Table 4.1: Boundary conditions as specified in the simulations (OpenFOAM terminology [38]).

Surface	Velocity	Dynamic Pressure	Mass Fraction	Temperature
Inlet	fixedValue 0.325	zeroGradient	fixedValue 1.0	fixedValue 285
CoFlow	fixedValue 0.01	zeroGradient	fixedValue 0.0	fixedValue 285
Sides	zeroGradient	totalPressure	inletOutlet	inletOutlet
Outlet	inletOutlet	zeroGradient	inletOutlet	inletOutlet
Plate	fixedValue 0.0	zeroGradient	fixedValue 0.0	fixedValue 285

At every point in the domain, the composition of the gas phase corresponds to a mixture of helium and air. Air has molecular weight $W_{air} = 28.9$ g/mol while the experimental mixture of helium (He, 96.4% by vol.), acetone (CH_3COCH_3, 1.7% by vol.) and oxygen (O_2, 1.9% by vol.) is treated as a single gas with molecular weight $W_{He} = 5.45$ g/mol. Ambient temperature and pressure are $T = 285$ K and $P = 80900$ Pa, respectively, to match the experimental conditions.

Figure 4.2 illustrates how the mixture density, ρ, varies with the helium volume fraction ϕ_f. Densities of air and helium are $\rho_{air} = 0.987$ kg/m^3 and $\rho_{He} = 0.186$ kg/m^3 respectively, in agreement with the conditions of the experiment presented in the next section. The laminar viscosity of helium is calculated by the experimental conditions and inlet Reynolds number to be $\mu = 1.8774 \times 10^{-5}$ kg/ms. The molecular Schmidt number of helium is assigned the value $Sc_{He} = 0.2$ [18].

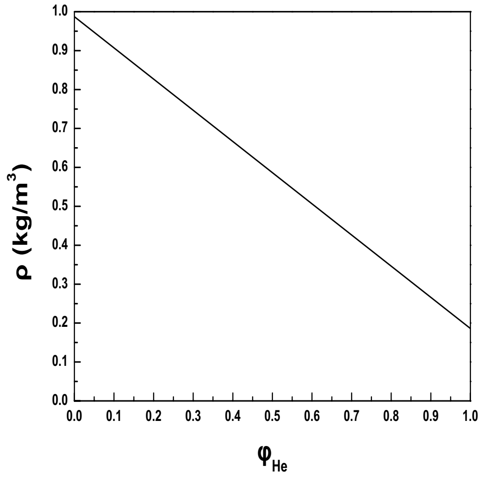

Figure 4.2: Density as a function of helium volume fraction ϕ_{He}

The LES calculations are set up to run for 30 sec. The first 20 seconds allow for the initial computational flow transients to move downstream and to reach statistically stationary flow conditions. Results from the final 10 seconds of the simulation are compiled to produce density-weighted, time-averaged quantities. A constant time step is used in the simulations ($t_{coarse} = 0.0005$ s and $t_{fine} = 0.00025$ s), corresponding to an average Courant number of $Co \approx 0.2$. A domain decomposition parallelization strategy was employed by dividing the computational domain into equally sized mesh blocks across 12 processors. The total physical running time for the coarse and fine mesh was 11 h and 195 h, respectively, on a Dell PowerEdge R610 server with 2x Six-core Intel Xeon X5680, 3.33GHz and 48GB RAM.

4.5 Results

4.5.1 Instability modes

Figure 4.3 presents instantaneous snapshots of the density field over one puffing cycle, in which the generation of the instabilities near the base of the plume is evident (Fig. 4.3(a) - 4.3(b)) due to the misalignment of vertical pressure gradient and density gradient pointing radially outwards (baroclinic torque), generating localized torque as shown in Figure 4.3. These instabilities grow in size and eventually form large coherent structures (Fig. 4.3(c) - 4.3(d)). These processes repeat themselves in every puffing cycle.

Figure 4.4 shows the generation of the localized torque discussed above, generated by the misalignment of density and pressure gradients at the beginning of the simulation, at the base of the plume, where helium is released into still air. It consists of snapshots of density, covering half of the inlet plume diameter, with superimposed density (white arrows) and pressure gradients (black arrows) showing the roll-up of the vortex at the plume edge.

The inflow conditions of the plume in this buoyancy driven flow are laminar [79]. However, strong turbulent structures form at the helium - air interface very close to the plume source, Figure 4.3(b). The lack of source turbulence and the strong deflection of the low velocity helium plume from the inlet vertical direction at the edges of the plume, indicate that vorticity from the plume source is not responsible for the formation of these turbulent structures at the helium - air interface. Rather, they are formed by buoyancy-driven (gravitational and baroclinic) vorticity generation. This vorticity generation mechanism will trigger the Rayleigh-Taylor and Kelvin-Helmholtz instabilities, near the base of the plume, and eventually form toroidal vortices [18, 79], shown in Figure 4.3(d).

4.5.2 Vortex dynamics

A measure of the local 'spin' or 'rotation' of a fluid can be given by vorticity. An analysis of the vorticity equation provides a better understanding of how vorticity is generated and transported downstream by convection and diffusion:

$$\frac{D\omega}{Dt} = \underbrace{(\omega \cdot \nabla)u}_{\substack{\text{vortex}\\ \text{stretching}}} - \underbrace{\omega(\nabla \cdot u)}_{\substack{\text{dilatation}\\ \text{term}}} + \underbrace{\frac{1}{\rho^2}(\nabla\rho \times \nabla p)}_{\substack{\text{baroclinic}\\ \text{torque}}} + \underbrace{\frac{\rho_\infty}{\rho^2}(\nabla\rho \times g)}_{\substack{\text{gravitational}\\ \text{torque}}} + \underbrace{\nabla \times (\frac{1}{\rho}\nabla \cdot \tau)}_{\substack{\text{viscous}\\ \text{diffusion}}} \tag{4.6}$$

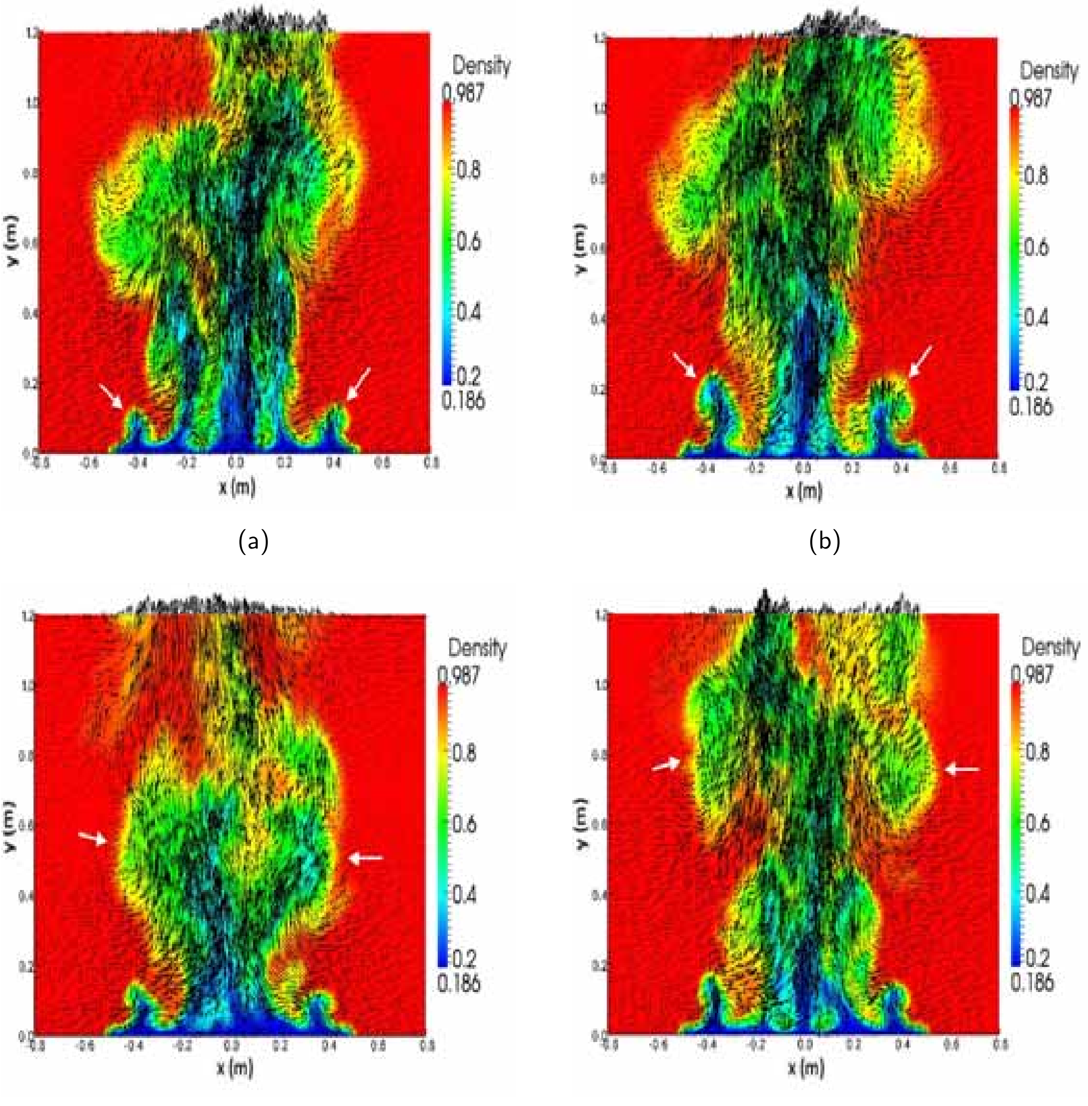

(a) (b)

(c) (d)

Figure 4.3: Instantaneous snapshots of a typical puffing cycle from LES showing isocountours of density (kg/m^3) with superimposed velocity magnitude (m/s) vectors for the fine grid with SGS model at times (a) 10.2 s, (b) 10.26 s, (c) 10.74 s and (d) 11.02 s.

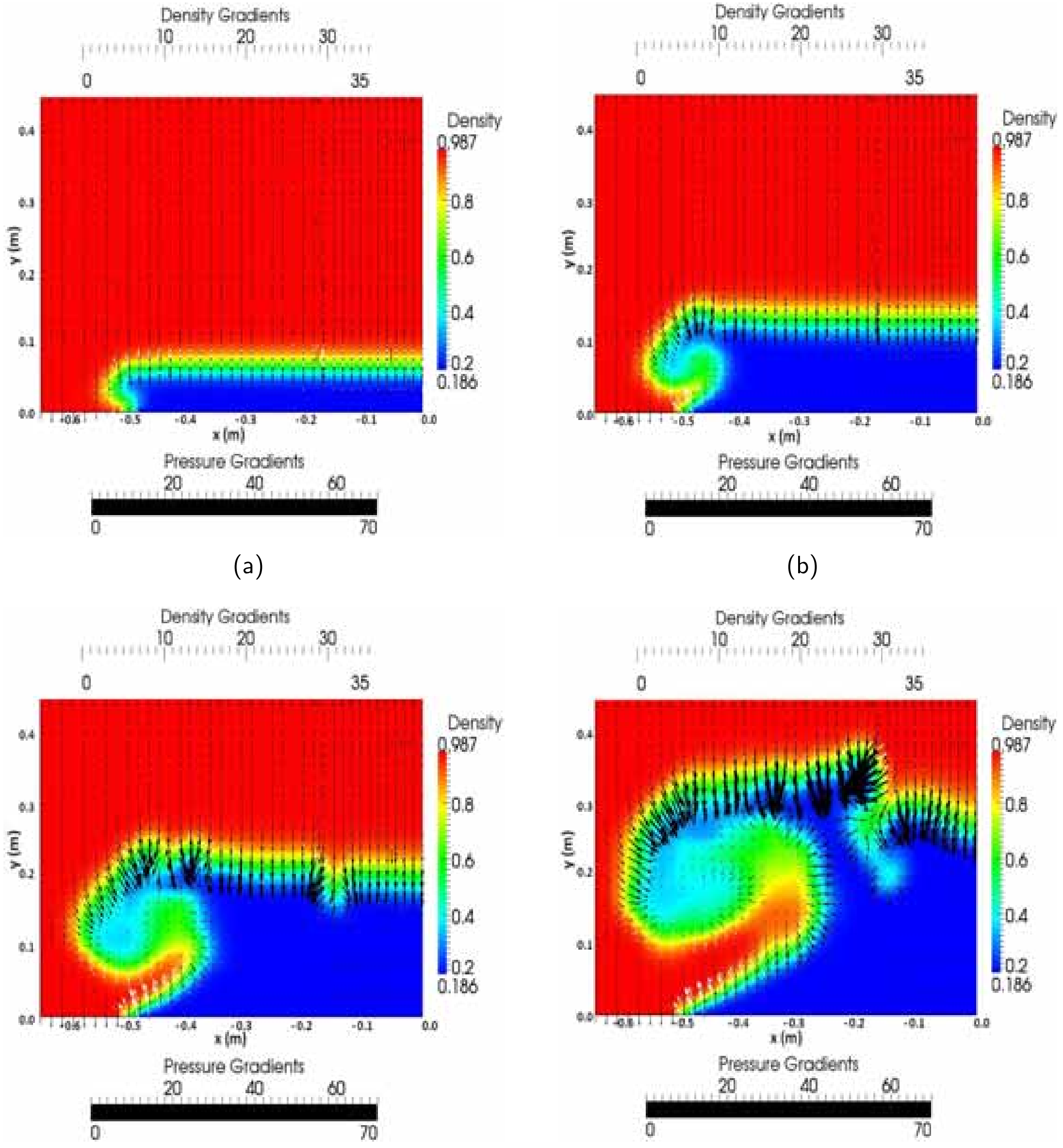

(a) (b)

(c) (d)

Figure 4.4: Misalignment of density gradients (kg/m^4) (white arrows) and pressure gradients (kg/m^{2}s^2) (black arrows) near the base of the plume at times (a) 0.2 sec, (b) 0.4 sec, (c) 0.6 sec and (d) 0.8 sec.

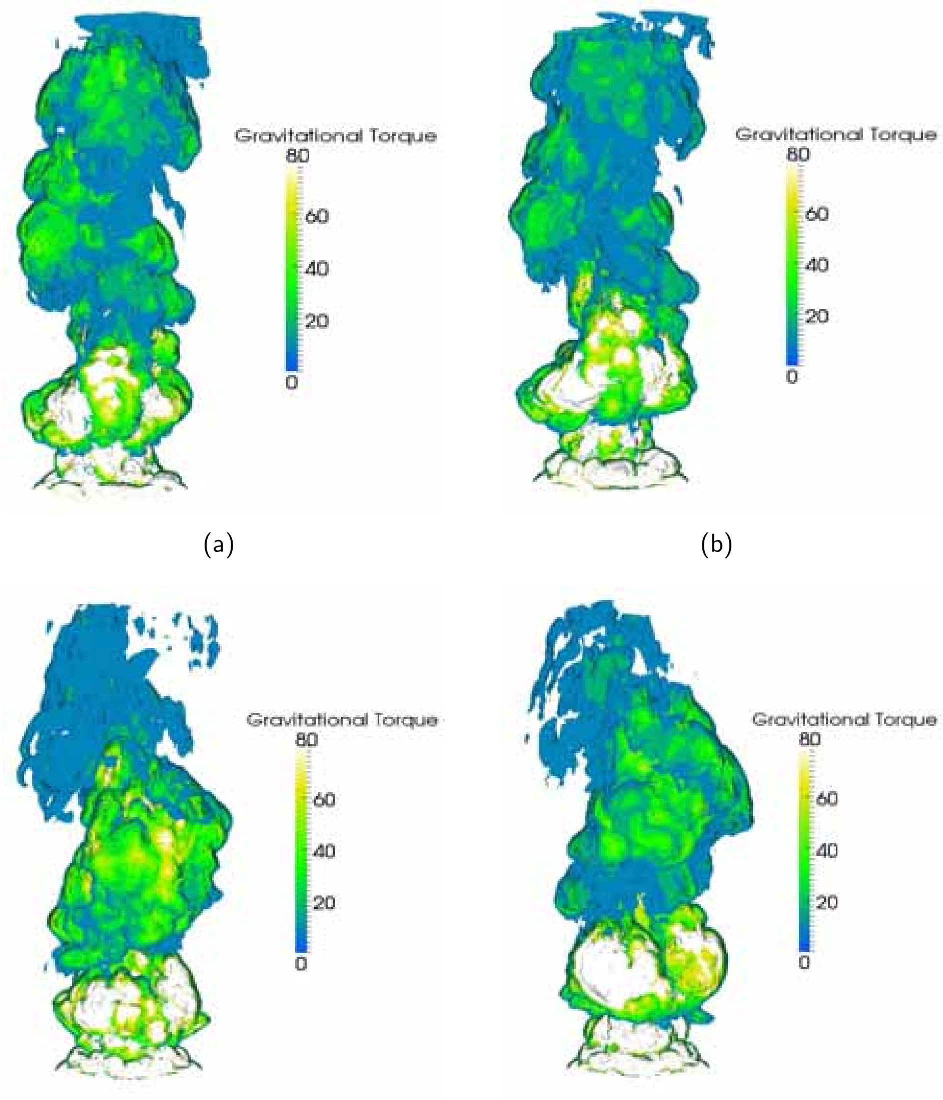
Gravitational Torque
80
60
40
20
0
Gravitational Torque
80
60
40
20
0
Gravitational Torque
80
60
40
20
0
Gravitational Torque
80
60
40
20
0

(a) (b)

(c) (d)

Figure 4.5: Instantaneous snapshots of puff cycle showing isosurfaces of gravitational torque magnitude at 1% of the maximum value at times (a) 10.2 s, (b) 10.26 s, (c) 10.74 s and (d) 11.02 s.

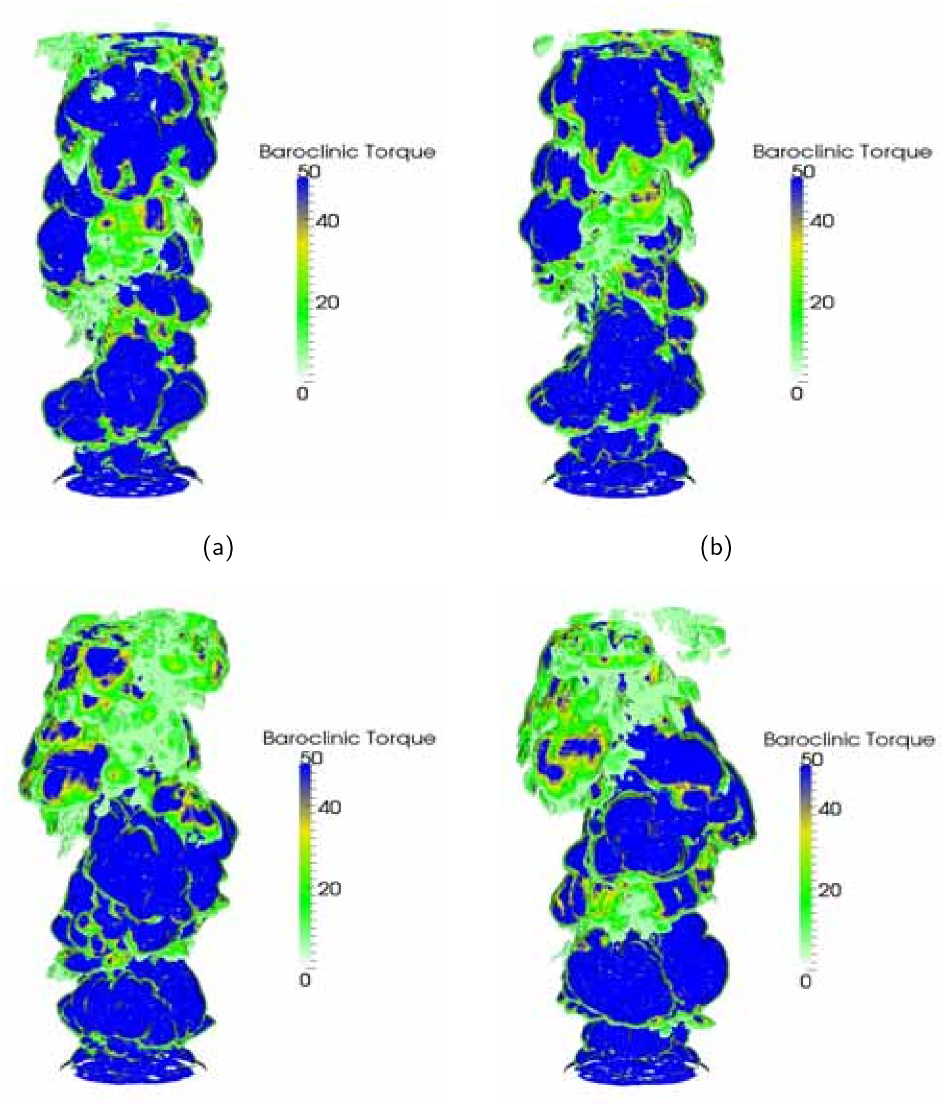
Baroclinic Torque
50
40
20
0
Baroclinic Torque
50
40
20
0
Baroclinic Torque
50
40
20
0
Baroclinic Torque
50
40
20
0

(a) (b)

(c) (d)

Figure 4.6: Instantaneous snapshots of puffing cycle showing isosurfaces of baroclinic torque magnitude at 1% of the maximum value at times (a) 10.2 s, (b) 10.26 s, (c) 10.74 s and (d) 11.02 s.

Five different physical mechanisms affect the vorticity transport. The terms on the right hand side of the vorticity equation are identified [44] as vortex stretching term, dilatation term, baroclinic torque, gravitational torque and viscous diffusion. In incompressible flows, only the first term prevails. Vortex stretching is a very important mechanism in the turbulent dynamics as it represents the enhancement of vorticity by stretching. It is the mechanism by which turbulent energy is transferred to smaller scales. The dilatation term represents the effects of expansion of the vorticity field and results in a decrease in the magnitude of vorticity (minus sign in Eq. (4.6)). Gravitational torque generates vorticity due to non-aligned gravity and density gradients, while baroclinic torque is the mechanism by which vorticity is generated from non-aligned pressure and density gradients. In buoyancy-driven flows, both the baroclinic and gravitational torque terms, along with vortex stretching, are the main mechanisms promoting flow vorticity [42, 43]. A DNS study [44] identified the gravitational term as key mechanism promoting cross - streamwise vorticity. DesJardin et al. [18] showed that, during a typical puffing cycle, the maximum gravitational torque is located at the base of the plume. Similar behavior is also observed in the current study, as seen in Figure 4.5, in which the maximum gravitational torque is observed at the base of the plume. Of similar importance is the influence of baroclinic torque, presented in Figure 4.6. The maximum baroclinic torque is located in regions where large pressure and density gradients are present. Both these torques initiate the base instability and then promote its rapid growth. For large plumes and pool fires, this vortex quickly destabilizes, forming secondary azimuthal, or 'finger-like', instabilities similar to the ones reported in smaller scale experimental studies [123]. The formation of secondary instabilities creates streamwise vorticity that serves to promote the breakdown of large-scale toroidal structures and enhances local mixing processes.

The influence of each of the five terms in the vorticity equation (Eq. (4.6)) is shown in Figures 4.7 for the fine grid with SGS model. It is clear that, at height $y = 0.0$ m, the generation of instabilities is maximum at the edge of the plume ($x = \pm$ 0.5 m), creating a net maximum vorticity of 1300 s^{-2}. At this location, there vorticity is also generated about 0.1 m away from the centerline, where a net vorticity of 1200 s^{-2} is observed. This is where the Rayleigh-Taylor instability is triggered, causing a mass of helium to be convected downstream (Figure 4.3). Higher in the domain the influence of the gravitational torque and vortex stretching decreases while the influence of the baroclinic torque and the dilatation term increases, causing the vorticity field to expand and reduce its magnitude.

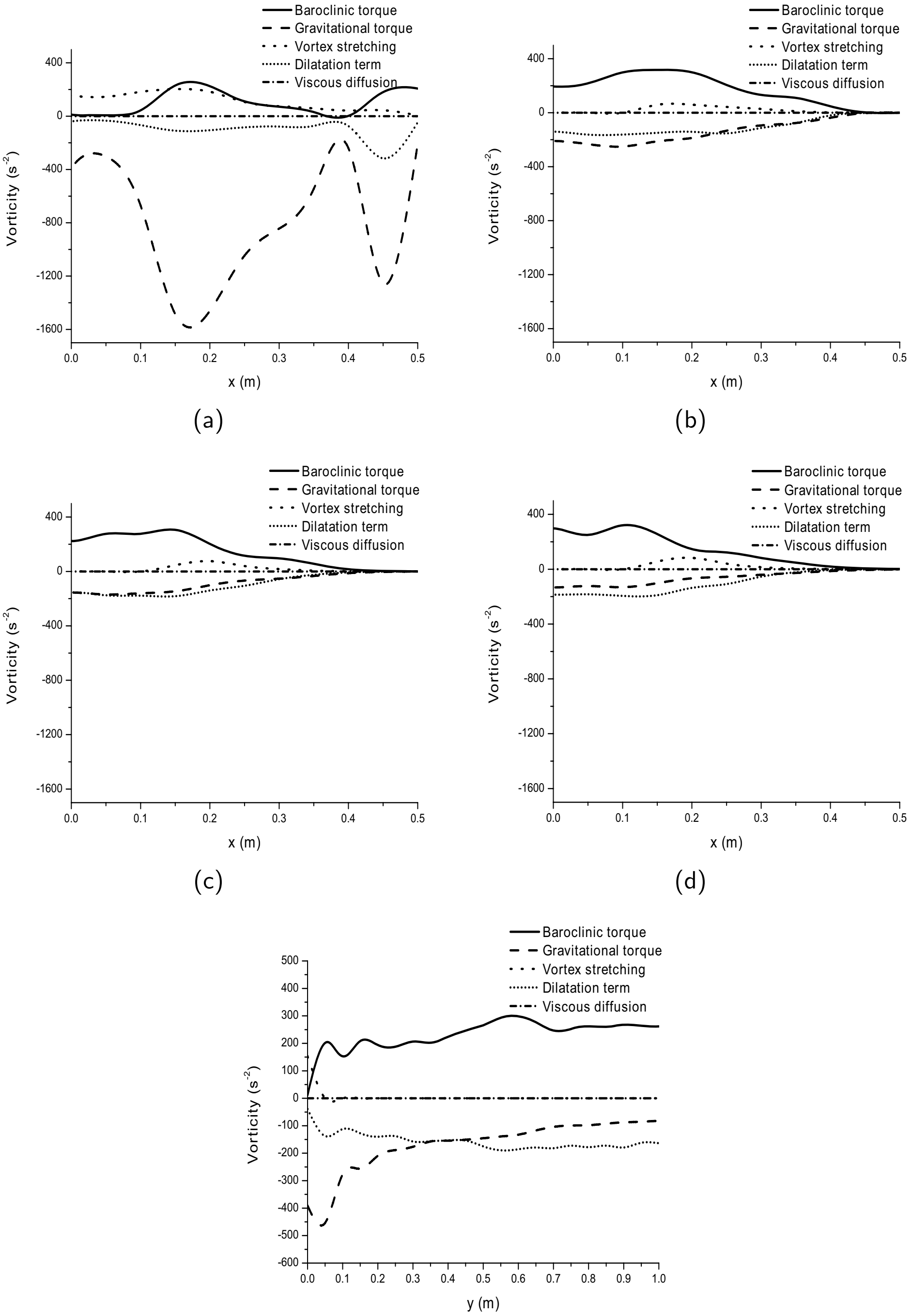

(a) (b)

(c) (d)

(e)

Figure 4.7: Vorticity budgets from Equation (11) for the fine grid with the Smagorinsky SGS model at (a) $y = 0.0$ m, (b) $y = 0.2$ m, (c) $y = 0.4$ m, (d) $y = 0.6$ m and (e) on the centerline up to $y = 1.0$ m.

4.5.3 Puffing frequency

The effect of grid spacing and SGS modelling on the puffing cycle of the helium plume is presented in Figure 4.8, showing time traces of the centerline streamwise velocity at location $y = 0.5$ m above the inlet, for a total of 5 seconds in the simulations. The puffing frequency corresponds to the number of puffing cycles encountered, a maximum peak in the streamwise velocity followed by a minimum, in the given timeline examined. The simulation results revealed a phase shift in the periodic cycles, as compared to the experiments. Therefore, the time signals in Figure 4.8(b) have been shifted along the time axis to make the comparison with the experiments more clear. For the coarse mesh, low frequency large scale puffing can be observed with the use of SGS model. Without SGS model a higher frequency mode is more obvious and the puffing frequency is hard to identify. As the mesh is refined, a clear puffing frequency is evident. Regardless of the use of a SGS model, a total of 7 cycles, corresponding to the passage of large turbulent structures, are distinguished, followed by an occasional smaller puff. The use of the SGS model reduces the dynamic range (defined as the difference between the maximum and the minimum results observed) of the streamwise velocity due to the damping of the flow, as has also been reported in [18]. More fluctuations appear when no SGS model is applied.

The puffing frequency results are further analyzed to produce a Fourier transformation on the time signal, taken over the last 10 seconds in the simulation, of the streamwise velocity on the centerline at $y = 0.5$ m. The result is presented in Figure 4.9. For the coarse grid without SGS model, there is no clear peak. The highest peak in the puffing frequency prediction is at 2.31 Hz, but there is e.g. also a peak at 1.29 Hz. When the SGS is applied, the frequency peak is clear at 1.11 Hz. The influence of the SGS is clear, but the agreement with the experimentally observed frequency is not satisfactory. The experimental puffing frequency obtained by O'Hern et al. [79] is 1.37± 0.1 Hz. The experimental correlation, $f = 0.8Ri^{0.38}u/d$, suggested by Cetegen et al. [12] for $Ri < 100$, leads to a puffing frequency of 1.34 Hz for the set-up at hand, while the established puffing frequency correlation for buoyant diffusion flames of various fuels by Cetegen et al. [11], $f = 1.5/\sqrt{d}$, yields a frequency of 1.5 Hz, independent of flow conditions. On the fine grid, a distinct peak around 1.31 Hz for the case without SGS model is found. This peak shifts to 1.41 Hz when the SGS model is applied. The influence of the SGS model is not very large on the fine mesh and the results agree very well with the experimental correlations mentioned.

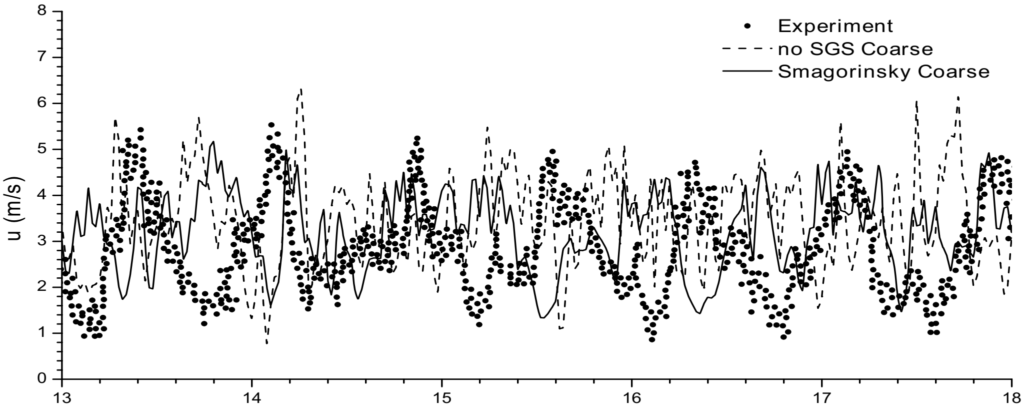

(a)

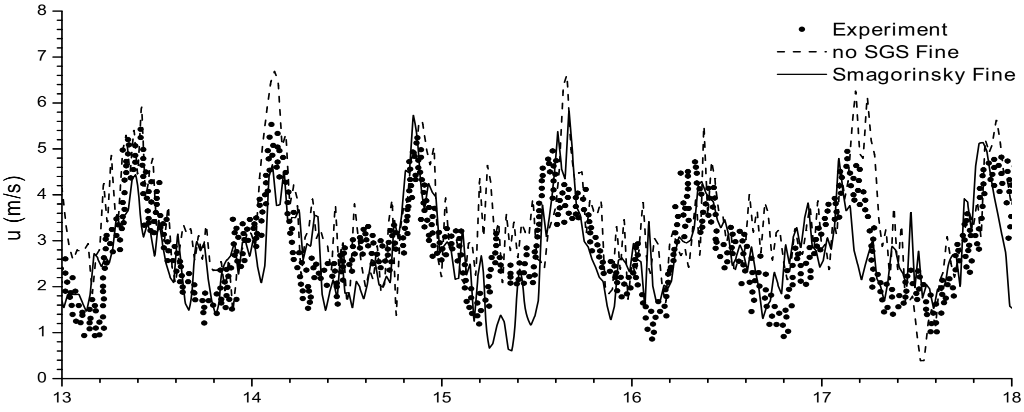

(b)

Figure 4.8: Time trace of centerline streamwise velocity at $y = 0.5$ m above the base of the plume for (a) coarse grid and (b) fine grid.

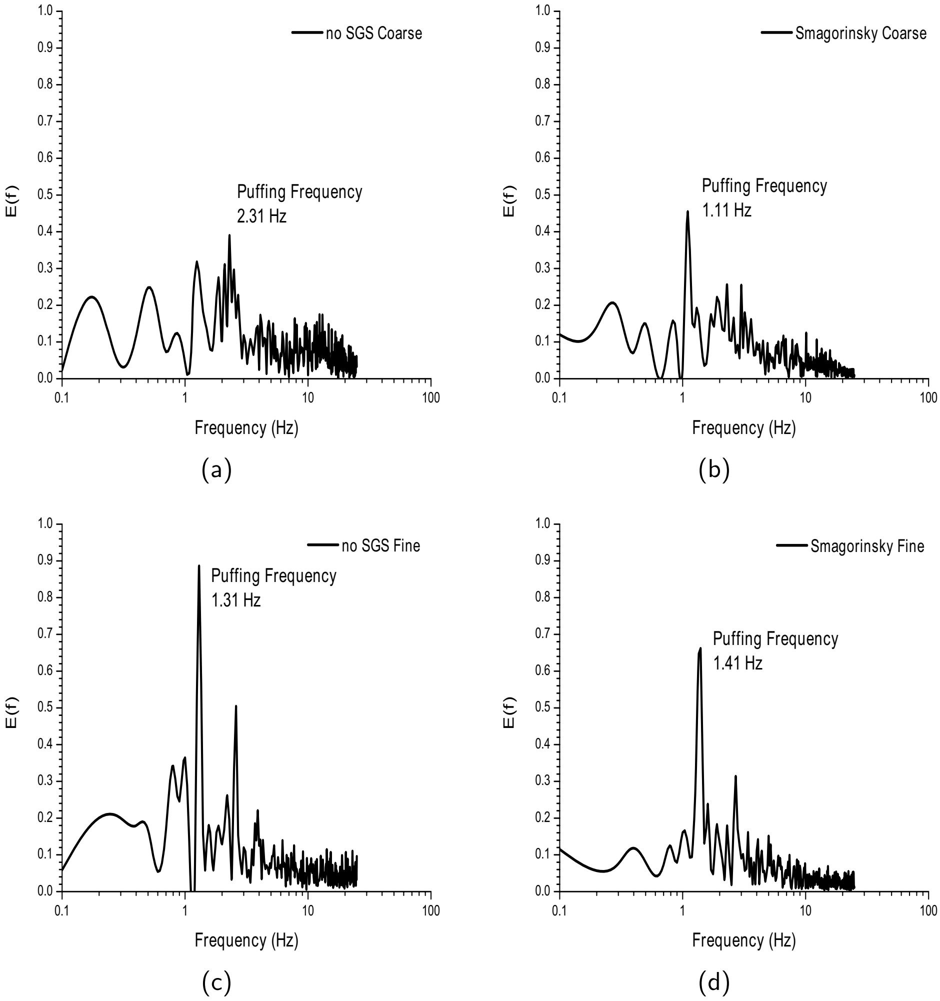

Figure 4.9: Power spectrum of streamwise velocity on the centerline at $y = 0.5$ m above the base of the plume for coarse grid with (a) no SGS , (b) Smagorinsky model and fine grid with (c) no SGS, (d) Smagorinsky model.

4.5.4 Mean and rms values for velocities and helium mass fractions

Figure 4.10 presents the centerline profiles of mean and rms of the streamwise velocity components up to $y = 0.8$ m above the base of the plume. For the mean values, all simulation results remain within the experimental uncertainty at practically all locations. Best agreement is observed on the fine mesh with SGS model. For the rms values also good agreement is observed, especially when the SGS model is applied. Overall all simulation results remain within experimental uncertainty (except for the coarse grid case without SGS model, where the rms values are over-predicted close to the inlet).

The mean and rms values for helium mass fractions on the centerline up to a height of $y = 0.8$ m are presented in Figure 4.11. Agreement is less satisfactory than for the flow field: the decay of the mean values is too slow in the simulations from $y = 0.2$ m onward. The rms values are over-predicted as well.

Results for the density-weighted, time-averaged streamwise velocities at several heights ($y =$ 0.2 m, 0.4 m and 0.6 m above the inlet) are presented in Figure 4.12. Generally at all three locations, the streamwise velocity is well predicted. Also noticeable is that downstream, away from the plume inlet, there is an increase in the streamwise velocity due to acceleration caused by buoyancy forces.

Figure 4.13 presents results for the density-weighted, time-averaged rms values of the streamwise velocities. The differences between the simulation results are small at all heights. The cases with the fine grid show good agreement with the experiments, particularly when the SGS is applied.

For the cross-stream velocities, presented in Figure 4.14, good agreement with the experiment is observed for all cases examined. A small over-prediction on the left hand side of the source, at locations around $x = -0.2$ m is observed. However, the experimental data are not perfectly symmetric. For obvious reasons, this asymmetry could not be predicted in the simulations. The application of a SGS model causes an increase in the cross-stream velocity at all three heights. Note that, as a consequence of mass conservation, an increase in the cross-stream velocities will result in an increase in the streamwise velocities. Accurate results for the cross-stream velocities are important because in this kind of flows entrainment controls mixing, a parameter very important in pool fires where combustion processes are mixing-controlled.

Figure 4.15 presents results for the density-weighted, time-averaged rms values of the

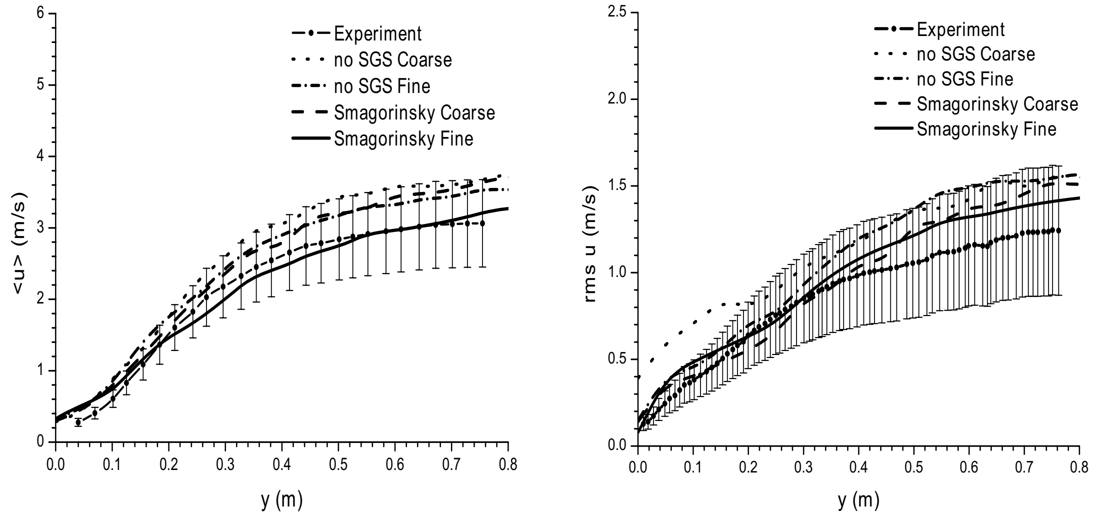

(a) (b)

Figure 4.10: Comparison of density-weighted, time-averaged (a) mean and (b) rms values for the centerline streamwise velocity up to $y = 0.8$ m above the base of the plume.

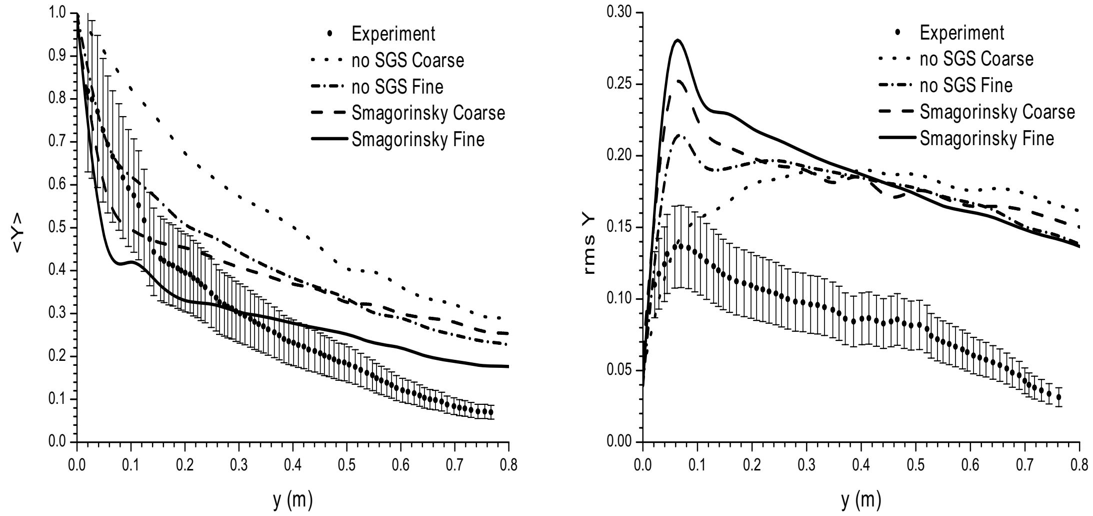

(a) (b)

Figure 4.11: Comparison of density-weighted, time-averaged (a) mean and (b) rms centerline values for the helium mass fraction up to $y = 0.8$ m above the base of the plume.

cross-stream velocities at the same locations. Near the plume edge, the results do not differ much. In the central region, the results at the coarse mesh without SGS model are far off. Best agreement is observed with the use of SGS model, particularly at the fine mesh. It is evident from both Figures 4.13 and 4.15 that the use of a fine mesh reduces the rms values in the central region, in better with the experiments. The simulations with SGS model predict a bimodal shape for the rms cross-stream velocities, similar to what was observed by Chung et al. [14] and DesJardin et al. [18]. The use of a SGS model also reduces the rms values.

Figure 4.16 presents results of the density-weighted, time-averaged helium mass fractions. The mean mass fraction values are over-predicted on the centerline, with larger discrepancies higher in the domain. Best results are obtained, at all three locations, on the fine grid with the use of a SGS model. Without SGS model, diffusion is clearly under-estimated. The turbulent diffusion term, proportional to μ_t/Sc_t, is then indeed absent. Globally, the mass fraction values obtained with the current simulations agree more favorably with the experimental data as compared to previously published CFD studies [14, 18].

Figure 4.17 presents results of the density-weighted, time-averaged rms values of helium mass fraction. An over-prediction of the experimental values is observed close to the base of the plume, for all cases tested. These discrepancies reduce higher in the domain, with overall better agreement when the SGS model is applied.

Results of the density-weighted, time-averaged product of rms streamwise and rms cross-stream velocities, $u'v'$, are presented in Figure 4.18. Except for the simulation on the coarse mesh with no SGS model, the results are very close to the experimental values and the trends are captured, showing that the second order statistics in the present LES calculations are quite well predicted.

The density-weighted, time-averaged turbulent kinetic energy ($k = \frac{1}{2}[\overline{(u')^2} + \overline{(v')^2} + \overline{(w')^2}]$) results are presented in Figure 4.19. At all three locations, the results on the fine grid with SGS model have the best agreement with the experiment. Without the SGS model the turbulent kinetic energies are over-predicted, especially near the centerline.

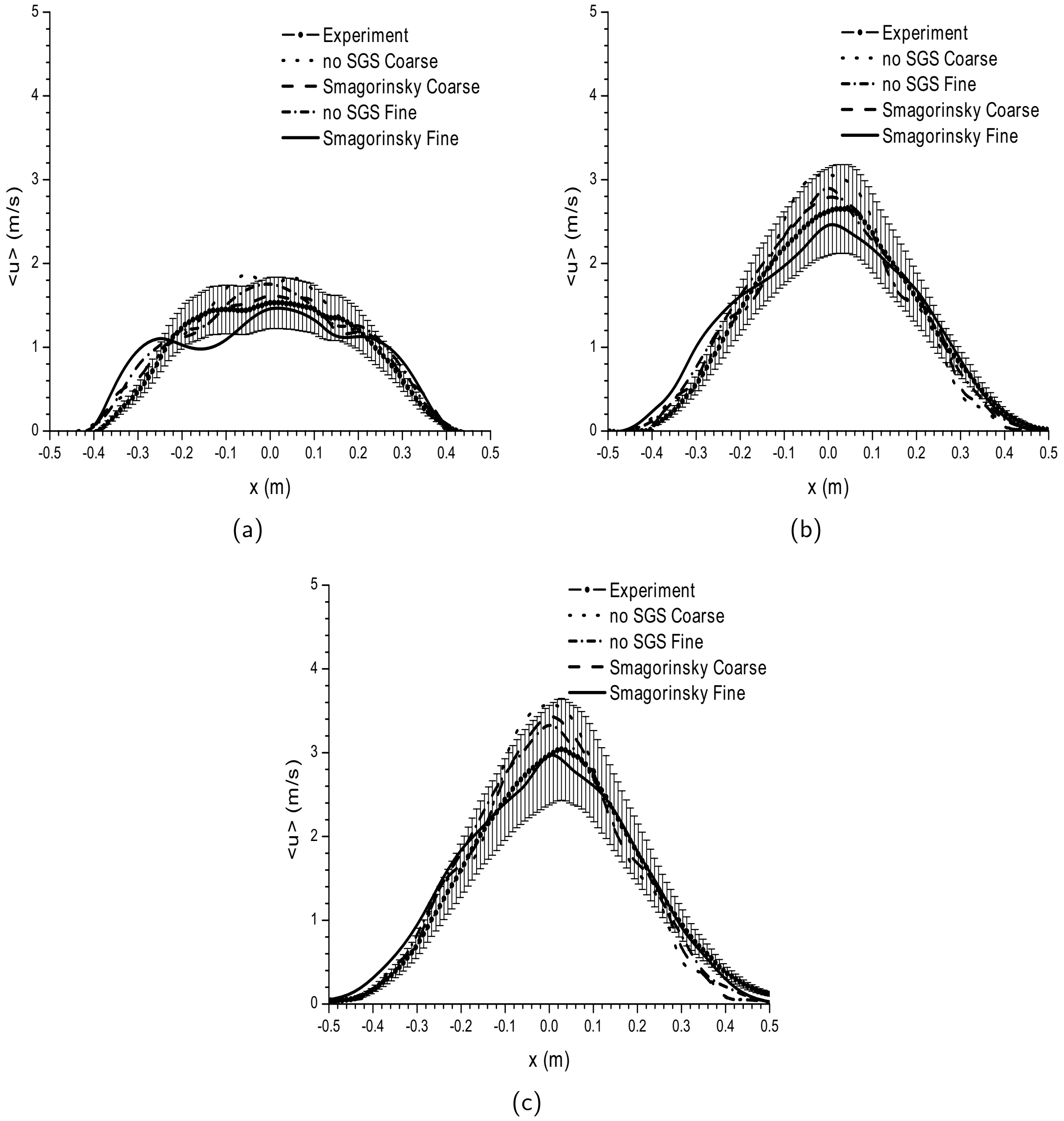

(a)

(b)

(c)

Figure 4.12: Comparison of density-weighted, time-averaged streamwise velocities at heights $y =$ (a) 0.2 m, (b) 0.4 m and (c) 0.6 m.

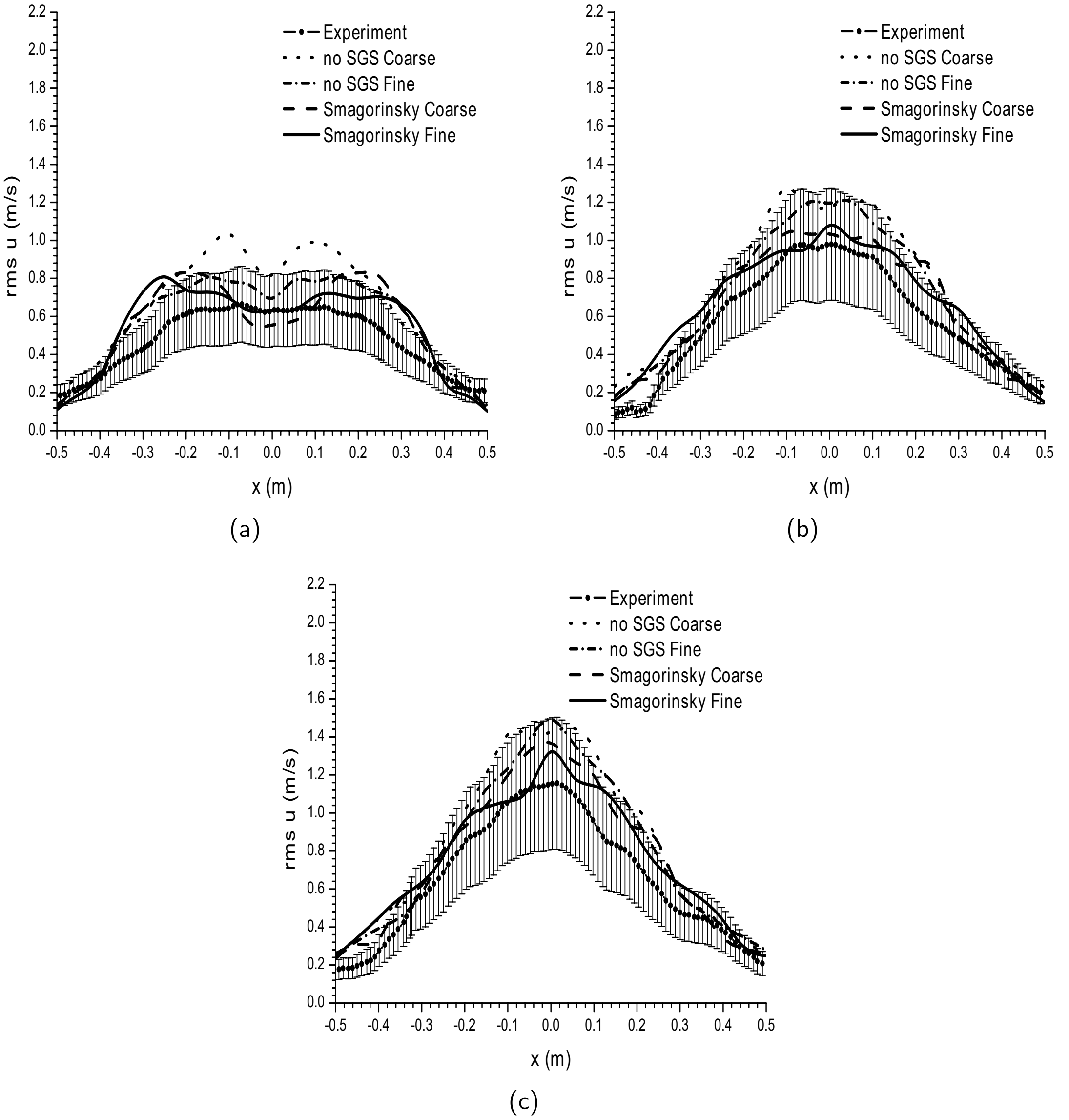

(a) (b)

(c)

Figure 4.13: Comparison of density-weighted, time-averaged rms streamwise velocities at heights $y =$ (a) 0.2 m, (b) 0.4 m and (c) 0.6 m.

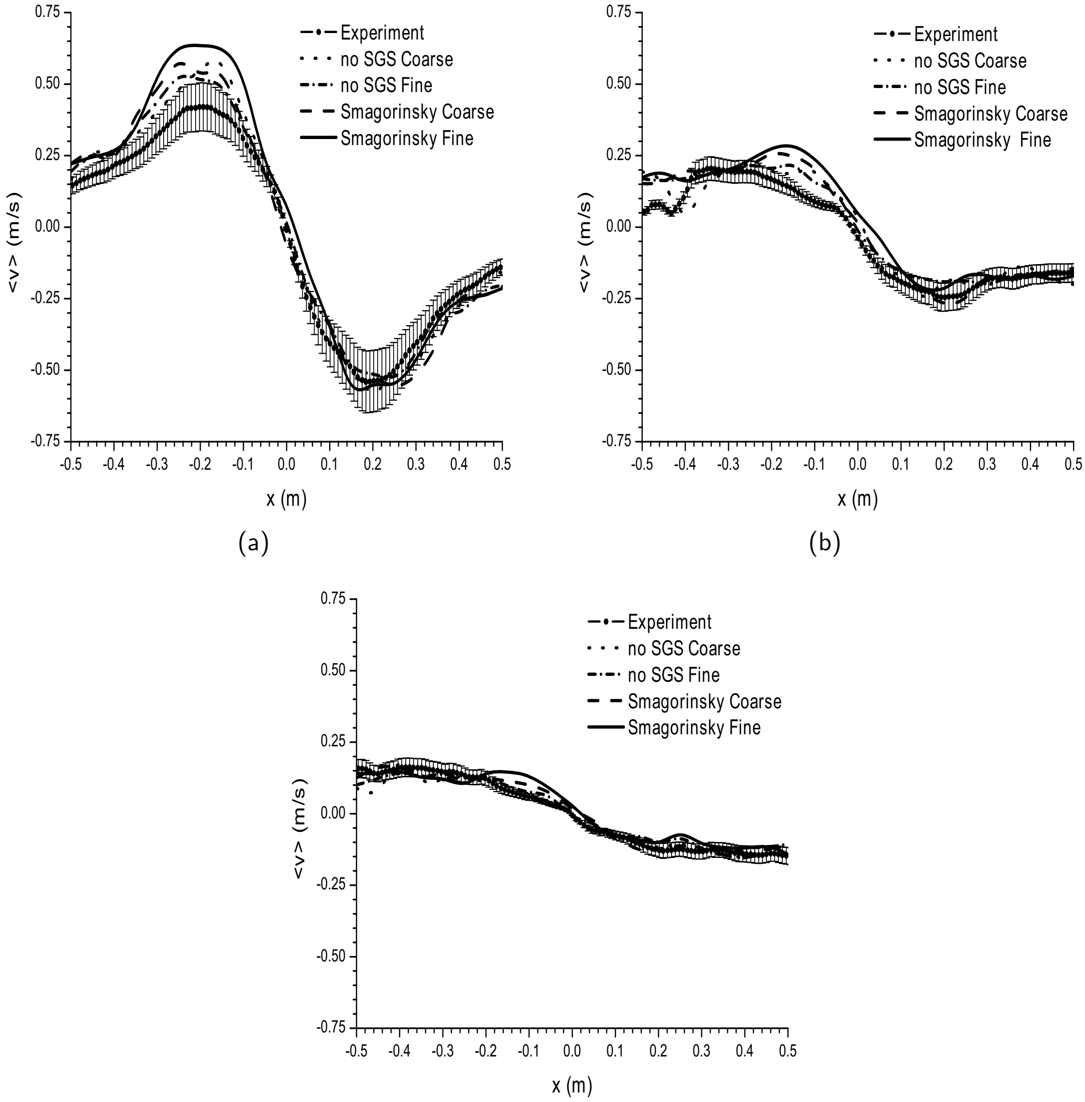

(a)

(b)

(c)

Figure 4.14: Comparison of density-weighted, time-averaged cross-stream velocities at heights $y =$ (a) 0.2 m, (b) 0.4 m and (c) 0.6 m.

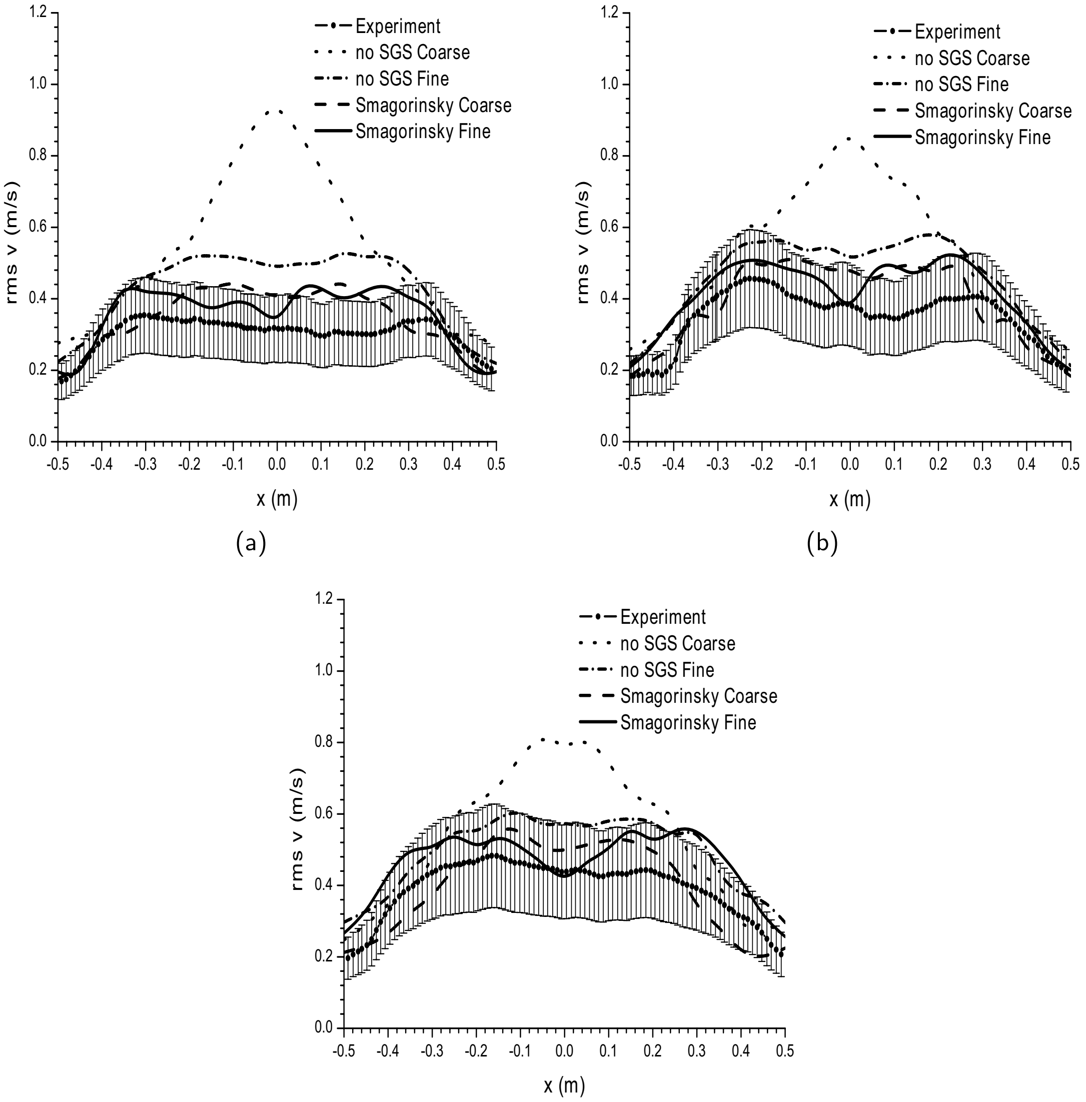

(a)

(b)

(c)

Figure 4.15: Comparison of density-weighted, time-averaged rms cross-stream velocities at heights $y =$ (a) 0.2 m, (b) 0.4 m and (c) 0.6 m.

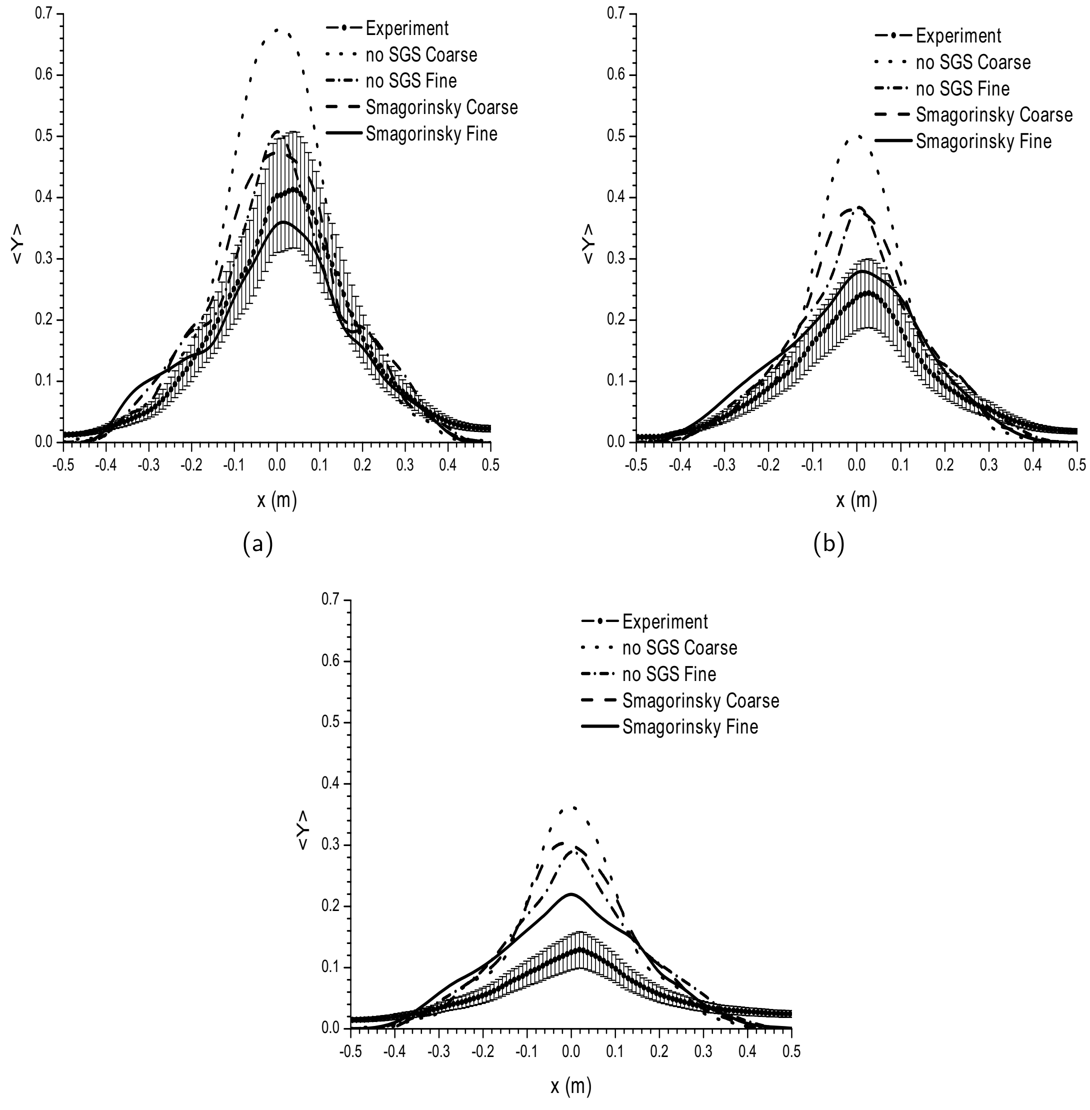

(a)

(b)

(c)

Figure 4.16: Comparison of density-weighted, time-averaged mass fractions at heights $y =$ (a) 0.2 m, (b) 0.4 m and (c) 0.6 m.

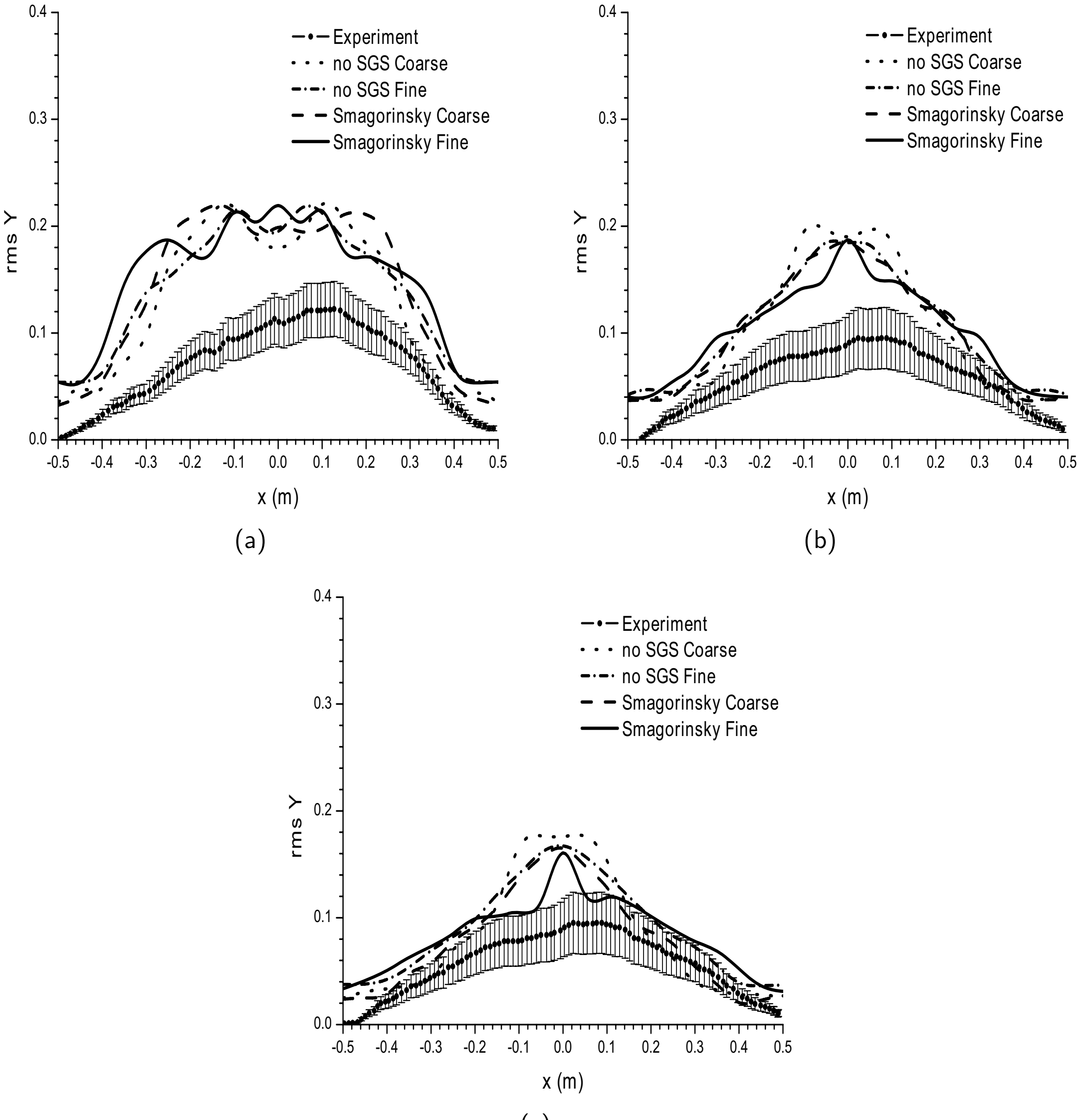

(a)

(b)

(c)

Figure 4.17: Comparison of density-weighted, time-averaged rms mass fractions at heights $y =$ (a) 0.2 m, (b) 0.4 m and (c) 0.6 m.

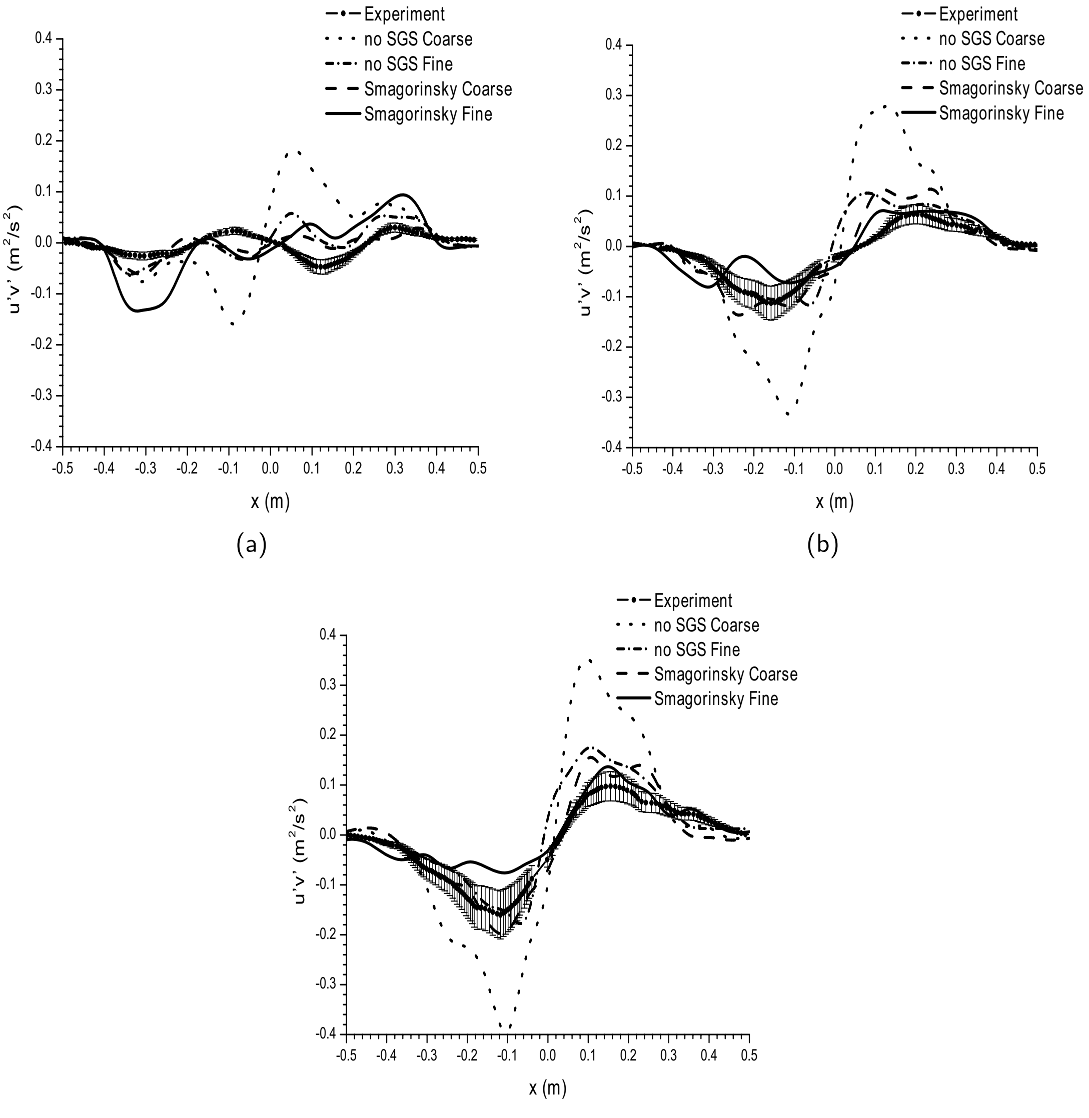

(a)

(b)

(c)

Figure 4.18: Comparison of density-weighted, time-averaged product of rms streamwise and rms cross-stream velocities at heights $y =$ (a) 0.2 m, (b) 0.4 m and (c) 0.6 m.

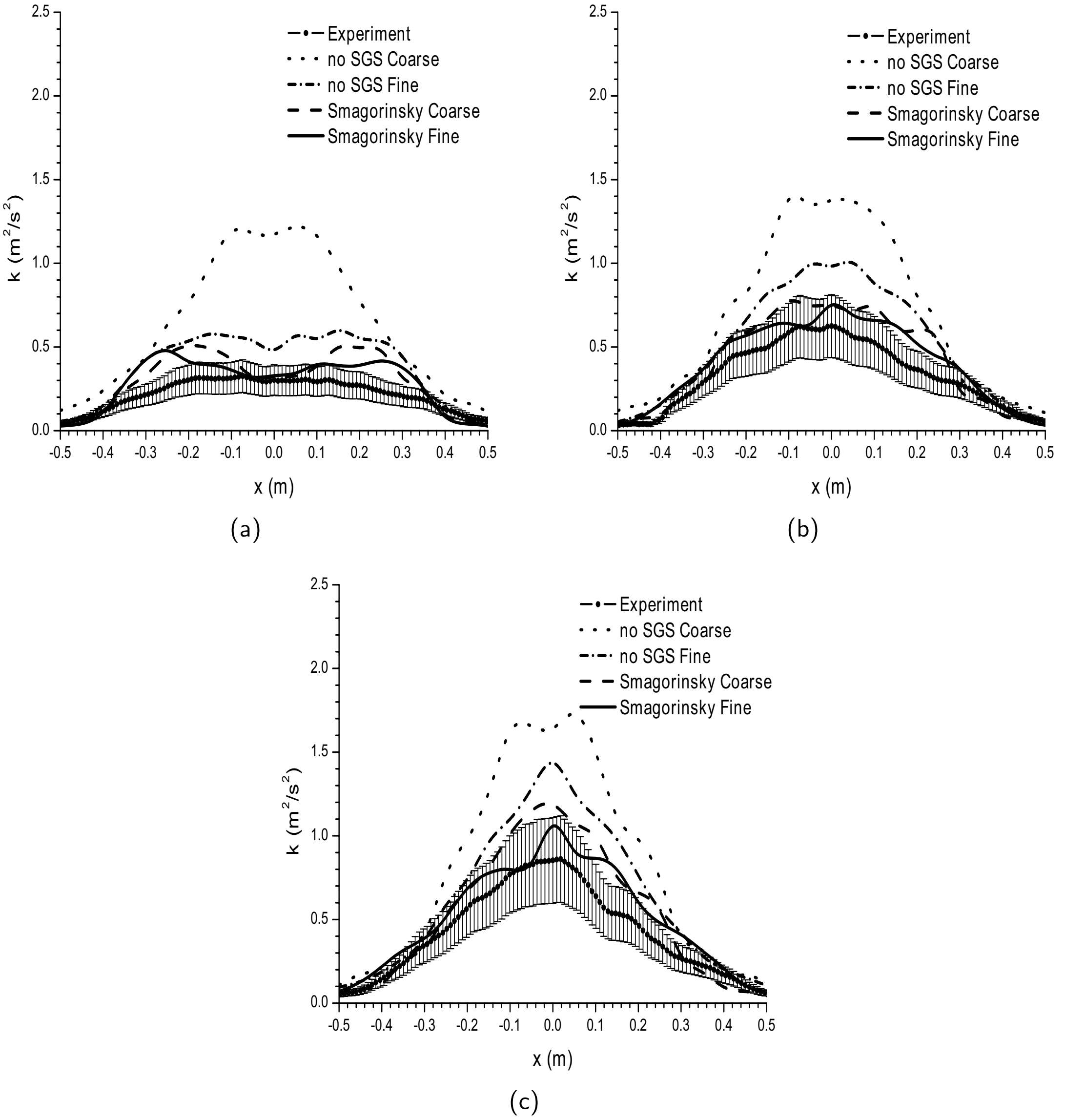

(a)

(b)

(c)

Figure 4.19: Comparison of density-weighted, time-averaged turbulent kinetic energy at heights $y =$ (a) 0.2 m, (b) 0.4 m and (c) 0.6 m.

4.5.5 Correlation between velocity and density

Figure 4.20 shows scatter plots of instantaneous vertical velocity vs density at location $x = 0.03$ m, $y = 0.46$ m, as was reported in the experimental study of O'Hern et al. [79]. The strong anti-correlation between the streamwise velocity and density is confirmed. The maximum vertical velocities are observed in the low density region of the flow field. This is not surprising, as stronger acceleration can be expected in a lower density fluid for a certain differential pressure. When the SGS is applied, the scatter plot cloud is more dense and shifted towards higher density and lower streamwise velocity values, matching well the experimental measurements in [79].

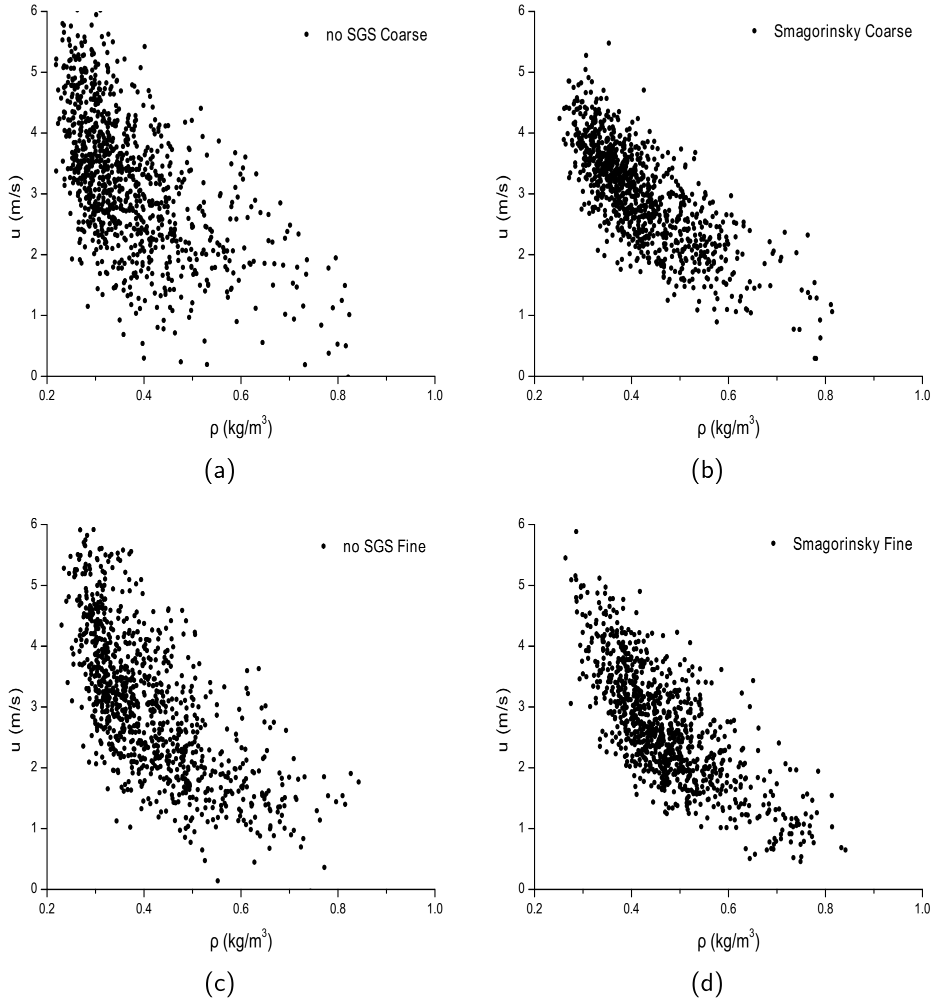

(a) (b) (c) (d)

Figure 4.20: Instantaneous vertical velocity component u vs density at x =0.03 m, y =0.46 m for coarse grid with (a) no SGS , (b) Smagorinsky model and fine grid with (c) no SGS, (d) Smagorinsky model.

The spatial distribution of the density - streamwise velocity correlation coefficient, $\overline{\rho' u'}/\sqrt{\overline{\rho'^2}\ \overline{u'^2}}$, on the centerline up to $y = 3.5$ m above the base of the plume, is presented in Figure 4.21. The correlation coefficient expresses the negative correlation between density and streamwise velocity. Sufficiently far away from the plume base, the value evolves to -0.7 (except for the results on the coarse mesh without SGS model). The value -0.7 agrees well with the small scale, thermal plume experiment by Shabbir & George et al. [103].

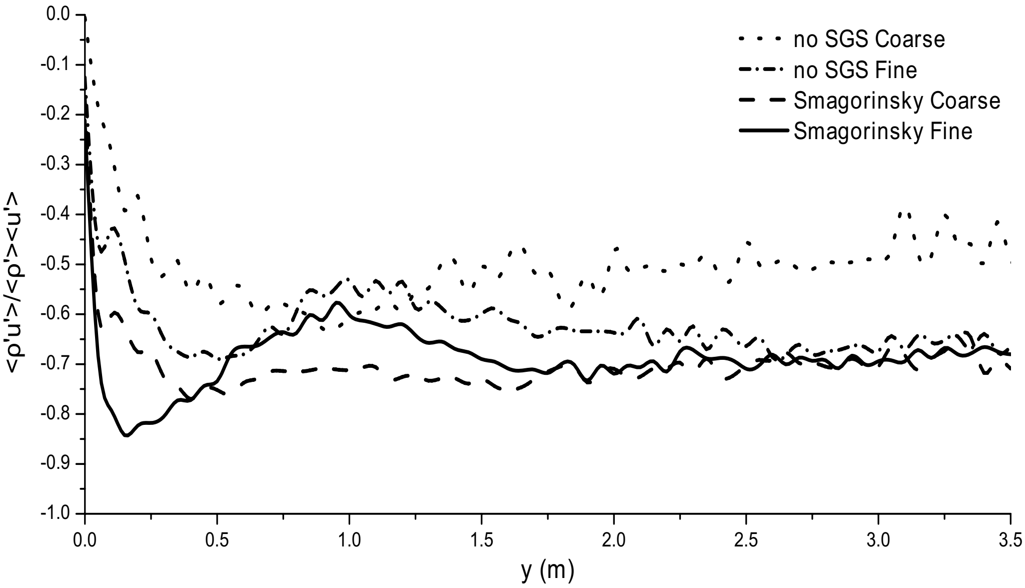

Figure 4.21: Density - streamwise velocity correlation coefficient up to $y = 3.5$ m above the base of the plume.

4.6 LES resolution

The ratio of the turbulent to laminar viscosity, μ_t/μ, is shown in Figure 4.22. When compared to the coarse grid, the ratio on the fine grid is about 3 times smaller at the edge of the plume, where the generation of the instabilities occurs, and about 2-2.5 times smaller on the centerline. This is also seen in Figure 4.23 showing that the ratio on the centerline increases with vertical distance from the plume base. This reveals that the influence of the SGS model on the fine grid is much smaller than on the coarse grid.

The ratio of grid spacing, Δ, to the Kolmogorov length scale, $\eta_K = (\frac{\nu^3}{\varepsilon})^{\frac{1}{4}}$, is presented in Figure 4.24 for the near-field region of the plume, with the total dissipation rate expressed as $\varepsilon = 2(\nu + \nu_t)\overline{S}_{ij}\overline{S}_{ij}$. According to Pope [?] the demarcation between the inertial and dissipation range for homogeneous isotropic turbulence is located at $k\eta \approx 0.1$

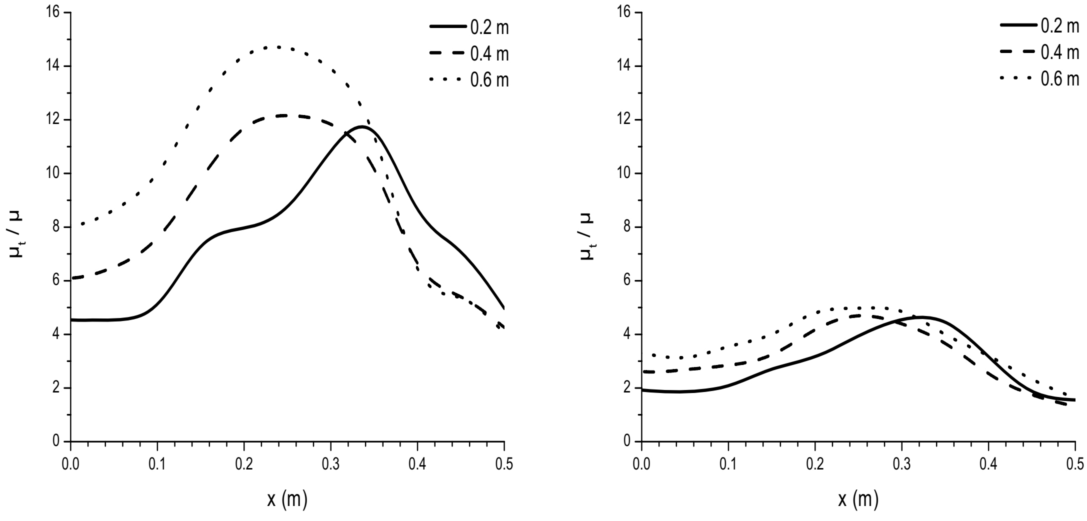

(a) (b)

Figure 4.22: Ratio of turbulent to laminar viscosity, μ_t/μ, with the Smagorinsky model for the (a) coarse and (b) fine grid.

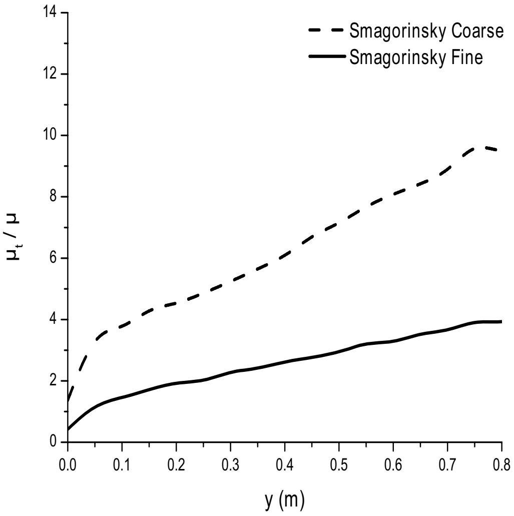

Figure 4.23: Ratio of turbulent to laminar viscosity, μ_t/μ, with the Smagorinsky model on the centerline.

or $\Delta/\eta \approx 32$. Assuming that this criterion remains valid sufficiently far from boundaries, it is used in this work to study the LES resolution. On the fine grid with the Smagorinsky model the ratio is about 10 to 15 on the centerline, depending on the vertical distance y examined, and goes up to 30 near the edge of the plume inlet, at $x = 0.35\ m$. The values obtained from the numerical simulations on the fine grid are within the dissipation range, implying a very well resolved LES calculation.

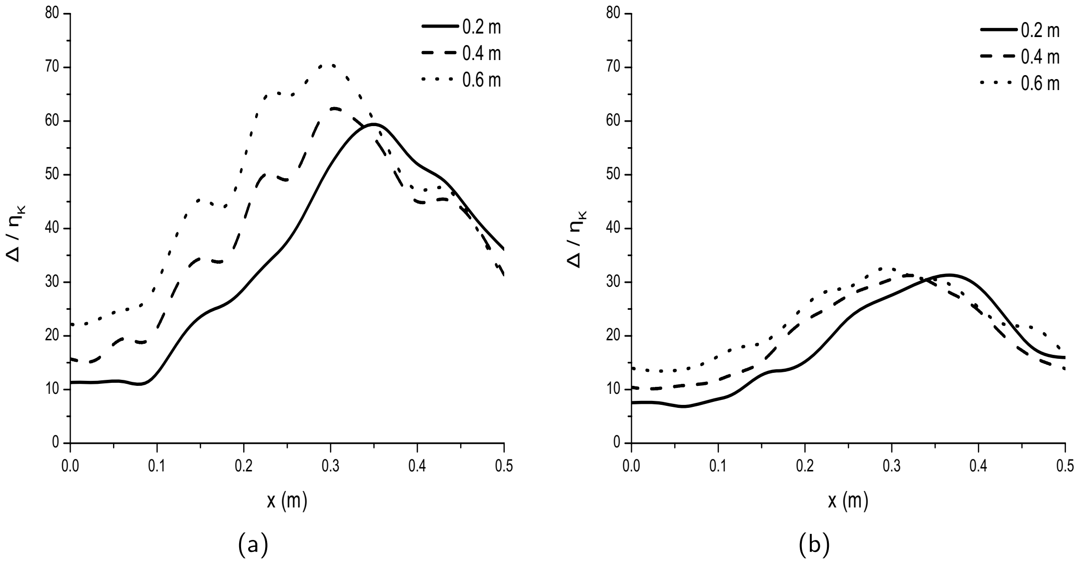

(a)

(b)

Figure 4.24: Ratio of grid spacing, Δ, to the Kolmogorov length scale, η_K, for (a) Smagorinsky coarse and (b) Smagorinsky fine.

4.7 Sensitivity analysis

An important parameter in the LES calculations is the Smagorinsky constant, c_s, which controls the amount of dissipation introduced by the SGS model. The amount of dissipation is also related to the filter width , Δ, used in the numerical simulations. As the grid becomes finer the amount of dissipation added by the SGS model decreases. Simulation results, for fine mesh, with Smagorinsky constants $c_s = 0.0, 0.1, 0.2$ at height $y = 0.6$ m are shown in Figure 4.25. Best agreement is observed with Smagorinsky constant $c_s = 0.1$ for mean and rms results. Therefore, a Smagorinsky constant of $c_s = 0.1$ is a good estimate for this case. Results with $c_s = 0.0$ correspond to ‘no SGS’. Overall, the sensitivity on c_s is not substantial on the fine mesh, as could be expected from the previous section, where the high LES resolution was described.

The second parameter considered in this sensitivity analysis is the turbulent Schmidt

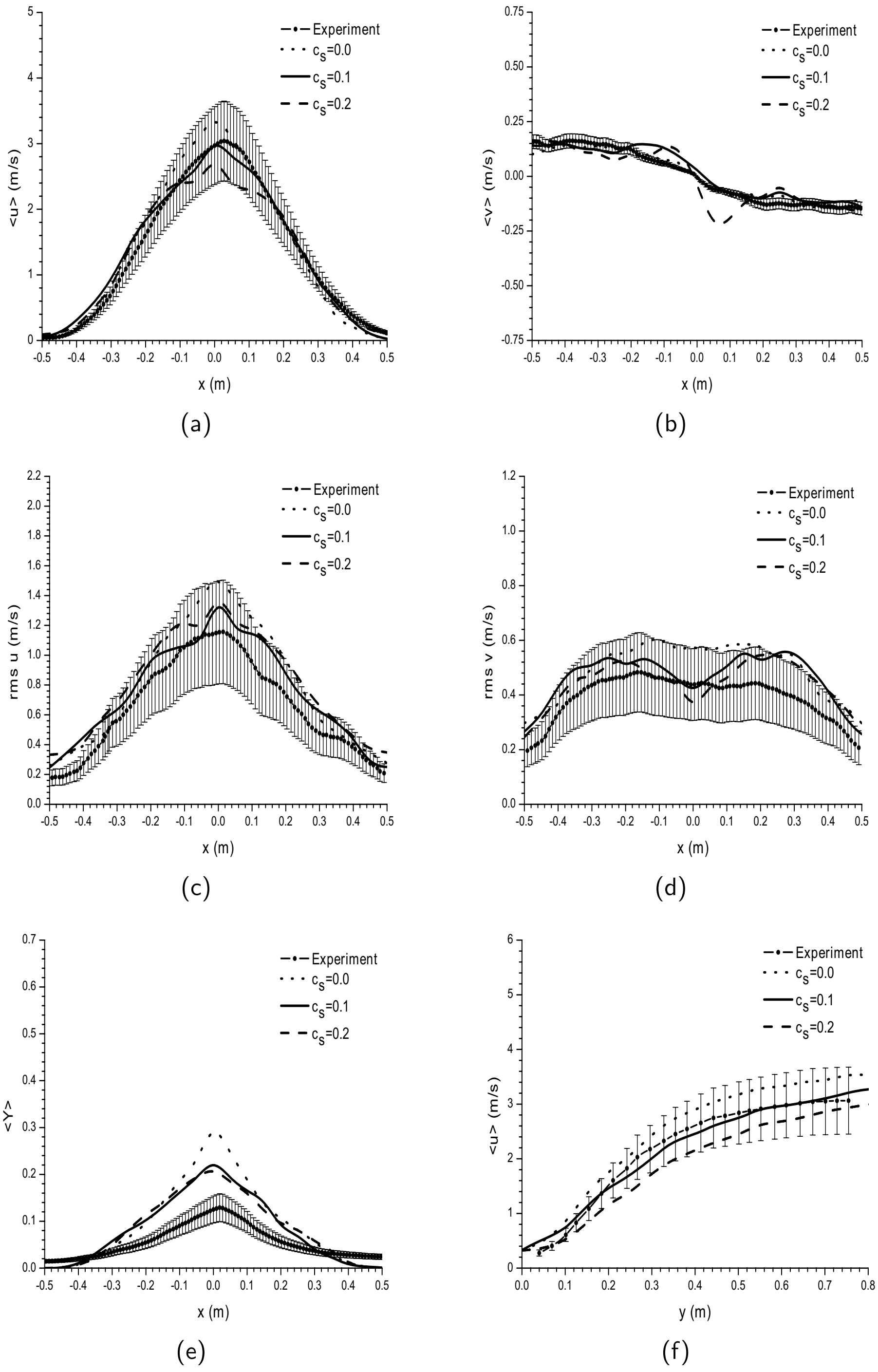

(a) (b)

(c) (d)

(e) (f)

Figure 4.25: Effect of Smagorinsky constant, c_s, in the fine mesh with turbulent Schmidt number, $Sc_t = 0.5$, at height $y = 0.6$ m on (a) streamwise velocity, (b) cross-stream velocity, (c) rms streamwise velocity, (d) rms cross-stream velocity, (e) mass fraction and (f) centerline streamwise velocity.

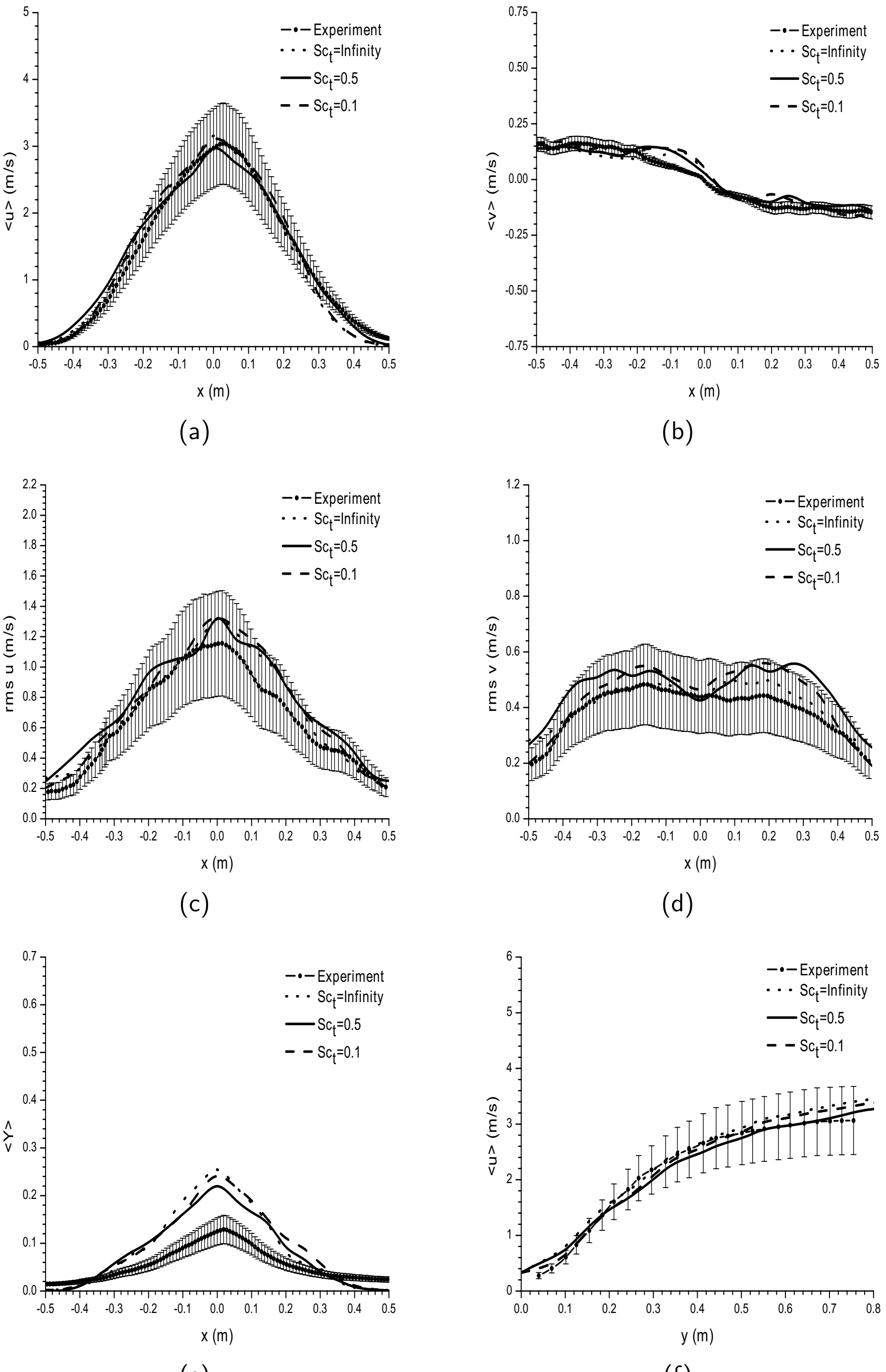

(a) (b)

(c) (d)

(e) (f)

Figure 4.26: Effect of turbulent Schmidt number, Sc_t, in the fine mesh with Smagorinsky model, $c_s = 0.1$, at height $y = 0.6$ m on (a) streamwise velocity, (b) cross-stream velocity, (c) rms streamwise velocity, (d) rms cross-stream velocity, (e) mass fraction and (f) centerline streamwise velocity.

number, Sc_t, used in Equation (10) for the SGS species flux. In Figure 4.26 results for various turbulent Schmidt numbers, $Sc_t = \infty$ (no SGS diffusion), $Sc_t = 0.5$ and $Sc_t = 0.1$ are presented, for the fine mesh with Smagorinsky constant, $c_s = 0.1$, at height $y = 0.6$ m. The variation of the turbulent Schmidt number does not have a strong influence on the simulation results.

4.8 Conclusions

In this study LES results for a large turbulent buoyant helium plume have been presented. The mechanism creating the characteristic puffing cycle of the plume has been analyzed and a qualitatively and quantitatively analysis of the instability generation, at the edge of the plume, mainly due to baroclinic and gravitational torque, has been presented.

The comparisons to experimental data reveal that for the near-field region of the plume, overall best agreement is obtained with the use of a SGS model. The puffing frequency, the mean and rms values of the velocity components obtained with FireFOAM are in very good agreement with the experiments. Agreement for the helium mass fraction (mean and rms) is less satisfactory, but in line with previously published results [14, 18].

The sensitivity analysis on the Smagorinsky constant, c_s, shows that $c_s = 0.1$ is a good choice. The fine mesh resolution has been shown to be such that the results do not depend strongly on the actual value of the Smagorinsky constant ($c_s = 0.1 - 0.2$). These observations contradict the conclusion in [18] that the use of a SGS model would not exhibit good predictions for the case at hand. The conclusions of the present study are in line with [14]. The impact of the turbulent Schmidt number, Sc_t, in the diffusion flux is very small.

Overall, the quality of the results is very satisfactory when compared to results previously published in the literature [14, 18] with other CFD packages, which is encouraging for the application of FireFOAM to study the effect of differential diffusion in numerical simulations of reactive flows.

Chapter 5

Non-reacting, turbulent jets of H_2/CO_2 mixing with air

5.1 Introduction

Before applying the newly proposed methodology to study the effects of differential diffusion in reactive flows, first a numerical study of the influence of differential diffusion in non-reacting turbulent jets is presented.

The goal of this study is two-fold: First, to model the effects of differential diffusion in the mixing of non-reacting turbulent jets and to quantify the relative influence of these effects, at various downstream locations, with increasing Reynolds numbers. Second, to examine the validity of the typical assumption made in turbulent flows of neglecting differential diffusion effects and to investigate any potential implications of this assumption in turbulent reacting flows. We consider in this work non-reacting jets, in order to avoid uncertainties due to combustion modelling. In concreto, we perform various large eddy simulations (LES) of a non-reacting turbulent H_2/CO_2 jets mixing with air and compare the simulation results with the experiments of Smith et al. [106]. Contrary to the helium plume test case, previously presented in Chapter 4, which was a buoyancy driven flow, the present study is a jet configuration which is a momentum driven flow.

The current numerical study is inspired by this experimental work of Smith et al. [106] for the following reasons. First of all, it is a jet configuration, which is a representative configuration for practical flames. Secondly, the H_2 concentration in the mixture (36% by volume) is high, so that the effects of differential diffusion can be easily identified. Third, the experiments were performed for a wide range of Reynolds numbers, spanning from very low ($Re = 1000$) to really high ($Re = 64000$), providing this way a clear relationship between differential diffusion and increasing Reynolds number. To the authors' best knowledge no other numerical studies on this experimental case have appeared in the literature. However, the amount of experimental data reported is limited (no velocity field measurements or species concentrations in physical space were reported) and the comparison with the simulation results will be made to the degree that this is possible. Contrary to previous studies, the influence of differential diffusion will be examined over a wide range of downstream locations from the inlet ($y/d = 5, 15, 30$) and for a wide range of Reynolds numbers ($Re = 1000 - 8000$). It is worth to note that many previous studies have not examined the influence of differential diffusion close to the inlet for moderate Reynolds numbers. In addition, there are not many other LES studies, in total, reporting on the influence of differential diffusion, where numerical results have been presented with and without differential diffusion effects.

Several experimental and numerical papers studying the effects of differential diffusion in non-reacting cases exist. Kerstein et al [48] performed one-dimensional measurements of differential diffusion in a hydrogen-freon jet at $Re = 20000$ while Dibble and Long [19] reported two-dimensional measurements of differential diffusion of the same flow. Bilger and Dibble [5] performed experiments in a non-reacting hydrogen-propane jet flowing into air. Long et al. [58] presented a different approach, compared to Bilger and Dibble, to study differential diffusion using Planar Laser Induced Fluorescence (PLIF) and Lorenz-Mie scattering techniques. Lavertu et al. [56] studied the effects of differential diffusion in high Schmidt number jets and Saylor and Sreenivasan [100] on low Reynolds number water jets. Several experimental studies exist on the dependence of differential diffusion on Reynolds number [106, 47], while direct numerical simulations (DNS) studying differential diffusion in isotropic turbulence have also been reported [116, 130, 128, 53, 76, 129, 25, 131, 41].

5.2 Experimental set-up

The experiments conducted in the Turbulent Diffusion Flames (TDF) laboratory at Sandia National Laboratories and reported by Smith et al. [106], are considered here. The case consists of a non-reacting turbulent jets of 36% H_2 and 64% CO_2 (by volume), issued into air from a round tube with inner diameter $d = 7.7$ mm. The tube was placed at the exit of a wind tunnel, which provided a co-flow of air at 1.5 m/s. The jet exit velocities varied from 1.7 m/s to 108 m/s, resulting in a range of jet Reynolds numbers of 1000 to 64000. The tube had sufficient length to produce a fully developed laminar or turbulent velocity profile at the exit. Measurements were made at 15, 30 and 60 pipe diameters downstream of the jet exit.

5.3 Mathematical formulation

5.3.1 Governing equations

A modified version of FireFOAM 1.6 [36] is used in this numerical study. The modifications made in the original implementation of FireFOAM 1.6 include:

- Elimination of enthalpy equation.
- Replacement of mixture fraction equation by transport equations for chemical species.
- Calculation of mixture viscosity as a linear combination of the species viscosities instead of being constant or temperature dependant.
- Calculation of mixture density as a linear combination of the species densities instead of using the ideal gas law.
- Calculation of species total diffusion velocities from Hirschfelder - Curtis formula instead of Fick's law.
- Calculation of species mass diffusion coefficients from Stefan's zero-th order expression instead of assuming constant species Schmidt numbers.

The code now solves the conservation equations for mass and momentum, along with transport equations for species mass fractions for a non-reacting, isothermal system. The set of governing equations needed for the numerical simulations is then:

$$\frac{\partial\overline{\rho}}{\partial t}+\frac{\partial(\overline{\rho}\widetilde{u}_i)}{\partial x_i}=0 \tag{5.1}$$

$$\frac{\partial(\overline{\rho}\widetilde{u}_j)}{\partial t}+\frac{\partial(\overline{\rho}\widetilde{u}_i\widetilde{u}_j)}{\partial x_i}=-\frac{\partial\overline{p}}{\partial x_j}+\frac{\partial}{\partial x_i}\left[(\mu+\mu_t)\left(\frac{\partial\widetilde{u}_i}{\partial x_j}+\frac{\partial\widetilde{u}_j}{\partial x_i}\right)\right]+\overline{\rho}g_j, \qquad j=1,2,3 \tag{5.2}$$

$$\frac{\partial(\overline{\rho}\widetilde{Y}_k)}{\partial t}+\frac{\partial(\overline{\rho}\widetilde{u}_i\widetilde{Y}_k)}{\partial x_i}=\frac{\partial}{\partial x_i}\left[\left(\overline{\rho}D_k+\frac{\mu_t}{Sc_t}\right)\frac{\partial\widetilde{Y}_k}{\partial x_i}\right], \qquad k=1,...,N_s \tag{5.3}$$

The laminar viscosity of the mixture, μ, is calculated as a linear function of the species individual viscosities:

$$\mu = \sum \mu_k \overline{X}_k \tag{5.4}$$

where μ_k and $\overline{X}_k$ are the species laminar viscosity and the filtered species mole fraction, respectively.

The diffusion velocities of species are approximated by the Hirschfelder and Curtis formula (Eq 2.13) for a multicomponent mixture, with a correction velocity to ensure mass conservation [29]. The species mass diffusion coefficients, D_k, are calculated by the zero-th order expression proposed by Stefan (Eq 2.14), with the species binary diffusion coefficients, D_{kl}, calculated by kinetic theory [110].

The filtered density of the mixture, $\overline{\rho}$, is calculated as a linear function of the individual species densities as:

$$\overline{\rho} = \sum \rho_k \overline{X}_k \tag{5.5}$$

where ρ_k is the species density, calculated by the ideal gas law.

5.3.2 Turbulence modelling

The standard Smagorinsky model [104] is used as a turbulence model with a Smagorinsky constant of $c_s = 0.1$ [132]. The un-resolved sub-grid scale species fluxes are modeled by the gradient diffusion hypothesis model, assuming a constant turbulent Schmidt number of $Sc_t = 0.5$ [14]. A sensitivity study on this value ($Sc_t = 0.5, 0.7, 1.0$), not shown here, did not reveal any significant influence of this parameter on the simulation results (maximum deviation of less than 4% in the maximum value of the species mole fractions).

5.4 Numerical set-up

The simulations are performed on a cylindrical mesh, $10d \times 35d$, with a rectangular grid in the central region (2 mm × 2 mm). The inflow of the H_2/CO_2 mixture is located in the center of the bottom plane. The grid resolution for the inlet patch is set to 8 × 8 cells (rectangular) and 8 × 32 (cylindrical), resulting in 24 cells across the inlet. Outside the inlet patch, 55 cells were used radially (compressed towards the inlet). In the axial direction 400 cells are used. The total number of cells is then 0.832 million cells, resulting in a minimum and maximum grid spacing of 0.32 mm and 1.73 mm.

A fixed inlet velocity is applied to the inlet patch, according to the average inlet Reynolds number reported in the experiments. In the simulations, only the range $u_{inlet} = 1.7 - 13.6$ m/s ($Re = 1000 - 8000$) is considered (since differential diffusion effects become small for high Re numbers (see below)). In the bottom plane of the domain ($y = 0$ m) outside the tube, a fixed streamwise co-flow velocity $u_{co-flow} = 1.5$ m/s is imposed. The thickness of the tube is negligible. A Neumann boundary condition (zeroGradient) is assigned for velocity at the sides of the domain and a Dirichlet boundary condition (totalPressure) for pressure. For the top (outlet) plane a mixed boundary condition (inletOutlet) is used for velocity and a Neumann boundary condition (zeroGradient) for pressure. The inlet boundary conditions for the mass fractions of H_2 and CO_2 are of Dirichlet type and set to uniform values (fixedValue).

In order to reproduce the break up of the jet core reported in the experiments, turbulence must be generated at the inlet. In this case, the axial inlet velocity component is excited with azimuthal forcing of the form proposed by Menon and Rizk [68]:

$$u' = Au_{inlet} \sum_{n=1}^{N} sin(2\pi ft/n + \theta) \tag{5.6}$$

where A is the amplitude of forcing, N is the number of modes (set to 6), t is the time and θ the polar azimuthal angle. The frequency, f, is calculated from a corresponding Strouhal number of 0.3 [132]. In the present simulations a relatively high level of forcing is used with an amplitude of 20% of the mean axial velocity. No forcing is applied to the other two velocity components. This method has already been used in previous numerical studies of turbulent jets [132].

The governing equations are advanced in time using a second order implicit ‘backward’ scheme. A variable time step is used in the simulations, setting the maximum Courant number to $Co = 0.3$. The convective terms are second order centrally differenced using ‘Gauss linear’ interpolation. For scalar transport, the bounded second order TVD scheme ‘limitedLinear’ is used, while the diffusive terms are centrally differenced and corrected for the non-orthogonality of the mesh with ‘Gauss linear corrected’. Data are collected when statistically-steady flow conditions have been reached in every case.

At every point in the domain, the composition of the gas phase corresponds to a mixture of H_2, CO_2, O_2 and N_2 with corresponding molecular weights of $W_{H_2} = 2.016$ g/mol, $W_{CO_2} = 44.01$ g/mol, $W_{O_2} = 32.0$ g/mol and $W_{N_2} = 28.013$ g/mol, respectively. Ambient (inlet) temperature and pressure are 300 K and 101325 Pa. Effects of buoyancy are negligible as the resulting Froude number, shown in Table 5.1, is much higher than unity for all test cases.

Table 5.1: Flow parameters at the inlet

d (m)	u_{inlet} (m/s)	$u_{co-flow}$ (m/s)	$Re = \frac{\rho u d}{\mu}$	$Fr = \frac{\rho u^2}{\Delta \rho g d}$
0.0077	1.7 - 13.6	1.5	1000 - 8000	26 - 1685

5.5 Results

5.5.1 Instantaneous results

In order to give a first global impression, Figures 5.1 - 5.2 present instantaneous plots of mole fractions of H_2 for Reynolds numbers $Re = 1000 - 8000$ with and without equal species diffusivities. A clear evolution of the flow field from laminar ($Re = 1000 - 2000$), to transition to turbulent ($Re = 4000$) to fully turbulent ($Re = 8000$) with increasing Re is observed (left to right). Larger X_{H_2} are evident, on the centerline and close to the inlet, in the case of equal species diffusivities for the lower Reynolds number cases, $Re = 1000 - 2000$, indicating that molecular diffusion is more important in these cases. As the Reynolds number increases ($Re = 4000 - 8000$), however, turbulent mixing becomes dominant. In addition, a 'puffing' behavior is evident for the lower Reynolds number cases ($Re = 1000 - 2000$) due to the azimuthal forcing prescribed at the inlet (Eq. 5.6).

In order to have a quantitative measurement of differential diffusion, a differential diffusion parameter, ξ, is calculated as:

$$\xi = \frac{X_{H_2} - X_{H_{2O}}}{X_{H_{2F}} - X_{H_{2O}}} - \frac{X_{CO_2} - X_{CO_{2O}}}{X_{CO_{2F}} - X_{CO_{2O}}} = \frac{X_{H_2}}{X_{H_{2F}}} - \frac{X_{CO_2}}{X_{CO_{2F}}} \tag{5.7}$$

where $X_{H_{2F}}$ and $X_{CO_{2F}}$ are the 'fuel' stream mole fractions of H_2 and CO_2, and $X_{H_{2O}}$ and $X_{CO_{2O}}$ are the 'oxidizer' stream mole fractions of H_2 and CO_2, here to be taken zero. This definition of ξ, inspired by Bilger and Dibble [5] and Kerstein et al. [46], takes on non-zero values only when the X_{H_2}/X_{CO_2} ratio differs from its initial 'fuel' stream value. Other methods to quantify differential diffusion effects exist in the literature [53, 111], but for this test case we adopt the one that was used by Smith et al. [106] so that the comparison with the experimental data is consistent.

Figure 5.3 presents instantaneous plots of the ξ field for $Re = 1000 - 8000$ (left to

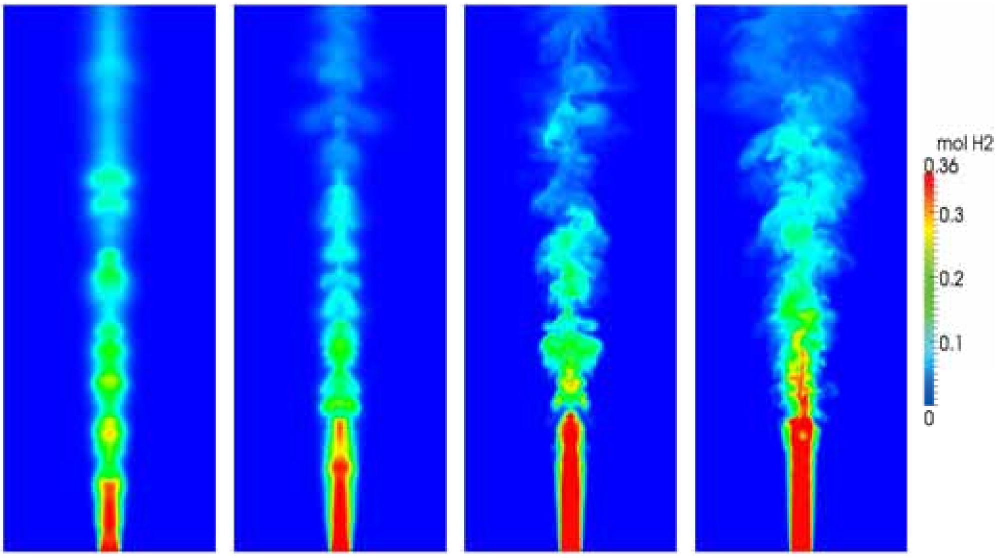

(a) (b) (c) (d)

Figure 5.1: Plots of instantaneous X_{H_2} in a symmetry plane for (a) $Re = 1000$, (b) $Re = 2000$, (c) $Re = 4000$ and (d) $Re = 8000$ with different diffusivities.

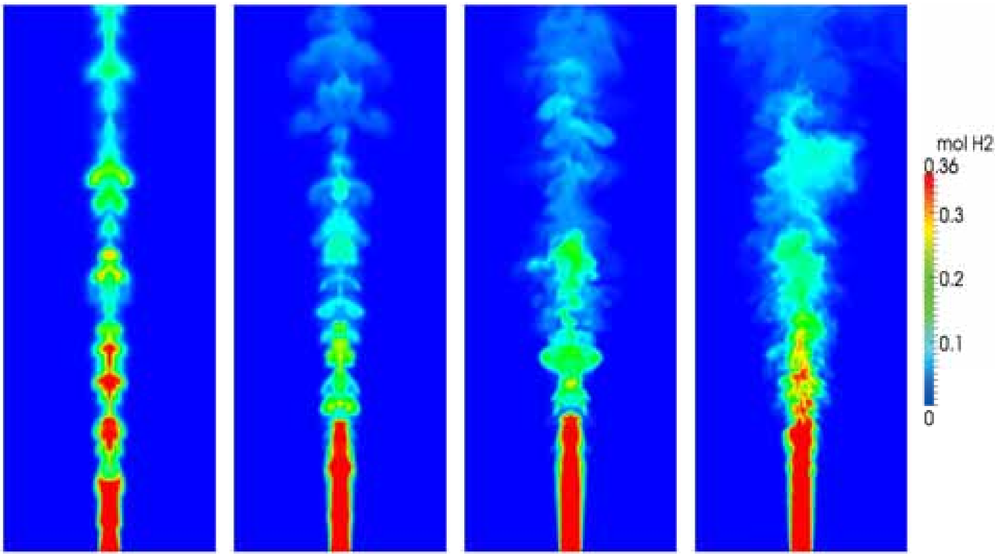

(a) (b) (c) (d)

Figure 5.2: Plots of instantaneous X_{H_2} in a symmetry plane for (a) $Re = 1000$, (b) $Re = 2000$, (c) $Re = 4000$ and (d) $Re = 8000$ with equal diffusivities.

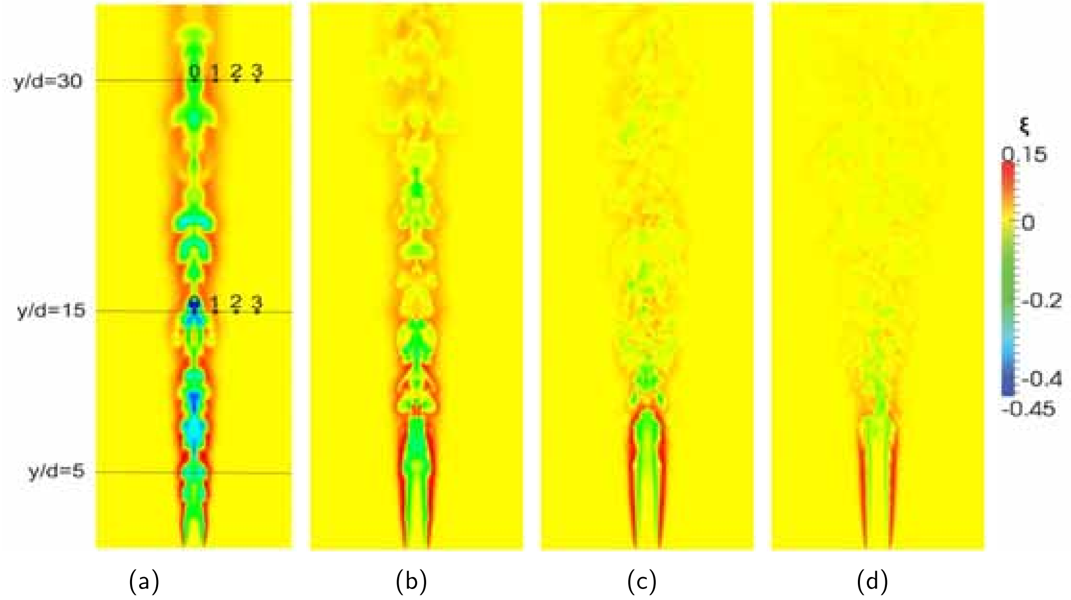

Figure 5.3: Instantaneous plots of the differential diffusion parameter, ξ (Eq. 5.7), for (a) $Re = 1000$, (b) $Re = 2000$, (c) $Re = 4000$ and (d) $Re = 8000$. Locations $y/d = 5, 15, 30$ and radial distances $r/d = 0, 1, 2, 3$ are indicated.

right). Clearly, differential diffusion effects become significantly smaller with increasing Reynolds number at downstream locations ($y/d > 15$). However, close to the inlet ($y/d < 10$) differential diffusion effects, remain present at the edge of the jet for all Reynolds number cases. A more detailed analysis is presented below.

5.5.2 Scatter plots

Figure 5.4 presents scatter plots of instantaneous X_{H_2} and X_{CO_2}, normalized by their inlet value, at location $y/d = 30$ for Reynolds numbers $Re = 1000 - 8000$. Data from various radial locations have been used. The diagonal line represents the line of equal mixing, i.e. the line where the data points are when all species have the same mass diffusivity. The dispersion of points is clearly much wider for the lower Reynolds numbers. The points cluster around the equal diffusivity mixing line as Re is increasing, in line with the observations reported by Smith et al. [106] (Figure 5.5). For $Re = 1000$, Figure 5.4(a), many points are observed both above and below the line of equal mixing. The points above the equal mixing line are located in off-axis locations and are due to the faster diffusivity of H_2 from the central part of the jet towards to the outer edge. The points observed underneath the line of equal mixing are located around the jet axis, where X_{CO_2}

are relatively larger. For $Re = 2000$, Figure 5.4(b), the points cluster more around the line of equal mixing and the spreading of the jet increases (more blue points are visible). Even though there are still points both above and below the line of equal mixing, the effect of differential diffusion has significantly decreased. For higher Reynolds numbers, Figures 5.4(c) - 5.4(d), the points follow the line of equal mixing closely. In this case, turbulent mixing is far more dominant than molecular diffusion. The range of values slightly increases with Re, since more mixture is injected, and thus higher concentrations are observed.

5.5.3 Results for mean quantities

Figures 5.6 - 5.9 present the mean X_{CO_2} and X_{H_2} for Reynolds numbers $Re = 1000 - 8000$ at locations $y/d = 15, 30$ with and without equal species diffusivities. It is observed that with the equal diffusivity assumption, the X_{H_2} are about 50% larger than if differential diffusion effects were taken into account for the cases with $Re = 1000$ at locations $y/d = 15, 30$ (Figures 5.6(b) - 5.8(b), respectively). This is indeed expected since, in this case, the diffusivity of H_2 is much less than its actual value. For the rest of the test cases the differences remain relatively small.

The mean X_{H_2} vs X_{CO_2}, normalized by their inlet value, at locations $y/d = 5, 15, 30$ are plotted in Figure 5.10 for Reynolds numbers $Re = 1000 - 8000$. The experimental data are also given for the $Re = 1000 - 2000$ cases since the effects of differential diffusion are more clearly evident at the lower Reynolds number cases. A curved line is seen for $Re = 1000$, indicating the case where the effects of differential diffusion are mostly evident. As the jet fluid is convected downstream, it is diluted with air and the concentration decreases. Due to differential diffusion effects, H_2, diffuses faster than CO_2, and the ratio of X_{H_2}/X_{CO_2} on the centerline of the jet decreases. This is seen as results below the equal diffusivity mixing line in Figure 5.10. The opposite is seen for large distances from the axis. For obvious reasons, such effects are completely missed if equal diffusivity is assumed for all species in the simulations. The agreement with the experimental data is overall satisfactory, however, for the case with $Re = 1000$ at location $y/d = 15$, both X_{H_2} and X_{CO_2} are somewhat under-predicted.

A clearer indication of the behavior of the X_{H_2}/X_{CO_2}ratio in locations with lower jet fluid concentrations is given in Figure 5.11.Indeed, as the X_{H_2} and X_{CO_2} tend to zero, it is better to plot the ratio of X_{CO_2}/X_{H_2} against X_{CO_2}. In this case, equal diffusivities of CO_2 and H_2 produce a horizontal line. However, for all Reynolds numbers the averaged results drop below the line of equal mixing for small X_{CO_2}. This occurs near the interface of the

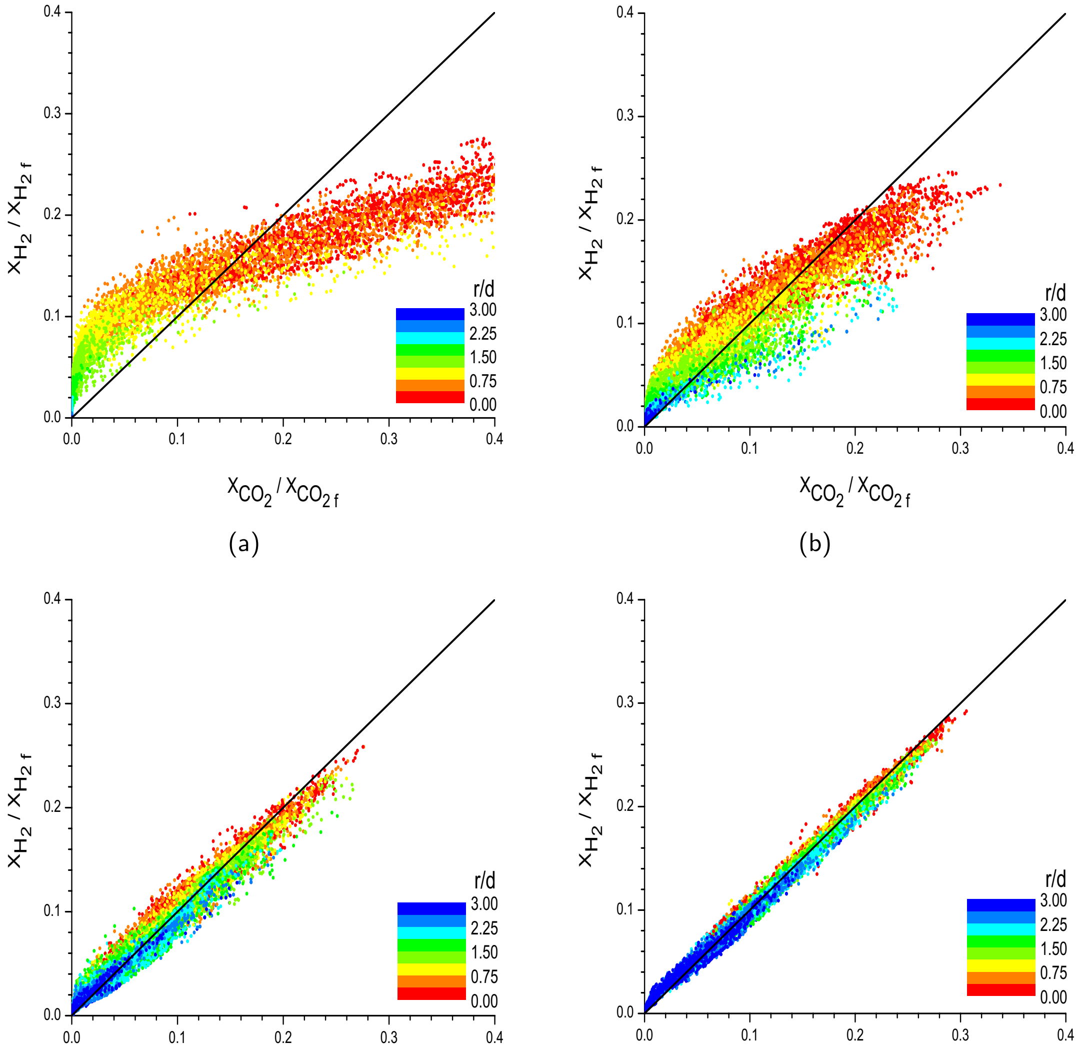

(a) (b) (c) (d)

Figure 5.4: Scatter plots of instantaneous X_{H_2} vs X_{CO_2}, normalized by their inlet value, at location $y/d = 30$ for (a) $Re = 1000$, (b) $Re = 2000$, (c) $Re = 4000$ and (d) $Re = 8000$.

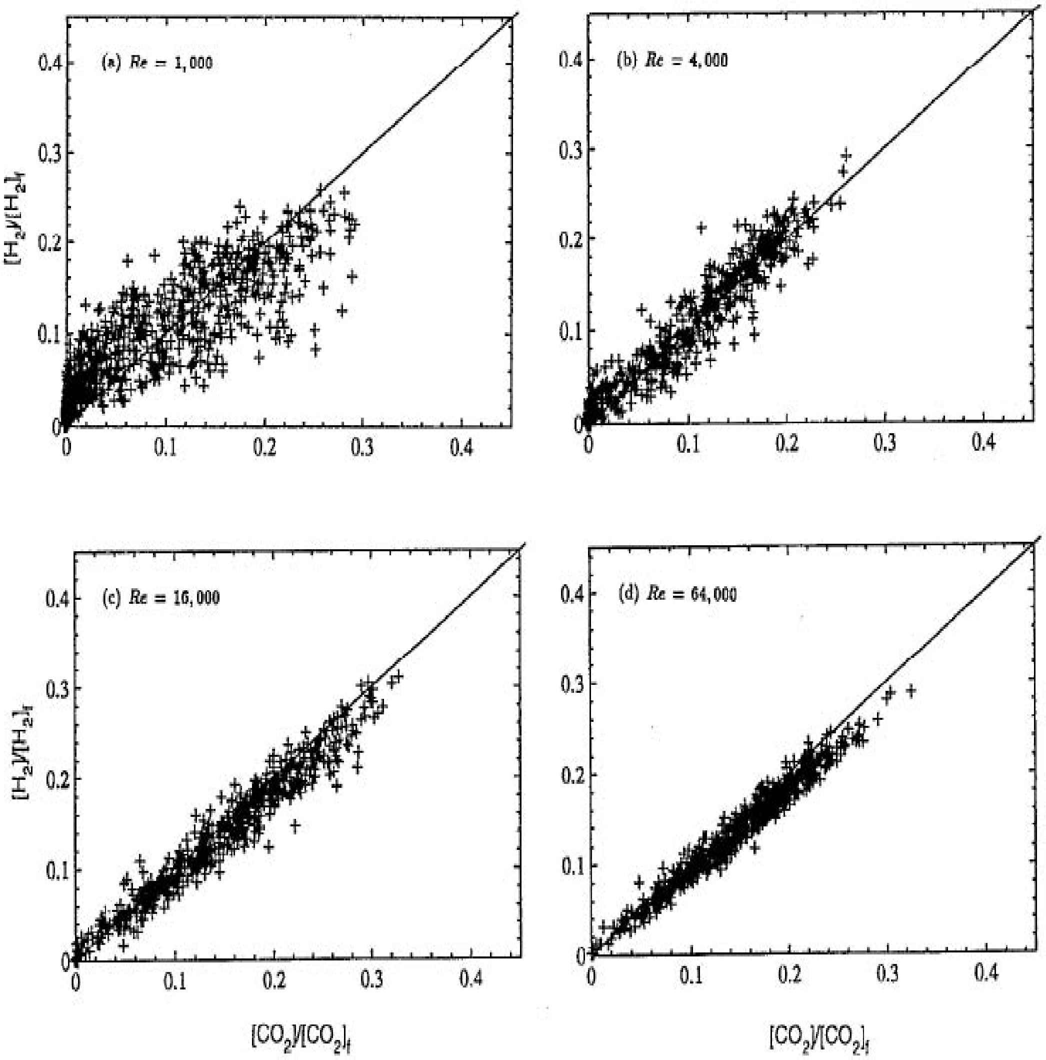

Figure 5.5: Scatter plots of instantaneous X_{H_2} vs X_{CO_2}, normalized by their inlet value, at location $y/d = 30$ for (a) $Re = 1000$, (b) $Re = 4000$, (c) $Re = 16000$ and (d) $Re = 64000$ as reported by Smith et al. [106].

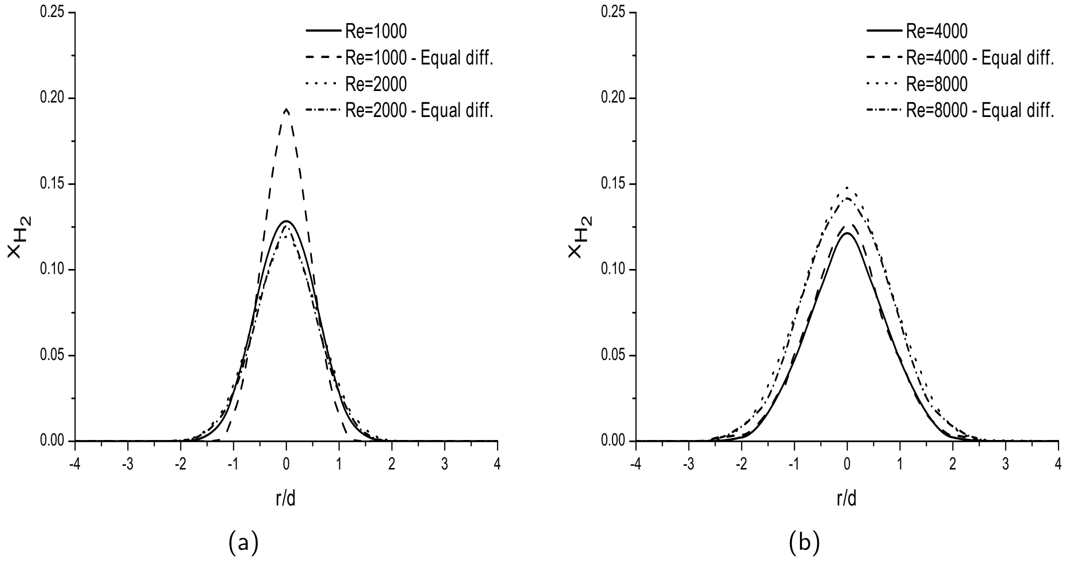

(a) (b)

Figure 5.6: Mean X_{H_2} at location $y/D = 15$ for (a) $Re = 1000 - 2000$ and (b) $Re = 4000 - 8000$

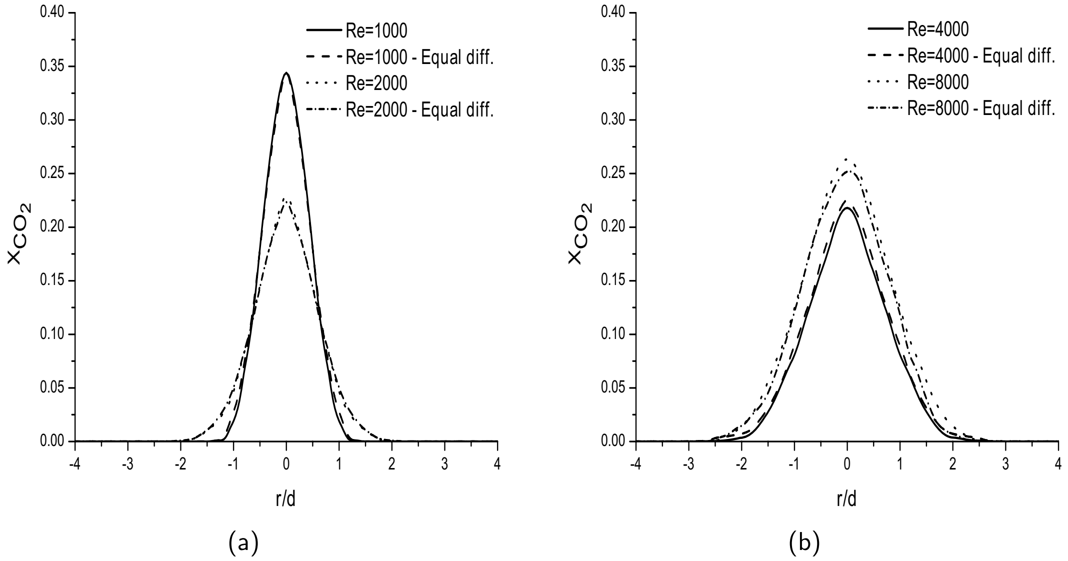

(a) (b)

Figure 5.7: Mean X_{CO_2} at location $y/D = 15$ for (a) $Re = 1000 - 2000$ and (b) $Re = 4000 - 8000$

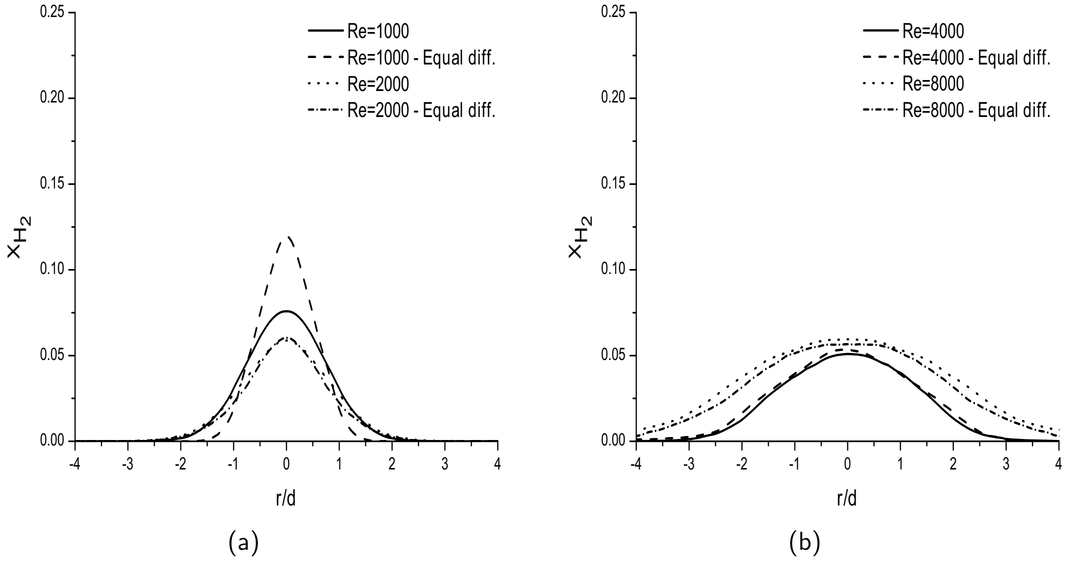

Figure 5.8: Mean X_{H_2} at location $y/D = 30$ for (a) $Re = 1000 - 2000$ and (b) $Re = 4000 - 8000$

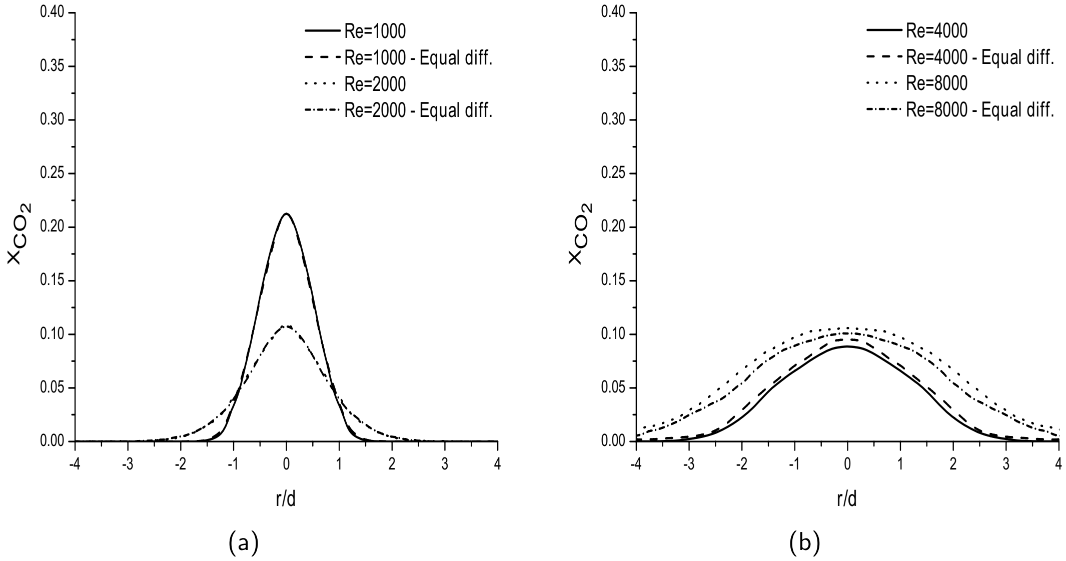

Figure 5.9: Mean X_{CO_2} at location $y/D = 30$ for (a) $Re = 1000 - 2000$ and (b) $Re = 4000 - 8000$

jet fluid and the co-flowing air, where H_2, diffuses outside the jet faster than CO_2.

The averaged results of the differential diffusion parameter, ξ, for Reynolds numbers $Re = 1000-8000$ at locations $y/d = 5, 15, 30$ are presented in Figure 5.12. Effects of differential diffusion are confirmed for the lower Reynolds number cases ($Re = 1000-2000$) at locations $y/d = 15, 30$. The faster diffusion of H_2 from the core of the jet to the edge creates large negative values of ξ on the centerline ($y/d = 0$). Moving radially outwards, there is more H_2 than CO_2, which creates positive ξ values with a maximum peak around $y/d = 1$. For the higher Reynolds number cases the absolute values of ξ are relatively small. However, close to the inlet (Figure 5.12(c)), significant differential diffusion effects are present for all Reynolds number cases ($Re = 1000-8000$).

5.5.4 Histograms

in this section, histograms of the differential diffusion parameter, ξ, are presented for various downstream and radial positions. The histograms have been built by monitoring ξ for a period of 1 sec (200 samples) at locations ± 0.0025 m of the one considered. For the lower Reynolds number range ($Re = 1000-2000$), histograms only for $Re = 2000$ were reported by Smith et al. [106]. For this reason histograms of the differential diffusion parameter, ξ, are presented only for this Reynolds number case.

Figure 5.13 presents histograms for $Re = 2000$ at location $y/d = 15$ and different radial positions. As the jet is convected downstream, H_2, being a much lighter specie, diffuses much faster than CO_2 from the centerline to the jet edge, creating this way mostly negative values of ξ on the centerline (Figure 5.13(a)). Moving radially outwards ($r/d = 1$) there is more H_2 than CO_2 and the negative range of ξ values decreases (Figure 5.13(b)). At distance $r/d = 2$ there is not a lot of H_2 and CO_2 present, thus the range of ξ values is centered around zero (Figure 5.13(c)). Similar observations apply for the histogram results at location $y/d = 30$ shown in Figure 5.14. At this location the jet is diluted even more with air and the H_2 and CO_2 concentrations are smaller than at $y/d = 15$, creating a smaller negative range of ξ values and shifting the histograms closer to zero with increasing radial distance.

In general, there is a relatively poor agreement between the simulation results (Figures 5.13-5.14) and the experimental results (Figures 5.15-5.16). The shape of the histograms from the simulations is negatively skewed in the centerline ($r/d = 0$) while the experimental ones are symmetric around zero. In addition, there is a difference of $r/d = 1$ in the radial location between the histograms obtained from the simulations and the ones

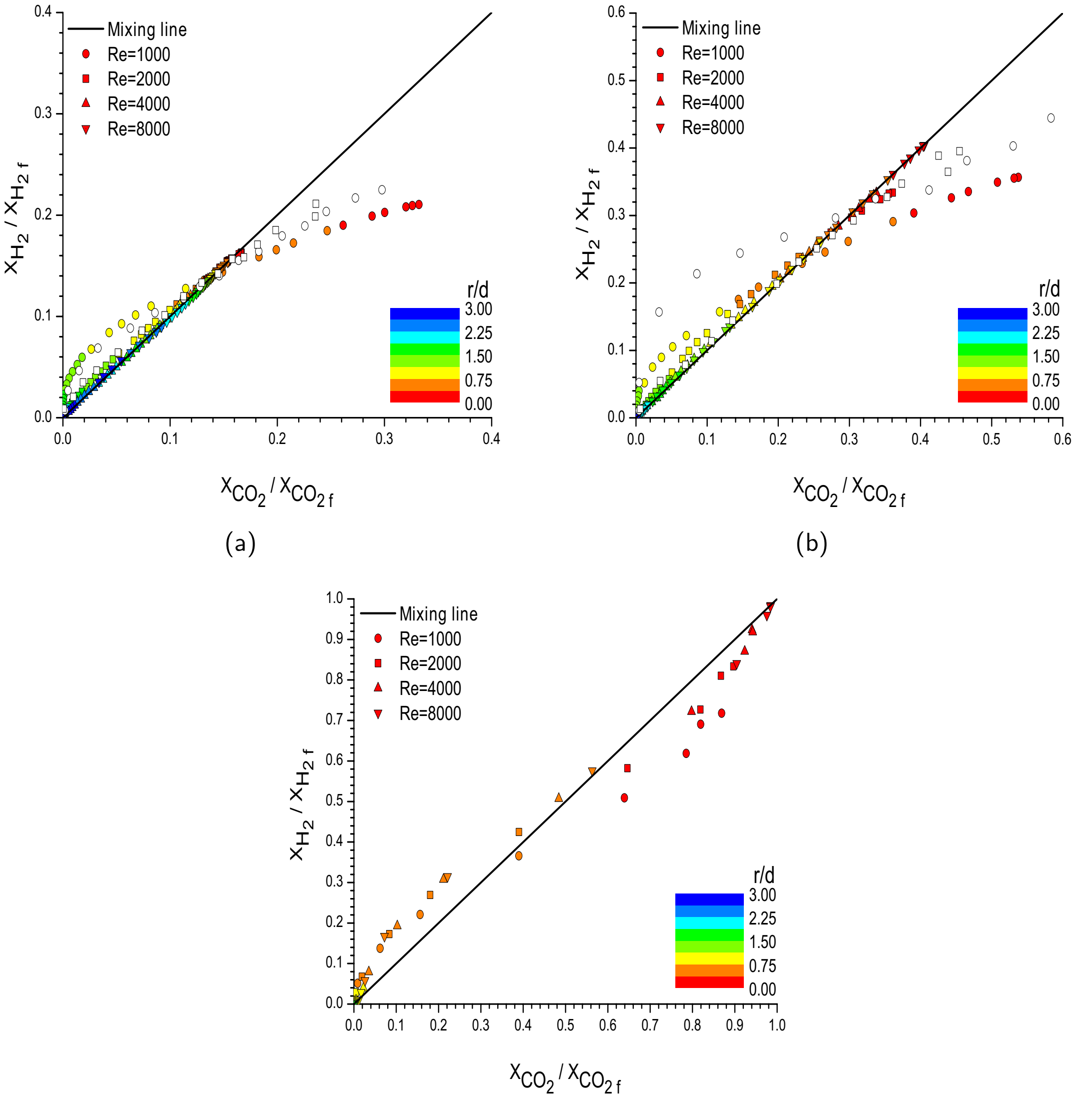

(a) (b)

(c)

Figure 5.10: Mean X_{H_2} vs X_{CO_2}, normalized by their inlet value, for Reynolds numbers $Re = 1000 - 8000$ at location (a) $y/d = 30$, (b) $y/d = 15$ and (c) $y/d = 5$. White symbols: experimental data.

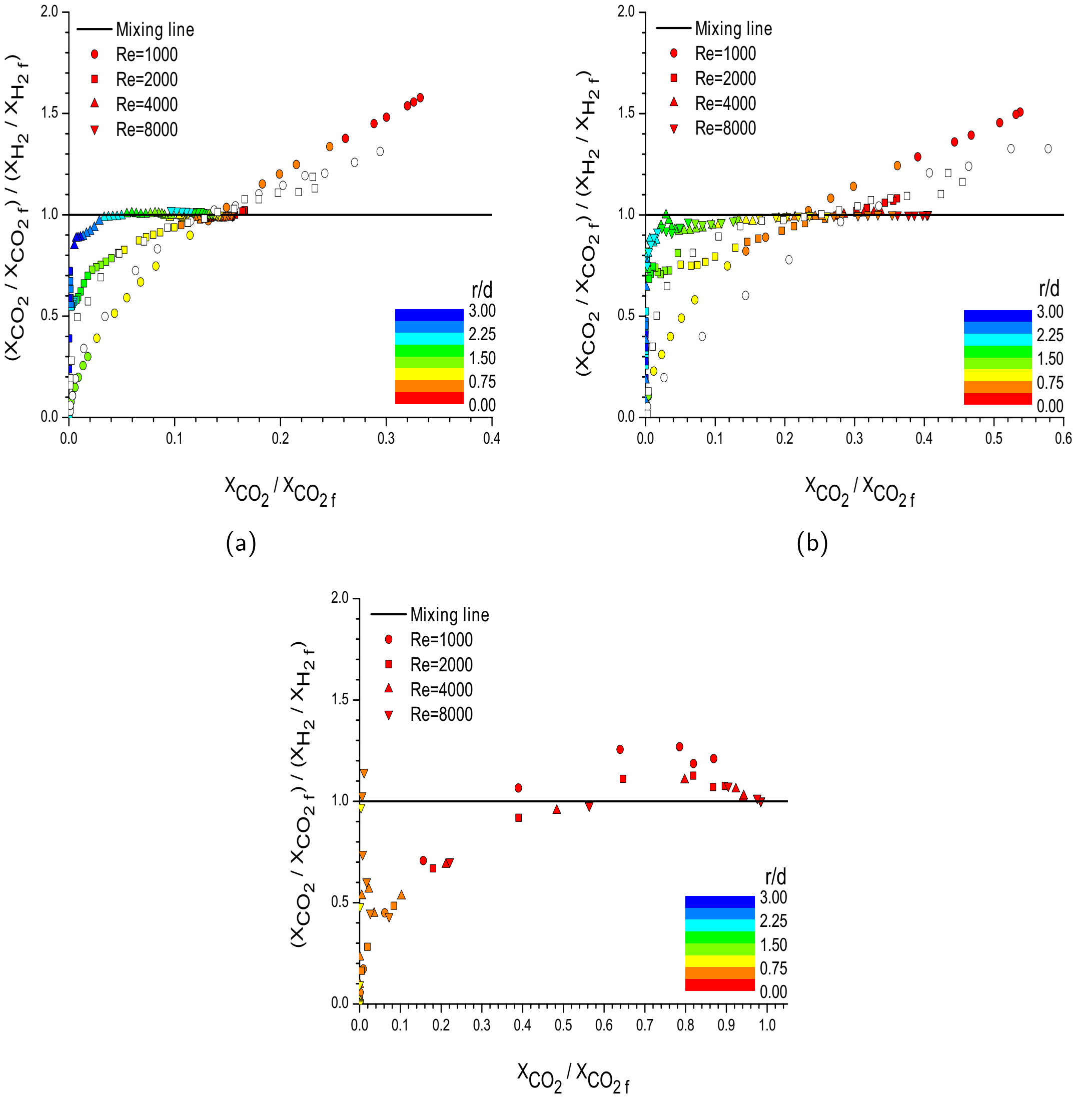

(a)

(b)

(c)

Figure 5.11: Mean X_{CO_2}/X_{H_2} vs X_{CO_2}, normalized by their inlet value, for Reynolds numbers $Re = 1000 - 8000$ at location (a) $y/d = 30$, (b) $y/d = 15$ and (c) $y/d = 5$. White symbols: experimental data.

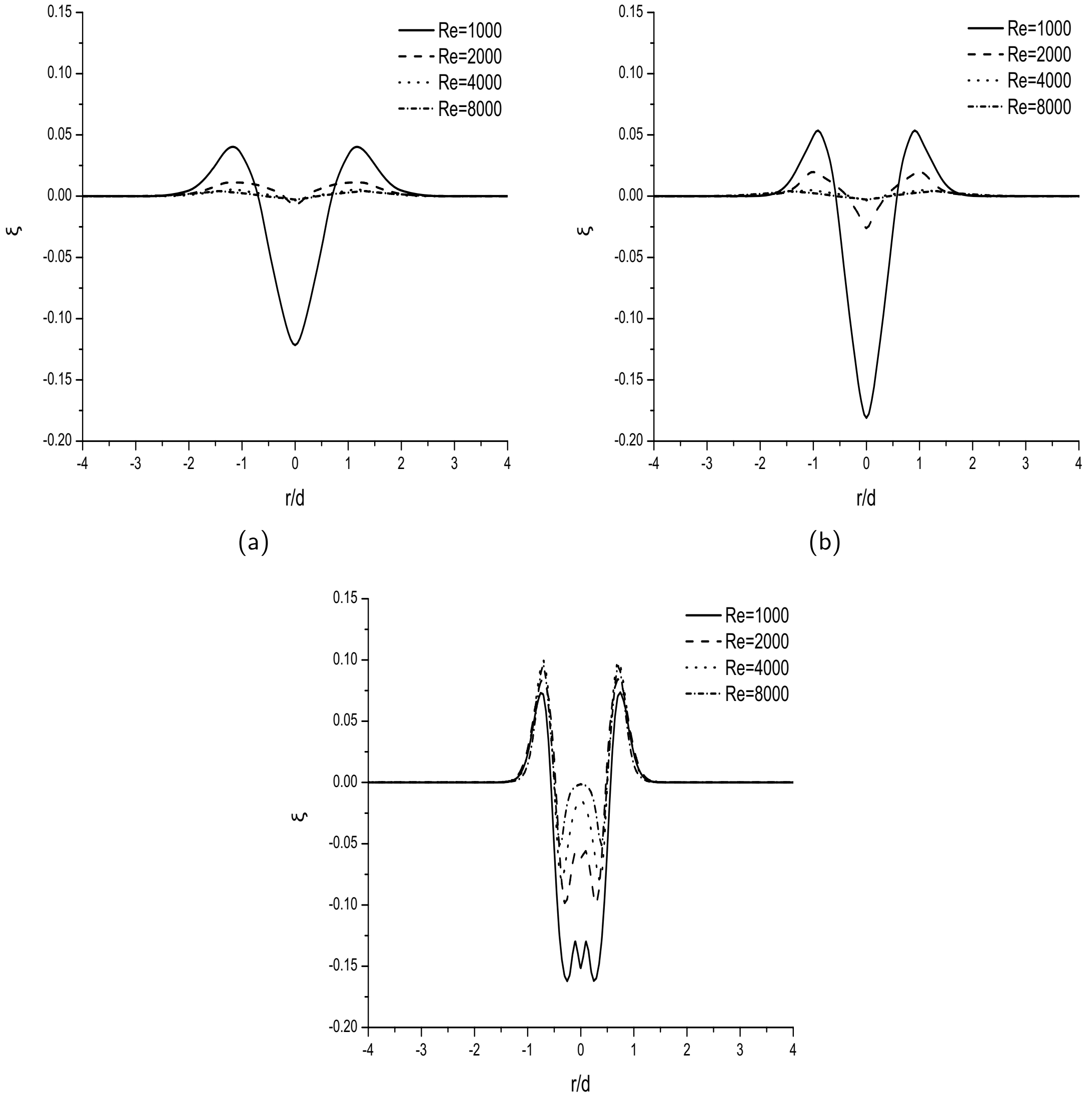

(a)

(b)

(c)

Figure 5.12: Mean differential diffusion parameter, ξ (Eq. 5.7), for $Re = 1000 - 8000$ at location (a) $y/D = 30$, (b) $y/D = 15$ and (c) $y/D = 5$.

reported in the experiments. This indicates that the spreading of the jet in the simulations is lower than in the experiments. It was verified that the main source of discrepancies is attributed to the inlet boundary condition used for generating turbulence. There are different parameters that influence the azimuthal forcing applied at the inlet, such as the frequency *f*, the amplitude *A* and the number of modes *N*. It is possible that with a fine tuning of these parameters, a better comparison between numerical simulations and experimental data can be achieved. However, even though this fine tuning can improve the numerical results quantitatively the main qualitative conclusions of this work will remain the same. It is for this reason that no further research was carried out in this area.

5.5.5 LES resolution

The ratio of turbulent to laminar viscosity, μ_t/μ, is shown in Figure 5.17. The maximum value of the ratio is 2, observed in the highest Reynolds number case considered ($Re = 8000$). Only in this Reynolds number case, the added sub-grid scale viscosity from the turbulence model is comparable to the molecular viscosity, indicating that the LES grid is fine enough to accurately simulate all the Renolds number cases examined.

The above conclusion is also confirmed by looking at the ratio of grid spacing, Δ, to Kolmogorov length scale, $\eta_K = (\frac{\nu^3}{\varepsilon})^{\frac{1}{4}}$, presented in Figure 5.18. According to Pope [**?**] the demarcation between the inertial and dissipation range for homogeneous isotropic turbulence is located at $k\eta \approx 0.1$ or $\Delta/\eta \approx 32$. Assuming that this criterion remains valid sufficiently far from boundaries, it is used in this work to study the LES resolution. The total dissipation rate is expressed as $\varepsilon = 2(\nu + \nu_t)\overline{S}_{ij}\overline{S}_{ij}$. For the lower Reynolds number cases ($Re = 1000 - 2000$) the ratio is less than 5 and goes up to 10 and 18 for the cases with $Re = 4000$ and $Re = 8000$, respectively. Therefore, the values obtained from the numerical simulations are within the dissipation range, implying a very well resolved LES calculation

5.6 Conclusions

In this study LES results of non-reacting jets of H_2/CO_2 mixing with air for Reynolds numbers $Re = 1000 - 8000$ have been presented and compared with the experiments reported by Smith et al. [106]. There is a fair agreement between the simulation results and the experimental data. The main source of discrepancies between the numerical simulations and the experimental results is attributed to the inlet boundary condition for generating turbulence. Tuning of the inlet boundary condition can potentially lead to better

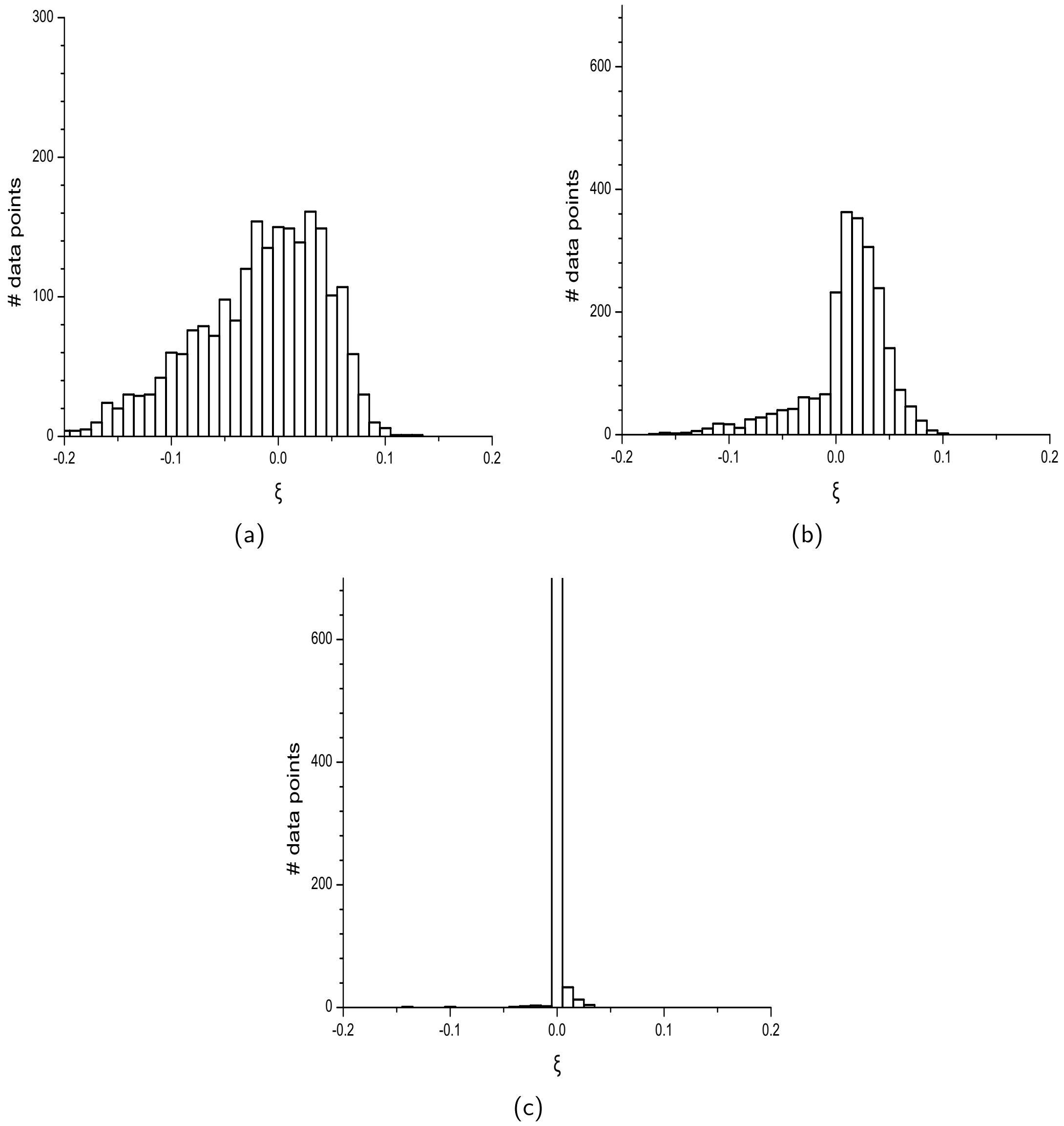

(a)

(b)

(c)

Figure 5.13: Histograms of ξ distribution for $Re = 2000$ at location $y/d = 15$ for (a) $r/d = 0$, (b) $r/d = 1$ and (c) $r/d = 2$.

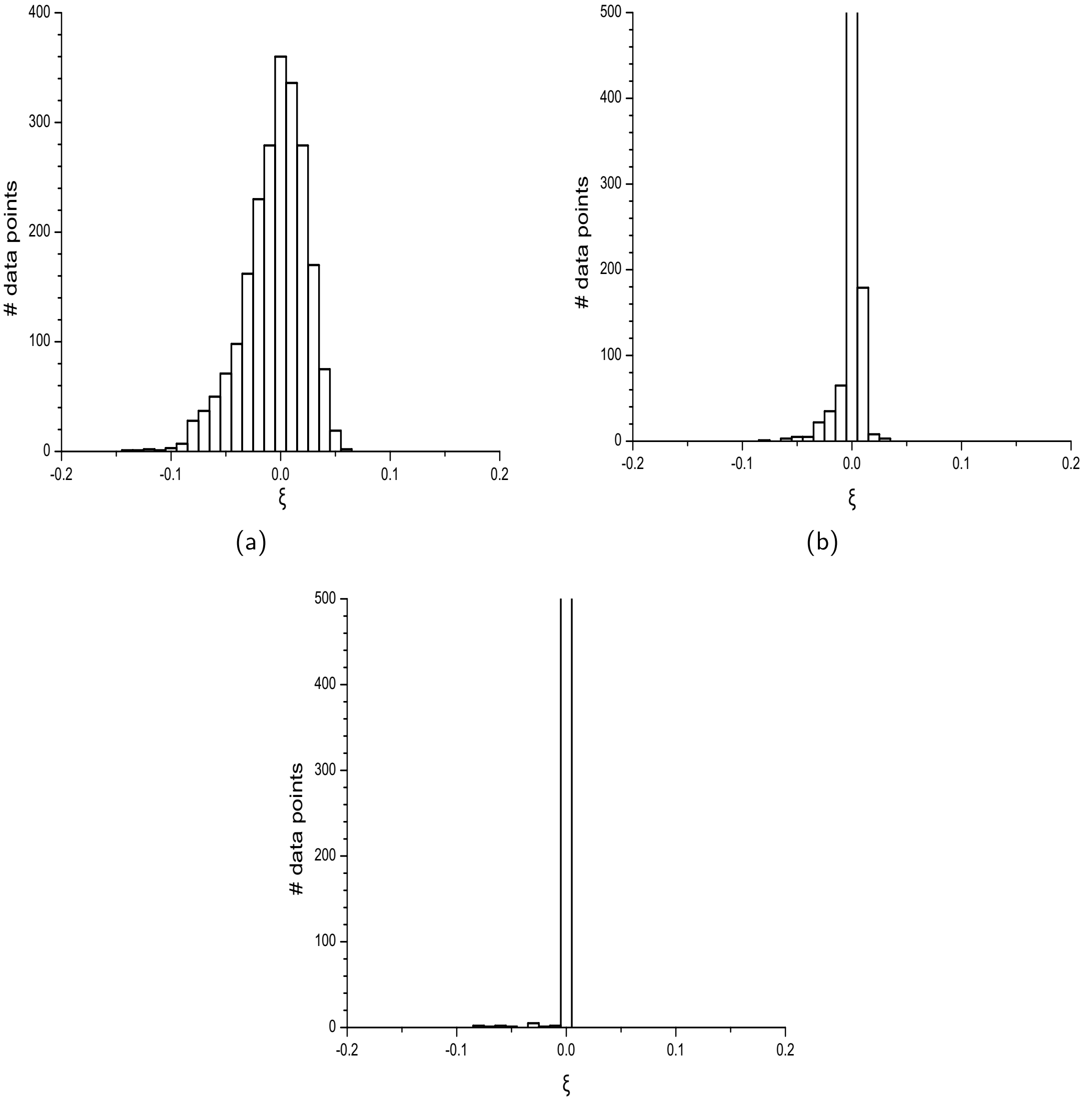

(a) (b)

(c)

Figure 5.14: Histograms of ξ distribution for $Re = 2000$ at location $y/d = 30$ for (a) $r/d = 0$, (b) $r/d = 2$ and (c) $r/d = 3$.

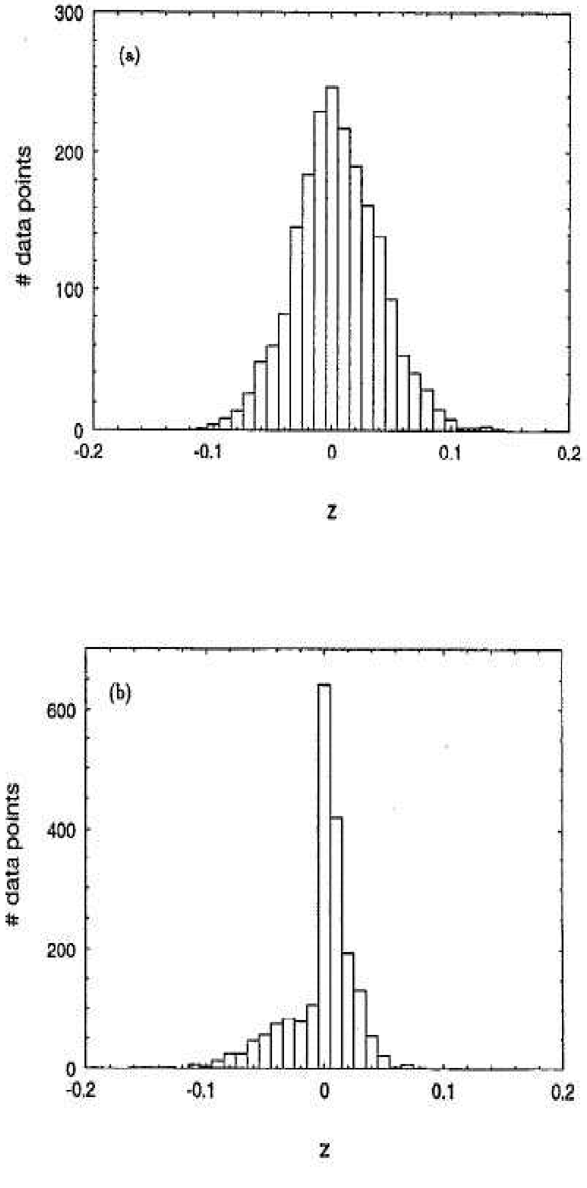

Figure 5.15: Histograms of ξ distribution for $Re = 2000$ at location $y/d = 15$ for (a) $r/d = 0$ and (b) $r/d = 2$ as reported by Smith et al. [106].

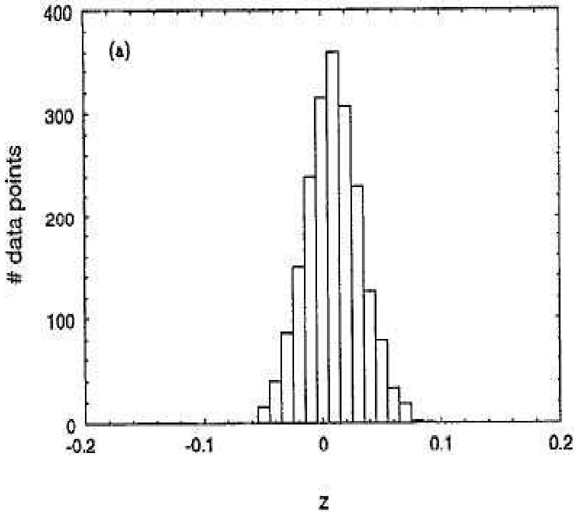

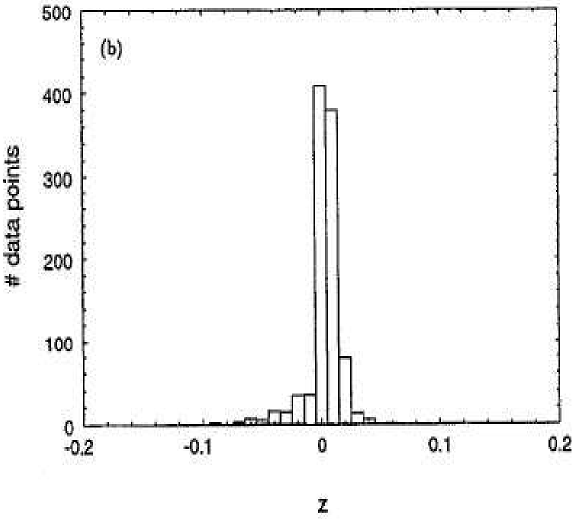

Figure 5.16: Histograms of ξ distribution for $Re = 2000$ at location $y/d = 15$ for (a) $r/d = 0$ and (b) $r/d = 3$ as reported by Smith et al. [106].

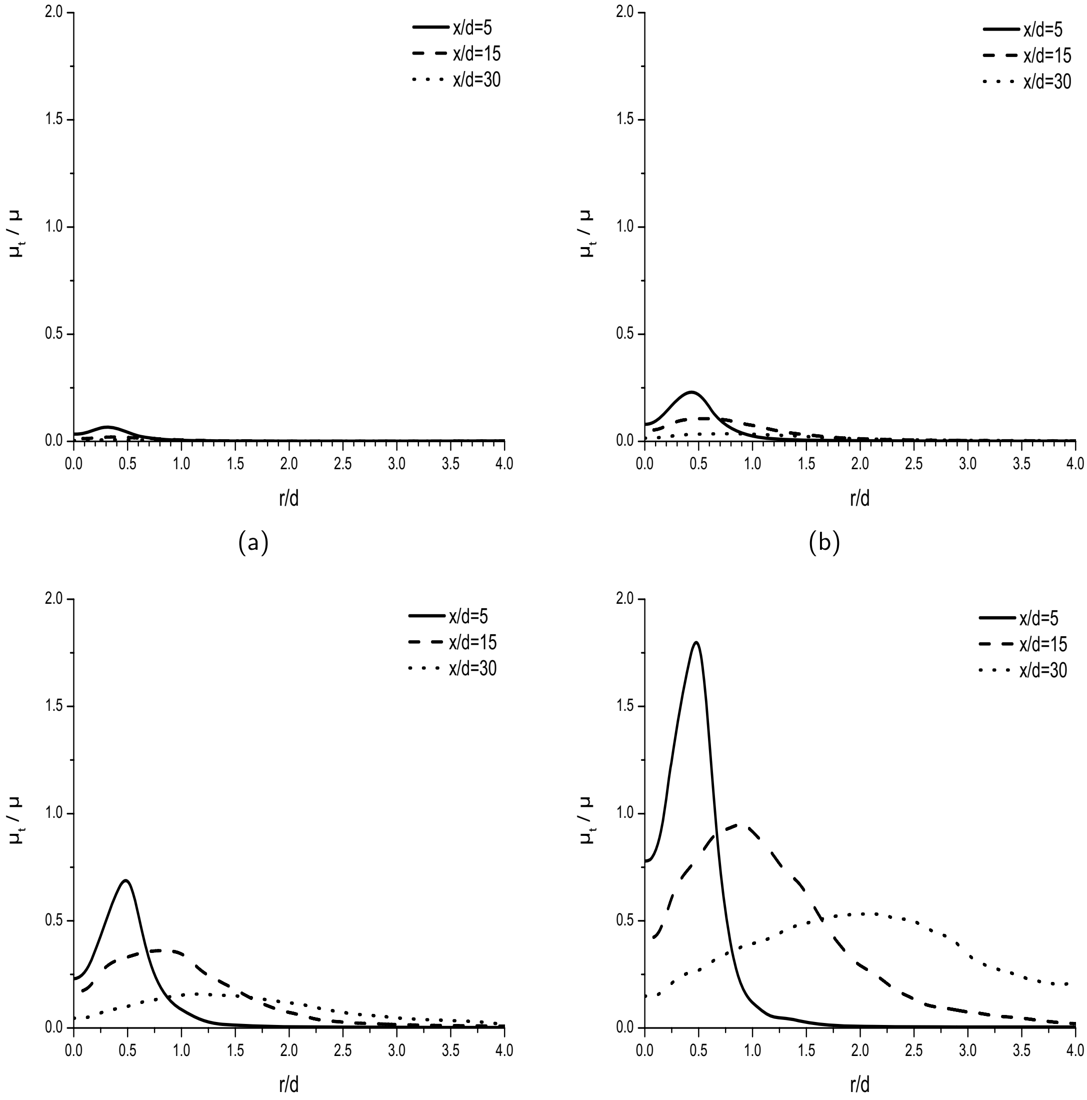

(a) (b) (c) (d)

Figure 5.17: Ratio of turbulent to laminar viscosity, μ_t/μ, for (a) $Re = 1000$, (b) $Re = 2000$, (c) $Re = 4000$ and (d) $Re = 8000$.

agreement with experiments, however, the main conclusions of this work will not change. The amount of experimental data reported was limited (no velocity field measurements or species concentrations were reported) and the comparison of the experimental data with the simulation results was made up to the degree that this was possible.

At locations far downstream $(y/d > 15)$ effects of differential diffusion are visible only for the lower Reynolds number cases ($Re = 1000 - 2000$). In this case the mean results and scatter plots of the H_2 vs CO_2 concentrations cluster around the line of equal mixing as the

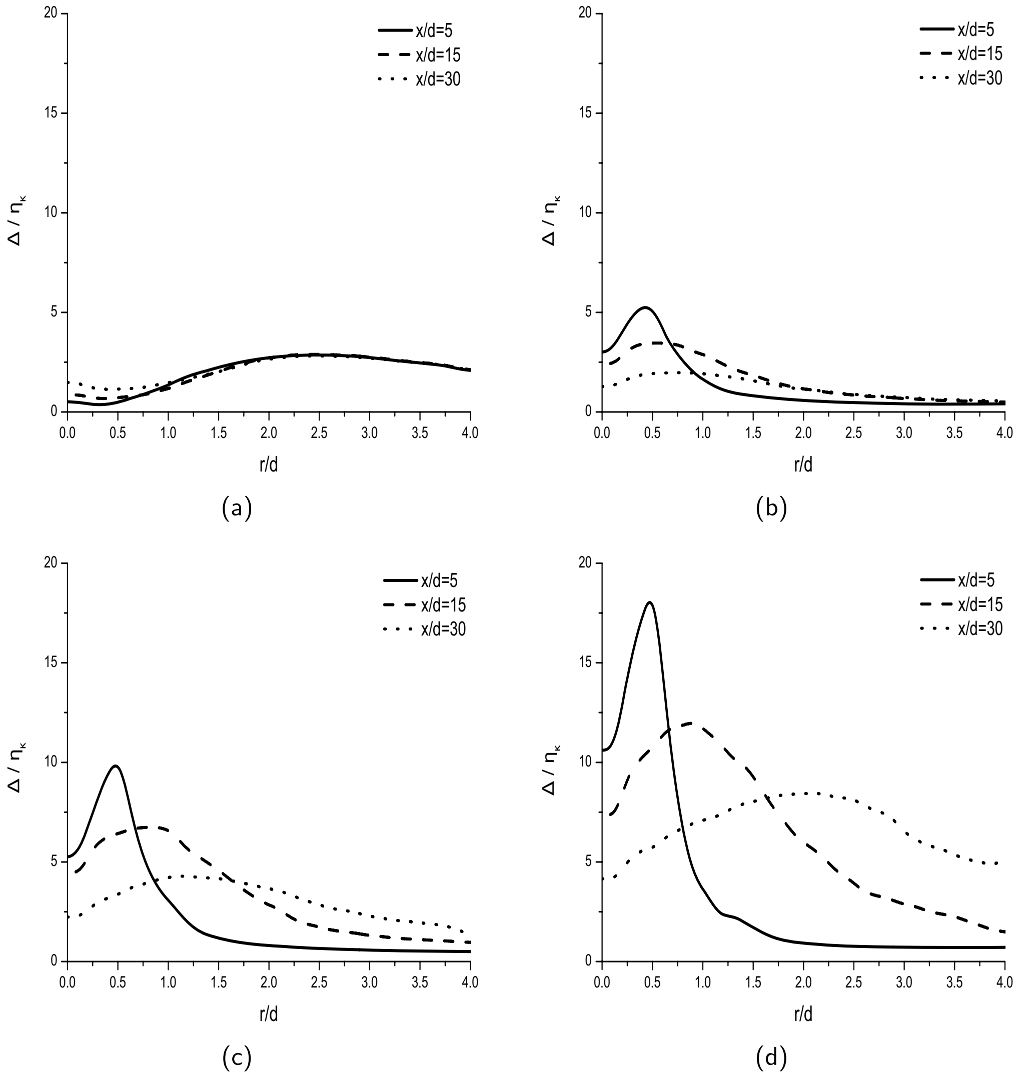

(a) (b) (c) (d)

Figure 5.18: Ratio of grid spacing, Δ, to the Kolmogorov length scale, η_K, for (a) $Re = 1000$, (b) $Re = 2000$, (c) $Re = 4000$ and (d) $Re = 8000$.

Reynolds number increases. However, close to the inlet $(y/d < 10)$ effects of differential diffusion are observed for all the cases examined $(Re = 1000-8000)$, particularly near the edge of the jet. These findings are also confirmed by the mean results of the differential diffusion parameter, ξ, with which a quantification of the differential diffusion effects is made in the simulations.

Results obtained assuming equal mass diffusivities for all species reveal that differential diffusion does not have a significant effect in the velocity field. However, differential diffusion strongly affects the H_2 concentration on the centerline at all locations examined for $Re = 1000$, where an over-prediction of up to 50% is observed. With increasing Reynold number ($Re = 2000 - 8000$) the differences in the H_2 concentrations are negligible.

The analysis on the histograms of the differential diffusion parameter, ξ, reveal that at downstream locations, $y/d = 15, 30$, differential diffusion effects are significant on the centerline, $r/d = 0$, and at radial location $r/d = 1$, where mostly negative values are obtained, due to the higher diffusivity of H_2 from the centerline to the edge of the jet.

The main conclusions of this non-reacting study of differential diffusion have direct implications to turbulent reacting flows as well. The fact that differential diffusion effects were present close to the inlet for moderate to high Reynolds (Re=8000) is an important indication that differential diffusion should not be neglected in numerical simulations of turbulent reacting flows. Differential diffusion effects can have a significant influence on the stabilization of these flames, typically occurring close to the nozzle. Differential diffusion effects should, therefore, be included in numerical simulations of turbulent reacting flows in order to improve accuracy.

Chapter 6

Laminar, axi-symmetric H_2/N_2 diffusion flame

6.1 Introduction

The goal of this numerical study is to apply the proposed methodology, presented earlier in Chapter 3, to the laminar, axi-symmetric H_2/N_2 - air diffusion flame in order to assess its accuracy but also to examine the influence of differential diffusion in laminar hydrogen flames. Comparisons are made with both the experimental data and with results obtained with and without differential diffusion of species and heat in order to examine the influence of differential diffusion. In addition, an evaluation of the magnitude of diffusion terms D_1 and D_2 in Eqs (3.8) will be made.

The influence of differential diffusion on the structure of laminar hydrogen - air flames has been the focus of several numerical studies in the past. The differential diffusion effects species and heat in a $H_2/CH_4/N_2$ - air flame were examined in [112] while the effects of differential diffusion on temperature of usual and inverse diffusion flames, taking into account detailed chemical kinetics and multi-component diffusion, were presented in [113]. The effects of non-unity Lewis number and finite rate chemistry on the dynamics of a H_2 - air diffusion flame were reported in [45] while the influence of chemical non-equilibrium effects in hydrogen - air jet diffusion flames, using detailed chemistry and multi-component diffusion, were presented in [70]. There also exist combined numerical and experimental studies examining the structure of laminar hydrogen - air diffusion flames with the inclusion of thermal diffusion [115, 127, 32].

This chapter is based on Maragkos et al. [60].

6.2 Experimental set-up

The experiments reported by Toro et al. [115] are considered in this work. The mixture of H_2/N_2 (1:1 in mole ratio), issued into air by a round tube of inner diameter $d = 0.9$ cm, is surrounded by a co-flow of air (inner diameter 9.5 cm). The inflow of the mixture, located in the center of the bottom plane, is positioned 0.8 cm above the exit of the co-flow and exits at an average velocity of 0.5 m/s with a parabolic profile. The inlet velocity of the co-flow is set at the average exit velocity of the mixture. Ambient temperature and pressure are $T = 298$ K and $P = 101325$ Pa, respectively, with a resulting Reynolds number of $Re = 175$.

6.3 Mathematical formulation

6.3.1 Governing equations

In order to study the effects of differential diffusion in this laminar H_2/N_2 flame, the newly proposed methodology was implemented in FireFOAM 1.6 [36]. The modified FireFOAM code, solves transport equations for mass, momentum, conserved scalars η, and enthalpy, accounting for differential diffusion of species and non-unity Lewis number. The set of governing equations needed for the numerical simulations is then:

$$\frac{\partial\rho}{\partial t} + \frac{\partial(\rho u_i)}{\partial x_i} = 0 \tag{6.1}$$

$$\frac{\partial(\rho u_j)}{\partial t} + \frac{\partial(\rho u_i u_j)}{\partial x_i} = -\frac{\partial p}{\partial x_j} + \frac{\partial}{\partial x_i}\left[\mu\left(\frac{\partial u_i}{\partial x_j} + \frac{\partial u_j}{\partial x_i}\right)\right] + \rho g_j, \quad j = 1,2,3 \tag{6.2}$$

$$\frac{\partial(\rho\eta_\lambda)}{\partial t} + \frac{\partial(\rho u_i \eta_\lambda)}{\partial x_i} = \frac{\partial}{\partial x_i}\left[\rho\left(\underbrace{BDB^T}_{D_1} + \underbrace{BDU^T\frac{\partial\mathscr{C}}{\partial\eta_\lambda}}_{D_2}\right)\frac{\partial\eta_\lambda}{\partial x_i}\right], \quad \lambda = 1,...,N_e \tag{6.3}$$

$$\frac{\partial(\rho h)}{\partial t} + \frac{\partial(\rho u_i h)}{\partial x_i} = \frac{Dp}{Dt} + \frac{\partial}{\partial x_i}\left(\alpha\frac{\partial h}{\partial x_i}\right) + \sum_{k=1}^{N_s}\left[\frac{\partial}{\partial x_i}\left(h_k(\rho D - \alpha)\right)\frac{\partial Y_k}{\partial x_i}\right] + \dot{Q} \tag{6.4}$$

The species mass diffusion coefficients, D_k, are calculated by Eq 2.15, with the species Schmidt numbers assigned the constant values $Sc_{H_2} = 0.21$, $Sc_{H_2O} = 0.63$, $Sc_{O_2} = 0.76$ and $Sc_{N_2} = 0.81$ [29]. Dynamic viscosity, μ, is a function of temperature and calculated by Sutherland's law, with the two Sutherland coefficients assigned the values $A_s = 1.358519 \cdot 10^{-6}$ and $T_s = 110.04$ for the H_2/N_2 mixture [99]. Radiation is modeled by the finite volume Discrete Ordinates Method (fvDOM), assuming that the only significant radiating species is H_2O [115].

6.3.2 Combustion modelling

For this test case, $N_s = 4$ species k (H_2, H_2O, O_2, N_2) and $N_e = 3$ elements λ (H, O, N) are considered. The species mass fractions relate to the elemental mass fractions η'_H and η'_N through the Burke - Schumann solution, shown in Figure 6.1. In this case, differential diffusion effects are considered only in physical space (transport equations for the conserved scalars) and not in the combustion model (Burke - Schumann solution).

6.4 Numerical set-up

A cylindrical mesh is used, $10d \times 25d$, with 18 cells across the inlet shown in Figure 6.2. Outside the inlet, 66 cells are used radially (compressed towards the inlet) and 300 cells in the axial direction. The total number of cells is then 0.562 million cells, resulting in a minimum and maximum grid spacing of 0.5 mm (on the centerline) and 1.84 cm (side planes of the domain), respectively.

A parabolic profile, taken from a separate simulation with a fully developed velocity profile in a pipe, is used for velocity at the exit plane of the tube, similar to the one reported in the experiments. Outside the exit plane of the inlet tube, a fixed streamwise co-flow velocity of 0.5 m/s is imposed. The thickness of the tube is set to 1.0 mm. A Neumann boundary condition (zeroGradient) is assigned for velocity at the sides of the domain and a Dirichlet boundary condition (totalPressure) for pressure. For the top (outlet) plane a mixed boundary condition (inletOutlet) is used for velocity, which sets the outwards velocity to zeroGradient and sets the inwards velocity to zero, and a Neumann boundary condition (zeroGradient) for pressure. The inlet boundary conditions for the orthogonal elemental mass fractions, η, are of Dirichlet type and set to uniform value (fixedValue).

The governing equations are advanced in time using a first order implicit Euler scheme. A variable time step is used in the simulations, setting the maximum Courant number to $Co = 0.2$. Results only after steady state conditions were reached are presented. All quan-

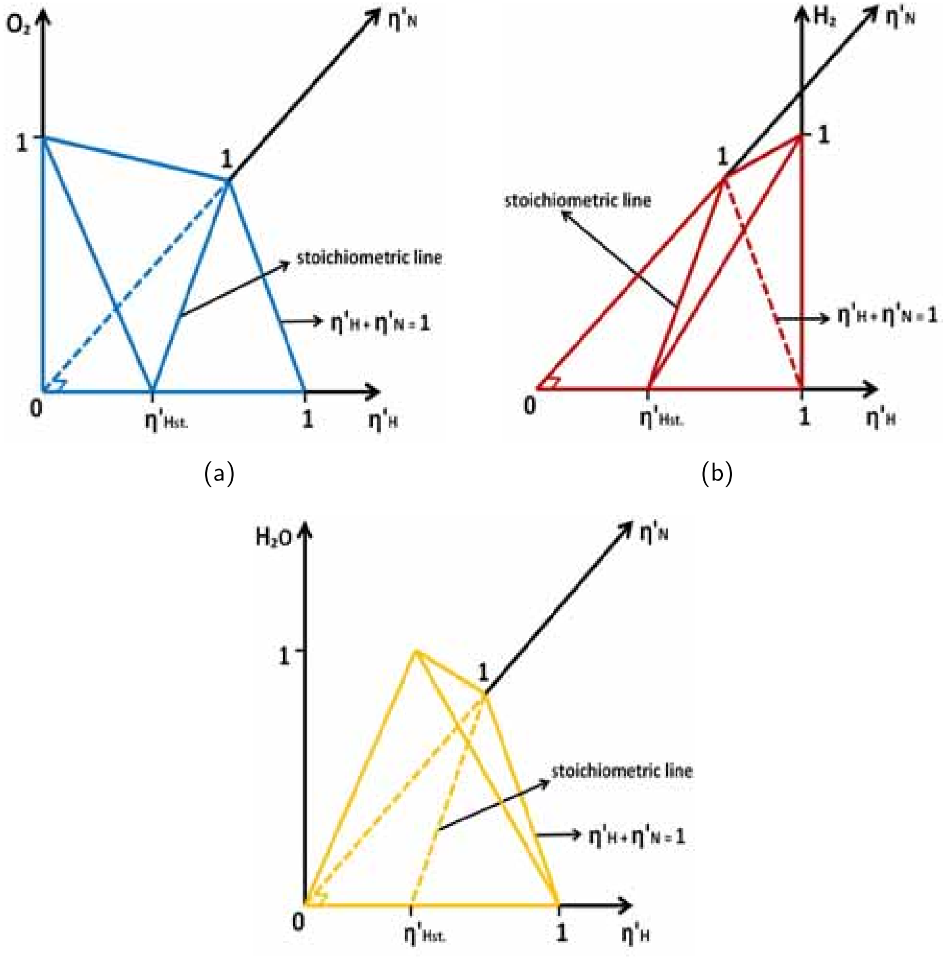
O₂
η'N
1
1
stoichiometric line
η'H+η'N=1
0
η'Hst.
1
η'H
H₂
η'N
1
1
stoichiometric line
η'H+η'N=1
0
η'Hst.
1
η'H
H₂O
η'N
1
1
stoichiometric line
η'H+η'N=1
0
η'Hst.
1
η'H

(a)

(b)

(c)

Figure 6.1: Burke-Schumann solution for irreversible infinitely fast chemistry, based on elemental mass fractions η'_H and η'_N, for (a) O_2, (b) H_2 and (c) H_2O. The stoichiometric elemental mass fraction of H is $\eta'_{H_{st}} = 0.1119$.

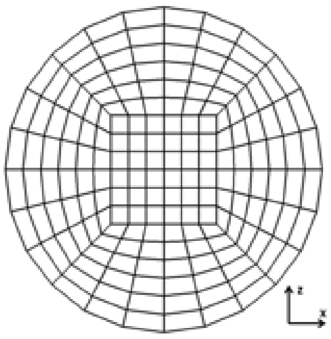

Figure 6.2: Schematic of mesh for fuel inlet used in the simulations

tities are assigned to the cell centers (collocated grid) with velocities linearly interpolated to the cell faces. A second order central difference scheme is used for the convective and diffusive terms with a correction for the non-orthogonality of the mesh.

6.5 Results

6.5.1 Flame structure

The computed temperature distribution for the cases with and without differential diffusion of species and heat are presented as two-dimensional contour plots in Figure 6.3. The adiabatic stoichiometric temperature of the H_2/N_2 mixture is 2040 K. As expected, substantial differences are observed. Taking into account the much higher diffusivity of H_2, the characteristic wishbone flame structure [78, 71, 73, 2, 108] is obtained. As H_2 diffuses radially outward more rapidly, the flame reaches its maximum temperature very close to the inlet, at the edges of the jet if differential diffusion effects are taken into account. Ignoring differential diffusion effects, on the other hand, the rapid radially outward diffusion is not captured and the maximum flame temperature is found on the centerline, at a location about $10d$ downstream.

6.5.2 Mean results

Figure 6.4 presents results for the streamwise velocities obtained from the numerical simulations on the centerline up to $y = 100$ mm and in horizontal planes at locations $y = 3, 10, 20, 30$ mm downstream. No velocity measurements were performed in the experiments by Toro et al. [115] so a comparison of the simulation results with experiments is not possible. However, the simulation results for the streamwise velocities are presented for completeness of the study.

Figures 6.5 - 6.9 present results for temperature and mole fractions of species (H_2, H_2O, O_2, N_2) on the centerline up to $y = 100$ mm and in horizontal planes at locations $y = 3, 10, 20, 30$ mm downstream. The results of the new methodology are presented with and without differential diffusion effects and compared with the experimental data. The experimental data are indicated by symbols while the results with (only D_1 term included and terms D_1 and D_2 included) and without differential diffusion are presented with solid, dotted and dashed lines, respectively. Black symbols correspond to temperature while blue, red, green and orange correspond to H_2, H_2O, O_2 and N_2 mole fractions, respectively.

Results for temperature and species mole fractions on the centerline at location up

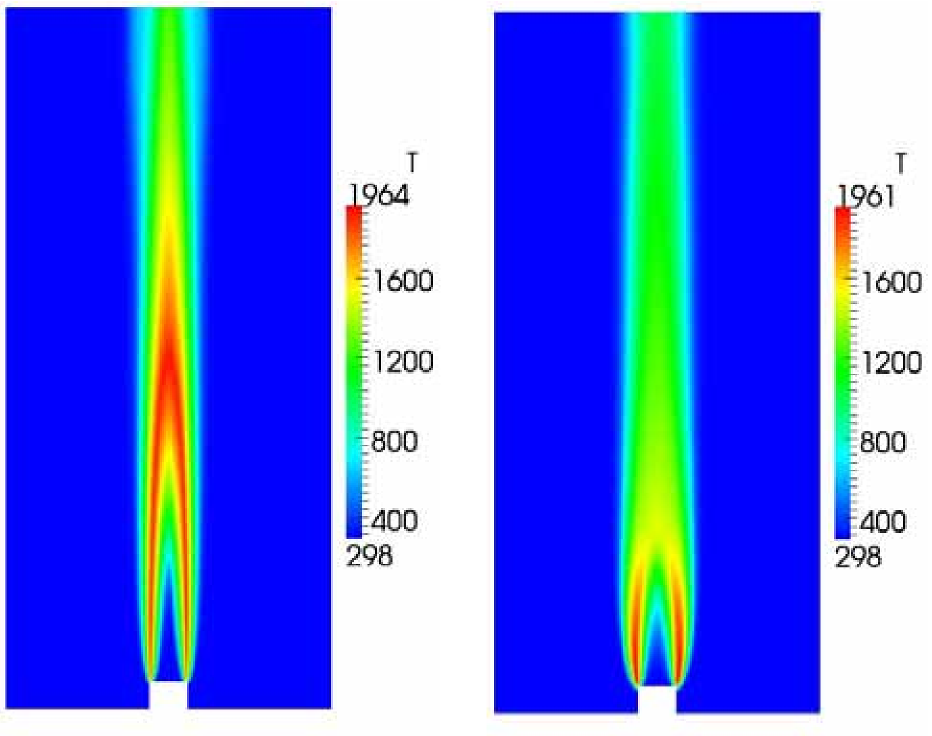

(a) (b)

Figure 6.3: Two-dimensional snapshots of temperature distribution (a) without differential diffusion and (b) with differential diffusion

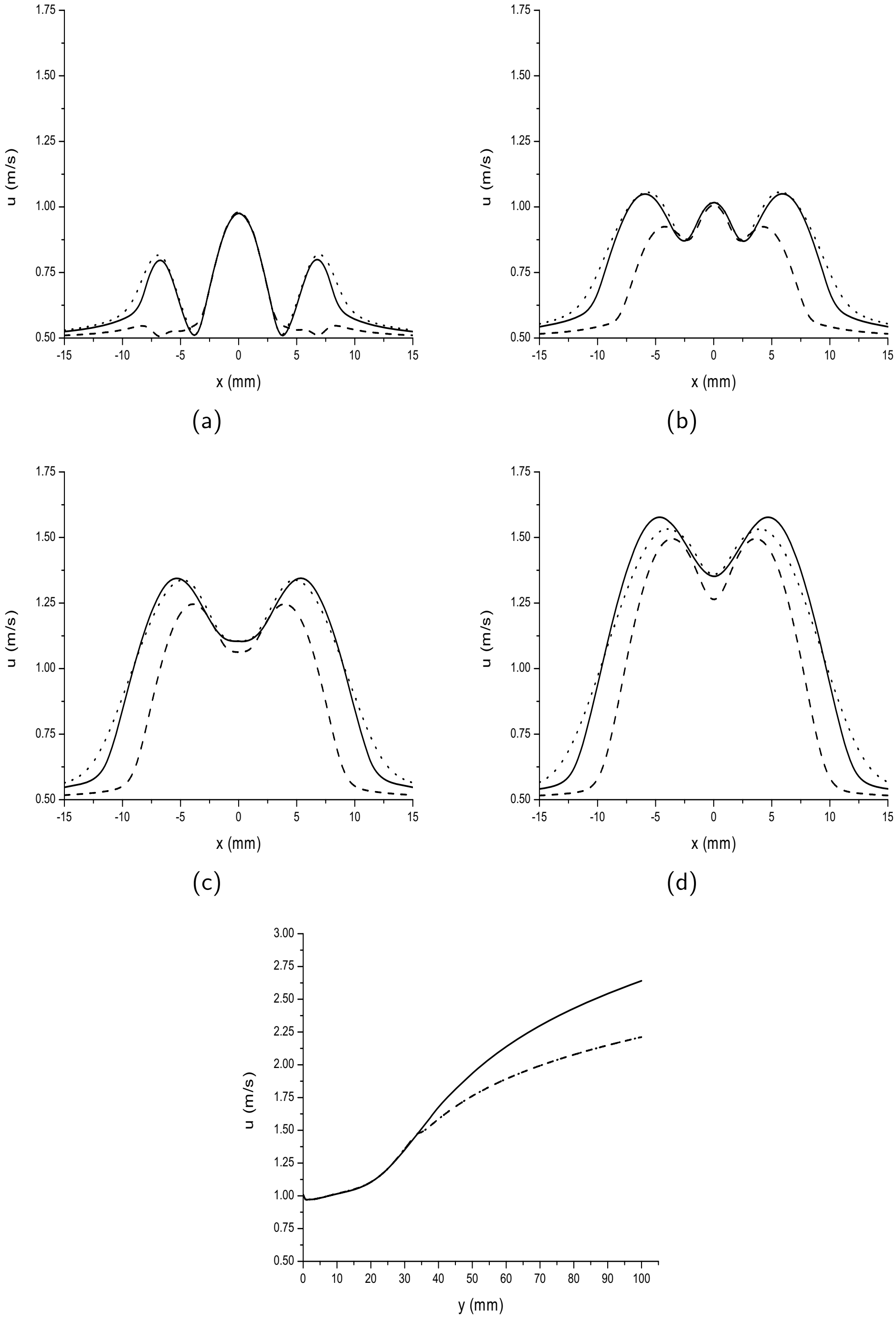

(a)

(b)

(c)

(d)

(e)

Figure 6.4: Streamwise velocities at (a) $y = 3$ mm, (b) $y = 10$ mm, (c) $y = 20$ mm, (d) $y = 30$ mm and (e) axially. With diff. diff. (D_1 and D_2): solid lines, with diff. diff. (only D_1): dotted lines, without diff. diff.: dashed lines.

to $y = 100$ mm above the inlet are presented in Figure 6.5. It is observed that fuel is completely consumed by $y = 45 - 50$ mm, coinciding with the maximum values for temperature and H_2O mole fraction. The temperature profile is well captured by the simulations with differential diffusion (including terms D_1 and D_2) and the same applies for the mole fractions of species mole fractions. It is also clear that by neglecting the D_2 term, the streamwise evolution of temperature and species mole fractions is not well captured. On the other hand if differential diffusion effects are neglected, the peak temperature on the centerline shifts much further downstream and the temperature distribution is not well captured. This also leads to discrepancies in the species mole fraction results when compared with the experimental data.

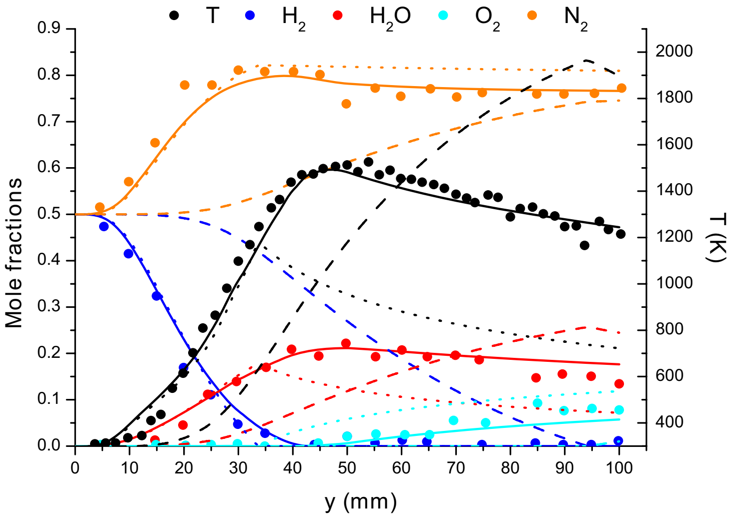

Figure 6.5: Axial temperature and species mole fractions up to $y = 100$ mm. Exp. data: symbols, with diff. diff. (D_1 and D_2): solid lines, with diff. diff. (only D_1): dotted lines, without diff. diff.: dashed lines.

At location $y = 3$ mm above the inlet (Figure 6.6), a peak in the temperature of $T = 1941$ K at location $x = 5.8$ mm, about 1.3 mm outside the radius of the inlet is predicted if differential diffusion effects are considered. This is due to the high diffusivity of H_2 which causes the flame to stabilize at a location outside the inlet radius. A thin zone of high temperature is observed with the peaks of T and H_2O mole fraction, as expected, to coincide. The fuel rich (inner) and fuel lean (outer) sides of the jet are well predicted by the simulations and compare well with the experiments. The non-monotonic change of the mole fraction of N_2, as observed by the experiments, is also observed in the simulations with differential diffusion. The peak values of H_2 and N_2 mole fractions are well predicted, although the profiles are a little wider than the experimental ones. Without differential diffusion effects, the peak value of the flame temperature is similar but the lean side of the jet is under-predicted, having a much narrower profile. In this case the profiles of species mole fractions are also not well captured.

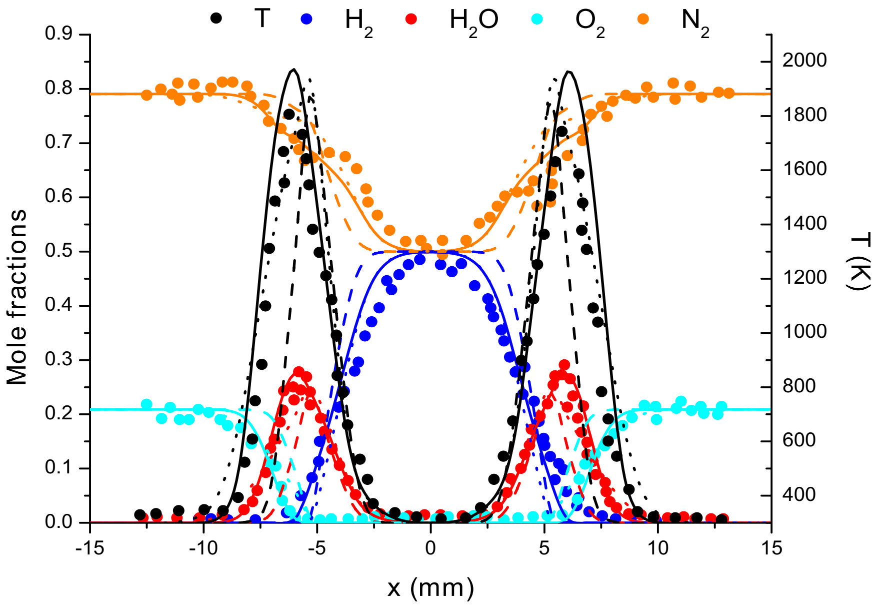

Figure 6.6: Radial temperature and species mole fractions at $y = 3$ mm. Experimental data: symbols, with diff. diff. (D_1 and D_2): solid lines, with diff. diff. (only D_1): dotted lines, without diff. diff.: dashed lines.

At location $y = 10$ mm (Figure 6.7), an increase in the width of the high temperature zone is observed. The peak temperature of $T = 1917$ K compares quite well with the experimental data, however the lean side of the flame is slightly wider than the experiments. Even though the centerline temperature is still close to the ambient one, now H_2, due to its high diffusivity, has decreased followed by an increase of N_2. At this location, the non monotonic change of N_2 is again quite well captured by the simulation results. The results without differential diffusion capture also quite well the peak temperature but greatly under-predict the temperature at the lean side of the flame. At this location, the profiles of species mole fractions are again not well predicted.

At location $y = 20$ mm (Figure 6.8), an increase of the centerline temperature is observed, followed by a decrease of H_2 and the diffusion of H_2O from the reaction zone to the centerline. Here, the width of the high temperature zone has increased even more when compared to $y = 10$ mm. The simulations with differential diffusion effects are able to predict the temperature field and the species mole fractions quite well, however, there is a 30% over-prediction of H_2 on the centerline, followed by an under-prediction

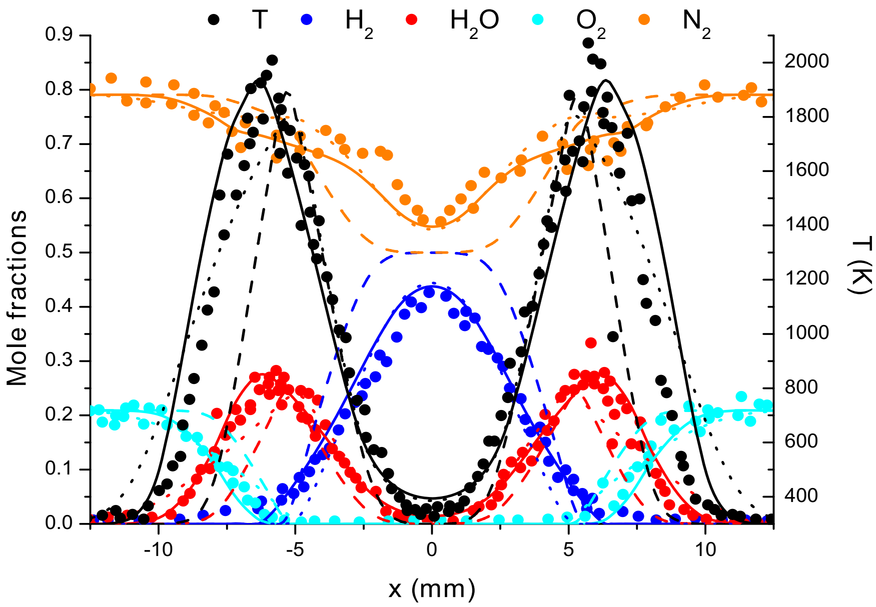

Figure 6.7: Radial temperature and species mole fractions at $y = 10$ mm. Experimental data: symbols, with diff. diff. (D_1 and D_2): solid lines, with diff. diff. (only D_1): dotted lines, without diff. diff.: dashed lines.

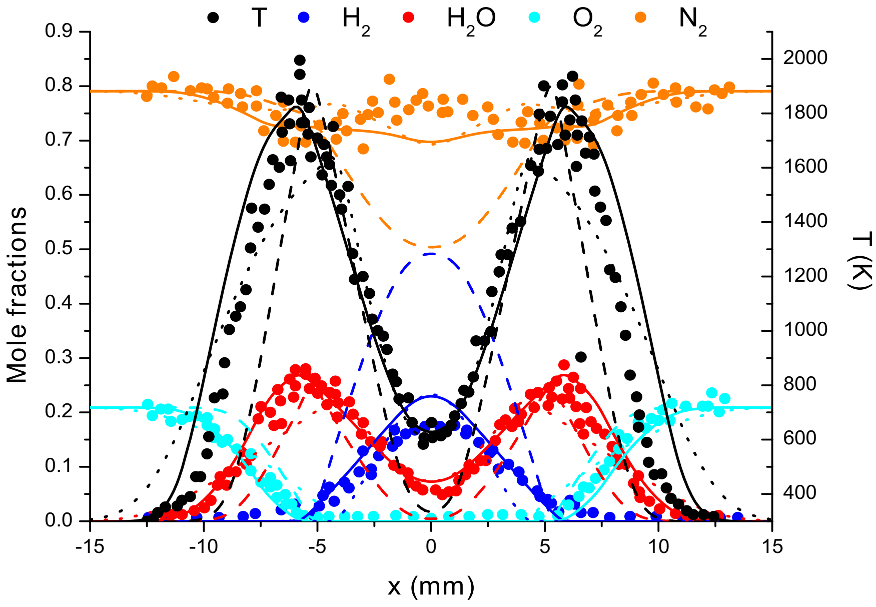

Figure 6.8: Radial temperature and species mole fractions at $y = 20$ mm. Experimental data: symbols, with diff. diff. (D_1 and D_2): solid lines, with diff. diff. (only D_1): dotted lines, without diff. diff.: dashed lines.

of N_2. At this location, the temperature profile in the lean side of the flame is again wider when compared with the experimental data. For the simulation results without differential diffusion similar observations apply like in the previous locations examined. The temperature profiles are much narrower, under-predicting the lean side of the flame, but also the species mole fractions are not well predicted.

A further increase in the centerline temperature is observed at location $y = 30$ mm (Figure 6.9), followed by a decrease in the mole fraction of H_2. At this location, dilution with co-flow air begins to dominate the further development of the flame. Again the temperature and the species mole fractions are well captured if differential diffusion effects are taken into account, apart from a 15% over-prediction of H_2 on the centerline and similar under-prediction of N_2. At this location the simulation results without differential diffusion don't compare well with the experiments. At much lower centerline temperature is predicted, while the H_2 and N_2 mole fractions are greatly over and under-predicted, respectively.

In addition to the experimental work, also numerical results from the solution of transport equations for mass, momentum, species and enthalpy with detailed chemistry and transport were reported by Toro et al. [115]. Overall, the results for temperature and

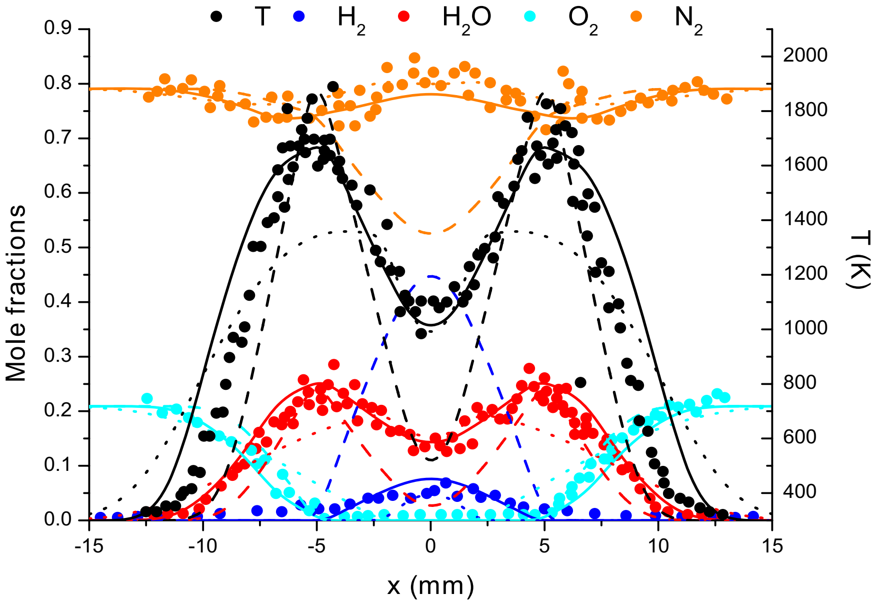

Figure 6.9: Radial temperature and species mole fractions at $y = 30$ mm. Experimental data: symbols, with diff. diff. (D_1 and D_2): solid lines, with diff. diff. (only D_1): dotted lines, without diff. diff.: dashed lines.

species mole fractions obtained from the application of the newly proposed methodology compare very well with both the experimental data and the numerical results reported in [115]. This shows that the newly proposed methodology is accurate enough when compared to other methods of including differential diffusion effects in reactive flows.

In order to have a quantitatively measurement of differential diffusion, a differential diffusion variable, ξ, can be defined as $\xi = z_H - z_N$, where z_H and z_N are the mixture fractions of elements H and N, respectively, defined as [107]:

$$z_\lambda = \frac{\eta'_\lambda - \eta'_{\lambda_O}}{\eta'_{\lambda_F} - \eta'_{\lambda_O}} \tag{6.5}$$

where η'_λ is the mass fraction of element λ and the subscripts F and O denote the fuel and oxidizer streams, respectively. The parameter takes non zero values only when the differential diffusion effects are present (when the diffusivities of species are different).

Results of the differential diffusion parameter, ξ, at various locations are presented in Figure 6.10. The parameter takes positive values at locations outside the inlet radius, $x > 4.5$ mm, due to the faster diffusivity of H_2 to this region, compared to the other species. The opposite occurs at locations closer to the centerline, where H_2 has diffused and more N_2 can be found, creating negative values of ξ. Differential diffusion effects are also present further downstream, shown in Figure 6.11(b), with a maximum negative value at height $y = 25$ mm.

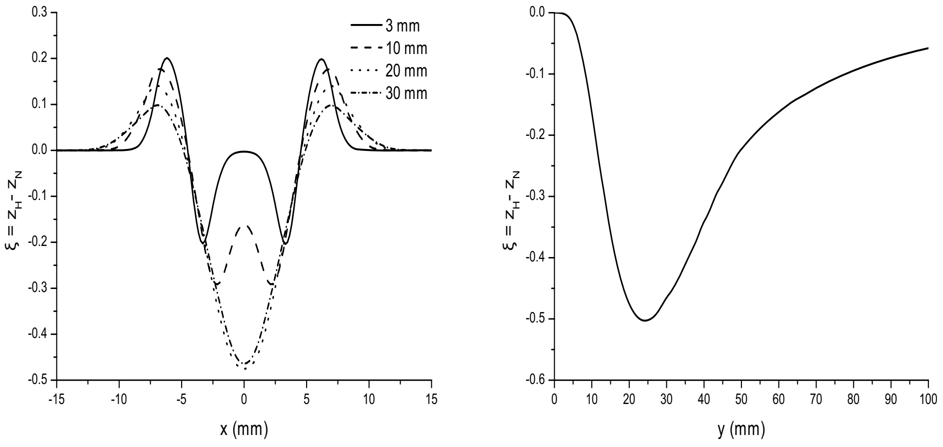

(a) (b)

Figure 6.10: Mean differential diffusion parameter, $\xi = z_H - z_N$, at (a) different heights and (b) axial locations.

6.5.3 Magnitude of diffusion terms D_1 and D_2

The magnitude of diffusion terms D_1 and D_2 in Eqs (3.8) is presented in Figures 6.11 and 6.12. Each one of the D_1 and D_2 terms in the η_H and η_N conserved scalar transport equations depends on both η_H and η_N so the magnitude of each of the terms $D_1^{\eta_H}(\eta_H)$, $D_1^{\eta_H}(\eta_N)$, $D_2^{\eta_H}(\eta_H)$, $D_2^{\eta_H}(\eta_N)$ and $D_1^{\eta_N}(\eta_H)$, $D_1^{\eta_N}(\eta_N)$, $D_2^{\eta_N}(\eta_H)$, $D_2^{\eta_N}(\eta_N)$ will be presented. The results have been normalized by $D_1^{\eta_H}(\eta_H)$ and $D_1^{\eta_N}(\eta_N)$ for the terms related to the η_H and η_N transport equations, respectively.

It is clear that the D_1 terms, expressing the diffusion between the conserved scalars, are always positive, causing η_H and η_N to diffuse. The strongest influence stems from the main diffusion terms ($D_1^{\eta_H}(\eta_H)$, $D_1^{\eta_N}(\eta_N)$) and much less from the cross-diffusion terms ($D_1^{\eta_H}(\eta_N)$, $D_1^{\eta_N}(\eta_H)$). The D_2 terms, expressing the feedback from the combustion model, are positive at the rich side of the flame but negative at the lean side of the flame. This makes η_H and η_N to diffuse more in the core of the mixture but reduces their diffusivity in regions outside the maximum flame temperature. In this case, terms $D_2^{\eta_H}(\eta_H)$ and $D_2^{\eta_N}(\eta_H)$ are the predominant ones. The influence of the D_2 terms is also clearly obvious in Figures 6.11(e), 6.12(e) where they obtain large negative values, at locations downstream from the maximum flame temperature, reducing the diffusion of η_H and η_N on the centerline. Neglecting the D_2 term leads to a great under-prediction of the streamwise temperature and species mole fractions, seen in Figure 6.5.

6.5.4 Conclusions

The method has been illustrated for a laminar H_2/N_2 - air diffusion flame, reporting results for temperature and main species (H_2, H_2O, O_2, N_2) mole fractions. If differential diffusion effects are taken into account, the comparison of the simulated results with the experimental data is very good for the temperature and species mole fractions, at all locations examined. Without differential diffusion effects, the predicted results are not in good agreement with the experiments, due to lack of H_2 diffusion close to the jet inlet. This leads to a wrong prediction of the location and the peak of the flame temperature but also to a great over-prediction of the species mole fractions at all locations. Differential diffusion effects were present at the edges of the inlet, where H_2 has diffused faster that the other species, but also on the centerline at locations more than $10d$ downstream, where there is less H_2 compared to other species. In addition, the influence of the diffusion term D_2 in the transport equations of the conserved scalars, η, has been proved to be important and cannot be neglected.

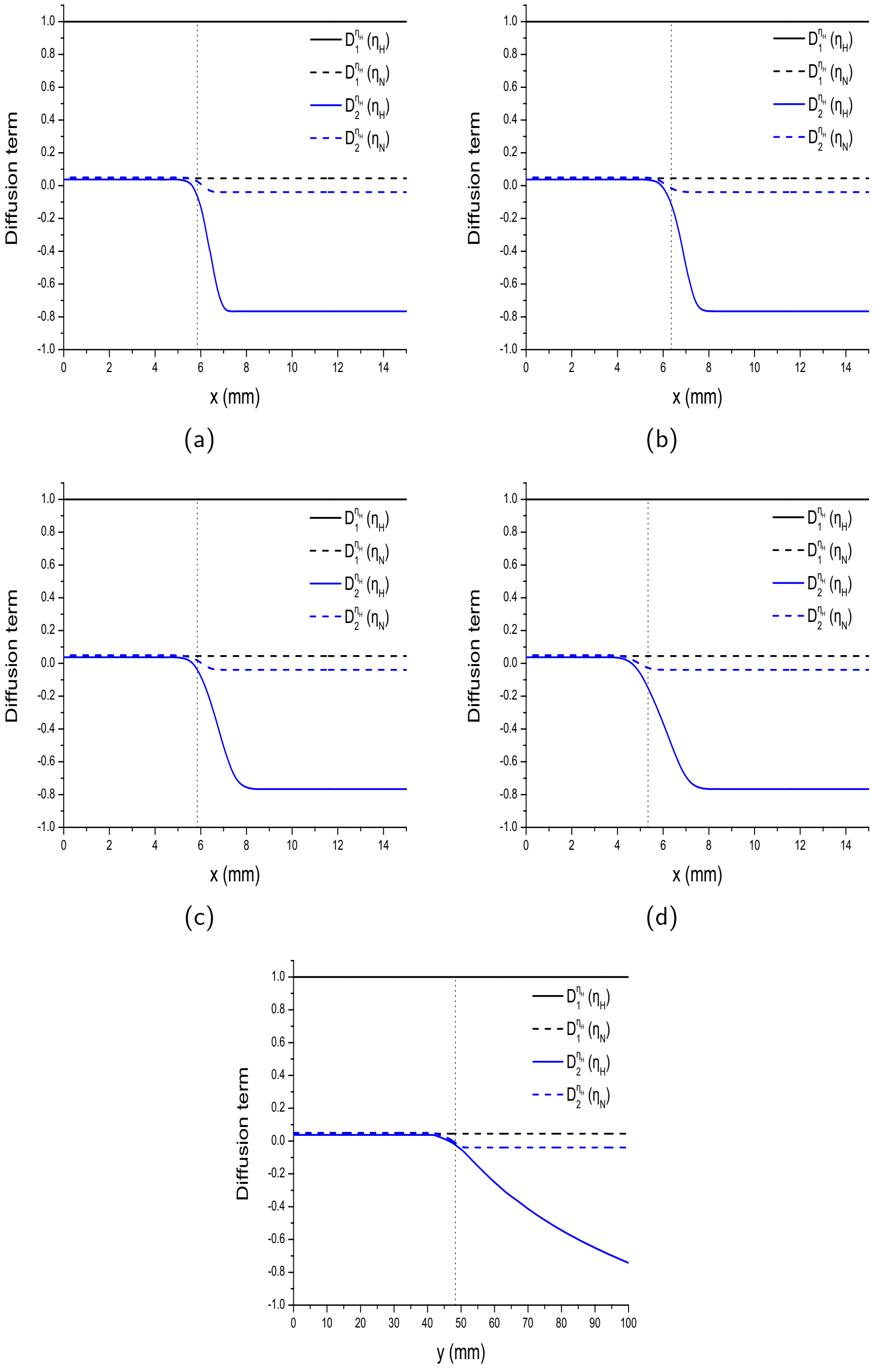

(a) (b) (c) (d) (e)

Figure 6.11: Magnitude of normalized diffusion terms D_1 and D_2 for η_H at (a) $y = 3$ mm, (b) $y = 10$ mm, (c) $y = 20$ mm, (d) $y = 30$ mm and (e) on the centerline up to height $y = 100$ mm. The dotted black line indicates the location of the maximum flame temperature.

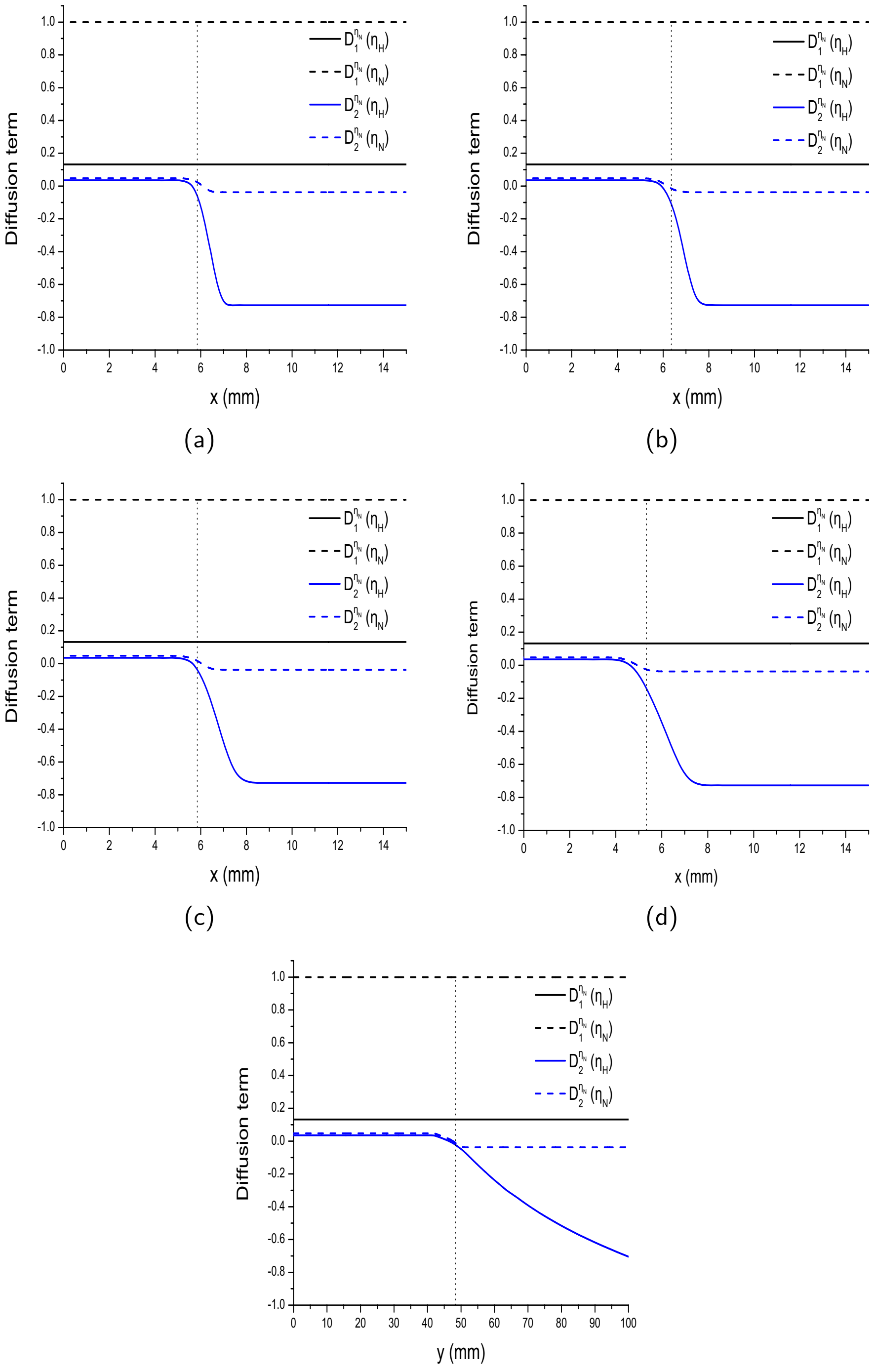

(a) (b)

(c) (d)

(e)

Figure 6.12: Magnitude of normalized diffusion terms D_1 and D_2 for η_N at (a) $y = 3$ mm, (b) $y = 10$ mm, (c) $y = 20$ mm, (d) $y = 30$ mm and (e) on the centerline up to height $y = 100$ mm. The dotted black line indicates the location of the maximum flame temperature.

Differential diffusion effects are generally significant in laminar flames since it is the species molecular diffusion that controls mixing and in turn chemical reactions. Including differential diffusion effects in numerical simulations can, therefore, be important for improving accuracy, especially when mixtures of species with vastly different diffusivities (such as H_2) are to be considered.

Chapter 7

Turbulent, axi-symmetric H_2/N_2 diffusion flame

7.1 Introduction

The specific goal of the present study is twofold: First, to apply the newly proposed methodology to a well documented benchmark test case in order to assess its accuracy in incorporating differential diffusion in numerical simulations of turbulent reactive flows. Second, there is an interest of examining and quantifying the effects of differential diffusion and determining whether they can have a significant effect in numerical simulations of turbulent combustion. For this reason, the flame commonly known as 'H3' is considered in this study [67, 83], a benchmark test case from the Turbulent Non-premixed Flames (TNF) workshop. It is a turbulent H_2/N_2 diffusion flame with detailed measurements of flow field, species concentrations and temperature at a wide range of distances from the fuel inlet. Differential diffusion effects were observed experimentally close to the inlet and up to 20 nozzle diameters downstream distance, making this test case a good candidate for studying differential diffusion.

This benchmark test case has been the focus of several other experimental and numerical works in the past. Neuber et al. [74] investigated both numerically and experimentally, by means of laser spectroscopic methods, the effects of finite rate chemistry and NO production. Forkel et al. [24] performed large eddy simulations of the 'H3' flame and reported on the influence of the inlet boundary conditions while Pitsch et al. [89] applied the unsteady flamelet model and reported on its accuracy compared to the use of steady flamelet libraries. Echekki et al. [22] simulated the test case with a novel modeling approach based on the One-Dimensional Turbulence (ODT) model and reported on strong differential diffusion effects in the near field, with attenuation further downstream. Ranganath et al. [94] also applied the ODT model in numerical simulations of the 'H3' flame and reported on the accuracy of the model when compared with experimental data and the flamelet model. Renfro et al. [95] compared the OH time-series measurements against large-eddy simulation results of the 'H3' flame while Flemming et al. [23] used a hybrid approach based on large eddy simulation (LES) and the equivalent source method (ESM) as well as the boundary element method (BEM) to evaluate the radiated noise from turbulent non-premixed jet flames. More recently, Lorenzzetti et al. [15] developed an analytical solution for a H_2/N_2 jet diffusion flame at moderate Reynolds number and high Damköhler while Schmitt et al. [101] performed large eddy simulations of the 'H3' flame in order to validate a new spatially filtered combustion model which can be used to determine the volumetric reaction rates. Mühlbauer et al. [64] presented numerical broadband combustion noise simulations of the 'H3' jet flame by applying the Random Particle-Mesh for Combustion Noise approach.

It is worth noting that none of the above mentioned numerical studies considered differential diffusion effects in their calculations. The present study will examine the importance of incorporating differential diffusion effects in numerical simulations of the 'H3' flame and will report on their influence on maximum flame temperature and species concentration. The present numerical study is, therefore, considered of added value when compared to previous numerical studies of the 'H3' flame.

7.2 Mathematical formulation

7.2.1 Governing equations

The proposed methodology, previously described in section 3.2.2, is applied in order to study the effects of differential diffusion in a turbulent H_2/N_2 diffusion flame. A modified version of FireFOAM 1.6 [36] is used in this numerical study. The modified FireFOAM code, solves transport equations for mass, momentum, conserved scalars, η, and enthalpy, accounting for differential diffusion of species and non-unity Lewis number. By performing a spatial filtering in the instantaneous balance equations leads to the following transport equations needed for the numerical simulations:

$$\frac{\partial \overline{\rho}}{\partial t} + \frac{\partial (\overline{\rho} \widetilde{u}_i)}{\partial x_i} = 0 \tag{7.1}$$

$$\frac{\partial(\overline{\rho}\widetilde{u}_j)}{\partial t}+\frac{\partial(\overline{\rho}\widetilde{u}_i\widetilde{u}_j)}{\partial x_i}=-\frac{\partial\overline{p}}{\partial x_j}+\frac{\partial}{\partial x_i}\left[(\mu+\mu_t)\left(\frac{\partial\widetilde{u}_i}{\partial x_j}+\frac{\partial\widetilde{u}_j}{\partial x_i}\right)\right]+\overline{\rho}g_j,\quad j=1,2,3 \tag{7.2}$$

$$\frac{\partial(\overline{\rho}\widetilde{\eta}_\lambda)}{\partial t}+\frac{\partial(\overline{\rho}\widetilde{u}_i\widetilde{\eta}_\lambda)}{\partial x_i}=\frac{\partial}{\partial x_i}\left[\overline{\rho}\left(\underbrace{BDB^T}_{D_1}+D_t+\underbrace{BDU^T\frac{\partial\widetilde{\mathscr{C}}}{\partial\widetilde{\eta}_\lambda}}_{D_2}\right)\frac{\partial\widetilde{\eta}_\lambda}{\partial x_i}\right],\quad \lambda=1,...,N_e \tag{7.3}$$

$$\frac{\partial(\overline{\rho}\widetilde{h})}{\partial t}+\frac{\partial(\overline{\rho}\widetilde{u}_i\widetilde{h})}{\partial x_i}=\overline{\frac{Dp}{Dt}}+\frac{\partial}{\partial x_i}\left(\alpha_{eff}\frac{\partial\widetilde{h}}{\partial x_i}\right)+\sum_{k=1}^{N_s}\left[\frac{\partial}{\partial x_i}\left(h_k(\overline{\rho}D_{eff}-\alpha_{eff})\right)\frac{\partial\widetilde{Y}_k}{\partial x_i}\right]+\overline{\dot{Q}} \tag{7.4}$$

The effective mass, D_{eff}, and thermal, α_{eff}, diffusivities are calculated as:

$$D_{eff}=D_k+D_t \tag{7.5}$$

$$\alpha_{eff}=\alpha+\alpha_t \tag{7.6}$$

The species mass diffusion coefficients, D_k, are calculated by Eqs 2.15, with the species Schmidt numbers assigned the constant values $Sc_{H_2}=0.21$, $Sc_{H_2O}=0.63$, $Sc_{O_2}=0.76$ and $Sc_{N_2}=0.81$ [29]. The molecular dynamic viscosity, μ, is a function of temperature and calculated by Sutherland's law, with the two Sutherland coefficients assigned the values $A_s=1.358519\cdot10^{-6}$ and $T_s=110.04$ for the H_2/N_2 mixture [99].

7.2.2 Turbulence modelling

Turbulence is modelled by the one-equation turbulence model [102] with the model constant, c_k, determined dynamically in the simulation. The dimensionless model coefficient, c_ε, is assigned the value $c_\varepsilon=1.05$ [26]. The un-resolved sub-grid scale species and enthalpy fluxes in the species and enthalpy transport equations, respectively, are modelled by the gradient diffusion hypothesis model, assuming constant turbulent Schmidt and Prandtl numbers of $Sc_t=0.7$ and $Pr_t=0.6$ [101]. A sensitivity study of these values is presented later.

7.2.3 Combustion modelling

For this test case, $N_s = 4$ species k (H_2, H_2O, O_2, N_2) and $N_e = 3$ elements λ (H, O, N) are considered. The species mass fractions relate to the elemental mass fractions η'_H and η'_N through the Burke - Schumann solution, previously shown in Figure 6.2. In this case, differential diffusion effects are considered only in physical space (transport equations for the conserved scalars) and not in the combustion model (Burke - Schumann solution).

7.2.4 Turbulence - Chemistry interaction

The turbulence-chemistry interaction is modelled through a presumed sub-grid probability density function (pdf) [90] which follows a beta distribution, fully defined by the filtered, $\widetilde{\eta}$, and sub-grid variance, $\widetilde{\eta''^2}$, of the conserved scalars η, so that the filtered species mass fractions, assuming statistical independence of the conserved scalars ($P(\eta_H, \eta_N) = P(\eta_H)\ P(\eta_N)$), are computed as:

$$\widetilde{Y}_k = \int_{\eta_{H_{lb}}}^{\eta_{H_{ub}}} \int_{\eta_{N_{lb}}}^{\eta_{N_{ub}}} Y_k(\eta_H, \eta_N)\ P(\eta_H)\ P(\eta_N)\ d\eta_H\ d\eta_N \tag{7.7}$$

where the subscripts lb and ub denote the lower and upper bounds of the conserved scalars η, respectively. It is worth to note that the assumption of statistical independence of the conserved scalars is not totally valid, which has been reported in the past [55]. However, it has been adopted in the present work for simplicity and in order to investigate whether this assumption can lead to a reasonable comparison between numerical simulations and experiments. The sub-grid probability density function, P, is defined as:

$$P(\eta) = \frac{(\eta - \eta_{lb})^{a-1}(\eta_{ub} - \eta)^{b-1}}{B(a,b)(\eta_{ub} - \eta_{lb})^{a+b-1}} \tag{7.8}$$

where $B(a,b)$ is a beta function and the properties $\eta_{lb} \leq \eta \leq \eta_{ub}$ and $a, b \geq 0$ are satisfied. The pdf parameters a and b are determined from $\widetilde{\eta}$ and $\widetilde{\eta''^2}$ as:

$$a = \widetilde{\eta}_{norm} \left[\frac{\widetilde{\eta}_{norm}(1 - \widetilde{\eta}_{norm})}{\widetilde{\eta''^2_{norm}}} - 1 \right], \quad b = \frac{a}{\widetilde{\eta}_{norm}} - a \tag{7.9}$$

where the normalized conserved scalars $\widetilde{\eta}_{norm}$ and normalized variances of the conserved scalars $\widetilde{\eta''^2_{norm}}$ are computed as:

$$\widetilde{\eta}_{norm} = \frac{\widetilde{\eta} - \eta_{lb}}{\eta_{ub} - \eta_{lb}}, \quad \widetilde{\eta''^2_{norm}} = \frac{\widetilde{\eta''^2}}{(\eta_{ub} - \eta_{lb})^2} \tag{7.10}$$

The filtered variances of the conserved scalars are obtained by using a scale similarity assumption [90] as:

$$\widetilde{\eta''^2} = c_z \Delta^2 (\nabla \widetilde{\eta})^2 \tag{7.11}$$

where the model parameter is assigned the constant value $c_z = 0.15$ [101].

7.3 Experimental set-up

The case considered in this study is the 'H3' benchmark flame from the International Workshop on Measurements and Computation of Turbulent Non-premixed Flames (TNF), reported in [66, 83]. It is a jet diffusion flame with fuel composition of 50% H_2 and 50% N_2 (by volume), issued into air from a 35 cm long round tube, of inner diameter $d = 8$ mm, at an average bulk velocity of 34.8 m/s (Re=10000). The inlet tube is surrounded by a contoured nozzle (inner diameter of 140 mm) providing a co-flow of air at 0.2 m/s. The flame height, as reported by the experiments, is measured to be $35d$ downstream from the tube inlet while the stoichiometric mixture fraction is $z_{st.} = 0.31$.

7.4 Numerical set-up

The numerical simulations are performed on a $22d \times 65d$ mesh, with the inlet, located at the bottom plane, consisting of a uniform rectangular grid surrounded by a cylindrical mesh. The grid resolution for the inlet is set to 4×4 cells (rectangular) and 4×16 (cylindrical), resulting in 12 cells across the inlet, shown in Figure 7.1. Outside the inlet, 50 cells are used radially (compressed towards the inlet). In the axial direction 500 cells are used. The total number of cells is then 0.444 million cells, resulting in a minimum and maximum grid spacing of 0.74 mm (on the centerline) and 4.87 cm (sides of the domain).

The governing equations are advanced in time using a first order bounded implicit 'Euler' scheme. All quantities are assigned to the cell centers (collocated grid) with velocities linearly interpolated to the cell faces. The convective terms are second order centrally differenced using 'Gauss linear' interpolation. For scalar transport, the bounded second order

TVD scheme 'limitedVanLeer' is used while the diffusive terms are centrally differenced and corrected for the non-orthogonality of the mesh with 'Gauss linear corrected'. A PISO algorithm is used for the pressure - velocity coupling with a Rhie-Chow interpolation to avoid odd-even decoupling.

A parabolic velocity profile is used for the H_2/N_2 mixture at the inlet. Velocity fluctuations with an amplitude of 3% of the injection velocity are added at the inlet ('white noise') in order to match the position of the maximum centerline flame temperature reported by the experiments. In the bottom plane of the domain $(y = 0\ m)$ outside the inlet a fixed co-flow velocity of 0.2 m/s is imposed, as reported in the experiments. The thickness of the tube is negligible. A mixed boundary condition (pressureInletOutletVelocity) is assigned for velocity at the sides of the domain, setting zero gradient for any outward flow and calculating the inlet velocity from pressure. A Dirichlet boundary condition (totalPressure) is assigned for pressure at the sides of the domain, which fixes total pressure and when velocity changes then pressure is adjusted accordingly. For the top (outlet) plane a mixed boundary condition (inletOutlet) is used for velocity and a Neumann boundary condition (zeroGradient) for pressure. The inlet boundary conditions of the conserved scalars η_H and η_N are of Dirichlet type and set to uniform values (fixedValue).

7.5 Results

7.5.1 Flame structure

The computed mean temperature distributions for the cases with and without differential diffusion are presented in two-dimensional plots in Figure 7.2. The adiabatic flame temperature of the H_2/N_2 mixture is 2040 K. The inclusion or not of differential diffusion has a clear influence on the maximum flame temperature but also on the stabilization

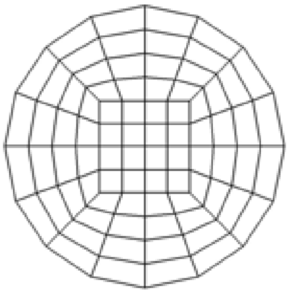

Figure 7.1: Schematic representation of the mesh used in the fuel inlet in the simulations.

of the flame. If differential diffusion effects are considered (Figure 7.2(a)) the maximum flame temperature obtained from the numerical simulations exceeds the adiabatic one. This has been reported in the past both experimentally [66, 67] and numerically [33] and is attributed to differential diffusion effects (differential diffusion causes more H_2 to be present on the lean side of the flame changing this way the local composition). In this case, the maximum flame temperature is observed very close to the inlet, at the edges of the jet. On the other hand if differential diffusion effects are neglected (Figure 7.2(b)) temperatures below the adiabatic one are obtained. In this case heat does not diffuse as fast towards the edge of the jet as before. As such, it is convected downstream, shifting the maximum flame temperature downstream as well. In addition a thinner reaction zone is observed close to the inlet due to a lower species diffusion rate at this location.

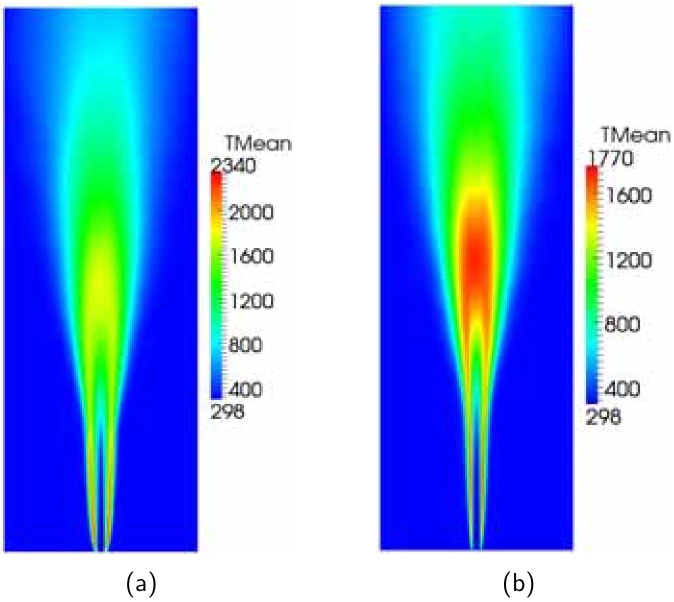

(a) (b)

Figure 7.2: Two-dimensional plots of mean temperature distribution (a) with differential diffusion and (b) without differential diffusion.

7.5.2 Mean and rms results

Figure 7.3 shows the mean and rms profiles of the streamwise velocity at various downstream locations with and without differential diffusion effects included. There are visible differences on the velocity field in the cases with and without differential diffusion effects considered. Overall, a better agreement is observed if differential diffusion effects are included. Discrepancies are observed close to the nozzle, at location $y/d = 5$ (Figure 7.3(a)), where the spreading of the jet is not well captured. This can be attributed to the boundary condition used to generate turbulence at the inlet ('white noise'). The influence of the diffusion term, D_2, is not significant on the velocity field.

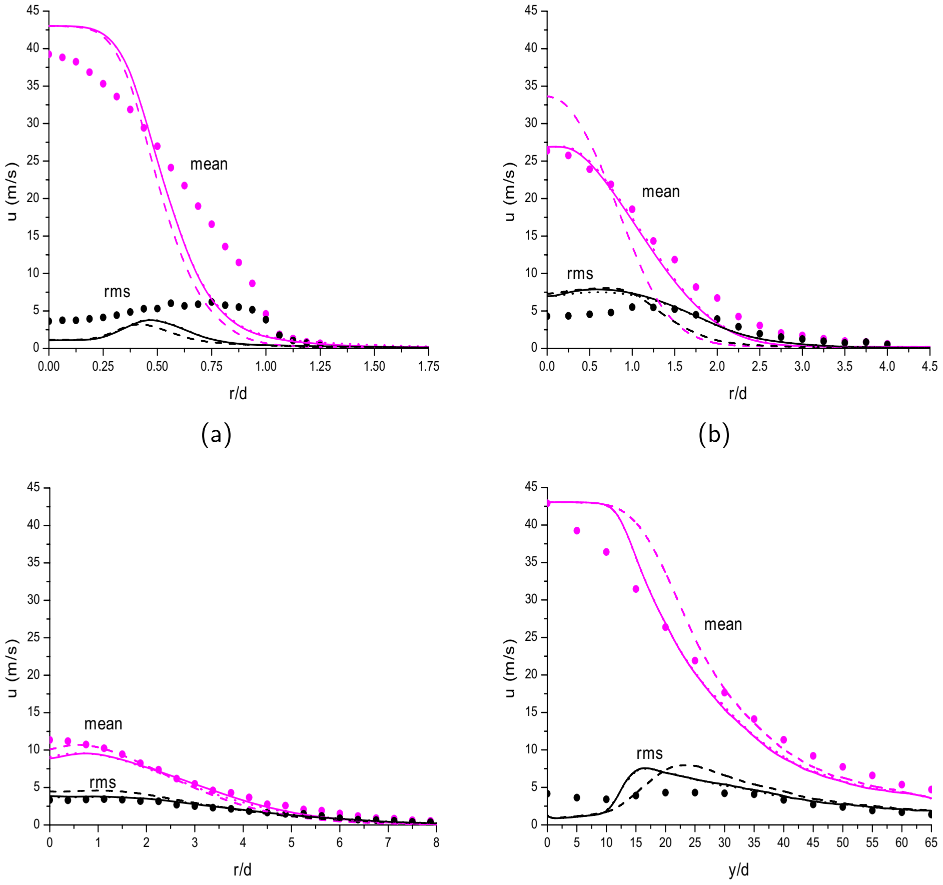

(a) (b) (c) (d)

Figure 7.3: Mean and rms streamwise velocity at location (a) $y/d = 5$, (b) $y/d = 20$, (c) $y/d = 40$ and (d) axially. Experimental data: symbols, with diff. diff. (D_1 and D_2): solid lines, with diff. diff. (only D_1): dotted lines, without diff. diff.: dashed lines.

Results of the main species (H_2, H_2O, O_2, N_2) concentrations, temperature and mixture fraction, z, are shown, for various downstream locations, in Figures 7.4-7.9. Results are presented with (D_1 and D_2) and without differential diffusion effects included, as well as results with only the D_1 diffusion term included in order to examine the influence of the diffusion term D_2 (feedback from the combustion model).

The mixture fraction, z, has been calculated based on Bilger's formulation [6]. Bilger's definition of the mixture fraction has the advantage that not only differential diffusion effects are included but it also preserves the stoichiometric value of the mixture fraction.

In this case, the mixture fraction is calculated as:

$$z = \frac{(\eta'_H - \eta'_{H,O})/2W_H - (\eta'_O - \eta'_{O,O})/W_O}{(\eta'_{H,F} - \eta'_{H,O})/2W_H - (\eta'_{O,F} - \eta'_{O,O})/W_O} \tag{7.12}$$

where the subscripts F and O denote the fuel and oxidizer streams, respectively.

The mean and rms profiles of axial temperature, species concentration and mixture fraction are shown in Figure 7.4. There is, in general, a good agreement between the numerical simulations and the experimental results if differential diffusion effects are considered. In this case, the influence of the diffusion term D_2 is not significant. However, there was a significant influence of the diffusion term D_2 in the axial temperature and species profiles in laminar calculations, previously reported by Maragkos et al. [60]. If differential diffusion effects are neglected, a slower rise in axial temperature is observed, followed by a slower decay of species concentrations and mixture fraction. This is a direct consequence of the slower decay of the streamwise velocity previously shown in Figure 7.3(d).

Figures 7.5-7.9 present the mean and rms profiles of temperature, species concentration and mixture fraction at various downstream locations. Overall, a good agreement is observed between numerical simulations and experiments if differential diffusion effects are considered. The discrepancies between simulations and experiments close to the inlet $(y/d = 2.5, 5)$ are attributed to the not well captured spreading of the streamwise velocity at this location, previously shown in Figure 7.3. Close to the nozzle the turbulent fluctuations are under-predicted and this can be attributed to the boundary condition used to generate turbulence at the inlet. The 'white noise' applied at the inlet generates turbulence that does not have coherent structures and is, therefore, dying fast [24]. The main observation, though, is that if differential diffusion effects are neglected, the position and the value of the maximum flame temperature are not well predicted by the numerical simulations. More specific, the flame temperature is under-predicted by about 400 K (20%) and the position of the maximum flame temperature is shifted towards the rich side of the flame at location $y/d = 2.5$. Similar results were also reported in previous numerical studies [22, 94, 23, 64] where differential diffusion effects were neglected. The inclusion of the diffusion term D_2 has a substantial influence in the results, especially on the lean side of the flame, limiting the diffusion of temperature and species. Similar observations apply for locations $y/d = 5$ and $y/d = 10$ as well, where significant differential diffusion effects are present. Moving further downstream, at location $y/d = 20$, the influence of differential diffusion decreases but remains significant in the radial profiles of temperature,

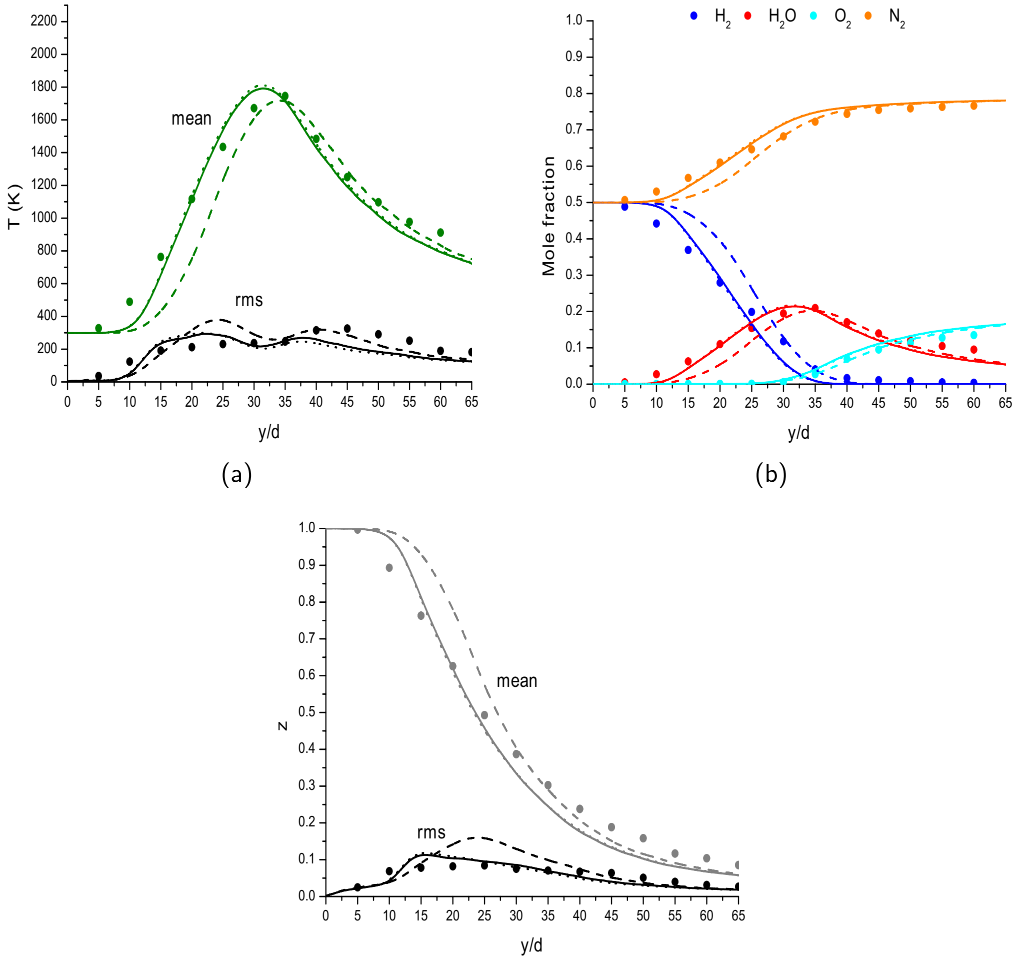

(a) (b) (c)

Figure 7.4: Mean and rms results versus downstream distance for (a) T, (b) species and (c) mixture fraction. Experimental data: symbols, with diff. diff. (D_1 and D_2): solid lines, with diff. diff. (only D_1): dotted lines, without diff. diff.: dashed lines.

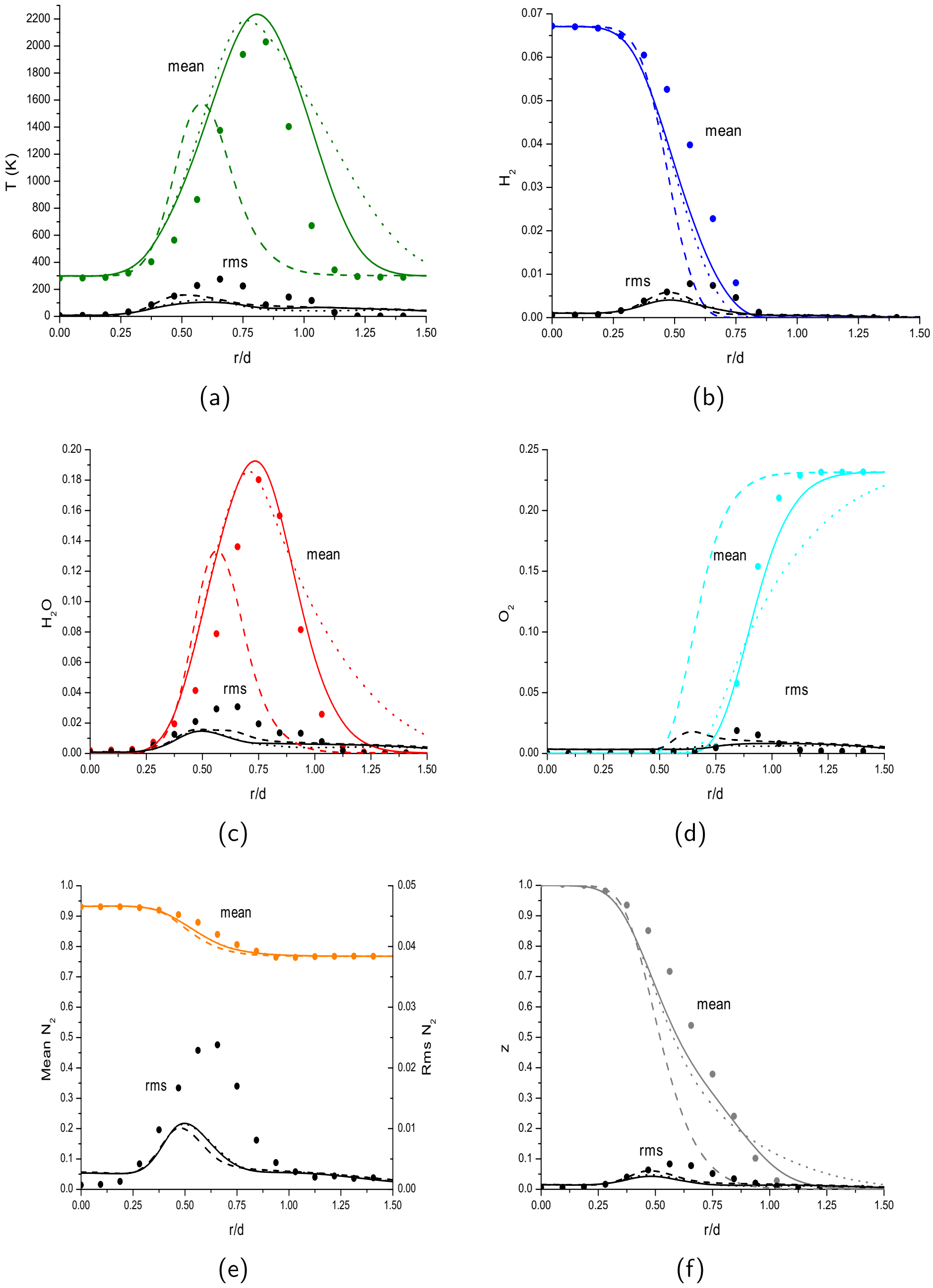

(a) (b)

(c) (d)

(e) (f)

Figure 7.5: Mean and rms results at location $y/d = 2.5$ for (a) T, (b) H_2, (c) H_2O, (d) O_2, (e) N_2 and (f) mixture fraction. Experimental data: symbols, with diff. diff. (D_1 and D_2): solid lines, with diff. diff. (only D_1): dotted lines, without diff. diff.: dashed lines.

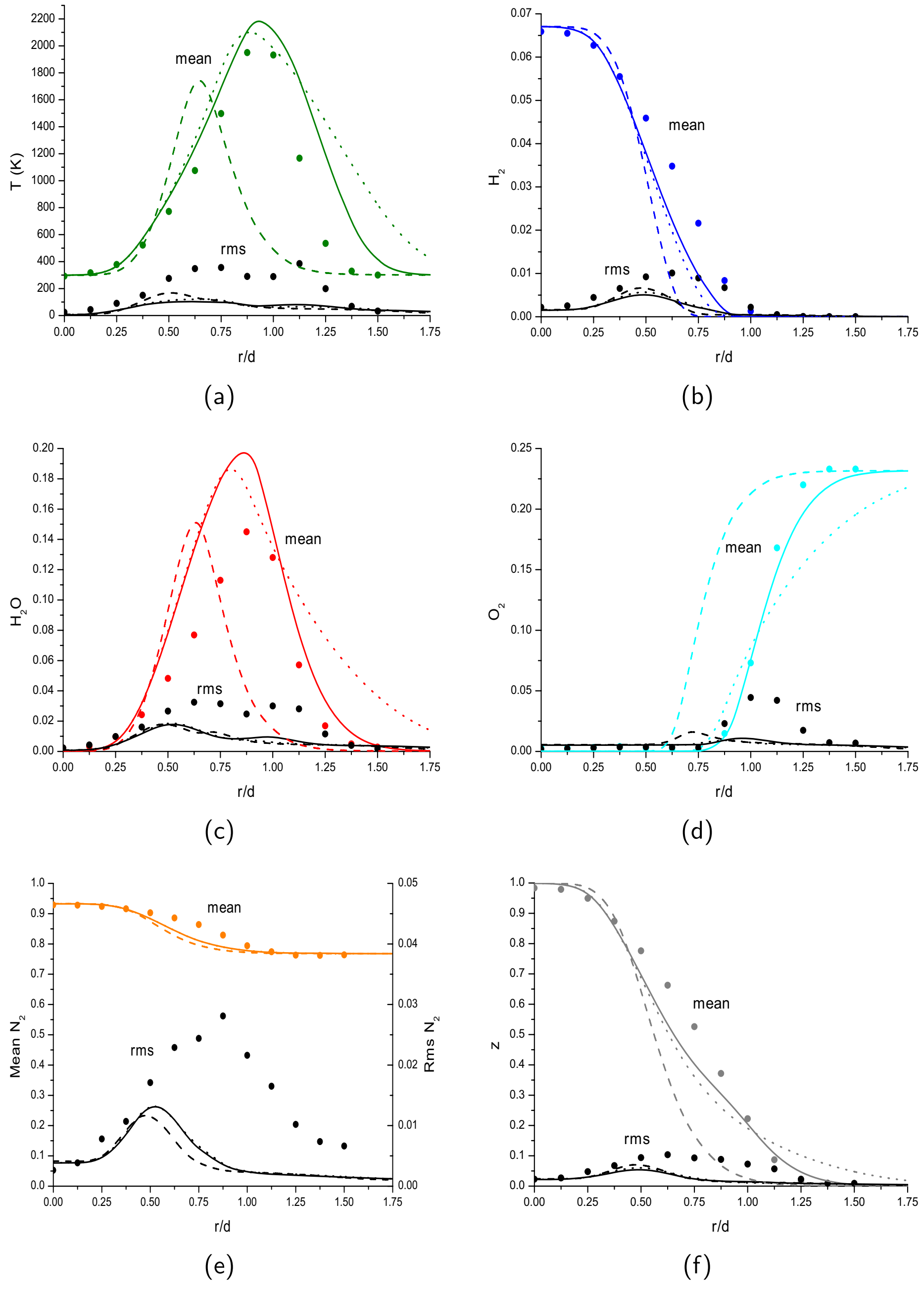

(a) (b)

(c) (d)

(e) (f)

Figure 7.6: Mean and rms results at location $y/d = 5$ for (a) T, (b) H_2, (c) H_2O, (d) O_2, (e) N_2 and (f) mixture fraction. Experimental data: symbols, with diff. diff. (D_1 and D_2): solid lines, with diff. diff. (only D_1): dotted lines, without diff. diff.: dashed lines.

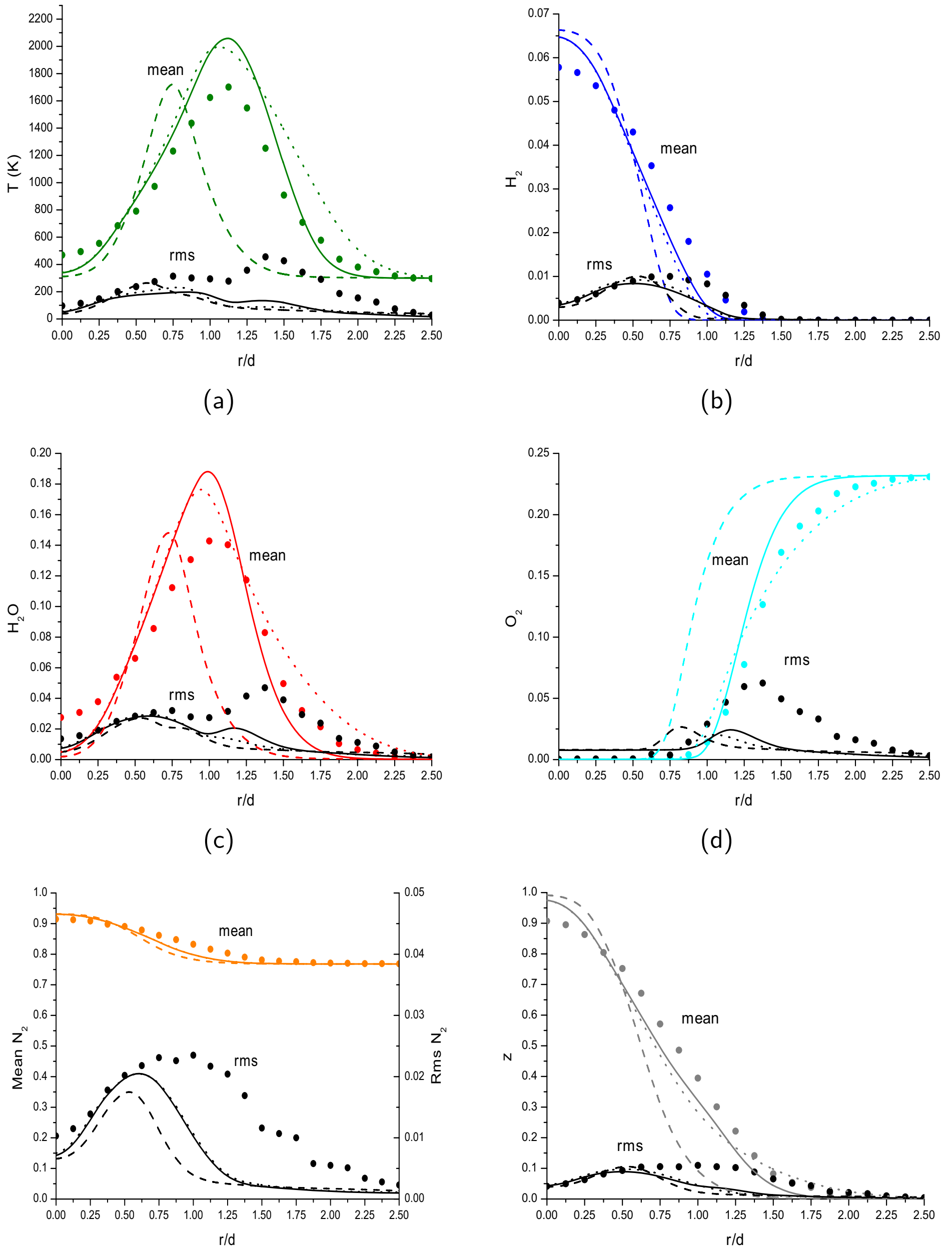

(a)

(b)

(c)

(d)

(e)

(f)

Figure 7.7: Mean and rms results at location $y/d = 10$ for (a) T, (b) H_2, (c) H_2O, (d) O_2, (e) N_2 and (f) mixture fraction. Experimental data: symbols, with diff. diff. (D_1 and D_2): solid lines, with diff. diff. (only D_1): dotted lines, without diff. diff.: dashed lines.

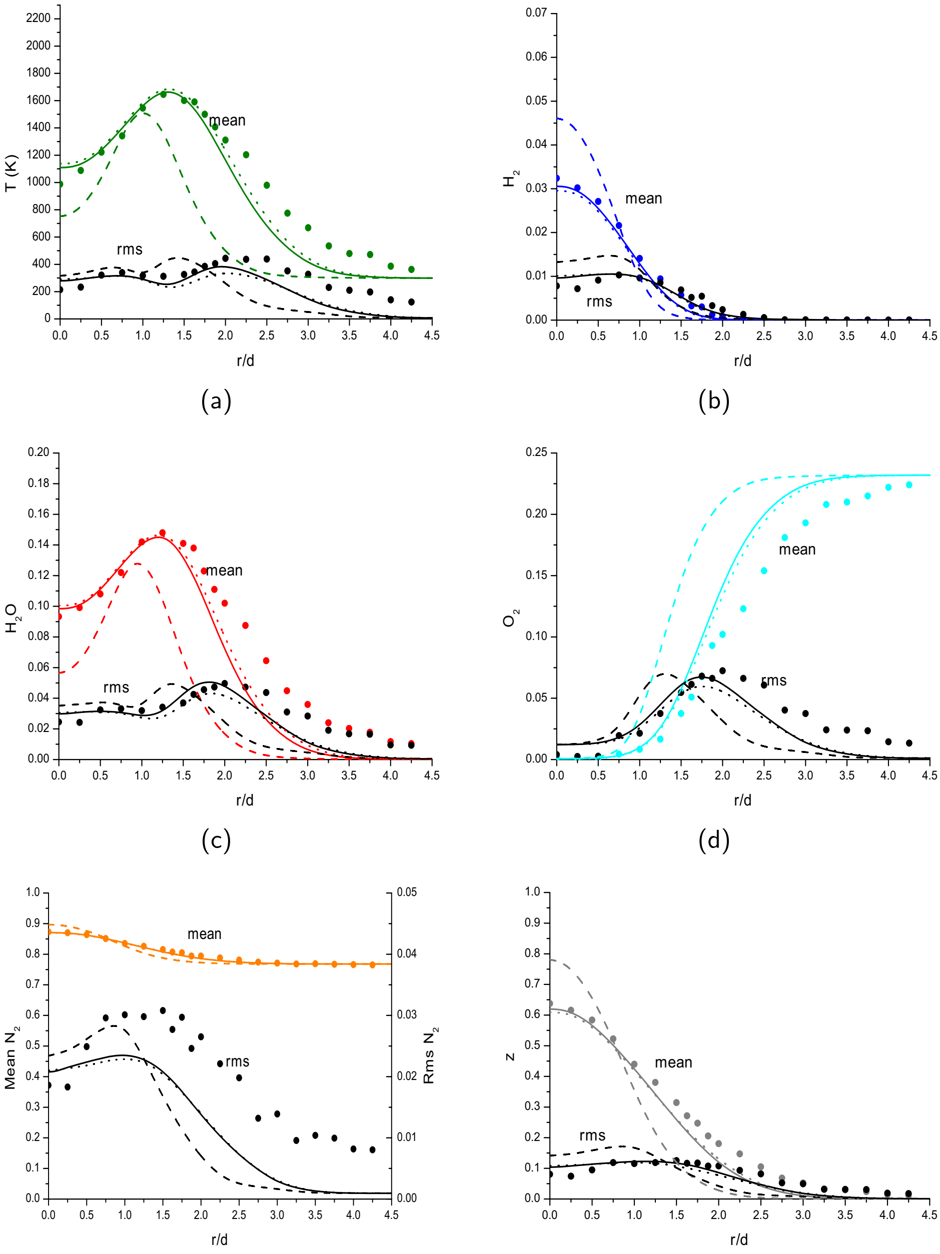

(a)

(b)

(c)

(d)

(e)

(f)

Figure 7.8: Mean and rms results at location $y/d = 20$ for (a) T, (b) H_2, (c) H_2O, (d) O_2, (e) N_2 and (f) mixture fraction. Experimental data: symbols, with diff. diff. (D_1 and D_2): solid lines, with diff. diff. (only D_1): dotted lines, without diff. diff.: dashed lines.

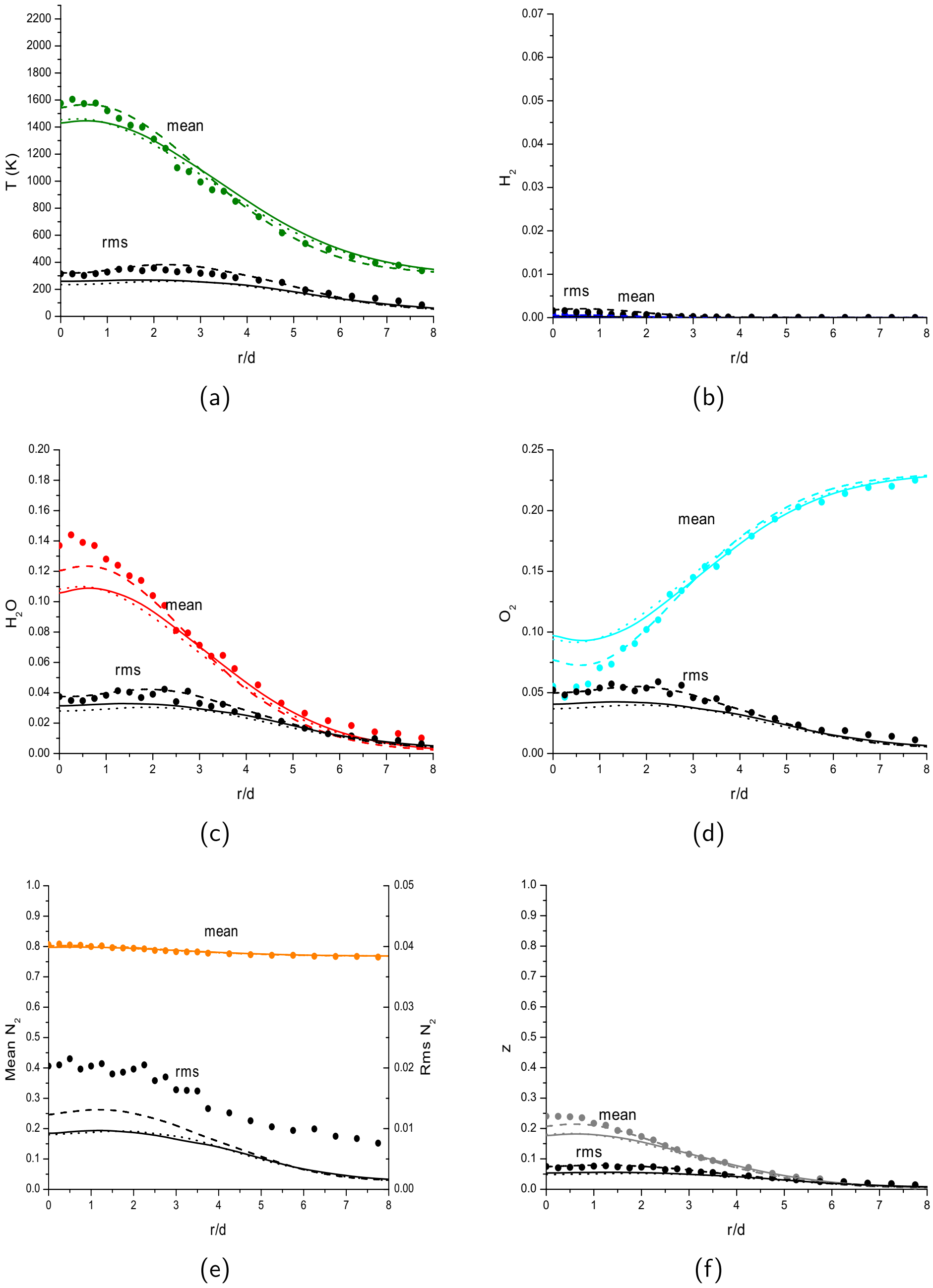

Figure 7.9: Mean and rms results at location $y/d = 40$ for (a) T, (b) H_2, (c) H_2O, (d) O_2, (e) N_2 and (f) mixture fraction. Experimental data: symbols, with diff. diff. (D_1 and D_2): solid lines, with diff. diff. (only D_1): dotted lines, without diff. diff.: dashed lines.

species and mixture fraction. Finally, at location $y/d = 40$, results obtained with and without differential diffusion are similar, indicating that at this location turbulent mixing is a far more dominant process than molecular mixing and differential diffusion effects are not important anymore. An error analysis on the absolute value and the position of the maximum flame temperature obtained from the numerical simulations is presented in Tables (7.1) and (7.2), respectively.

Table 7.1: Error analysis of the maximum flame temperature in the numerical simulations.

y/d	$T_{max}^{exp}(K)$	$T_{max}^{sim}(K)$ (diff. diff.)	$T_{max}^{sim}(K)$ (no diff. diff.)	$error_{max}^{sim}(\%)$ (diff. diff.)	$error_{max}^{sim}(\%)$ (no diff. diff.)
2.5	2030	2245	1637	10.59	-19.36
5	1950	2204	1817	13.02	-6.82
10	1701	2046	1745	21.34	2.55
20	1646	1664	1513	1.09	-8.08
40	1605	1445	1564	-9.97	-2.55

Table 7.2: Error analysis of the position of the maximum flame temperature in the numerical simulations.

y/d	$r/d_{T_{max}}^{exp}$	$r/d_{T_{max}}^{sim}$ (diff. diff.)	$r/d_{T_{max}}^{sim}$ (no diff. diff.)	$error_{T_{max}}^{sim}(\%)$ (diff. diff.)	$error_{T_{max}}^{sim}(\%)$ (no diff. diff.)
2.5	0.844	0.776	0.582	-8.06	-31.04
5	0.875	0.905	0.646	3.43	-26.17
10	1.125	1.154	0.769	2.58	-31.64
20	1.250	1.271	1.017	1.68	-18.64
40	0.250	0.379	0.379	51.60	51.60

In this study a relatively simple combustion model, the Burke-Schumann solution, is used. It is interesting to examine the influence and the accuracy of this simple combustion model when compared to other more sophisticated combustion models. Previous numerical studies of the 'H3' flame have made use of various combustion models from finite rate chemistry [74, 22], flamelet model [89, 94], chemical equilibrium model [83, 24] and infinitely fast chemistry [23, 111]. Results of temperature profiles close to the inlet, where differential diffusion effects are significant, were only reported in [24, 22, 94, 23] for downstream location $y/d = 5$. From the results reported in these studies it is clear that the maximum flame temperature and in some cases the position of the flame are not well captured by the numerical simulations, regardless of the combustion model used, which is a direct consequence of the neglection of differential diffusion. Overall, the results obtained in the present study with the Burke-Schumann solution as combustion model are comparable with results obtained from previous numerical studies with more sophisticated combustion models, particularly at downstream locations $y/d > 20$ where the effects of differential diffusion are not important. Finite rate chemistry effects are expected to play a minor role in the mean species concentrations and to a lesser extent to temperature. However, they will yield more accurate results for less major species such as OH and NO [74], which cannot be considered with the Burke-Schumann solution.

7.5.3 Quantification of differential diffusion

In order to have a quantitative measurement of differential diffusion, a differential diffusion parameter, ξ, is defined as $\xi = z_H - z_N$, where z_H and z_N are the mixture fractions of elements H and N, respectively, defined as [3]:

$$z_\lambda = \frac{\eta'_\lambda - \eta'_{\lambda_O}}{\eta'_{\lambda_F} - \eta'_{\lambda_O}} \tag{7.13}$$

The differential diffusion parameter ξ takes non-zero values only when differential diffusion effects are present, that is when the species mass diffusivities are different.

The elemental mixture fractions, z_H and z_N, and differential diffusion parameter, $\xi = z_H - z_N$, versus Bilger's mixture fraction, z, are plotted in Figure 7.10 only for downstream locations $y/d = 5$ and 20 since there are no significant differential diffusion effects for $y/d > 20$. At location $y/d = 5$, there is a deficit of H element evident for the rich mixtures ($z > 0.7$) due to differential diffusion of H_2 towards the reaction zone. In addition, the maximum positive peak of the differential diffusion parameter, ξ, is observed just on the lean side of the stoichiometric conditions. Similar observations apply for locations $y/d = 20$, although, the influence of differential diffusion has substantially decreased.

The mean elemental mixture fraction, z_H, versus the mean elemental mixture fraction, z_N, for various downstream locations is shown in Figure 7.11. Without differential diffusion effects the lines would coincide with the black symbols, representing the equal diffusivity line. The z_H exceeds z_N for all mixture fractions at locations $y/d \leq 20$ except for the very rich mixtures, obtained around the flame axis. The biggest deviation between z_H and z_N is observed around z≈0.1-0.15, corresponding to a radial location on the air side close to the reaction zone. This is caused by the high diffusivity of H_2, enriching the reaction zone with more H_2 than N_2. As a consequence, H_2O (combustion products) will also be present

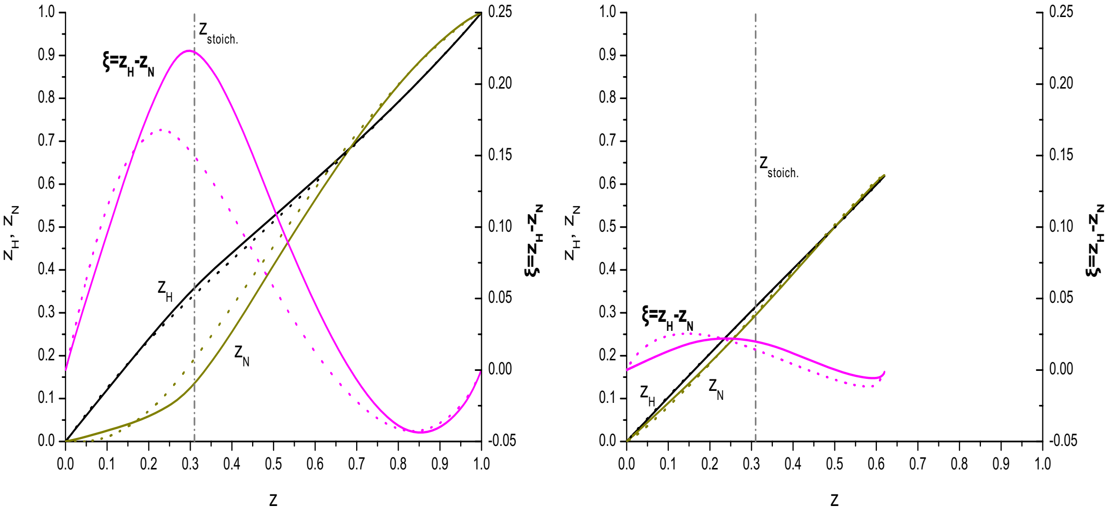

(a) (b)

Figure 7.10: Elemental mixture fractions, z_H and z_N, and differential diffusion parameter, $\xi = z_H - z_N$, versus mixture fraction, z, at location (a) $y/d = 5$ and (b) $y/d = 20$. With diff. diff. (D_1 and D_2): solid lines, with diff. diff. (only D_1): dotted lines.

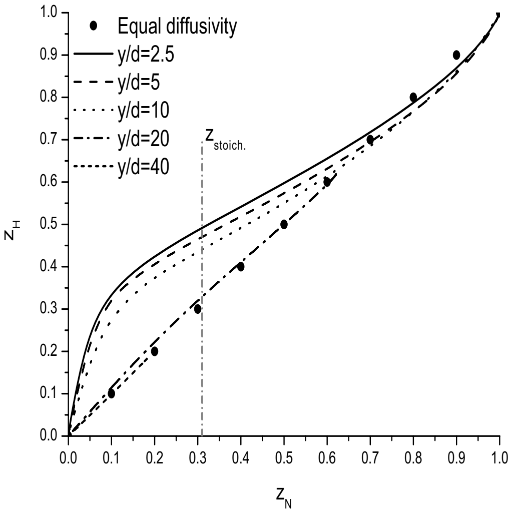

Figure 7.11: Elemental mixture fraction z_H versus elemental mixture fraction z_N at various downstream locations.

in this location, shifting the lines in Figure 7.11 on the z_H side. At locations $y/d > 20$ there is no significant difference between z_H and z_N and the line closely follows the equal diffusivity line.

It is expected that at relatively high Reynolds number flows, molecular differential diffusion will only affect the high wavenumber structure of turbulence [57]. Even though the flow in the inner core of the jet is turbulent, at locations $y/d = 2.5, 5, 10$, there is a laminar-like flow in the reaction zone and on the lean side of the flame. This makes molecular mixing an important transport mechanism in this region that will in turn affect the gas composition and the maximum flame temperature. With increasing downstream distance, differential diffusion effects diminish and the flame develops into a state of unity Lewis number. This can be seen in Figure 7.12 where temperature versus mixture fraction, in comparison to adiabatic equilibrium results, is presented at locations $y/d = 5, 20$. The significant influence of differential diffusion close to the inlet is evident (Figure 7.12(a)), in which the scatter plot exhibits a high curvature on the lean side of the flame, for the reasons explained above. Temperatures above the adiabatic flame temperature of this mixture are obtained at both locations due to differential diffusion effects.

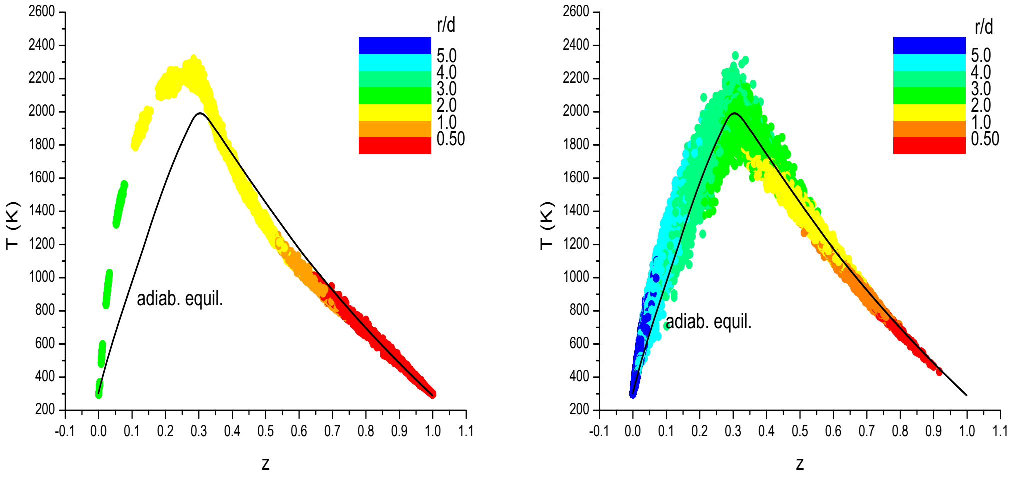

(a) (b)

Figure 7.12: Temperature versus mixture fraction in comparison to adiabatic equilibrium results at location (a) $y/d = 5$ and (b) $y/d = 20$.

7.6 Sensitivity analysis

7.6.1 LES resolution

The ratio of turbulent to laminar viscosity, μ_t/μ, is shown in Figure 7.13. Overall, the added turbulent viscosity from the turbulence model is of the same order of magnitude as the molecular viscosity, indicating that the LES grid is fine enough to accurately simulate this test case. The maximum value of the ratio is less than 3, if differential diffusion effects are considered, observed at downstream distance $y/d = 40$ at radial location $r/d = 6$.

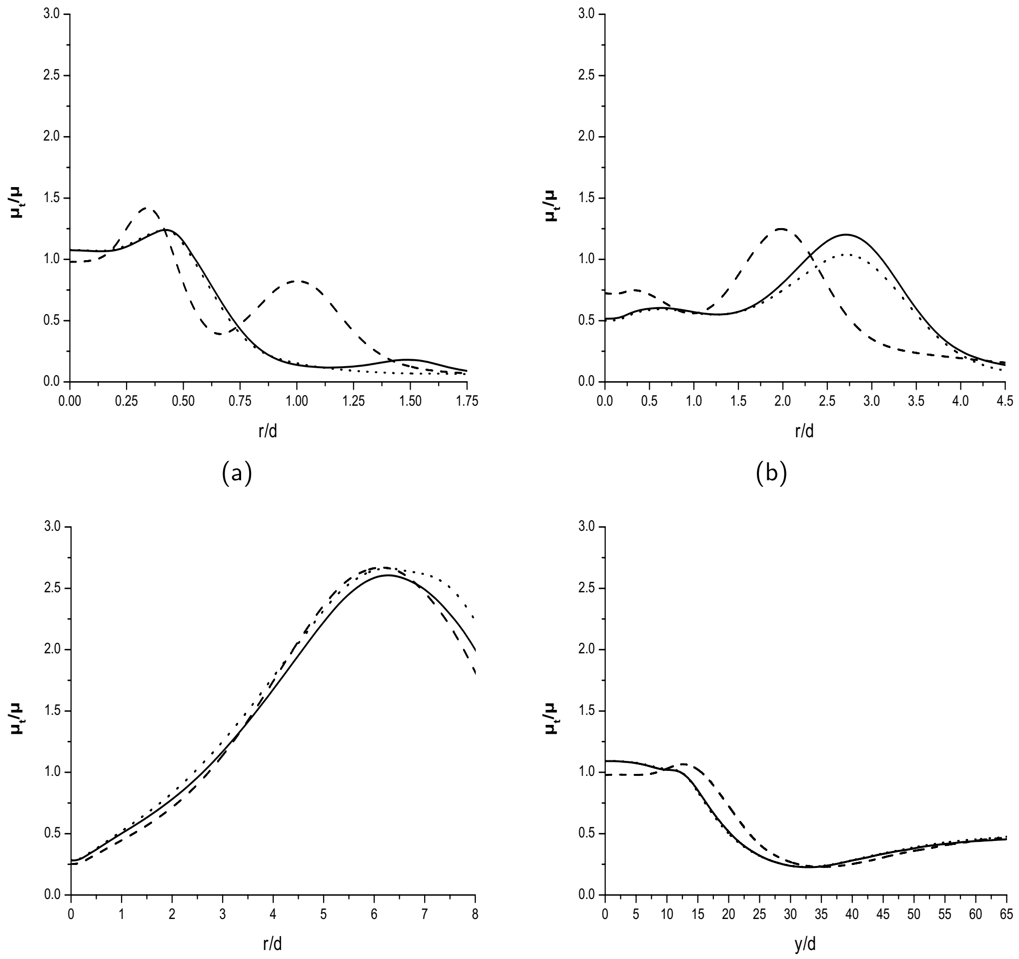

(a) (b)

(c) (d)

Figure 7.13: Ratio of turbulent to laminar viscosity, μ_t/μ, at location (a) $y/d = 5$, (b) $y/d = 20$, (c) $y/d = 40$ and (d) axially. With diff. diff. (D_1 and D_2): solid lines, with diff. diff. (only D_1): dotted lines, without diff. diff.: dashed lines.

The quality of the LES grid can also be examined by looking at the ratio of grid spacing, Δ, to the Kolmogorov length scale, $\eta_K = (\frac{\nu^3}{\varepsilon})^{\frac{1}{4}}$, presented in Figure 7.14. According to Pope [?] the demarcation between the inertial and dissipation range for homogeneous isotropic turbulence is located at $k\eta \approx 0.1$ or $\Delta/\eta \approx 32$. Assuming that this criterion remains valid sufficiently far from boundaries, it is used in this work to study the LES resolution. The total dissipation rate is expressed as $\varepsilon = 2(\nu + \nu_t)\overline{S}_{ij}\overline{S}_{ij}$. The maximum value of the ratio is 13, if differential diffusion effects are considered, and goes up to 8 at various downstream locations. Therefore, the values obtained from the numerical simulations are within the dissipation range, implying a very well resolved LES calculation.

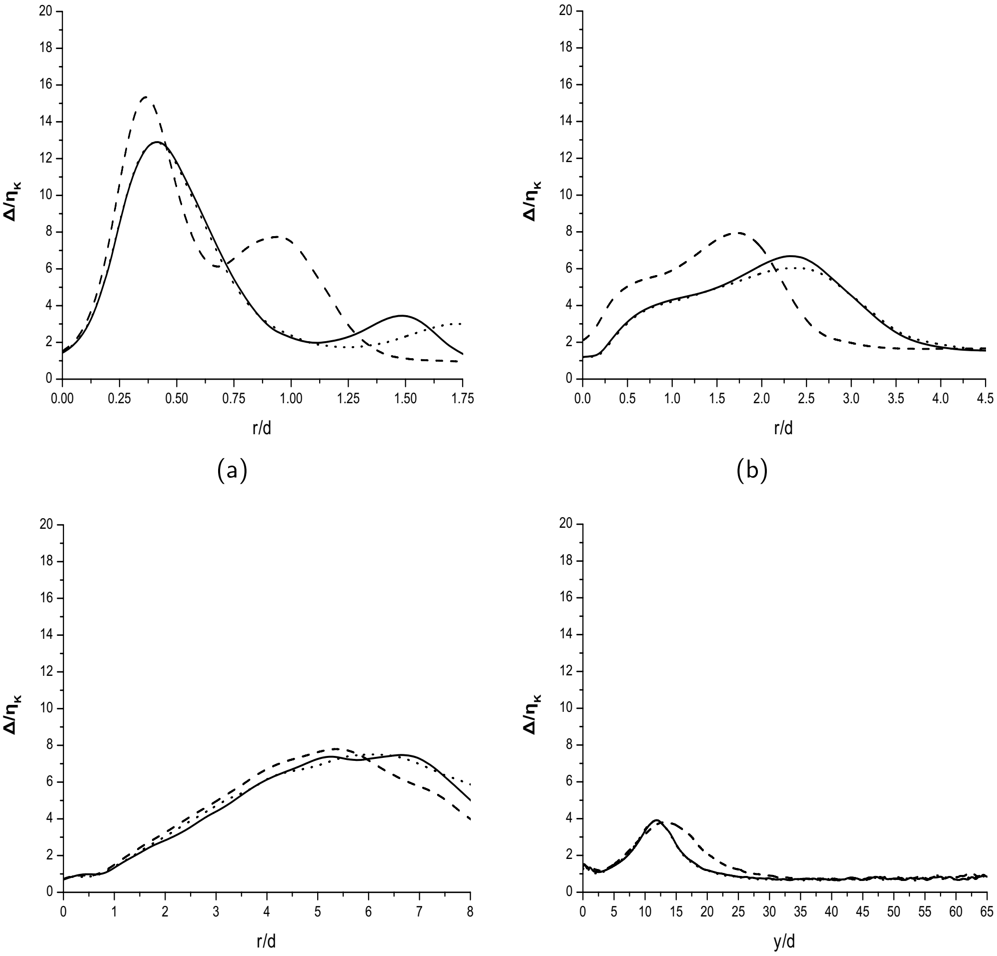

(a) (b)

(c) (d)

Figure 7.14: Ratio of grid spacing, Δ, to the Kolmogorov length scale, η_K, at location (a) $y/d = 5$, (b) $y/d = 20$, (c) $y/d = 40$ and (d) axially. With diff. diff. (D_1 and D_2): solid lines, with diff. diff. (only D_1): dotted lines, without diff. diff.: dashed lines.

7.6.2 Turbulent Schmidt and Prandtl numbers

Two important parameters in the LES calculations are the turbulent Schmidt, Sc_t, and Prandtl, Pr_t, numbers used in Equations (2.81) and (2.82) in order to calculate the turbulent species mass and thermal diffusivities, respectively. In Figure 7.15 results for different combinations of the turbulent Schmidt and Prandtl numbers are presented, in order to demonstrate the influence of these parameters on the temperature and species concentration profiles. The turbulent Schmidt number, Sc_t, directly influences the diffusion transport of species since it modifies the turbulent mass diffusivity of the species. On the other hand, the turbulent thermal diffusivity, Pr_t, has an influence on the diffusion of enthalpy (temperature). The most common values of these coefficients that appear in literature are 0.7 so the sensitivity study, presented below, is focused around this value. The influence of these two parameters was mostly evident close to the inlet so only results at location $y/d = 5$ are presented. It is clear that the most significant influence on the simulation results is that of the turbulent Prandtl number. A good agreement between simulations and experiments for the temperature profile is obtained with $Sc_t = 0.7,\ Pr_t = 0.6$ (Figure 7.15(a)) while, on the other hand, an increase of about 400 K in temperature is observed if $Sc_t = 0.7,\ Pr_t = 0.7$ is used.

7.6.3 Influence of diffusion terms D_1 and D_2

The magnitude of diffusion terms D_1 and D_2 in Eqs (3.13) is presented in Figures 7.16 and 7.17. Each of the D_1 and D_2 terms in the η_H and η_N conserved scalar equations depend on both η_H and η_N so the influence of each of the terms $D_1^{\eta_H}(\eta_H)$, $D_1^{\eta_H}(\eta_N)$, $D_2^{\eta_H}(\eta_H)$, $D_2^{\eta_H}(\eta_N)$ and $D_1^{\eta_N}(\eta_H)$, $D_1^{\eta_N}(\eta_N)$, $D_2^{\eta_N}(\eta_H)$, $D_2^{\eta_N}(\eta_N)$ will be analyzed. The results have been normalized by $D_1^{\eta_H}(\eta_H)$ and $D_1^{\eta_N}(\eta_N)$ for the terms related to the η_H and η_N conserved scalar equations, respectively.

Observations similar to the ones previously reported in chapter for the laminar H_2/N_2 flame (section 6.5.3) can be drawn here as well. The D_1 terms, expressing the diffusion between the conserved scalars, are always positive, causing η_H and η_N to diffuse. The strongest influence stems from the main diffusion terms ($D_1^{\eta_H}(\eta_H)$, $D_1^{\eta_N}(\eta_N)$) and less from the cross-diffusion terms ($D_1^{\eta_H}(\eta_N)$, $D_1^{\eta_N}(\eta_H)$). The D_2 terms, expressing the feedback from the combustion model, are positive at the rich side of the flame but negative at the lean side of the flame. This makes η_H and η_N to diffuse more in the core of the mixture (rich side of the flame) but reduces their diffusivity in regions outside the maximum flame temperature (lean side of the flame). In this case, the main diffusion terms $D_2^{\eta_H}(\eta_H)$ and

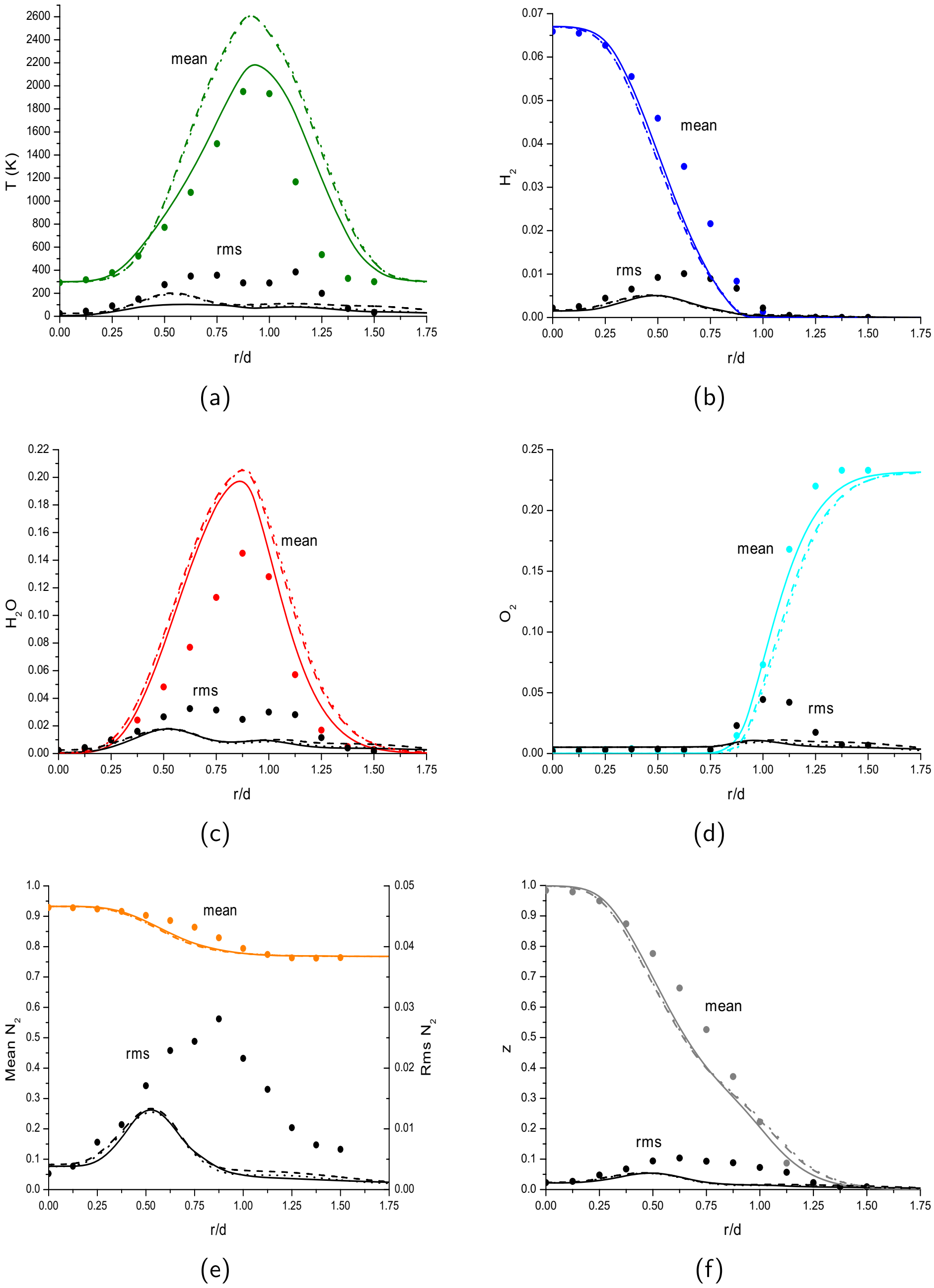

(a) (b)

(c) (d)

(e) (f)

Figure 7.15: Influence of turbulent Schmidt, Sc_t, and Prandtl, Pr_t, numbers on mean and rms results at location $y/d = 5$ for (a) T, (b) H_2, (c) H_2O, (d) O_2, (e) N_2 and (f) mixture fraction. Symbols: experimental data, solid lines: $Sc_t = 0.7$, $Pr_t = 0.6$, dashed lines: $Sc_t = 0.7$, $Pr_t = 0.7$, dotted lines: $Sc_t = 0.6$, $Pr_t = 0.6$.

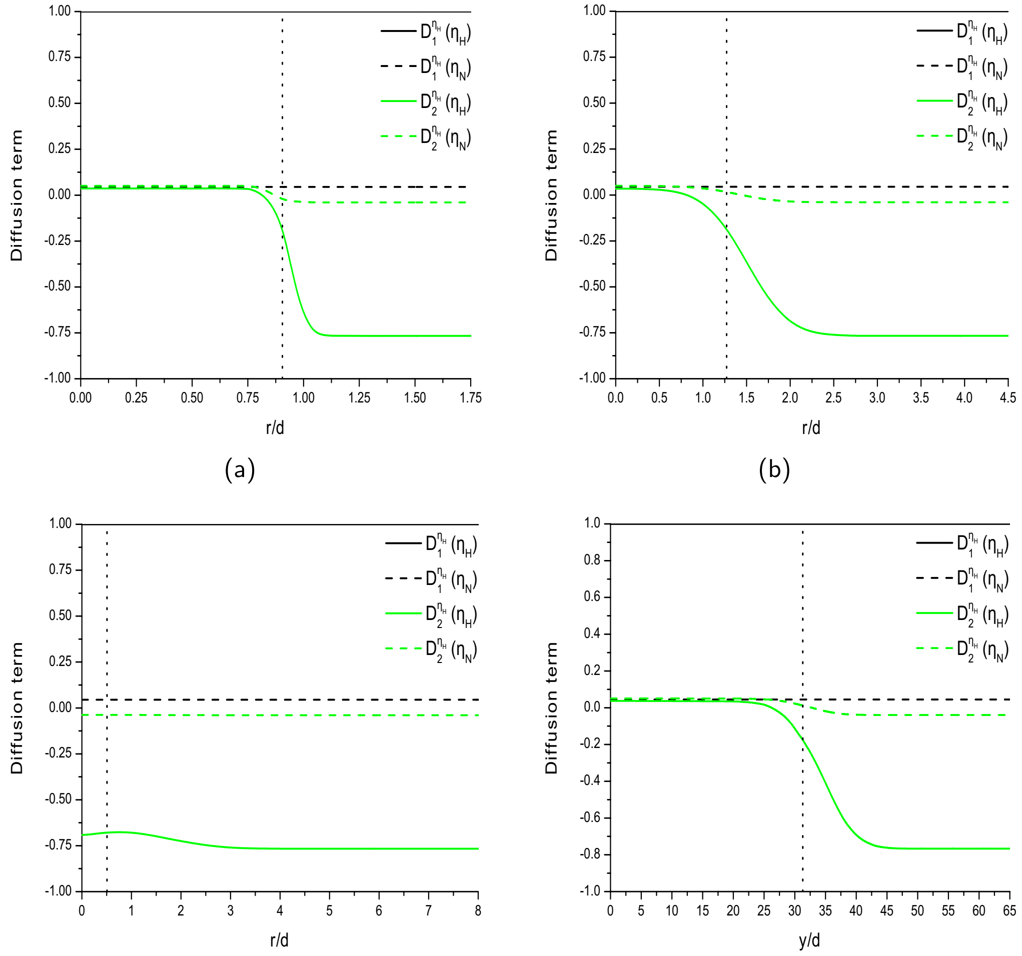

(a) (b)

(c) (d)

Figure 7.16: Magnitude of normalized diffusion terms D_1 and D_2 for η_H at location (a) $y/d = 5$, (b) $y/d = 20$, (c) $y/d = 40$ and (d) axially. The dotted black line indicates the location of the maximum flame temperature.

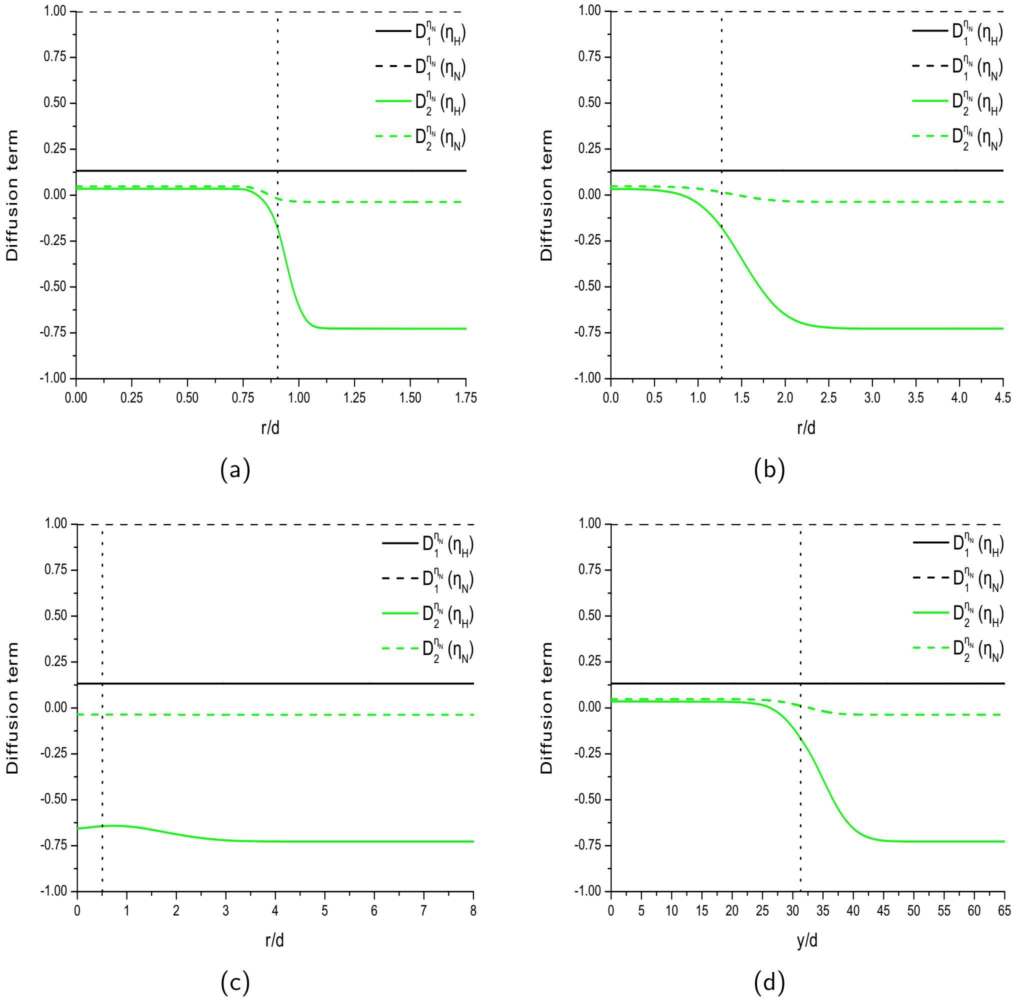

(a) (b)

(c) (d)

Figure 7.17: Magnitude of normalized diffusion terms D_1 and D_2 for η_N at location (a) $y/d = 5$, (b) $y/d = 20$, (c) $y/d = 40$ and (d) axially. The dotted black line indicates the location of the maximum flame temperature.

$D_2^{\eta_N}(\eta_H)$ are the predominant ones. The influence of the D_2 terms is also clearly obvious in Figures 7.15(d), 7.16(d) where they obtain large negative values at locations downstream from the maximum flame temperature, reducing the diffusion of the conserved scalars η_H and η_N on the centerline.

7.7 Conclusions

The extension of the methodology, previously described in [60] for laminar flames, to incorporate differential diffusion effects in CFD simulations of turbulent reactive flows has been presented and applied to the 'H3' benchmark flame [67, 83] from the Turbulent Non-premixed Flames (TNF) workshop. The main focus of the paper was to assess the accuracy of the proposed methodology but also to examine the influence of differential diffusion in the gas composition and maximum flame temperature in large eddy simulations of the 'H3' flame. Overall, there was a good agreement between numerical simulations and experiments, indicating that the newly proposed methodology is capable of accurately incorporating differential diffusion in numerical simulations of turbulent reactive flows.

There was a clear influence of differential diffusion in the stabilization mechanism of the 'H3' flame. If differential diffusion effects were considered the maximum flame temperature exceeded the adiabatic one and was obtained close to the inlet, at the edges of the jet. Ignoring differential diffusion effects, the maximum flame temperature was way below the adiabatic one and was found on the centerline, further downstream.

Differential diffusion had a big influence on the radial and axial profiles of temperature and species concentrations. If differential diffusion effects were ignored, the flame temperature was under-predicted by up to 400 K (20%) and the position of the maximum flame temperature was shifted more towards the lean side of the flame, at locations close to the inlet $(y/d = 2.5, 5, 10)$. In this case the distribution of main species (H_2, H_2O, O_2, N_2) was also not well captured. Differential diffusion effects were also present at location $y/d = 20$ even though their influence had significantly decreased. At locations $y/d > 20$ there were no significant differential diffusion effects present.

Results of the differential diffusion parameter $\xi = z_H - z_N$, defined as the difference between the elemental mass fractions of H and N, showed that differential diffusion effects were significant just on the left side of the stoichiometric conditions, on the lean side of the flame. This was caused by the higher diffusivity of H_2 towards the reaction zone which in turn produced more H_2O (combustion products), creating this way more H than N element at this location.

The influence of diffusion term D_2 was substantial close to the inlet ($y/d \leq 10$), limiting the radial diffusion of species and temperature on the lean side of the flame. Any discrepancies are attributed to the boundary condition chosen for generating fluctuations at the inlet ('white' noise), which cannot create turbulence with coherent structures and die relatively fast.

It is concluded that differential diffusion effects were important in the 'H3' flame, especially close to the nozzle but also to downstream locations up to $y/d = 20$. Differential diffusion had a significant influence on the gas composition but also on the maximum flame temperature, which in turn can affect the pollutant concentrations. It can, therefore, be important to include differential diffusion effects in numerical simulations of turbulent combustion in order to improve accuracy, especially if chemical species with vastly different properties are considered and/or laminarization of the flow occurs.

Chapter 8

Conclusions and future work

8.1 Conclusions

The thesis describes research undertaken into modelling differential diffusion in numerical simulations of flows involving hydrogen mixtures. The importance of incorporating differential diffusion was examined for both reactive and non-reactive flows, spanning from laminar to fully turbulent. Several documented experiments served as target cases where the importance of including differential diffusion in the numerical simulations was investigated.

An overview of the different ways of modelling differential diffusion in reactive flows was given in Chapter 1, along with the motivation and objectives of this thesis. The governing equations and the various sub-models used for the numerical simulation in the thesis were discussed in Chapter 2, while the development of the newly proposed methodology to incorporate differential diffusion effects in CFD simulations of reactive flows was presented in Chapter 3. Within this new methodology, the diffusion term in the transport equations of the conserved scalars consisted of two parts, one expressing the diffusion between the conserved scalars (diffusion term D_1) and the second expressing the feedback from the combustion model (diffusion term D_2). In addition, with the present methodology there was also a reduction of the number of transport equations to be solved from the number of species (minus one) to the number of elements (minus one).

In Chapter 4, a validation study of the CFD package FireFOAM 1.6, used for the numerical simulations in the thesis, was performed in order to examine the capabilities and accuracy of the solver in simulating turbulent flows. Large eddy simulations were conducted in the near-field region of a large turbulent buoyant helium plume and were compared to the well-documented experiment performed by O‘Hern et al. [79]. The transient and mean flow dynamics were discussed as a function of grid resolution, with and without the use of the standard Smagorinsky sub-grid scale (SGS) model. Small scale structures, formed at the edge of the plume inlet due to baroclinic and gravitational mechanisms and subject to flow instabilities, interacted with large scale features of the flow, resulting in a puffing cycle. In general, the LES calculations reproduced the main features of the turbulent plume, with better agreement when the Smagorinsky type SGS model was applied. In particular, the puffing cycle was recovered in the simulations with correct frequency. The mean and rms values of the velocity components were well predicted with use of the SGS model, even on relatively coarse meshes. Agreement for the species mass fraction (mean and rms values) was less satisfactory, but in line with results found in the literature.

In Chapter 5, large eddy simulations of non-reacting H_2/CO_2 jets mixing with air were performed and the calculations were compared with the experiments reported by Smith et al. [106]. The influence of differential diffusion effects for Reynolds numbers $Re = 1000 - 8000$ was analyzed and a differential diffusion parameter, ξ, was defined on the basis of normalized H_2 and CO_2 concentrations in order to quantify the effects of differential diffusion with increasing Reynolds number. The analysis was made not only in physical space but also with scatter plots and histograms. The simulation results revealed that differential diffusion effects were significant at downstream locations (more than 15 nozzle diameters away from the inlet) only for the lower Reynolds numbers ($Re = 1000 - 2000$). However, differential diffusion effects were present for all Reynolds numbers examined close to the inlet (closer than 10 nozzle diameters). This was confirmed by the mean results of the differential diffusion parameter, ξ, but also by looking at the histograms of ξ. This was an important indication that differential diffusion should be included in numerical simulations of turbulent reacting flows in order to improve accuracy. The H_2 concentrations were over-predicted by up to 50% on the centerline at all downstream locations examined.

In Chapter 6, the newly proposed methodology was applied to a laminar, axi-symmetric H_2/N_2 - air diffusion flame and the calculations were compared with the experimental data of Toro et al. [115]. If differential diffusion effects were taken into account, the comparison of the simulated results with the experimental data was very good for the temperature and main species mole fractions, at all locations examined. Without differential diffusion effects, the predicted results were not in good agreement with the experiments, due to lack of H_2 diffusion close to the jet inlet. This led to a wrong prediction of the location and the peak of the flame temperature but also to a strong over-prediction of the species mole fractions at all locations. Differential diffusion effects were present at the edges of the inlet, where H_2 diffused faster that the other species, but also on the centerline at locations more than ten inlet diameters downstream, where there was less H_2 compared to other species. The inclusion of the diffusion term D_2 was shown to be important in order to accurately predict the temperature and species mole fractions.

In Chapter 7, results from the application of the newly proposed methodology to the 'H3' benchmark flame [66, 83] from the Turbulent Non-premixed Flames (TNF) workshop were presented. The study focused on assessing the accuracy of the proposed methodology but also on examining the influence of differential diffusion in numerical simulations of turbulent reactive flows involving species with vastly different mass diffusivities. A good agreement was obtained between numerical simulations of the proposed methodology and experimental data if differential diffusion effects were considered. Differential diffusion effects were shown to be significant close to the inlet but also to downstream locations up to 20 nozzle diameters and had a great influence on the stabilization mechanism of the flame but also on the predicted profiles of temperature and species concentration. Temperatures above the adiabatic one were obtained if differential diffusion effects are considered, in line with what was reported in literature in the past, due to faster diffusion of H_2 towards the reaction zone, altering the gas composition at this location. On the other hand, large discrepancies between numerical simulations and experiments were found in the radial and axial profiles of temperature and species concentration if differential diffusion effects were ignored. The diffusion term D_2 was shown to have a substantial influence in the flow field of this test case as well. It was concluded that incorporation of differential diffusion in numerical simulations of turbulent reactive flows is necessary in order to improve accuracy.

The main conclusions and novelties of this thesis are:

- Development of a new methodology to incorporate differential diffusion effects in CFD simulations of reacting flows. It is a general methodology, easily programmable and can be used in conjunction with different combustion models (e.g. Burke-Schumann, equilibrium chemistry or a flamelet table). From the application of the methodology to laminar and turbulent hydrogen flames it was concluded that it is accurate enough when compared to other methods of incorporating differential diffusion effects in CFD simulations of reactive flows. The influence of the diffusion term D_2 (feedback from the combustion model) was shown to have a substantial influence in the flow field in all reacting test cases examined.

- There is substantial influence of differential diffusion in gas composition (non-reactive/ reactive flows), maximum flame temperature and stabilization mechanism of the flame (reactive flows), leading to the conclusion that inclusion of differential diffusion in CFD simulations of hydrogen mixtures is essential for improving accuracy. Including differential diffusion effects in numerical simulations of hydrogen combustion can, therefore, help towards the optimization of combustion devices used in practical applications (e.g. furnaces, diesel engines or gas turbines) by considering a more accurate description of the diffusion processes occurring within the combustion device. The profits of such optimized combustion devices can be both economic and ecologic for our society.

- A validation study of CFD package FireFOAM 1.6 has been performed. The validation of the code will be of great interest to the fire safety science community and will give the opportunity to more researchers to use it for fire and combustion applications.

8.2 Future work

In this thesis, a new methodology to incorporate differential diffusion effects in CFD simulations of reactive flows was presented. There is, however, a lot of further research that can be done in order to extend the methodology.

In the numerical simulations performed in the thesis, differential diffusion effects were only included in physical space (transport equations for the conserved scalars) and not in chemical space (in the combustion model). In this case, a simple combustion model, the Burke-Schumann solution, was used. A first step in extending the methodology would be to use it in conjunction with a more sophisticated combustion model (e.g. flamelet model). With the flamelet model, differential diffusion effects could then also be considered in chemical space and minor chemical species, like OH or NO, could be studied as well. A further interesting development would be to apply the methodology to a hydrocarbon flame where more chemical species and elements would be involved. In this case, a selection of which and how many transport equations for conserved scalars to be solved would have to be made.

Even though the focus of the research presented in the thesis was on non-premixed combustion, the methodology can be applied to premixed combustion applications as well. For example a transport equation for a progress variable could be included and would then be just one extra variable in the resolved space, which would then not only contain conserved scalars but also progress variables. In other words, the method presented is not restricted to conserved scalars.

Finally, several models and sub-models related to the diffusion process of scalars can be tested in order to examine their influence on the simulation results. More accurate expressions than assuming a constant species Schmidt number can be used for calculating the species mass diffusion coefficients, such as the expression proposed by Stefan (Eqs (2.14)). In addition, the Hirschfelder-Curtiss law (Eqs (2.13)) can be used to calculate the species molecular diffusive mass flux with the inclusion of the Soret effect.

Bibliography

[1] R.S. Barlow, G.J. Fiechtner, C.D. Carter, and J.-Y. Chen. Experiments on the scalar structure of turbulent $CO/H_2/N_2$ jet flames. *Combust. Flame*, 120:549–569, 2000.

[2] B.A.V. Bennett, C.S. McEnally, L.D. Pfefferle, and M.D. Smooke. Computational and experimental study of axisymmetric coflow partially premixed methane-air flames. *Combust. Flame*, 23:522–546, 2000.

[3] V. Bergmann, W. Meier, D. Wolff, and W. Stricker. Application of spontaneous Raman and Rayleigh scattering and 2D LIF for the characterization of a turbulent $CH_4/H_2/N_2$ jet diffusion flame. *Applied Physics B: Lasers and Optics*, 66:489–502, 1998.

[4] R.W. Bilger. Molecular transport effects in turbulent diffusion flames at moderate Reynolds number. *AIAA J.*, 20:962–970, 1981.

[5] R.W. Bilger and R.W. Dibble. Differential molecular diffusion effects in turbulent mixing. *Combust. Sci. Technol.*, 28:161–172, 1982.

[6] R.W. Bilger, S.H. Ståarner, and R.J. Kee. On reduced mechanisms for methane-air combustion in nonpremixed flames. *Combust. Flame*, 80:135–149, 1990.

[7] R.B. Bird, W.E. Stewart, and E.N. Lightfoot. *Transport phenomena*. John Wiley and Sons, Inc., New York, USA, 1960.

[8] T.K. Blanchat. Characterization of the air source and plume source at FLAME. *Technical report SAND2005-2227, Sandia National Laboratory, Albuquerque, NM*, 2001.

[9] S.P. Burke and T.E.W. Schumann. Diffusion flames. *Industrial and Engineering Chemistry*, 20:998–1005, 1928.

[10] G.C. Burton. Large eddy simulation of a turbulent helium-air plume using the nLES method. *Center for turbulence research, Stanford University and NASA-Ames research center, Stanford, CA*, 2009.

[11] B.M. Cetegen and T.A. Ahmed. Experiments on the periodic instability of buoyant plumes and pool fires. *Combust. Flame*, 93:157–184, 1993.

[12] B.M. Cetegen and K.D. Kasper. Experiments on the oscillatory behavior of buoyant plumes of helium and helium-air mixtures. *Phys. Fluids*, 8:2974–2984, 1996.

[13] J.-Y. Chen and W.-C. Chang. Modeling differential diffusion effects in turbulent nonreacting/reacting jets with stochastic mixing models. *Combust. Sci. Technol.*, 133:343–375, 1998.

[14] W. Chung and C.B. Devaud. Buoyancy corrected k-ε models and large eddy simulation applied to a large axisymmetric helium plume. *Intl. J. Num. Meth. Fluids*, 58:57–89, 2008.

[15] G. da S. Lorenzzetti, F.A. Vaz, and Á.L. de Bortoli. An analytical solution for hydrogen/nitrogen jet diffusion flames. *Asociación Argentina de Mecánica Computacional*, XXIX:2399–2405, 2010.

[16] J.A.M. de Swart, R.J.M. Bastiaans, J.A. van Oijen, L.P.H. de Goey, and R.S. Cant. Inclusion of preferential diffusion in simulations of premixed combustion of hydrogen/methane mixtures with flamelet generated manifolds. *Flow Turb. Combust.*, 85:473–511, 2010.

[17] S. Delhaye, L. Somers, J.A. van Oijen, and L.P.H. de Goey. Incorporating unsteady flow-effects in flamelet-generated manifolds. *Combust. Flame*, 155:133–144, 2008.

[18] P.E. DesJardin, T.J. O'Hern, and S.R. Tieszen. Large eddy simulation and experimental measurements of the near-field of a large turbulent helium plume. *Phys. Fluids*, 16:1866–1883, 2004.

[19] R.W. Dibble and M.B. Long. Investigation of differential diffusion in turbulent jet flows using planar Rayleigh scattering. *Combust. Flame*, 143:644–649, 2005.

[20] M.C. Drake, M. Lapp, C.M. Penney, and S. Warshaw. Measurements of temperature and concentration fluctuations in turbulent diffusion flames using pulsed Raman spectroscopy. *Proc. Combust. Inst.*, 18:1521–1532, 1981.

[21] M.C. Drake, R.W. Pitz, and M. Lapp. Laser measurements on nonpremixed H_2-air flames for assessment of turbulent combustion models. *AIAA J.*, 24:905–917, 1986.

[22] T. Echekki, A.R. Kerstein, and T.D. Dreeben. 'one-Dimensional turbulence' simulation of turbulent jet diffusion flames: Model formulation and illustrative applications. *Combust. Flame*, 125:1083–1105, 2001.

[23] F. Flemming, A. Nauert, A. Sadiki, J. Janicka, H. Brick, R. Piscoya, M. Ochmann, and P. K$\ddot{o}$ltzsch. A hybrid approach for the evaluation of the radiated noise from a turbulent non-premixed jet flame based on large eddy simulation and equivalent source & boundary element methods. *International Congress on Sound and Vibration*, 12, 2005.

[24] H. Forkel and J. Janicka. Large-eddy simulations of a turbulent hydrogen diffusion flame. *Flow Turb. Combust.*, 65:163–175, 2000.

[25] R.O. Fox. The lagrangian spectral relaxation model for differential diffusion in homogeneous turbulence. *Phys. Fluids*, 11:1550–1571, 1999.

[26] C. Fureby and G. Tabor. Mathematical and physical constrains on large-eddy simulations. *Theoret. Comput. Fluid Dynamics*, 9:85–102, 1997.

[27] E. Garnier, P. Sagaut, and N. Adams. *Large Eddy Simulation for Compressible Flows*. Springer, 2009.

[28] M. Germano, U. Piomelli, P. Moin, and W.H. Cabot. A dynamic subgrid-scale eddy viscosity model. *Phys. Fluids*, 3:1760–1765, 1991.

[29] E. Giacomazzi, F.R. Picchia, and N. Arcidiacono. A review of chemical diffusion: Criticism and limits of simplified methods for diffusion coefficient calculation. *Comb. Theory Model.*, 12:135–158, 2008.

[30] O. Gicquel, D. Thévenin, and N. Darabiha. Influence of differential diffusion on super equilibrium temperatures in turbulent non-premixed hydrogen/air flames. *Flow Turb. Combust.*, 73:307–321, 2004.

[31] T.K. Gimmett. *A DNS study of differential diffusion in nonpremixed reacting turbulent flows using a generalized Burke-Schumann formulation*. PhD thesis, University of California, 2001.

[32] R.D. Hancock, F.R. Schauer, R.P. Lucht, V. R. Katta, and K.Y. Hsu. Thermal diffusion effects and vortex-flame interactions in hydrogen set diffusion flames. *Proc. Combust. Inst.*, 26:1087–1093, 1996.

[33] R. Hilbert and D. Thévenin. Influence of differential diffusion on maximum flame temperature in turbulent nonpremixed hydrogen/air flames. *Combust. Flame*, 138:175–187, 2004.

[34] J.O. Hirschfelder, C.F. Curtiss, and R.B. Bird. *The molecular theory of gases and liquids*. Wiley, 1954.

[35] http://code.google.com/p/fds smv/.

[36] http://code.google.com/p/firefoam dev.

[37] http://www.fmglobal.com/modelling.

[38] http://www.openfoam.com.

[39] M. Ihme and H. Pitsch. Prediction of extinction and reignition in non-premixed turbulent flames using a flamelet/progress variable model. 1. A priori study and presumed PDF closure. *Combust. Flame*, 155:70–89, 2008.

[40] R.I. Issa, A.D. Gosman, and A.P. Watkins. The computation of compressible and incompressible recirculating-flows by a non-iterative implicit scheme. *J. Comput. Phys.*, 62:66–82, 1986.

[41] F.A. Jaberi, R.S. Miller, F. Mashayek, and P. Givi. Differential diffusion in binary scalar mixing and reaction. *Combust. Flame*, 109:561–577, 1997.

[42] X. Jiang and K.H. Luo. Spatial direct numerical simulation of the large vortical structures in forced plumes. *Flow Turb. Combust.*, 64:43–69, 2000.

[43] X. Jiang and K.H. Luo. Spatial DNS of flow transition of a rectangular buoyant reacting free-jet. *Proc. Combust. Inst.*, 28:1989–1995, 2000.

[44] X. Jiang and K.H. Luo. Dynamics and structure of transitional buoyant jet diffusion flames with side-wall effects. *Combust. Flame*, 133:29–45, 2003.

[45] V. R. Katta and L.P. Goss. Effects of non-unity lewis number and finite-rate chemistry on the dynamics of a hydrogen - air diffusion flame. *Combust. Flame*, 96:60–74, 1994.

[46] A.R. Kerstein. Linear-eddy modeling of turbulent transport. Part 3: Mixing and differential molecular diffusion in round jets. *J. Fluid Mech.*, 216:411–435, 1990.

[47] A.R. Kerstein, M.A. Cremer, and P.A. McMurtry. Scaling properties of differential molecular diffusion effects in turbulence. *Phys. Fluids.*, 7:1999–2008, 1995.

[48] A.R. Kerstein, R.W. Dibble, M.B. Long, B. Yip, and K. Lyonsi. Measurements and computation of differential molecular diffusion in a turbulent jet. *Proc. Seventh Symp. on Turbulent Shear Flows*, 1:14.2.1–14.2.5, 1989.

[49] J.S. Kim, J. Park, O.B. Kwon, J.H. Jun, S.I. Keel, and T.K. Kim. Preferential diffusion effects on NO formation in methane/hydrogen-air diffusion flames. *Energy & Fuels.*, 22:278–283, 2008.

[50] J.S. Kim, J. Park, O.B. Kwon, E.J. Lee, J.H. Yun, and S.I. Keel. Preferential diffusion effects in opposed-flow diffusion flame with blended fuels of CH_4 and H_2. *Comb. Theory Model.*, 12:135–158, 2008.

[51] S.H. Kim and H. Pitsch. Conditional filtering method for large-eddy simulation of turbulent nonpremixed combustion. *Phys. Fluids*, 17:105103, 2005.

[52] A.Y. Klimenko and R.W. Bilger. Conditional moment closure for turbulent combustion. *Prog. Energy Combust. Sci.*, 25:595–687, 1999.

[53] A. Kronenburg and R.W. Bilger. Modelling of differential diffusion effects in non-premixed non-reacting turbulent flow. *Phys. Fluids*, 9:1435–1447, 1997.

[54] A. Kronenburg and R.W. Bilger. Modelling differential diffusion in nonpremixed reacting turbulent flow: Model development. *Combust. Sci. Technol.*, 166:195–227, 2001.

[55] T. Landenfeld, A. Sadiki, and J. Janicka. A turbulence-chemistry interaction model based on a multivariate presumed beta-PDF method for turbulent flames. *Flow Turb. Combust.*, 68:111–135, 2002.

[56] T. Lavertu, W. Pohl, S.J. Gaskin, and L. Mydlarsk. Punctual and planar measurements of differential diffusion in a turbulent jet. *Advances in Turbulence X: Proceedings of the 10th European Turbulence Conference*, pages 1–4, 2004.

[57] P.A. Libby and F.A. Williams. *Turbulent reacting flows*. Springer, 1980.

[58] M.B. Long, S.H. Starner, and R.W. Bilger. Differential diffusion in jets using joint PLIF and Lorenz-Mie imaging. *Combust. Sci. Technol.*, 92:209–224, 1993.

[59] G. Maragkos, P. Rauwoens, and B. Merci. Application of FDS and FireFOAM in Large Eddy Simulations of a Turbulent Buoyant Helium Plume. *Combust. Sci. Technol.*, 184:1108–1120, 2012.

[60] G. Maragkos, P. Rauwoens, and B. Merci. A new methodology to incorporate differential diffusion in CFD simulations of reactive flows. *Combust. Flame*, 160:1903–1905, 2013.

[61] G. Maragkos, P. Rauwoens, Y. Wang, and B. Merci. Large eddy simulations of the flow in the near-field region of a turbulent buoyant helium plume. *Flow Turb. Combust.*, 90:511–543, 2013.

[62] A.R. Masri, R.W. Dibble, and R.S. Barlow. Chemical kinetic effects in nonpremixed flames of H_2/CO_2 fuel. *Combust. Flame*, 91:285–309, 1992.

[63] R. McDermott and S.B. Pope. A particle formulation for treating differential diffusion in filtered density function methods. *J. Comput. Phys.*, 226:947–993, 2007.

[64] B. Mühlbauer, R. Ewert, O. Kornow, and B. Noll. Broadband combustion noise simulation of open non-premixed turbulent jet flames. *Int. J. Aeroacoust.*, 11:1–24, 2012.

[65] W. Meier, R.S. Barlow, Y.-L. Chen, and J.-Y. Chen. Raman/Rayleigh/LIF measurements in a turbulent $CH_4/H_2/N_2$ diffusion flame: Experimental techniques and turbulence - chemistry interaction. *Combust. Flame*, 123:326–343, 2000.

[66] W. Meier, S. Prucker, M.-H. Cao, and W. Stricker. Characterization of turbulent H_2/N_2/air jet diffusion flames by single-pulse spontaneous raman scattering. *Combust. Sci. Technol.*, 118:293–312, 1996.

[67] W. Meier, A.O. Vydorov, V. Bergmann, and W. Stricker. Simultaneous Raman/LIF measurements of major species and no in turbulent H_2/air diffusion flames. *Appl. Phys. B*, 63:79–90, 1996.

[68] A. Menon and M. Rizk. Large-eddy simulations of forced three-dimensional impinging jets. *Int. J. Comput. Fluid Dyn.*, 7:275–289, 1996.

[69] D.W. Meyer. A new particle interaction mixing model for turbulent dispersion and turbulent reactive flows. *Phys. Fluids*, 22:035103, 2010.

[70] J.A. Miller and R.J. Kee. Chemical non-equilibrium effects in hydrogen-air laminar jet diffusion flames. *J. Phys. Chem.*, 81:2534–2542, 1977.

[71] R.K. Mohammed, M.A. Tanoff, and M.D. Smooke. Computational and experimental study of a forced, timevarying, axisymmetric, laminar diffusion flame. *Proc. Combust. Inst.*, 27:693–702, 1998.

[72] P. Moin. Advances in large eddy simulation methodology for complex flows. *Int. J. Heat Fluid Flow*, 23:710–720, 2002.

[73] A.V. Mokhov, B.A.V. Bennett, H.B. Levinsky, and M.D. Smooke. Experimental and computational study of C_2H_2 and CO in a laminar axisymmetric methane-air diffusion flame. *Proc. Combust. Inst.*, 31:997–1004, 2007.

[74] A. Neuber, G. Krieger, M. Tacke, E. Hassel, and J. Janicka. Finite rate chemistry and NO molefraction in non-premixed turbulent flames. *Combust. Flame*, 113:198–211, 1998.

[75] V.F. Nicolette, S.R. Tieszen, S.P. Domino, A.R. Black, and T.J. O'Hern. A turbulence model for buoyant flows based on vorticity generation. *Technical report SAND2005-6273, Sandia National Laboratory, Albuquerque, NM*, 2005.

[76] V. Nilsen and G. Kosály. Differentially diffusing scalars in turbulence. *Phys. Fluids*, 9:3386–3397, 1997.

[77] V. Nilsen and G. Kosály. Differential diffusion in turbulent reacting flows. *Combust. Flame*, 117:493–513, 1999.

[78] S.A. Northrup and C.P.T. Groth. Solution of laminar combusting flows using a parallel implicit adaptive mesh refinement algorithm. *Comp. Fluid Dyn.*, 4:341–346, 2009.

[79] T.J. O'Hern, E.J. Weckman, A.L. Gerhart, S.R. Tieszen, and R.W. Schefer. Experimental study of a turbulent buoyant helium plume. *J. Fluid Mech*, 544:143–171, 2005.

[80] P.N. Papanikolaou and E.J. List. Investigations of round vertical turbulent buoyant jets. *J. Fluid Mech.*, 195:341–391, 1988.

[81] N. Peters. Laminar diffusion flamelet models in non-premixed turbulent combustion. *Prog. Energy Combust. Sci.*, 10:319–339, 1984.

[82] N. Peters. *Turbulent combustion*. Cambridge University press, 2000.

[83] D.G. Pfuderer, A.A. Neuber, G. Früchtel, E.P. Hassel, and J. Janicka. Turbulence modulation in jet diffusion flames: Modeling and experiments. *Combust. Flame*, 106:301–317, 1996.

[84] M.V. Pham, F. Plourde, and K.S. Doan. Direct and large eddy simulations of a pure thermal plume. *Phys. Fluids*, 19:125103, 2007.

[85] C.D. Pierce. *Progress-variable approach for large-eddy simulation of non-premixed turbulent combustion*. PhD thesis, Stanford University, 2001.

[86] C.D. Pierce and P. Moin. Progress-variable approach for large-eddy simulation of non-premixed turbulent combustion. *J. Fluid. Mech.*, 504:73–97, 2004.

[87] H. Pitsch. Unsteady flamelet modeling of differential diffusion in turbulent jet diffusion flames. *Combust. Flame*, 123:358–374, 2000.

[88] H. Pitsch. Large-eddy simulation of a turbulent combustion. *Annu. Rev. Fluid Mech.*, 38:453–482, 2006.

[89] H. Pitsch and N. Peters. A consistent flamelet formulation for non-premixed combustion considering differential diffusion effects. *Combust. Flame*, 114:26–40, 1998.

[90] T. Poinsot and D. Veynante. *Theoretical and Numerical combustion*. Edwards, Philadelphia, USA, 2005.

[91] S. B. Pope. *Turbulent Flows*. Cambridge University Press, 2000.

[92] S.B. Pope. PDF methods for turbulent reactive flows. *Prog. Energy Combust. Sci.*, 11:119–192, 1985.

[93] S.B. Pope. Computations of turbulent combustion: Progress and challenges. *Proc. Combust. Inst.*, 23:591–612, 1990.

[94] B. Ranganath and T. Echekki. One-dimensional turbulence-based closure for turbulent non-premixed flames. *Prog. Comput. Fluid Dyn.*, 6:409–418, 2006.

[95] M.W. Renfro, A. Chaturvedy, G.B. King, N.M. Laurendeau, A. Kempf, A. Dreizler, A. Sadiki, and J. Janicka. Comparison of OH time-series measurements and large-eddy simulations in hydrogen jet flames. *Combust. Flame*, 139:142–151, 2004.

[96] C.M. Rhie and W.L.Chow. Numerical study of the turbulent flow past an airfoil with trailing edge separation. *AIAA J.*, 21:1525–1532, 1983.

[97] E.S. Richardson and J.H Chen. Application of PDF mixing models to premixed flames with differential diffusion. *Combust. Flame*, 159:2398–2414, 2012.

[98] A.L. Sánchez, A. Liná, and F.A. Williams. A generalized burke-schumann formulation for hydrogen-oxygen diffusion flames maintaining partial equilibrium of the shuffle reactions. *Combust. Sci. Technol.*, 123:317–345, 1997.

[99] S.C. Saxena. Viscosity of multicomponent mixtures of gases. *Proceedings of the 6th Symposium on Thermophysical Properties*, pages 100–110, 1973.

[100] J.R. Saylor and K R. Sreenivasan. Differential diffusion in low reynolds number water jets. *Combust. Sci. Technol.*, 10:1135–1146, 1998.

[101] T. Schmitt, Y. Méry, M. Boileau, and S. Candel. Large-eddy simulation of oxygen/methane flames under transcritical conditions. *Proc. Combust. Inst.*, 33:1383–1390, 2011.

[102] U. Schumann. Subgrid scale model for finite differences simulation of turbulent flows in plane channels and annuli. *J. Comput. Phys.*, 18:376–404, 1975.

[103] A. Shabbir and W.K. George. Experiments on a round turbulent buoyant plume. *J. Fluid Mech.*, 275:1–32, 1994.

[104] J. Smagorinsky. General circulation experiments with the primitive equations. I. The basic experiment. *Mon. Weather Rev.*, 91:99–164, 1963.

[105] L.L. Smith, R.W. Dibble, L. Talbot, R.S. Barlow, and C.D. Caner. Laser Raman scattering measurements of differential diffusion in nonreacting and reacting laminar and turbulent jet flow. *31st Aerospace Science Meeting & Exhibit.*, AIAA-93-0804, 1993.

[106] L.L. Smith, R.W. Dibble, L. Talbot, R.S. Barlow, and C.D. Carter. Laser Raman scattering measurements of differential molecular diffusion in turbulent non-premixed jet flames of H_2/CO_2 fuel. *Combust. Flame*, 100:153–160, 1995.

[107] L.L. Smith, R.W. Dibble, L. Talbot, R.S. Barlow, and C.D. Carter. Laser Raman scattering measurements of differential molecular diffusion in turbulent nonpremixed jet flames of H_2/CO_2 fuel. *Combust. Flame*, 100:153–160, 1995.

[108] M.D. Smooke, Y. Xu, R.M. Zurn, P. Lin, J.H. Frank, and M.B. Long. Computational and experimental study of OH and CH radicals in axisymmetric laminar diffusion flames. *Proc. Combust. Inst.*, 24:813–821, 1992.

[109] M.C. Soteriou, Y. Dong, and B.M. Cetegen. Lagrangian simulation of unsteady near-field dynamics of planar buoyant plumes. *Phys. Fluids*, 14:3118–3140, 2002.

[110] J. Stefan. *Sitzungsberichte Akad. Wiss Wien*, 68:325, 1874.

[111] J.C. Sutherland, P.J. Smith, and J.H. Chen. Quantification of differential diffusion in nonpremixed systems. *Combust. Theory Model.*, 9:365–383, 2005.

[112] T. Takagi and Z. Xu. Numerical analysis of laminar diffusion flames - Effects of preferential diffusion of heat and species. *Combust. Flame*, 96:50–59, 1994.

[113] T. Takagi, Z. Xu, and M. Komiyama. Preferential diffusion effects on the temperature in usual and inverse diffusion flames. *Combust. Flame*, 106:252–260, 1996.

[114] S.R. Tieszen, S.P. Domino, and A.R. Black. Validation of a simple turbulence model suitable for closure of temporally-filtered Navier-Stokes equations using a helium plume. *Technical report SAND2005-3210, Sandia National Laboratory, Albuquerque, NM*, 2005.

[115] V.V. Toro, A.V. Mokhov, H.B. Levinsky, and M.D. Smooke. Combined experimental and computational study of laminar, axisymmetric hydrogen-air diffusion flames. *Proc. Combust. Inst.*, 30:485–492, 2005.

[116] M. Ulitsky, T. Vaithianathan, and L.R. Collins. A spectral study of differential diffusion of passive scalars in isotropic turbulence. *J. Fluid Mech.*, 460:1–38, 2002.

[117] J.A. van Oijen and L.P.H. de Goey. Modelling of premixed counterflow flames using the flamelet-generated manifold method. *Combust. Theory Model.*, 6:463–478, 2002.

[118] J.A. van Oijen, F.A. Lammers, and L.P.H. de Goey. Modeling of complex premixed burner systems by using flamelet-generated manifolds. *Combust. Flame*, 127:2124–2134, 2001.

[119] S. Verhelst and T. Wallner. Hydrogen-fueled internal combustion engines. *Prog. Energy Combust. Sci.*, 35:490–527, 2009.

[120] L.M. Verhoeven, W.J.S. Ramaekers, J.A. van Oijen, and L.P.H. de Goey. Modeling non-premixed laminar co-flow flames using flamelet-generated manifolds. *Combust. Flame*, 159:230–241, 2012.

[121] Y. Wang, P. Chatterjee, and J.L. de Ris. Large eddy simulation of fire plumes. *Proc. Combust. Inst.*, 33:2473–2480, 2011.

[122] Y. Wang, P. Chatterjee, and J.L. de Ris. Large eddy simulation of thermal and fire plumes. *Proc. International Seminar on Fire and Explosion Hazards*, 6:267–278, 2011.

[123] E.J. Weckman and A. Sobiesiak. The oscillatory behavior of medium-scale pool fires. *Proc. Combust. Inst.*, 22:1299–1310, 1998.

[124] H.G. Weller, G. Tabor, H. Jasak, and C. Fureby. A tensorial approach to computational continuum mechanics using object orientated techniques. *Comput. Phys.*, 12:620–631, 1998.

[125] F.A. Williams. *Combustion Theory (Second edition)*. Cambridge: Perseus Books, 1985.

[126] TNF. International workshop on measurements and computation of turbulent non-premixed flames. http://www.ca.sandia.gov/TNF.

[127] C.Y. Wu, C.P. Chen, Y. H. Li, Y.C. Chao, T. Yuan, and T.S. Leu. Detailed measurement and assessment of laminar hydrogen jet diffusion flames. *Combust. Flame*, 146:268–282, 2005.

[128] P. K. Yeung. Multi-scalar triadic interactions in differential diffusion with and without mean scalar gradients. *J. Fluid Mech.*, 321:235–278, 1996.

[129] P.K. Yeung. Correlations and conditional statistics in differential diffusion: Scalars with uniform mean gradients. *Phys. Fluids*, 10:2621–2635, 1998.

[130] P.K. Yeung and S.B. Pope. Differential diffusion of passive scalars in isotropic turbulence. *Phys. Fluids A*, 5:2467–2478, 1993.

[131] P.K. Yeung, M.C. Sykes, and P. Vedula. Direct numerical simulation of differential diffusion with schmidt numbers up to 4.0. *Phys. Fluids*, 12:1601–1604, 2000.

[132] X. Zhou, K.H. Luo, and J.J.R. Williams. Large-eddy simulation of turbulent forced plume. *Eur. J. Mech. B Fluids*, 20:233–254, 2001.